

***IN SITU* SENSING FOR CHEMICAL VAPOR
DEPOSITION BASED ON STATE ESTIMATION
THEORY**

A Thesis
Presented to
The Academic Faculty

by

Rentian Xiong

In Partial Fulfillment
of the Requirements for the Degree
Doctor of Philosophy in the
School of Chemical & Biomolecular Engineering

Georgia Institute of Technology
April 2008

***IN SITU* SENSING FOR CHEMICAL VAPOR
DEPOSITION BASED ON STATE ESTIMATION
THEORY**

Approved by:

Professor Martha Gallivan,
Committee Chair
School of Chemical & Biomolecular
Engineering
Georgia Institute of Technology

Professor Dennis Hess
School of Chemical & Biomolecular
Engineering
Georgia Institute of Technology

Professor Cliff Henderson
School of Chemical & Biomolecular
Engineering
Georgia Institute of Technology

Professor Jay Lee
School of Chemical & Biomolecular
Engineering
Georgia Institute of Technology

Professor Ian Ferguson
School of Electrical and Computer
Engineering
Georgia Institute of Technology

Date Approved: 4 December 2007

To my wife,

Meguru,

who supported me throughout this entire venture.

ACKNOWLEDGEMENTS

First and foremost, I would like to extend my deepest appreciation to my thesis advisor, Dr. Martha Grover Gallivan, for her tremendous support, guidance, and encouragement throughout my PhD research. I feel very fortunate to be Dr. Gallivan's student and to work on this very challenging project. It is through this project that I gained a wide breadth of knowledge and scientific skills. I firmly believe that I will continue to benefit from this experience in the future and because of this, I am forever indebted to my advisor Dr. Gallivan.

I would like to thank my other committee members, Dr. Dennis W. Hess, Dr. Jay H. Lee, Dr. Clifford L. Henderson and Dr. Ian Ferguson for taking their time to review this thesis.

I would like to say a special thanks to my machinist friends, Jeffery Andrews and Brad Parker, for their tremendous help in building and improving the chemical vapor deposition testbed. I would like to thank my labmate, Paul Wissmann, for sharing my struggles in making the CVD system work. I wish him best of luck with his own PhD studies. I would like to thank two undergraduate students, Derek Jamrog and Matthew Jolissaint, for their assistance with running the CVD experiments and thin film characterization. I would also like to thank Dr. Ashwini Sinha for teaching me to use the ellipsometer and for his constructive discussions on thin film technology.

I would like to thank my group members, Dr. Cihan Oguz, Jonathan Rawlston, and Andres Felipe Hernandez Moreno for their warm friendship.

I would like to thank my parents for their love, support and encouragement to pursue my dream. Finally I would like to thank my wife, Meguru, for all the wonderful things she has brought into my life, and my baby daughter, Natsumi, for putting a

big smile on my face.

This work was supported by National Science Foundation through CAREER grant *A Systems Approach to Materials Processing* and by the Georgia Tech Foundation.

TABLE OF CONTENTS

DEDICATION	iii
ACKNOWLEDGEMENTS	iv
LIST OF TABLES	ix
LIST OF FIGURES	x
SUMMARY	xvi
I INTRODUCTION	1
1.1 Overview of <i>in situ</i> sensing for chemical vapor deposition	1
1.2 <i>In situ</i> sensor data interpretation	7
1.3 Objective and chapter outline	10
II CHEMICAL VAPOR DEPOSITION TESTBED	12
2.1 Hardware	12
2.1.1 Upstream	12
2.1.2 Deposition chamber	18
2.1.3 <i>In situ</i> sensor	26
2.1.4 Downstream	29
2.2 Software	30
2.2.1 Gas flow sub-program	35
2.2.2 Pressure sub-program	35
2.2.3 Power supply sub-program	36
2.2.4 Temperature and solenoid valve sub-program	37
2.2.5 Emissivity-correcting pyrometer sub-program	38
2.2.6 UV spectrometer sub-program	41
2.2.7 Data logging sub-program	41
2.3 Operation of CVD system	42

III	SENSOR MODELS AND OBSERVABILITY	45
	3.1 Sensor models	45
	3.1.1 Reflection on film/substrate with smooth surface	45
	3.1.2 Scalar scattering model	47
	3.1.3 Effective medium model	49
	3.2 Sensor model validation	51
	3.3 Effects of film parameters on reflectance	64
	3.4 Observability	69
IV	STATE ESTIMATORS	74
	4.1 Batch least squares fitting	74
	4.2 Recursive least squares fitting	75
	4.3 Moving horizon estimation	77
	4.4 Modified moving horizon estimator	81
	4.5 Extended Kalman filter	82
V	SIMULATION	84
	5.1 Process model mismatch	84
	5.1.1 Single-wavelength reflection on smooth surface	84
	5.1.2 Dual-wavelength reflection on smooth surface	93
	5.1.3 Dual-wavelength reflection on rough surface	102
	5.2 Sensor model mismatch	112
	5.2.1 Single-wavelength reflection on smooth surface	112
	5.2.2 Dual-wavelength reflection on smooth surface	117
VI	EXPERIMENTAL	125
	6.1 Practical issues in the experimental data	125
	6.2 Dual-wavelength reflection on smooth surface	130
	6.3 Dual-wavelength reflection on rough surface	139
	6.4 Additional example	148

VII	CONCLUSIONS AND FUTURE WORK	161
7.1	Conclusions	161
7.2	Future work	163
APPENDIX A	IN-SITU 4000 COM PORT PROTOCOL	166
APPENDIX B	CVD PROCEDURE	168
REFERENCES	174
VITA	192

LIST OF TABLES

1	Precursor material properties. Vapor pressure can be found in [48]. . .	15
2	<i>Ex situ</i> AFM and ellipsometer characterization and optical model validation results.	56
3	Average estimation error by RLS and mMHE with different horizon size. Process dynamic model mismatch	90
4	Estimation error by mMHE at $N = 10$ with different $P_{1 0}$, Q , and R .	112
5	Average estimation error by RLS and mMHE with different horizon size. Sensor model mismatch	117
6	Experimental conditions. Ar2 is main carrier argon, Ar3 is precursor carrier argon, Ar5 is dummy argon. See Fig. 1 for details.	130
7	Estimated states at the end of the growth and <i>ex situ</i> ellipsometry characterization. The sensor model is based on dual-wavelength reflection on a smooth surface. This film was deposited on 10/1/2007.	135
8	Estimated states at the end of the growth and <i>ex situ</i> ellipsometry characterization. The sensor model is based on dual-wavelength reflection on a rough surface. This film was deposited on 10/1/2007.	143
9	Estimated states at end point by mMHE at $N = 10$ with different $P_{1 0}$, Q , and R	145
10	Estimated states at the end of the growth and <i>ex situ</i> ellipsometry characterization. The sensor model is based on dual-wavelength reflection on a smooth surface. This film was deposited on 10/3/2007.	151
11	Estimated states at the end of the growth and <i>ex situ</i> ellipsometry characterization. The sensor model is based on dual-wavelength reflection on a rough surface. This film was deposited on 10/3/2007.	156

LIST OF FIGURES

1	Schematic of the chemical vapor deposition testbed.	13
2	Photograph of the chemical vapor deposition testbed.	14
3	photograph of the chemical vapor deposition chamber.	19
4	Cross view of the chemical vapor deposition chamber.	20
5	Velocity field inside the deposition chamber.	21
6	Pressure rising curve with 1000 SCCM argon.	22
7	photograph of the heater assembly.	24
8	Reflectance change in a heating-cooling cycle experiment. Silicon substrate is on bare heater surface (Date acquired: 3/10/2006).	25
9	Temperature profile on the heater surface.	27
10	Temperature profile on the heater surface with a copper thermal diffuse plate.	27
11	Reflectance change in a heating-cooling cycle experiment. Silicon substrate is on an Inconel thermal diffuse plate (Date acquired: 4/24/2007).	28
12	photograph of the emissivity-correcting pyrometer.	30
13	Wiring diagram for data acquisition and instrument control.	31
14	Flowchart of data acquisition and instrument control software.	32
15	Front panel of the data acquisition and instrument control software.	33
16	Block diagram of the data acquisition and instrument control software.	34
17	Engine tab of ECP sub-program.	39
18	Reflectance tab of ECP sub-program.	40
19	Temperature tab of ECP sub-program.	40
20	Front panel of UV spectrometer sub-program.	42
21	Reflection on a film/substrate system with perfectly smooth surface.	47
22	Reflection on a rough surface. The height irregularity induced phase difference.	48
23	Light propagation in a system of 4 layers.	50
24	AFM image of yttria film deposited on 8/14/2006.	53

25	AFM image of yttria film deposited on 8/15/2006.	53
26	AFM image of yttria film deposited on 8/16/2006.	54
27	AFM image of yttria film deposited on 8/17/2006.	54
28	AFM image of yttria film deposited on 8/18/2006.	55
29	The surface height distribution from the AFM image in Fig. 24. The height distribution is well fit by a Gaussian.	55
30	Ellipsometer data and fit of yttria film deposited on 8/14/2006.	57
31	Ellipsometer data and fit of yttria film deposited on 8/15/2006.	57
32	Ellipsometer data and fit of yttria film deposited on 8/16/2006.	58
33	Ellipsometer data and fit of yttria film deposited on 8/17/2006.	58
34	Ellipsometer data and fit of yttria film deposited on 8/18/2006.	59
35	Effective layer thickness shows strong correlation with the RMS roughness.	59
36	Comparison between <i>ex situ</i> spectral reflectance and model prediction by SSM and EMA for yttria film deposited on 8/14/2006.	61
37	Comparison between <i>ex situ</i> spectral reflectance and model prediction by SSM and EMA for yttria film deposited on 8/15/2006.	61
38	Comparison between <i>ex situ</i> spectral reflectance and model prediction by SSM and EMA for yttria film deposited on 8/16/2006.	62
39	Comparison between <i>ex situ</i> spectral reflectance and model prediction by SSM and EMA for yttria film deposited on 8/17/2006.	62
40	Comparison between <i>ex situ</i> spectral reflectance and model prediction by SSM and EMA for yttria film deposited on 8/18/2006.	63
41	Improved EMA fit and calculated spectral reflectance when the surface is smooth for yttria film deposited on 8/14/2006.	63
42	Simulated 950 nm reflectance at three different growth rates (nm/min).	64
43	Simulated 950 nm reflectance at three different extinction coefficients.	65
44	Simulated 950 nm reflectance at three different RMS roughness (nm) using SSM.	66
45	Simulated 950 nm reflectance at three different effective layer thickness (nm) using EMA.	67
46	Simulated 950 nm reflectance at three different roughening rate (nm/min) using SSM.	68

47	Simulated 950 nm reflectance at three different effective layer growth rate (nm/min) using EMA.	68
48	Simulated 950 nm reflectance when the growth rates are varying within 10% of average rate of 15 nm/min.	69
49	Mean squared error surface shows many local minima indicating strong correlation between G and n	70
50	Simulated 950 nm reflectance for two cases with different n and G but the same $n \times G$	71
51	Simulated film growth process with decreasing growth rate. The sensor model is based on single-wavelength reflection on a smooth surface. (top) reflectance at 950 nm (bottom) states.	86
52	Estimation result by BLS from the reflectance measurement in Fig. 51. The initial guess is 10% offset from the true initial state. (top) fitted reflectance at 950 nm (bottom) true and estimated states.	88
53	Estimated states by RLS from the reflectance measurement in Fig. 51 with horizon size equal to 10, 20 and 30.	89
54	Estimated states by mMHE from the reflectance measurement in Fig. 51 with horizon size equal to 10, 20 and 30.	91
55	Variance of estimated states in Fig. 54 when $N = 20$	92
56	Estimation result by MHE from the reflectance measurement in Fig. 51. The initial guess is 10% offset from the true initial state. (top) true and estimated states (bottom) variance of estimated states.	94
57	Estimation result by EKF from the reflectance measurement in Fig. 51. The initial guess is 10% offset from the true initial state. (top) true and estimated states (bottom) variance of estimated states.	95
58	Simulated film growth process with decreasing growth rate. The sensor model is based on dual-wavelength reflection on a smooth surface. (top) reflectance at 950 nm and 470 nm (bottom) states.	97
59	Estimation result by BLS from the reflectance measurement in Fig. 58. The initial guess is 10% offset from the true initial state. (top) fitted reflectance at 950 nm and 470 nm (bottom) true and estimated states.	99
60	Estimated states by RLS from the reflectance measurement in Fig. 58 with horizon size equal to 10, 20 and 30.	100
61	Estimated states by mMHE from the reflectance measurement in Fig. 58 with horizon size equal to 10, 20 and 30.	101
62	Variance of estimated states in Fig. 61 when $N = 20$	101

63	Estimation result by MHE from the reflectance measurement in Fig. 58. The initial guess is 10% offset from the true initial state. (top) true and estimated states (bottom) variance of estimated states.	103
64	Estimation result by EKF from the reflectance measurement in Fig. 58. The initial guess is 10% offset from the true initial state. (top) true and estimated states (bottom) variance of estimated states.	104
65	Simulated film growth process with decreasing film growth rate and effective layer growth rate. The sensor model is based on dual-wavelength reflection on a rough surface. (top) reflectance at 950 nm and 470 nm (bottom) states.	106
66	Estimation result by BLS from the reflectance measurement in Fig. 65. The initial guess is 10% offset from the true initial state. (top) fitted reflectance at 950 nm and 470 nm (bottom) true and estimated states.	108
67	Estimated states by RLS from the reflectance measurement in Fig. 65 with horizon size equal to 10, 20 and 30.	109
68	Estimated states by mMHE from the reflectance measurement in Fig. 65 with horizon size equal to 10, 20 and 30.	110
69	Variance of estimated states in Fig. 68 when $N = 20$	111
70	Estimation result by EKF from the reflectance measurement in Fig. 65. The initial guess is 10% offset from the true initial state. (top) true and estimated states (bottom) variance of estimated states.	113
71	Simulated film growth process with decreasing growth rate. The sensor model simply times the reflectance calculated from Eq. (5) by 1.5 (top) reflectance at 950 nm (bottom) states.	115
72	Estimation result by RLS from the reflectance measurement in Fig. 71. The initial guess is 10% offset from the true initial state. (top) fitted output (bottom) true and estimated states.	116
73	Estimation result by mMHE from the reflectance measurement in Fig. 71. The initial guess is 10% offset from the true initial state. (top) fitted output (bottom) true and estimated states.	118
74	Variance of estimated states in Fig. 73 when $N = 20$	119
75	Simulated film growth process with decreasing growth rate. 950 nm reflectance is 1.5 times of that calculated from Eq. (5) and 470 nm reflectance is calculated from Eq. (5) (top) reflectance at 950 nm and 470 nm (bottom) states.	120

76	Estimation result by RLS from the reflectance measurement in Fig. 75. The initial guess is 10% offset from the true initial state. (top) fitted output (bottom) true and estimated states.	122
77	Estimation result by mMHE from the reflectance measurement in Fig. 75. The initial guess is 10% offset from the true initial state. (top) fitted output (bottom) true and estimated states.	123
78	Variance of estimated states in Fig. 77 when $N = 20$	124
79	Schematic of different growth zones on a nonuniform film (Date acquired: 5/30/2006).	128
80	Experimental reflectance curve of a nonuniform film and fitting result with and without assumption of film nonuniformity (Date acquired: 4/26/2007).	129
81	Experimental reflectance at 950 nm and 470 nm (Date acquired: 10/1/2007).	131
82	Estimation result by BLS from reflectance measurement in Fig. 81. The sensor model is based on dual-wavelength reflection on a smooth surface. (top) fitted reflectance at 950 nm and 470 nm (bottom) estimated states.	133
83	Estimation result by RLS from the reflectance measurement in Fig. 81. The sensor model is based on dual-wavelength reflection on a smooth surface. (top) fitted output (bottom) true and estimated states. . . .	134
84	Estimation result by mMHE from the reflectance measurement in Fig. 81. The sensor model is based on dual-wavelength reflection on a smooth surface. (top) fitted output (bottom) true and estimated states. . . .	137
85	Variance of estimated states in Fig. 84 when $N = 20$	138
86	Ellipsometer data and fit of yttria film deposited on 10/1/2007. . . .	139
87	Estimation result by EKF from the reflectance measurement in Fig. 81. The sensor model is based on dual-wavelength reflection on a smooth surface. (top) true and estimated states (bottom) variance of estimated states.	140
88	Estimation result by RLS from the reflectance measurement in Fig. 81. The sensor model is based on dual-wavelength reflection on a rough surface. (top) fitted output (bottom) true and estimated states. . . .	142
89	Estimation result by mMHE from the reflectance measurement in Fig. 81. The sensor model is based on dual-wavelength reflection on a rough surface. (top) fitted output (bottom) true and estimated states. . . .	144
90	Estimated states by mMHE from the reflectance measurement in Fig. 81 with different tuning matrices. $N = 10$	146

91	AFM image of yttria film deposited on 10/1/2007.	147
92	Variance of estimated states in Fig. 89 when $N = 20$	147
93	Estimation result by EKF from the reflectance measurement in Fig. 81. The sensor model is based on dual-wavelength reflection on a rough surface. (top) true and estimated states (bottom) variance of estimated states.	149
94	Experimental reflectance at 950 nm and 470 nm (Date acquired: 10/3/2007).150	
95	Estimation result by RLS from the reflectance measurement in Fig. 94. The sensor model is based on dual-wavelength reflection on a smooth surface. (top) fitted output (bottom) true and estimated states. . . .	152
96	Estimation result by mMHE from the reflectance measurement in Fig. 94. The sensor model is based on dual-wavelength reflection on a smooth surface. (top) fitted output (bottom) true and estimated states. . . .	153
97	Variance of estimated states in Fig. 96 when $N = 20$	154
98	Estimation result by EKF from the reflectance measurement in Fig. 94. The sensor model is based on dual-wavelength reflection on a smooth surface. (top) true and estimated states (bottom) variance of estimated states.	155
99	Estimation result by RLS from the reflectance measurement in Fig. 94. The sensor model is based on dual-wavelength reflection on a rough surface. (top) fitted output (bottom) true and estimated states. . . .	157
100	Estimation result by mMHE from the reflectance measurement in Fig. 94. The sensor model is based on dual-wavelength reflection on a rough surface. (top) fitted output (bottom) true and estimated states. . . .	158
101	Variance of estimated states in Fig. 100 when $N = 20$	159
102	Estimation result by EKF from the reflectance measurement in Fig. 94. The sensor model is based on dual-wavelength reflection on a rough surface. (top) true and estimated states (bottom) variance of estimated states.	160

SUMMARY

Chemical vapor deposition (CVD) is an industrially important process to deposit crystalline and amorphous thin films on solid substrates. *In situ* sensing for CVD is necessary for process monitoring, fault detection, and process control. The challenge of *in situ* sensing lies in the prohibitive environment of the CVD process. Optical sensors such as the reflectometer and the ellipsometer are the most promising sensors because they can be installed outside of the deposition chamber, and are sensitive and easy to implement. However, the optical sensors do not measure film properties directly. Mathematical methods are needed to extract film properties from indirect optical measurements. Currently the most commonly used method is least squares fitting.

In this project, we systematically investigated *in situ* reflectometry data interpretation based on state estimation theory. Optical models for light reflection on both smooth and rough surfaces were studied. The model validation results indicated that the effective medium model is better than the scalar scattering model when the surface is microscopically rough. The analysis of the observability for the sensor models indicated that the linearized observability does not always guarantee the true observability of a nonlinear system.

We studied various state estimators such as batch least squares fitting (BLS), recursive least squares fitting (RLS), extended Kalman filter (EKF), and moving horizon estimation (MHE). It was shown that MHE is the general least-squares-based state estimation and BLS, RLS, and EKF are special cases of MHE. To reduce the computational requirement of MHE, a modified moving horizon estimator (mMHE) was developed which combines the advantage of the computational efficiency in RLS

and the *a priori* estimate in MHE.

State estimators were compared in simulated film growth processes, including both process model mismatch and sensor model mismatch, and reflection of both single wavelength and dual wavelength. In the case of process model mismatch and reflection on a smooth surface, there exists an optimum horizon size for both RLS and mMHE, although mMHE is less sensitive to the horizon size and performs better than RLS at all horizon sizes. The estimate with dual wavelength is more accurate than that with single wavelength indicating that estimation improves with more independent measurements. In the case of reflection on a rough surface, RLS failed to give a reasonable estimate due to the strong correlation between roughness and the extinction coefficient. However, mMHE successfully estimated the extinction coefficient and surface roughness by using the *a priori* estimate. MHE is much more computationally intensive than mMHE and there is no significant improvement on the estimation results. In the case of sensor model mismatch, either state estimator gave a good result, although mMHE consistently gave a better estimate, especially at a shorter horizon size.

In order to test the state estimators in a real world environment, we built a cold-wall low-pressure chemical vapor deposition testbed with an *in situ* emissivity-correcting pyrometer. Fully automatic data-acquisition and instrument-control software was developed for the CVD testbed using LabVIEW. State estimators were compared using two experimental reflectance data sets acquired under different deposition conditions. The estimated film properties are compared with *ex situ* ellipsometry and AFM characterization results. In all cases, mMHE consistently yielded better estimates for processes under quite different deposition conditions. This indicated that mMHE is a useful and robust state estimator for *in situ* sensor data interpretation. By using the information from both the process and the sensor model, one can obtain a better estimate. A good feature of mMHE is that it provides such a versatile

framework to organize all these useful information and gives a user the opportunity to interact with fitting and make wise decisions in the *in situ* sensor data interpretation.

CHAPTER I

INTRODUCTION

1.1 Overview of in situ sensing for chemical vapor deposition

Chemical vapor deposition (CVD) is a chemical process that can be used to deposit crystalline and amorphous thin films on solid substrates. The thickness of the thin film is usually in the range of a few nanometers to tens of micrometers. In a typical CVD process, the substrate is heated to high temperature and is exposed to the vapor of one or more gas phase precursors, which react on the substrate surface to produce the desired deposit. Frequently, volatile byproducts are also produced, which are removed by gas flow through the deposition chamber. CVD has a number of forms depending on the process conditions and how the chemical reactions are initiated. Some of the forms that are frequently referenced in the literature include low-pressure CVD (LPCVD), atomic layer CVD (ALCVD), plasma enhanced CVD (PECVD), metalorganic CVD (MOCVD), and vapor phase epitaxy (VPE). CVD has become an important process technology in several industrial fields. The largest application of CVD is in the semiconductor industry where thin films of insulators, dielectrics, elemental and compound semiconductors, and conductors are extensively utilized in the fabrication of solid-state devices. CVD is also widely used to make numerous types of coatings such as hard and wear-resistant coatings like boron, diamond-like carbon, borides, carbides and nitrides in tool technology, and corrosion resistant coatings, especially oxides and nitrides for metal protection in metallurgical applications [110, 131].

The applications of CVD are largely dependent on the properties of the deposited

thin films such as film thickness, surface roughness, composition etc. An *in situ* thin film sensor is highly desirable because it can provide the information about the film in real-time during the deposition. The real-time information can be used for fault detection, process diagnostics, and ultimately to allow the feedback control of the CVD process. Currently, *in situ* sensors have not yet been widely applied in industry due to some unique challenges. First, CVD is usually operated at high temperature, low pressure, and with reactive materials. The *in situ* sensor must be compatible with the harsh processing environment of CVD. Furthermore, the *in situ* sensor must not disturb the deposition process. Finally, the *in situ* sensor must be fast, robust and easy to operate. Due to the lack of *in situ* sensors, currently the process control of CVD in the semiconductor industry is based on run to run control (R2R). In R2R control, the processing recipe such as gas flow rate, pressure, temperature, etc. is fixed during the deposition. After the deposition, the film is characterized *ex situ* and the results are used by the R2R controller which then decides whether a recipe change is needed. A modified recipe for use in the next deposition run is then computed. The shortcoming of R2R control is that the control actions only take place between deposition runs so it can not correct the problems that happen in one deposition run. Ideally one would like to control each deposition run *in situ* and this is why the *in situ* sensor is important. *In situ* sensing has always been a primary consideration for the development of process control in the semiconductor industry. The semiconductor industry is characterized by physically and chemically prohibitive environments and this makes *in situ* sensor development and application difficult or even impossible. *In situ* sensing has been identified as one of the grand challenges in the near term (through 2009) in The International Technology Roadmap for Semiconductors 2003 edition [41, 99].

Although not yet widely used in industry, *in situ* sensing has been extensively utilized in academia to study reaction mechanisms and monitor the film growth in

CVD. For example, *in situ* mass spectrometry is commonly used to identify the reactant species, gaseous reaction byproducts to study gas phase evolution, and precursor decomposition pathways to help understand the reaction mechanism [144, 70, 143, 29, 174, 53, 168, 175]. *In situ* Fourier transform infrared spectroscopy (FTIR) and Raman spectroscopy were used to study the decomposition of the precursor and gas phase reaction which can be correlated with the characteristics of the film [96, 97, 55, 69, 54, 126, 105, 56, 27, 1]. *In situ* Auger electron spectroscopy was used to study the composition and identify the contamination of the film [28, 102]. *In situ* X-ray diffraction (XRD) was used to obtain information about film thickness, growth rate and the chemical composition of compound thin films [74, 128]. *In situ* X-ray reflectivity (XRR) was used to study the kinetics and structural evolution of the deposit in the early stages [73, 101]. *In situ* scanning transmission electron microscopy was used to study the microstructure of the film and the effect of processing conditions on the microstructure [76, 49]. These *in situ* characterization tools, however, are not suitable in the production setting because they are expensive, difficult to install and operate, and the sensor data interpretation is difficult to do in real-time.

For *in situ* sensing of CVD in the production setting, another group of *in situ* sensors are particularly suitable and this includes the pyrometer, ellipsometer and reflectometer. These sensors are nonperturbing to the process, can be installed outside of the deposition chamber, and sensor data interpretation can utilize the well-understood models of interaction between light and matter. A pyrometer measures thermal radiation from the film/substrate and this measurement is used to determine surface temperature. During the growth, the intensity of thermal radiation changes because of the variations of the effective emissivity of the film/substrate system due to interferences, absorption, or scattering phenomena. The change of intensity causes a periodic variation of the pyrometer's apparent temperature reading. The oscillation period and amplitude are dependent on the growth rate, complex refractive index and

surface roughness of the film. Therefore a great deal of information about the film can be obtained by analyzing the oscillation of apparent temperature. The *in situ* pyrometer was extensively used to study the growth rate, complex refractive index and surface roughness of diamond thin film by CVD [12, 3, 13, 134, 9, 8, 26, 21]. Other applications include molecular beam epitaxy of GaAs/GaAlAs Bragg reflectors [15], silicon layers [75], AlGaAsSb materials [14], and MOCVD of metallic thin films [52]. The pyrometer is also used with a reflectometer (reflectance-correcting pyrometer) to accurately measure the true temperature of the film surface [19], in the presence of changing surface properties.

An ellipsometer measures the polarization state change of the probe light upon reflection from the film/substrate system [147]. The incident light is usually totally polarized with a known polarization state. The polarization state of the reflected light is described by a complex number $\tilde{\rho}$, which is the ratio of the complex reflection coefficient parallel to the plane of incidence \tilde{R}_p to the one perpendicular to the plane of incidence \tilde{R}_s . The ratio can be described by two real quantities, the ellipsometric angles ψ and Δ which are measured by the ellipsometer, by the equation $\tilde{\rho} = \tilde{R}_p/\tilde{R}_s = \tan\psi e^{i\Delta}$. The polarization state of the reflected light is dependent on the optical properties and thickness of the film. Ellipsometry is primarily used to determine film thickness and optical constants. However, it can also be used to determine characterization of composition, crystallinity, roughness, doping concentration, and other material properties associated with a change in optical response. By following the characteristic trajectory of ψ and Δ during the growth, the growth stages and mechanism can be studied. From the extracted complex refractive index, the composition, roughness of the film can be inferred. *In situ* ellipsometer has been used extensively to study the growth mechanism of III-V compound semiconductors such as GaN, AlN, and InN [17, 23, 38, 81, 108, 116, 129, 130, 133, 138, 142, 148, 173]. Other material systems that have been studied include II-VI semiconductors such as

HgCdTe and CdTe [100, 112], diamond film [84, 60, 31, 33], $\text{Si}_{1-x}\text{Ge}_x$ film [2, 80, 90], carbon thin film [62, 159, 65, 161, 160], TiO_2 film [4], Si film [82, 132], boron nitride and titanium nitride [92, 61], Bi_2Te_3 and Sb_2Te_3 films and $\text{Bi}_2\text{Te}_3\text{-Sb}_2\text{Te}_3$ superlattice [35], Al film [59], silicon oxide [39], $\text{YBa}_2\text{Cu}_3\text{O}_x$ thin film [169], and Polyphenylene oxide film [163]. *In situ* ellipsometer has been also used with reflectance-difference spectroscopy [40, 93, 137]. Some reviews on the status and challenge of *in situ* ellipsometry can be found in [16, 63, 68].

A reflectometer measures reflectance which is the fraction of incident light reflected by the film/substrate system. When a thin film is deposited on a substrate with a different refractive index, the reflectance will oscillate due to the Fabry-Perot interference. The oscillation period is determined by the growth rate and the refractive index of the film. The amplitude of the oscillation is dependent on the refractive index of both the film and the substrate. The decay of the amplitude is dependent on the extinction coefficient of the film. Other factors such as the grading of the refractive index in the film and surface roughness could also affect reflectance. Therefore a great deal of information about the film could be obtained from an *in situ* reflectance measurement. The reflectometer usually measures normal reflectance so the setup is simpler than the ellipsometer because it requires only one window for optical access. The normal reflectance is insensitive to incidence angle in the near-normal direction and this allows monitoring deposition on rotating substrates. The normal reflectance is also insensitive to light polarization and this allows one to use inexpensive and stable unpolarized light sources and optical relay systems such as multimode optical fibers that do not need to preserve polarization. In addition, the reflectometer does not require strain-free windows for the optical access which are necessary in ellipsometer. Numerical analysis is also easier at normal incidence because only s polarization needs be considered and the propagation angle inside the film does not need to be calculated [20]. The disadvantage of the reflectometer is that it is less sensitive than

the ellipsometer because the latter measures polarization state instead of the intensity of the reflected light which is more prone to noise.

An extensive body of literatures on *in situ* reflectometry has been focused on the study of growth of III-V compound semiconductors such as GaN, AlN, InN and their ternary compounds [86, 127, 85, 7, 42, 135, 120, 121, 36, 78, 57, 122]. These materials are widely used for the fabrication of short wavelength light-emitting devices and high power microwave transistors. GaN is commonly grown on a sapphire substrate by metalorganic vapor phase epitaxy (MOVPE). A sapphire substrate has a large lattice mismatch from GaN. In order to accommodate the lattice mismatch, a multiple-step growth process is usually used. First, a thin buffer layer of GaN is grown at a relatively low temperature. Then the buffer layer is annealed by increasing the temperature to that used for subsequent high temperature epitaxy growth of GaN. Finally GaN is grown on top of the annealed buffer layer. These growth steps can be well identified by *in situ* reflectometry. During the deposition of the buffer layer, reflectance decreases due to the light scattering by the deposited GaN islands on sapphire substrate. Then in the annealing stage, reflectance increases because GaN islands coalesce to produce an optically smooth film. Finally the reflectance exhibits regular oscillation due to 2D growth of GaN on the annealed buffer layer. By using an *in situ* reflectometer, various deposition conditions can be explored to obtain high quality growth of GaN. In fact MOVPE process of GaN is so well understood that the *in situ* reflectometer has become an established technique for monitoring growth of GaN. It is common for commercial nitride MOVPE reactors to be shipped with an *in situ* reflectometer as standard. In addition to III-V compound semiconductors, the *in situ* reflectometer has also been used to study and monitor the growth of diamond film [89, 177, 178], II-VI semiconductors such as ZnO [32], ZnTe [136, 165], and CdS/CdTe [64].

1.2 *In situ sensor data interpretation*

Most of the literatures on *in situ* sensing has been focused on using *in situ* sensors to help understand rather than control the film growth process. For example, the *in situ* reflectometer is used to help identify the different growth stages of GaN on sapphire substrate in MOVPE. This qualitative analysis of *in situ* sensor data is necessary for an unknown growth process and represents the first step toward controlling the process. However, in order to implement process control, film properties such as film thickness, refractive index and surface roughness must be quantified in real-time. The challenge of optical sensors is that they do not measure film properties directly. Film properties must be extracted from indirect measurements like polarization state and intensity of the reflected light through a model-based analysis using optical physics. In the following, we briefly review currently available techniques of extracting film properties from indirect *in situ* reflectance measurements.

Most reported data interpretation of *in situ* sensors are retrospective, i.e. sensor data interpretation is performed after the deposition process is finished. The retrospective sensor data interpretation can provide more precise information of the film than the qualitative analysis but is still not enough for real-time process control. Therefore this level of sensor data interpretation is somewhat between the qualitative analysis and the real *in situ* sensor data interpretation that is to be discussed next. The simplest and most common method of *in situ* reflectance interpretation is the peak-counting method. According to the optical model of thin film interference, each of the interference extrema corresponds to a film thickness of half the wavelength of the light in the film. Therefore by counting the number of interference extrema, film thickness could be estimated when the refractive index is known [178, 177]. The peak-counting method is extremely easy to use but it requires multiple interference extrema to process. But in some cases, depending on the film thickness desired and the wavelength of the light, there may be only a few oscillations during the entire film

growth. Besides, the peak-counting method cannot estimate film thickness between interference extremas so it is not a real-time method in the strict sense.

A more rigorous method is the least squares fitting method (LS) [20, 89, 32, 7, 136]. In LS, film parameters like growth rate and refractive index are assumed to be constant and are estimated by minimizing the square of the error between the sensor model prediction and the measurement. For example, Breiland and his coworkers used LS to extract five parameters (growth rate, complex refractive index of GaAs film, and complex refractive index of virtual substrate) from one normal reflectance measurement [20]. Least squares fitting method can process measurements between interference peaks but is very sensitive to the initial guess of film parameters. This is because the error surface of the least squares fit contains multiple local minima due to the high nonlinearity of the optical model and close correlation between film parameters. Another problem with LS is that it assumes constant film parameters over the entire deposition period and this may not be valid in practice. For example, the film growth rate may change with substrate temperature or decrease due to depletion of the precursor. The refractive index of the film may also change with the temperature, composition, and microstructure. An *in situ* sensor must be able to deal with a time-varying process if feedback control is to be used. One solution is to divide the film into sublayers and the growth rate and refractive index is assumed constant within each sublayers [121]. Another solution is to fit the data over a shorter window of data. When new measurement data is acquired, the window is shifted to include new data and at the same time discard part of the old data. The optimal solution in the previous window is then passed into the new window as an initial guess for the optimization. We refer to this approach as recursive least squares fitting (RLS). The optical models are usually complicated and for most of the LS based sensor data interpretation, assumptions are made to simplify the model. For example the film surface was usually assumed to be smooth. However, surface roughness could have

multiple effects on optical measurements such as emissivity of the surface and normal reflectance by scattering the light. By neglecting the roughness one loses information contained in the measurements, and introduces errors into the estimates of other parameters.

State estimator represents another approach for *in situ* sensor data interpretation. Estimation theory provides a theoretic framework to deal with estimating the values of interest from indirect and noise-corrupted measurements. While LS only uses a static sensor model, a state estimator utilizes the information from both process dynamic model and sensor model even if the models are not perfect. Currently, most of the reported work on *in situ* sensor data interpretation using a state estimator are focused on the Kalman filter. A Kalman filter is an optimal state estimator applied to a linear dynamic system that involves random perturbations. It gives a linear, unbiased, and minimum error variance recursive algorithm to optimally estimate the unknown state of a linear dynamic system from noisy data taken at discrete times [30, 91]. For a nonlinear system, a linearization has to be made at each local estimated state and has proved to be useful in many applications. Compared to peak-counting and least square fitting methods, the Kalman filter requires only the most recent measurements to process and thus is more computationally efficient and suitable for *in situ* sensing and feedback control. Kalman filters have been widely used in many areas of industrial applications such as video and laser tracking systems and satellite navigation. There are also a few applications of the Kalman filter in *in situ* sensing for CVD and other surface processing. An early application of Kalman filter to *in situ* monitoring of a deposition process appeared in 1984 [6]. Later Woo et al. applied a modified Kalman filter to estimate film thickness and growth rate from a laser reflectance measurement [165]. EKF was also used to estimate etch rate and end-point in a plasma etch system by Vincent and co-workers[158, 157]. In both their works, adjustable parameters called forgetting factor in Woo and optical gain

in Vincent have to be included to account for the deficiency of the sensor model. However, in many cases film roughness and changing extinction coefficient caused the reflected light amplitude to decay. By using adjustable parameters, the information contained in the amplitude change was lost. In addition, there is no systematic study of the uncertainties involved in the models. There is no study on model validation either.

1.3 Objective and chapter outline

The objective this research is to develop and demonstrate experimentally an *in situ* sensor based on estimation theory for real time sensing of thin film properties in chemical vapor deposition (CVD). In this research a commercially available emissivity-correcting pyrometer (ECP) is used as the sensing element. The ECP measures normal reflectance at 950 nm and 470 nm, and thermal radiation at 950 nm and 850 nm. Given these indirect measurements, this research aims to answer the following two questions: (i) what kind of thin film properties are embedded in ECP measurements? (ii) how to extract these properties from indirect and noise-corrupted ECP measurements? Specifically, this research will work on the development of sensor model, model validation, observability analysis, implementation and comparison of estimation algorithms. This state estimator based *in situ* sensor will also be demonstrated on an experimental CVD testbed where yttria thin film is deposited on silicon wafers by metal-organic chemical vapor deposition (MOCVD).

This thesis is divided into the following major chapters:

- Chapter 1 is the literature review on *in situ* sensing for CVD and currently available techniques for *in situ* sensor data interpretation.
- Chapter 2 presents detailed description of the chemical vapor deposition testbed and its data acquisition and instrument control software that have been built in this project. The operation procedure of the CVD and lessons that we have

learned in operating the CVD are also included in this chapter.

- Chapter 3 focused on sensor model development and validation. The sensor models for both smooth and rough film are described. Based on the sensor models, the effect of film parameters like growth rate, refractive index and roughness on the normal reflectance are discussed. Finally the analysis of the observability based on the nonlinear sensor model are presented.
- Chapter 4 presents the algorithms of state estimators that are studied in this project, which includes recursive least square estimator, extended Kalman filter, moving horizon estimator and a modified moving horizon estimator. The connections between these estimators and their pros and cons are also discussed.
- Chapter 5 presents the results of simulation study. We compare the performance of different state estimators in simulated film growth processes in terms of speed and accuracy. The simulation study helps one to understand the mechanism of how each estimator works and provides a guideline on how to tune the state estimators.
- Chapter 6 presents the results of experimental study. In this chapter, CVD of yttria film have been carried out under different processing conditions and interrupted at different time for *ex situ* characterization. We use state estimators to extract film properties from experimental reflectance data and compare the results with *ex situ* characterization.
- Chapter 7 gives some conclusions of this research and presents suggestions for future work.

CHAPTER II

CHEMICAL VAPOR DEPOSITION TESTBED

2.1 *Hardware*

Figure 1 and 2 show the schematic and the photograph of the CVD testbed, respectively. For ease of discussion, the CVD system is divided into three parts: upstream, deposition chamber and *in situ* sensor, and downstream. This CVD system was originally designed to deposit yttria-stabilized zirconia (YSZ) on silicon substrate. However in the work in this thesis, we decided to deposit only yttria (Y_2O_3) in order to simplify the experimental work and focus on *in situ* sensing. With that in mind, we discuss each part in details in the following sections.

2.1.1 Upstream

The upstream consists of six mass flow controllers (MFC) [MKS Instruments], two precursor evaporators [Kurt J. Lesker], two UV cells [Ocean Optics], a flow manifold and tubes connecting them [Swagelok]. The evaporators are cylinder-shaped containers made of stainless steel. The size of the containers is 5" tall \times 2" diameter. The container is covered by a 3-3/8" Conflat vacuum flange. There are three tubes on the flange. One is a 1/4" OD inlet tube that extends down 4-5/8" into the container. This tube is used to introduce carrier argon (Ar3 for Zr precursor and Ar4 for Y precursor) into the evaporator to dilute and flush out the evaporated precursors. The second one is a 1/8" sealed tube that extends down 3" into the container. This tube is used to house a K-type thermocouple to measure evaporator temperature. The last one is a 1/2" OD outlet tube for evaporated precursors. The larger diameter of the outlet tube is intended to prevent clogging of the tube with condensed or decomposed precursors. There is a valve on both inlet and outlet tubes

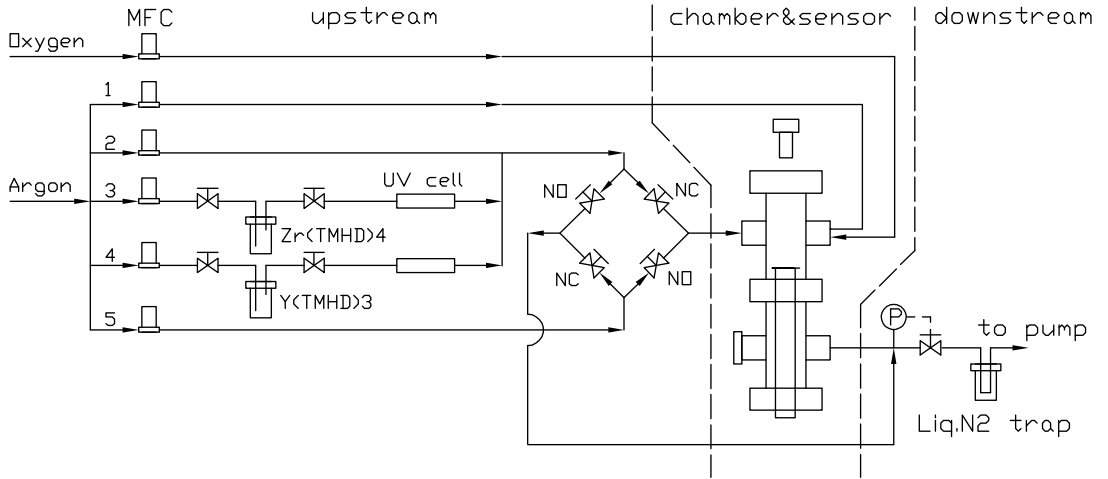


Figure 1: Schematic of the chemical vapor deposition testbed.

which allows the evaporator to be closed off and isolated from the rest of the system. The evaporators are placed in separate ovens due to the different volatility of the precursors. Oven temperatures are set manually but it is important to monitor the evaporator temperature through the thermocouple. The evaporators are heated by convection of the hot air inside the oven. Due to the large mass of the evaporators, it is common to take more than two hours to heat the evaporators to 150 °C when the oven temperature is 200 °C. The β -diketonates $\text{Zr}(\text{tmhd})_4$ and $\text{Y}(\text{tmhd})_3$ [Strem Chemicals, Inc.] are used as the precursors due to their high volatility at temperatures below 250 °C and thermal stability in the gas phase at elevated temperatures [114, 113]. The precursors material properties are summarized in Table 1. When packing the evaporators, the precursors are ground into fine powders and coated onto stainless steel ball bearings to maximize the surface area for evaporation. A simple calculation can give us a rough idea of how much precursors should be loaded. Suppose we have deposited 1 micrometer thick yttria (Y_2O_3) film on a 1" diameter silicon substrate. The density and the molecular weight of yttria are 5.010 g/cm³ and 225.81 g/mol, respectively. Therefore, the amount of 1 micrometer thick yttria film is $\frac{\pi \times 0.0254^2 \times 10^{-6} \times 5.010 \times 10^6}{4 \times 225.81} = 1.124 \times 10^{-5}$ mol. Because one mole of yttria requires two



Figure 2: Photograph of the chemical vapor deposition testbed.

Table 1: Precursor material properties. Vapor pressure can be found in [48].

Material	CAS No.	Formula	Molecular Weight	Melting Point
Y(TMHD) ₃	15632-39-0	Y(C ₁₁ H ₁₉ O ₂) ₃	638.71 g/mol	170-173 °C
Zr(TMHD) ₄	18865-74-2	Zr(C ₁₁ H ₁₉ O ₂) ₄	824.29 g/mol	318-320 °C

moles of Y(TMHD)₃ and the molecular weight of Y(TMHD)₃ is 638.71 g/mol, the amount of Y(TMHD)₃ required is $1.124 \times 10^{-5} \times 2 \times 638.71 = 0.0144$ g. In reality, however, only a small fraction of the precursor is deposited and rest amount is unreacted and flushed out of the system. Suppose the efficiency is 10% and we run 10 depositions after each repack, the amount of precursor needed is 1.44 g, which is what we usually load in practice. The volume of the evaporator is around 250 cm³ and the loaded ball bearings usually take about 20% volume of the evaporator. Given the vapor pressure of the precursor, we can calculate how much precursor is in the gas phase using the ideal gas law. Suppose the evaporator temperature is 160 °C, the vapor pressure of Y(TMHD)₃ is 48.2 Pa [48], we have $n = \frac{PV}{RT} = \frac{48.2 \times 200 \times 10^{-6}}{8.314 \times 433.15} = 2.68 \times 10^{-6}$ mol. When 1.44 g Y(TMHD)₃ is packed, the precursor in the gas phase is only about 0.12 % of the total amount. The amount of precursor in the gas phase can certainly affect the mole flow rate of precursor but it is not the only factor. Another factor is the flow rate of carrier argon and the mixing between precursor vapor and argon. The flow of carrier argon affects the precursor evaporation rate by influencing the mass transfer boundary layer thickness around the solid precursor. Because it is difficult to quantify the effect of argon flow, we cannot determine mole flow rate of precursor solely from thermal dynamic analysis and that is why we need an inline UV spectrometer which is to be discussed next.

The mixture of evaporated precursor and argon flows out of the evaporator and enters a UV cell which is connected to a UV spectrometer [Ocean Optics. Model S2000] via high temperature optical fibers. The UV spectrometer can measure three

channels of absorbance in the wavelength range from 200 to 1100 nm. Channel one (Master) measures absorbance of $\text{Zr}(\text{TMHD})_4$, channel two (Slave 1) measures absorbance of $\text{Y}(\text{TMHD})_3$, and channel three (Slave 2) is directly connected to light source so that we can monitor the stability of the UV lamp. $\text{Y}(\text{TMHD})_3$ has a maximum absorption at $\lambda_{max} = 286 \text{ nm}$ and its concentration can be determined from the UV absorbance at λ_{max} by using the Beer-Lambert relation, $c = \frac{A}{\epsilon b}$, where c is the concentration of the precursor with unit of mol/L, A is absorbance, ϵ is the molar absorptivity with unit of L/mol cm and is 34673.7 for $\text{Y}(\text{TMHD})_3$ [119, 37], b is the length of UV cell which is 12 cm. With the concentration known, the mole flow rate of precursor (n_Y) can be calculated from the mole flow rate of argon (n_{Ar}). Suppose the volume flow rate of the mixture of $\text{Y}(\text{TMHD})_3/\text{Ar}_4$ is V , the steady state pressure and temperature in the UV cell are P and T , then we have $c = \frac{n_Y}{V} = \frac{n_Y}{(n_Y+n_{Ar})RT/P}$. Rearranging the equation gives

$$n_Y = \frac{1}{\frac{P}{RTc} - 1} n_{Ar} \quad (1)$$

This inline UV spectrometer offers tremendous advantages for the operation of CVD. It allows us to monitor the flow of the precursors, to determine how much precursor has been used, and to decide when a repack of the evaporator is necessary. The concentration of the precursors in the gas phase can also be correlated with the film composition and other characteristics. MOCVD has been known to have poor repeatability partly due to the inability of existing MOCVD equipment to precisely control the precursor delivery [119, 37]. A PID controller is designed in this project to maintain constant precursor delivery rate by adjusting the flow rate of argon. This controller is discussed in the Software section.

After the UV cell, the mixtures meet the main carrier argon stream (Ar_2) and enter a flow manifold, which consists of four bellows-sealed valves, two normally closed (NC) and two normally open (NO). The manifold has two inlets and two outlets. The mixture of precursor and argon enters from one inlet and another stream of

dummy argon (Ar5) with the same flow rate enters from the other inlet. One of the outlets goes to the deposition chamber and the other one goes to the bypass line. The four valves on the manifold are controlled by four solenoid valves and allows us to either flow precursors into the reactor to deposit, or to bypass the reactor and flow pure argon (Ar5) over the substrate during the heat up and cool down steps of the process. The flow manifold is located outside of the oven so it must be heated separately to prevent precursor condensation. The rope heater, thermocouple and temperature controller are all purchased from OMEGA. The temperature set point of temperature controller is 20 °C higher than oven temperature to compensate for the poorer thermal insulation of the flow manifold. The flow manifold was designed to ensure smooth switching between the reaction line and bypass line. However, in practice the switching of the flow is far from ideal. We have consistently observed that UV absorbance had a sudden drop to zero when switching the lines. This may have been due to the pressure imbalance caused during the switch. We have noticed that normally closed valves switches slower than normally open valves.

All tubes in the upstream are placed inside the oven. Considering the flow rate of the gas, it is important to make sure the tubes are long enough so that the gas entering the deposition chamber and evaporators are hot enough. The appropriate tube length can be obtained by doing some simple thermal calculations [149]. Suppose the tube inner diameter is D , wall temperature is T_w , gas inlet temperature is T_i , heat transfer coefficient (from the wall to the gas) is h , the mass flow rate of gas is \dot{m} , the specific heat of the gas is C_p , then for gas outlet temperature T_o , the required tube length L can be obtained by solving the following ODE: $\dot{m}C_p \frac{dT}{dx} = h\pi D(T_w - T)$, with boundary condition of $T = T_i$ at $x = 0$. The solution is $L = \frac{\dot{m}C_p}{\pi h D} \ln\left(\frac{T_w - T_i}{T_w - T_o}\right)$. An additional 20% of calculated length was added for an extra margin of safety. The heat transfer coefficient h is highly dependent on the physical properties of the fluid and the type and velocity of flow. For fully developed laminar tube flow with a constant

wall temperature, h can be obtained from the Nusselt number $Nu = hD/k = 3.657$, where k is the thermal conductivity of the fluid [72]. One example of calculating Ar tube length is shown as follows. The parameters are $D = 0.18$ in, $T_w = 200^\circ\text{C}$, $T_i = 25^\circ\text{C}$, $T_o = 180^\circ\text{C}$, $k = 0.0177$ W/m K, $\dot{m} = 1000$ SCCM and $C_p = 519.65$ J/Kg K. Converting all parameters to SI unit, we have $h = \frac{3.657 \times 0.0177}{0.18 \times 0.0254} = 14.2$ W/m² K and $L = \frac{\dot{m} C_p}{\pi h D} \ln \left(\frac{T_w - T_i}{T_w - T_o} \right) = 0.16$ m. The above thermal calculation neglected the axial fluid conduction term which may be significant at low values of Re and or Pr [72]. However, the successful deposition of yttria film suggested that the calculated tube length is acceptable and we have not even had a problem with clogging of the lines.

2.1.2 Deposition chamber

Figure 3 and 4 show the photograph and cross-sectional view of the deposition chamber. The chamber consists of two standard stainless-steel ultra-high vacuum (UHV) reducing crosses [MDC Vacuum Products]. The size of the main flange and reducer flange are 4-1/2" and 2-3/4", respectively. For the upper reducing cross, the upper flange connects to an optical viewport and the lower main flanges connects to the lower reducing cross. One of the reducer flange is used to introduce precursor/argon mixture in operation mode or dummy argon in bypass mode. The other reducer flange is used to introduce oxygen and purge flow (Ar1). Both oxygen and Ar1 tubes are 1/4" diameter. The separated flow of oxygen and precursor is intended to minimize the possible premature reactions which could lead to undesired gas-phase particle formation. The purge flow has a relatively slower flow rate and is used to prevent precursor condensation on the viewport. For the lower reducing cross, the upper flange connects to the upper cross. The lower flange is where to insert a substrate heater assembly which is to be discussed later. One of the reducer flange is used for vent line. The other reducer flange connects to the downstream. The deposition chamber is placed in an oven to prevent precursor condensation on the chamber



Figure 3: photograph of the chemical vapor deposition chamber.

walls. A vertical flow geometry was selected for the MOCVD reactor because it is typically used in cold wall designs for rapid thermal processing and also suitable for *in situ* sensing. Another reason for the popularity of the vertical flow geometry is the existence of a one-dimensional similarity solution in the limit of an infinite wafer.

We have used COMSOL to study the gas flow pattern inside the deposition chamber, and Fig. 5 shows the two-dimensional velocity field. The size of the chamber in Fig. 5 is the same as that of real one except that the heater assembly is not included. The gas is Ar and its density and dynamic viscosity are corrected for $P = 2$ Torr and $T = 160$ °C which is a typical condition inside the chamber. The boundary condition is no-slip on all walls except at the inlets and outlet. The mass flow rate of argon is 50 SCCM for inlet 1 (1/4" diameter) and 140 SCCM for inlet 2 (1/2" diameter). The gas velocity can be calculated from mass flow rate and pressure and temperature inside the chamber. Although it is a highly simplified representation of our system, Fig. 5 offers some interesting insights. First, the flow inside the chamber is more likely to be laminar flow. The Reynolds number is in the range of 1-100, far

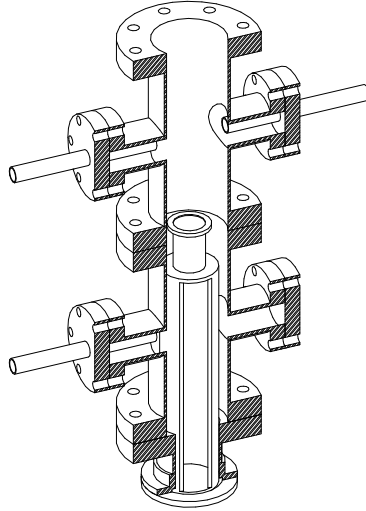


Figure 4: Cross view of the chemical vapor deposition chamber.

smaller than the transition Reynolds number which is 2100 for gas flowing in a tube. Second, the velocity appears to be higher around the edge of the substrate and this may contribute to the convective cooling of the substrate, which in turn may cause temperature nonuniformity across the substrate. Third, the gas flow has a tendency toward the pump side (left-hand side). In this CVD system, the exit port is on one side of wall instead of the bottom which is more common in MOCVD reactors. This may cause nonuniform delivery of materials to the substrate surface which causes film nonuniformity. Fig. 5 also shows some recirculation regions in the chamber. It is reasonable to believe that the precursors in these regions may be difficult to flush out. The COMSOL solution also gives the pressure profile. It is not presented here but the result indicated there is almost no pressure drop in the chamber. The biggest pressure drop appears at inlet 1 in Fig. 5. This makes sense because when gas flow from a tube with small diameter to a tube with large diameter, pressure will decrease. The chamber diameter (2-1/2") is much larger than tube diameter (1/2") so we expect less pressure drop inside the chamber.

We have also determined the volume of upstream plus the deposition chamber by a simple experiment. We first pumped down the system to its base pressure and

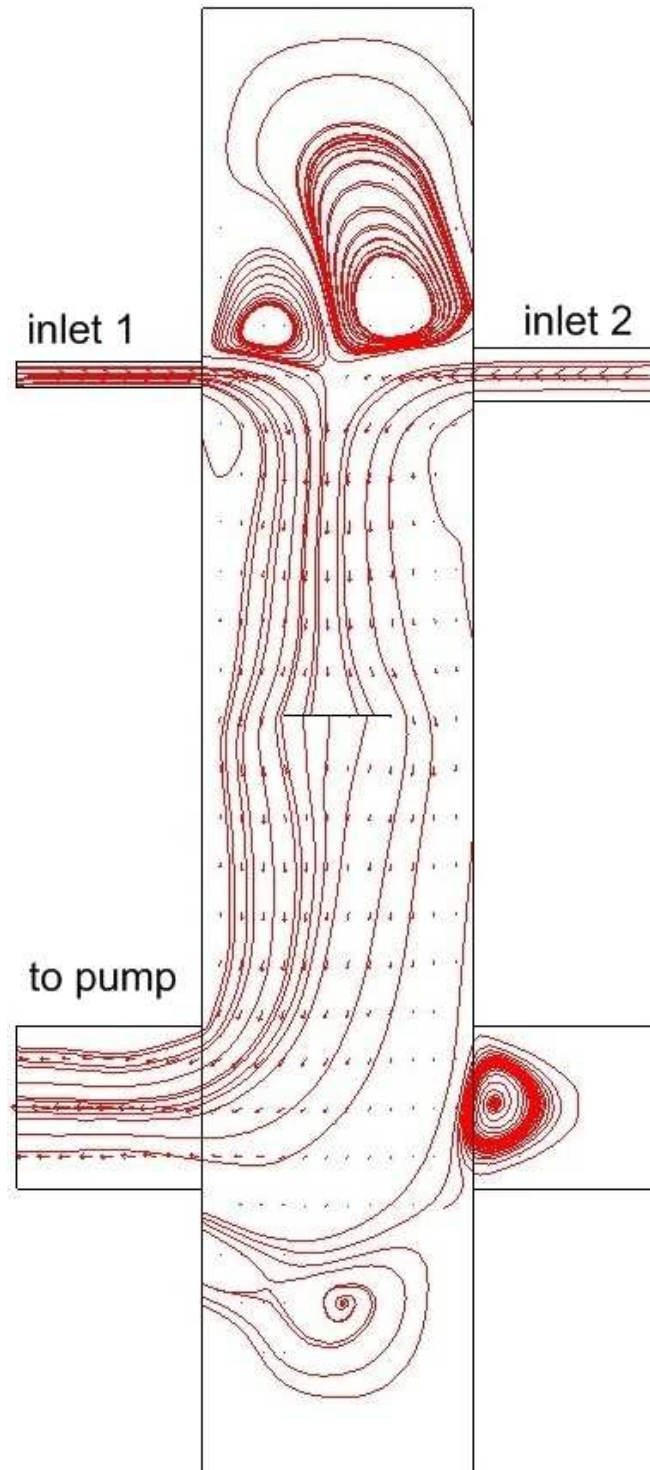


Figure 5: Velocity field inside the deposition chamber.

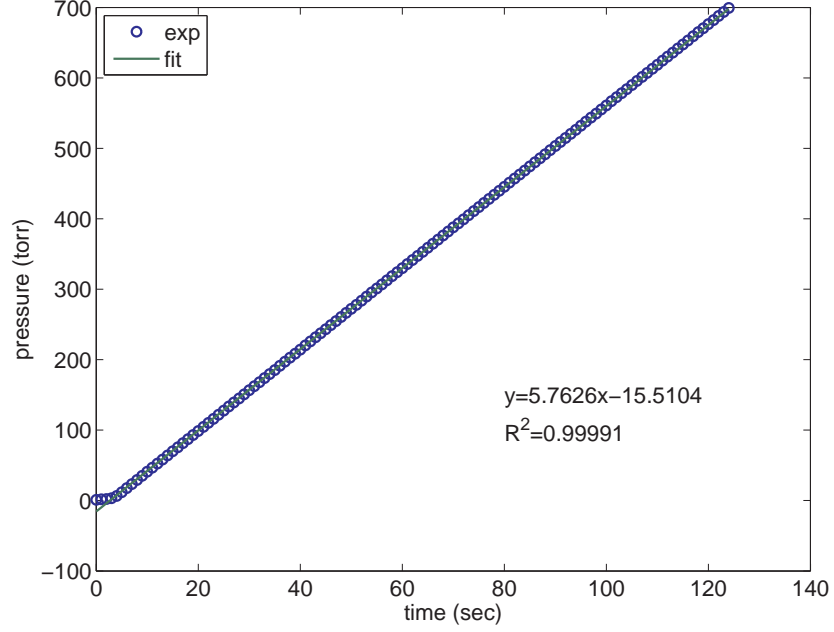


Figure 6: Pressure rising curve with 1000 SCCM argon.

closed the throttle valve in the downstream. Then argon with a constant flow rate is introduced into the system. From the pressure rising rate, the system volume can be determined by ideal gas law. Because $PV = nRT$, we have $V = \frac{\dot{n}RT}{dP/dt}$, where \dot{n} is the argon mole flow rate and dP/dt is the pressure rising rate. Figure 6 shows the pressure rising curve when Ar flow rate is 1000 SCCM and the chamber temperature is 25 °C. The pressure rising curve can be fitted by a line with slope equal to 5.8 Torr/sec. By using the above equation and SI unit, we obtained the system volume equal to 2401 cm³. Once the system volume is known, the residence time can be calculated. When gas flow rate is 140 SCCM which is what we typically use, at operation pressure of 2 Torr and temperature of 160 °C, the volume flow rate is $140/60 \times \frac{160+273.15}{273.15} \times \frac{760}{2} = 1406$ cm³. Therefore the residence time is $2401/1406 = 1.7$ sec. With the knowledge of the system volume, the effect of residence time on film growth can be studied.

Figure 7 shows the photograph of the heater assembly [Kurt J. Lesker]. As shown in Fig. 4, the heater assembly is inserted into the deposition chamber from the lower

main flange of the lower reducing cross. The heater assembly is about 9" tall. On top of the assembly is a substrate heater [HeatWave Labs. part No: 101275-27] which supports and heats the substrate. The heater is made of alumina ceramic around the filament, with moly shielding around the outside. The filament has a resistance of about 2Ω and can reach a maximum temperature of $1200 \text{ }^\circ\text{C}$. On the bottom of the assembly are power feedthrough and thermocouple feedthrough. The wire connecting the filament to the power feedthrough is exposed to the reactive gas in the deposition chamber and can easily break. A ceramic paste [Cotronics Corp.] is coated on the wire and it greatly increase the life span of the heater. The power feedthrough connects to a power supply with maximum output power of 1350 Watts [Behlman Electronics. Model P1350]. In practice, the heating voltage is increased gradually to protect the filament. A current sensor [Veris Industries] is used to monitor the actual current flowing through the filament and allows us to evaluate the stability of the heater. The thermocouple feedthrough connects to K-type thermocouple which measures the temperature behind the heater. This temperature is what is usually reported in the literature. However it can be quite different from the actual temperature on the substrate surface. The heater body is alumina which has a very low thermal conductivity (27 W/m K). It is also quite transparent to thermal radiation at elevated temperatures. Both of these lead to relatively poor temperature uniformity of the heater face. The mounting shielding, gas flow, spacing to the sample, etc. could also add to this nonuniformity. In fact, it turned out that temperature nonuniformity on the heater surface is one of the major problems in this CVD system. We have observed that when the substrate is heated up to $700 \text{ }^\circ\text{C}$, the reflected light from the substrate gradually shifted out of the view of the detector and caused significant decrease in the reflected light intensity. When the substrate is cooled down to room temperature, the reflected light moved back to its original position and the reflected light intensity increased back to its original value. Figure 8



Figure 7: photograph of the heater assembly.

shows reflectance change in a heating-cooling cycle experiment with voltage ramping rate of 0.3 V/min. The left axis is reflectance and the right axis is voltage. The shift of the light is due to the misalignment between the substrate and the detector, which is caused by the elastic deformation of the substrate. The deformation of the substrate is caused by the temperature nonuniformity which induced thermal stress in the substrate due to local differences in thermal expansion. In addition to the substrate deformation, temperature nonuniformity could also cause different film growth rates across the substrate, and this resulting film nonuniformity can have a profound effect on the reflected light intensity. The reflectometer measures the averaged reflected light intensity in a certain area on the substrate. If film is nonuniform inside the area, the measured reflectance will exhibit abnormal behaviors which would make the sensor data interpretation much more difficult.

The temperature nonuniformity can be lessened by inserting a thermal diffuse plate between the heater and the substrate. We have used COMSOL to study the surface temperature profile and the effect of a thermal diffuse plate. Figure 9 shows

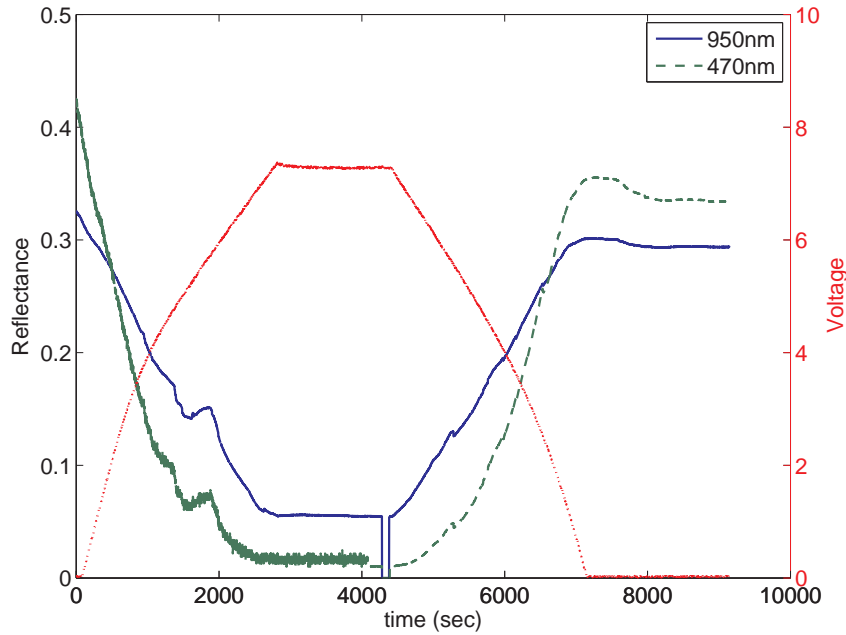


Figure 8: Reflectance change in a heating-cooling cycle experiment. Silicon substrate is on bare heater surface (Date acquired: 3/10/2006).

the temperature profile on the bare heater surface. The size of the heater in the model is very close to the real one. The material of the heater body is alumina with a thermal conductivity of 27 W/m^2 . The main form of heat dissipation is assumed to be radiation, which is reasonable considering high vacuum and low gas flow rate inside the chamber. The filament resistance is 2Ω and the heating voltage is 15 V . The only unknown parameter is the effective heating area of the filament, which is needed to set up the boundary condition. It can be easily obtained by trying some values until a reasonable surface temperature was obtained, e.g. 800°C . As shown in Fig. 9, the temperature isolines are circles sharing the same wafer center and the hottest spot is right above the heating filament. This is because the filament is arranged around the center of the heater. The temperature difference can be as large as 40°C over the heater body. Figure 10 shows the temperature profile when a copper thermal diffuse plate is placed on top of the heater. The copper plate size is $1/16''$ thick \times $1''$ diameter. As shown, the surface temperature is much more uniform than Fig. 9 due

to the high thermal conductivity of copper (400 W/m^2). In practice, however, copper cannot be used because it reacts with silicon at high temperature. Instead an Inconel (nickel-chromium-molybdenum alloy) is used. Inconel has a low thermal conductivity of 9.8 W/m^2 but it has good thermal and erosion resistance which is necessary for use inside the deposition chamber. Ideally, the thicker the thermal diffuse plate is, better temperature uniformity will be. However, thicker thermal diffuse plate limits the maximum surface temperature. The maximum surface temperature we can have with the Inconel plate is around $750 \text{ }^\circ\text{C}$. At the time of this writing, a boron nitride thermal diffuse plate is being fabricated to further improve the temperature uniformity. The thermal conductivity of boron nitride (30 W/m^2) is higher than that of Inconel so we should expect better uniformity and higher surface temperature at the same time. With the Inconel thermal diffuse plate, the heating-cooling cycle experiment was repeated (voltage ramping rate 0.5 V/min) and the result is shown in Fig. 11. As shown, even at a faster voltage ramping rate, both reflectance at 950 nm and 470 nm gradually increase with temperature. This is expected because the refractive index of silicon increases with temperature [67, 66]. Fig. 11 indicated that a much better thermal uniformity has been achieved.

2.1.3 *In situ* sensor

Figure 12 shows the photograph of the *in situ* emissivity-correcting pyrometer (ECP) [SVT Associates. Model: In-Situ 4000]. The ECP measures thermal radiation intensity at 950 and 850 nm and normal reflected light intensity at 950 and 470 nm . The bandwidths of both thermal radiation and reflection channels are around 15 nm . The idea of emissivity-correcting pyrometer can be found in [19]. In brief, the thermal radiation from a real surface can be described the blackbody radiation times the emissivity of the surface. However, as thin films are deposited, the emissivity of the

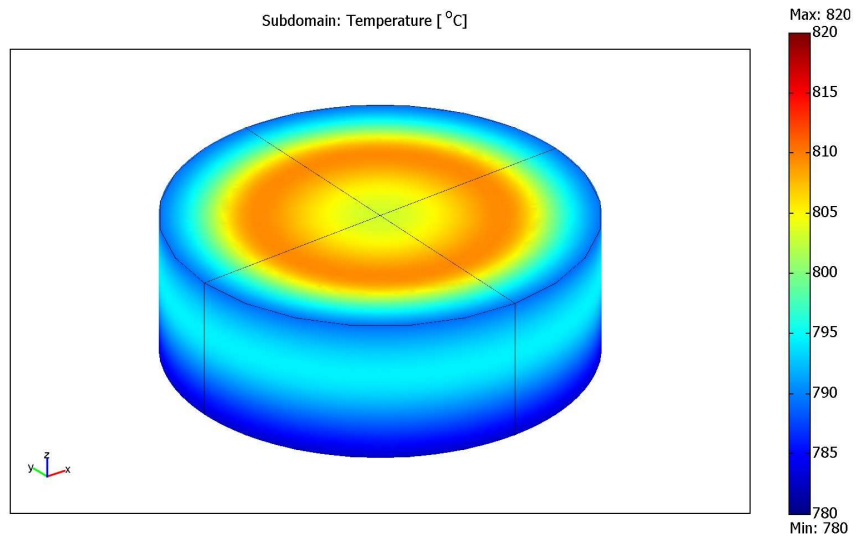


Figure 9: Temperature profile on the heater surface.

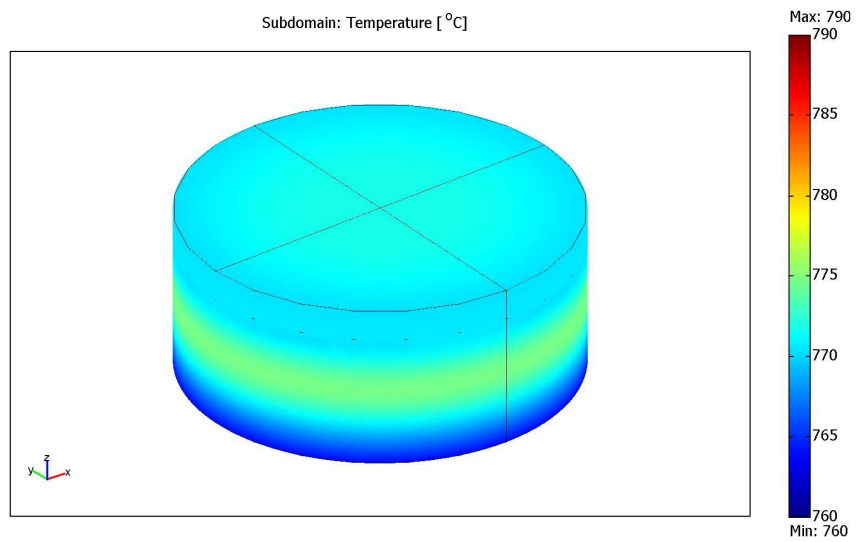


Figure 10: Temperature profile on the heater surface with a copper thermal diffuse plate.

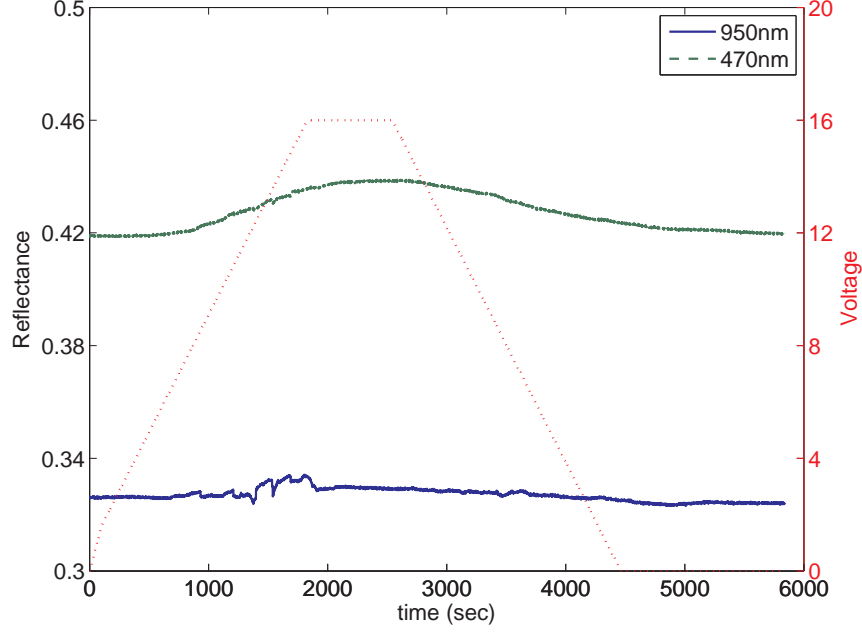


Figure 11: Reflectance change in a heating-cooling cycle experiment. Silicon substrate is on an Inconel thermal diffuse plate (Date acquired: 4/24/2007).

surface changes due to optical interference effects between film interfaces. A pyrometer that does not account for the emissivity changes will yield inaccurate surface temperature reading. If the emissivity can be independently measured, then accurate surface temperature may be obtained. Under the conditions of an opaque substrate, a perfectly specular substrate front surface, and perfect uniformity of the deposited films, the emissivity (ϵ) may be measured via reflectance (R) at the same wavelength, $\epsilon = 1 - R$. This is why one of the reflectometer wavelength is 950 nm, to match the 950 nm thermal radiation channel. The wavelength of 950 nm is chosen because it is short enough to ensure that silicon substrate is opaque, and long enough to ensure a measurable thermal radiation at growth temperatures. The opacity of the substrate also minimize the modeling effort for the thin film interference which is to be discussed in the next chapter.

The ECP is mounted on a quartz viewport [MDC Vacuum Products] which is connected to the upper main flange of the upper reducing cross by a straight tube. The

ECP has several connectors on the rear. The serial connector is used to communicate with the computer and the BNC connector is used to connect to a video monitor. There are two different fields of view for the pyrometer and the reflectometer. The pyrometer detectors have 2 degree field of view whereas the reflectometer detectors have a 3.6 degree of view. The video monitor views the reflectometer view so that dark boundary outside of the central video image corresponds to the limits of the reflectometer field. The pyrometer field is approximately 55% of the reflectometer and is centered on the video image. The field of view for the pyrometer can be calculated by $D = L/25$, where D is the diameter of the area the pyrometer views and L is the distance from the substrate to the pyrometer. In our CVD testbed, L is around 15" so we have D around 0.6". Because the area pyrometer views is 55% of the reflectometer, the diameter of the area the reflectometer views is around 0.8". The silicon substrate we use is 1" diameter so this means the measured reflectance is averaged over almost entire substrate. It is important to ensure film uniformity across the area the reflectometer views so that sensor data interpretation would not be complicated. However, this turned out to be quite difficult in our CVD testbed because of the temperature nonuniformity across the wafer due to the design of the heater. To solve this problem, we have made a simple shutter and placed it in front of the objective lens. The diameter of the shutter is made small enough to ensure only a small area on the substrate is viewed, and large enough to ensure the reflectometer can still detect enough signal. Currently, the diameter of the shutter is around 1/4" compared to 1" diameter of the objective lens.

2.1.4 Downstream

In the downstream portion of the system, a pressure transducer with a full scale of 760 Torr measures the pressure in the deposition chamber and passes it to a pressure controller [MKS Instruments], which adjusts a throttle valve in the downstream to

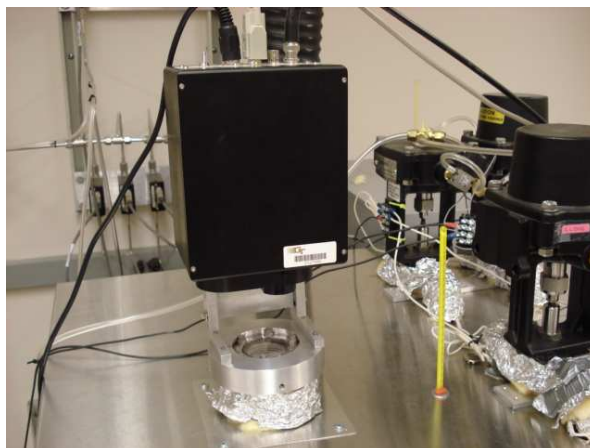


Figure 12: photograph of the emissivity-correcting pyrometer.

keep pressure stay close to the setpoint value. Another pressure transducer with smaller full scale of 10 Torr measures the pressure under 1 Torr and displays on its own readout. The exhaust passes through a liquid nitrogen trap before entering the vacuum pump [Alcatel] so that unreacted precursors can be captured. The vacuum pump is designed to operate at pumping speed of 40-50 cfm, which can easily allow working pressure 1 Torr at mass flow rate of 1000 SCCM.

2.2 Software

We have developed a data acquisition and control software for the CVD testbed by using LabVIEW [National Instruments]. Figure 13 shows the wiring diagram for all data acquisition and instrument control hardwares. Figure 14 shows the flow chart of the data acquisition and instrument control software. The program consists of eight sub-programs, each of which performs a specific task. Figure 15 and 16 show the front panel and block diagram of the software, respectively. The software is submitted together with the thesis. We now discuss each sub-program and its associated hardware wiring in details.

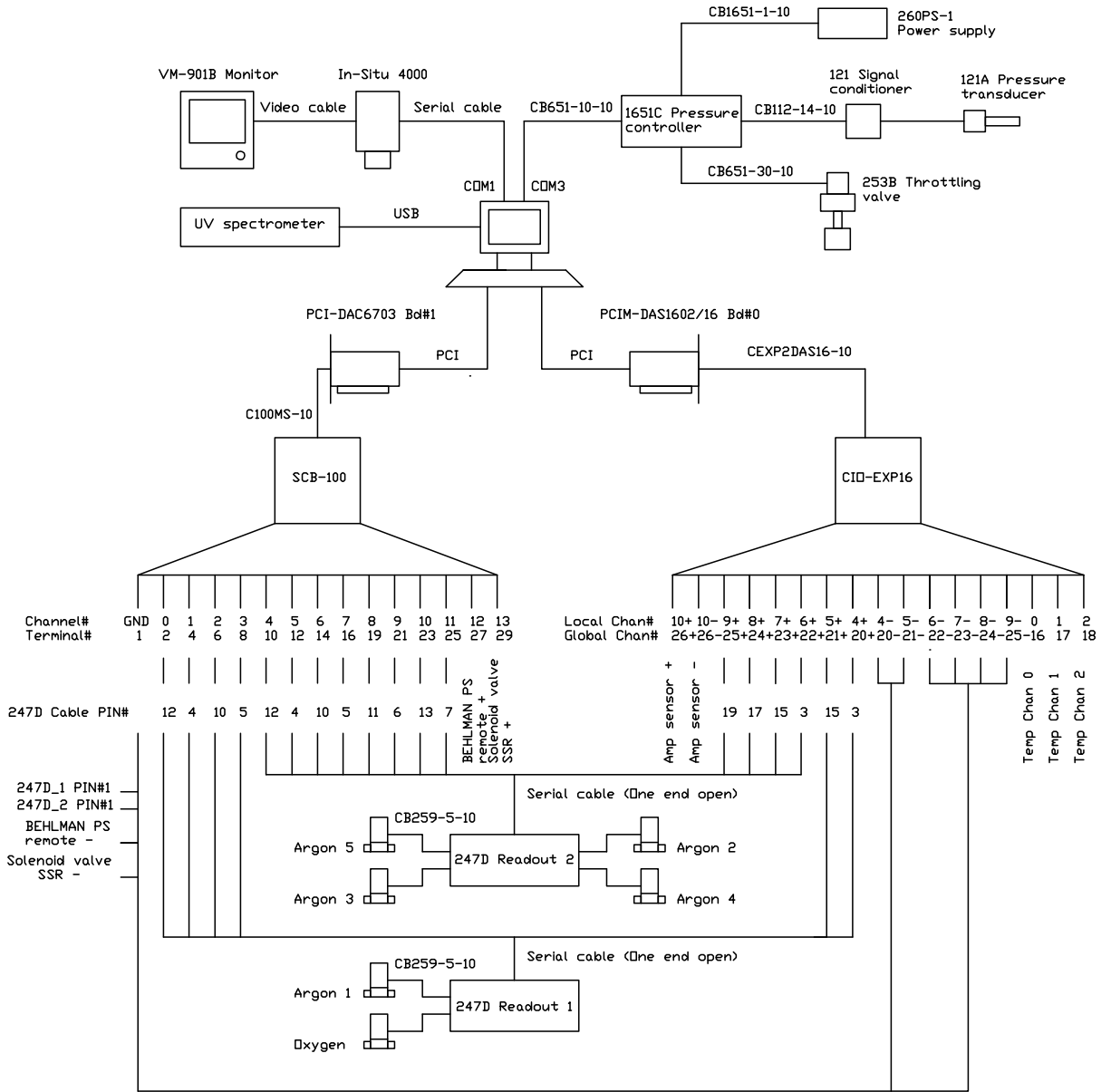


Figure 13: Wiring diagram for data acquisition and instrument control.

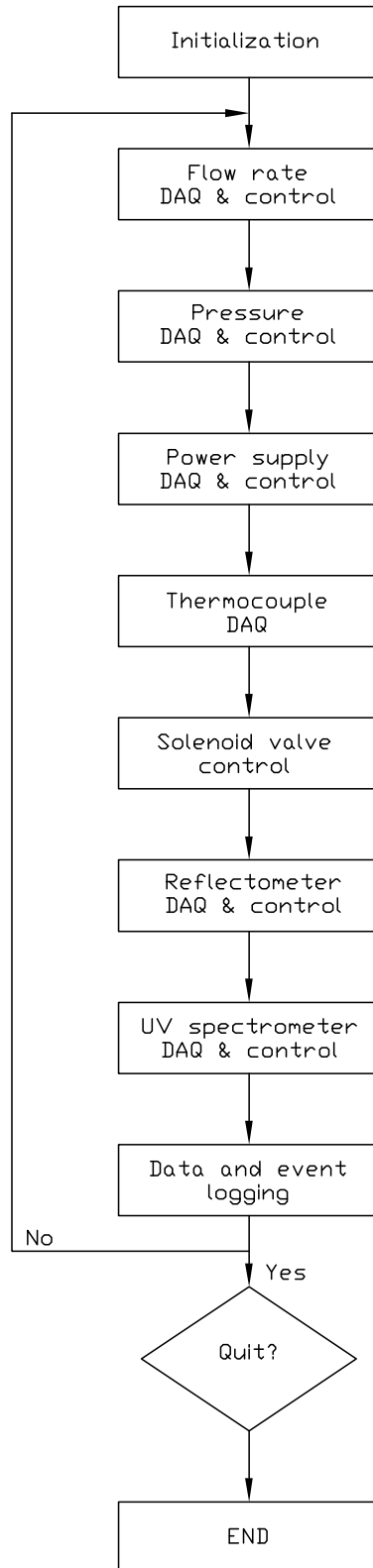


Figure 14: Flowchart of data acquisition and instrument control software.

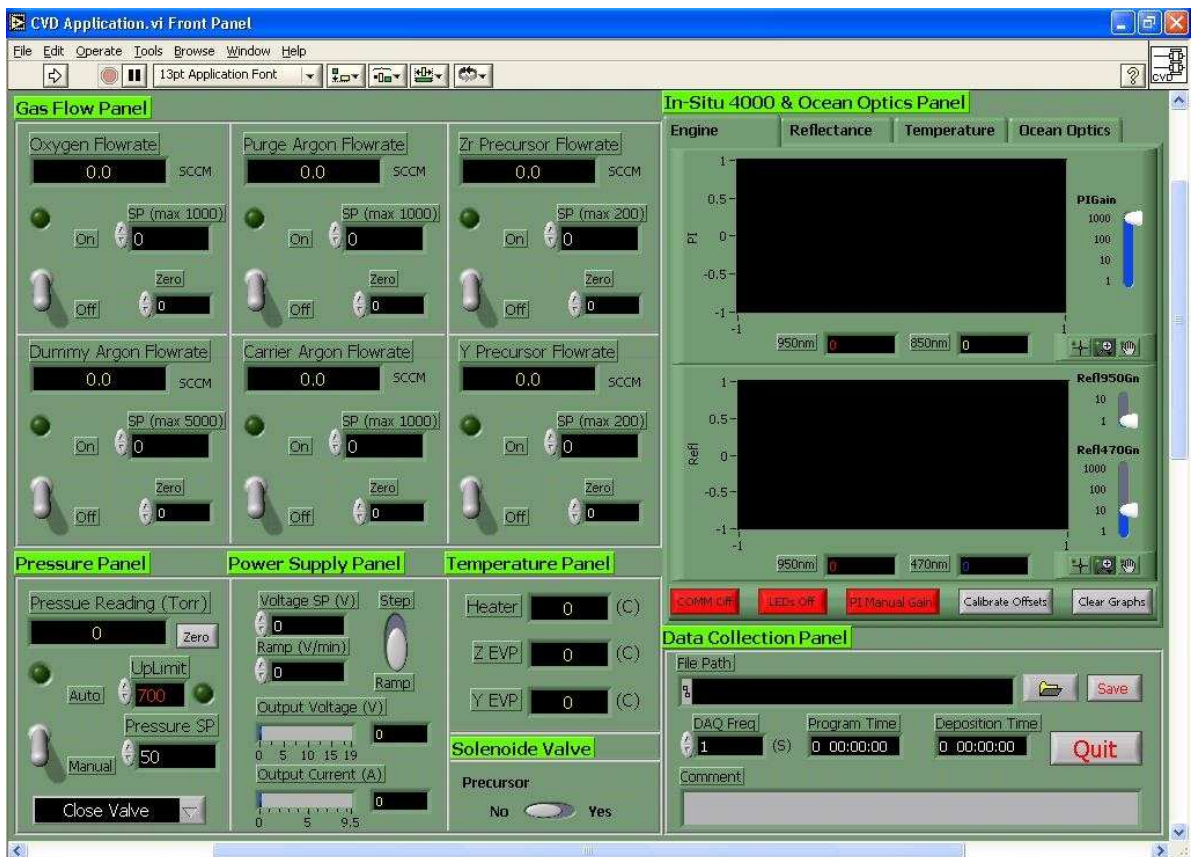


Figure 15: Front panel of the data acquisition and instrument control software.

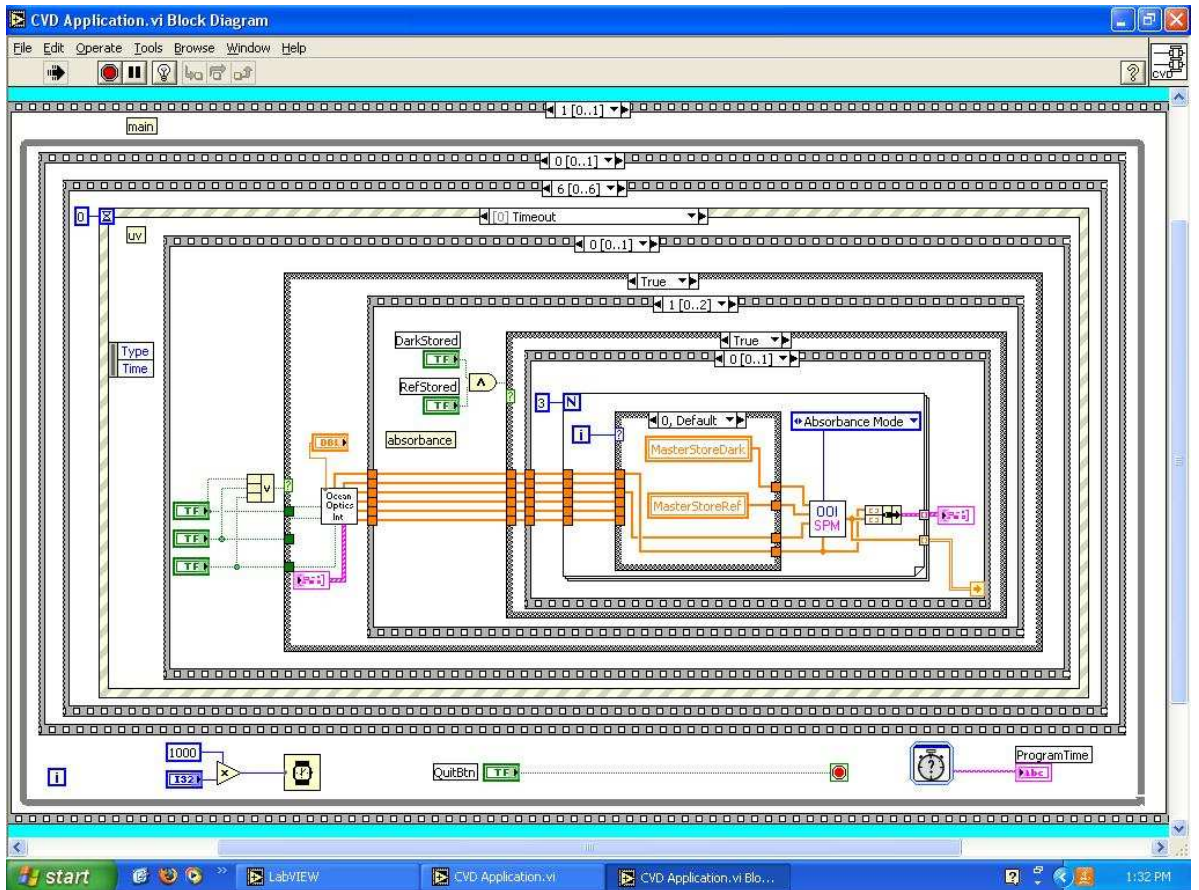


Figure 16: Block diagram of the data acquisition and instrument control software.

2.2.1 Gas flow sub-program

Gas flow sub-program allows user to acquire six channels of gas flow rate (oxygen and Ar1 5), to switch on and off the flow, and to set the setpoint of the flow rate. The program is placed in an event structure. When there is no user input, the program acquires flow rates and displays them on the front panel. When user switch on and off the flow, or change the setpoint of the flow rate, the program will capture the user input and automatically write a comment to the data file to record when and what change has been made. On the hardware level, the flow rate data acquisition and control are realized through six mass flow controllers. As shown in Fig. 13, these controllers are connected to two 4-channel readout [MKS Instrument. Model: 247D]. The readout has a serial connector on the rear and an open-end serial cable is used to connect the readout to an analog input board [Measurement Computing. Model: PCIM-DAS1602/16] for flow rate acquisition and to an analog output board [Measurement Computing. Model: PCI-DAC6703] for flow rate control. Each wire of the open-end cable has specific usage which can be found in readout's manual. The channel assignment to each wire on both input and output boards have been built into the software so they must be connected in the exactly the same way as shown in Fig. 13.

2.2.2 Pressure sub-program

Pressure sub-program allows user to acquire pressure, to zero the pressure transducer, and to switch between auto and manual mode for pressure control. In the auto mode, it allows user to set the setpoint of the pressure. In the manual mode, it allows user to open, close or hold the throttle valve. The program also implements an over-pressure protection mechanism. It allows user to set the upper limit of the pressure in the chamber. When pressure exceeds the upper limit, the program will automatically shut off all six channels of gas flow. The program is placed in an event structure.

When there is no user input, the program acquires pressure and displays it on the front panel. When user zero the pressure transducer, switch between auto and manual mode, change the pressure setpoint, open/close/hold the throttle valve, or change the pressure upper limit, the program will capture the user input and automatically write a comment to the data file to record when and what change has been made. On the hardware level, the pressure data acquisition and control are realized through a pressure controller [MKS Instruments. Model: 1651C]. As shown in Fig. 13, the controller is connected to a pressure transducer [MKS Instruments. Model: 121A] and a throttle valve [MKS Instruments. Model: 253B]. The controller communicates with the computer through COM3 port. The command syntax can be found in the pressure controller's manual.

2.2.3 Power supply sub-program

Power supply sub-program allows user to acquire current, to set the setpoint of heating voltage, and to switch between step and ramp mode. In the step mode, the program changes the voltage to the setpoint immediately. In the ramp mode, the program allows user to specify the ramping rate and it calculates the voltage increment for each iterative based on the ramping rate. The program is placed in an event structure. When there is no user input, the program acquires current and voltage and displays them on the front panel. When user change the setpoint of the voltage, switch between step and ramp mode, or change the ramping rate, the program will capture the user input and automatically write a comment to the data file to record when and what change has been made. On the hardware level, the current data acquisition is realized through a current sensor [Veris Industries] and the voltage control is realized through a power supply [Behlman Electronics. Model P1350]. As shown in Fig. 13, the current sensor is connected to the input board on channel number 10. The power supply has an input connector on the rear and is connected to the output board on

channel number 12. The power supply output AC voltage (V_o) is determined by the input DC voltage (V_i). The relationship has been determined experimentally and is $V_o = 13.66 \times V_i$.

2.2.4 Temperature and solenoid valve sub-program

Temperature and solenoid valve sub-program allows user to acquire three channels of temperature and to switch four solenoid valves on the flow manifold between the reaction and the bypass line. The program is placed in an event structure. When there is no user input, the program acquires temperatures and displays them on the front panel. When user switch the solenoid valves, the program will capture it and automatically write a comment to the data file to record when the solenoid valves are switched and its new state (On or Off). The program uses the time of switching the solenoid valves from the bypass to the reaction line as the starting point and the time of switching from the reaction to the bypass line as the ending point of the deposition process. The elapsed time since start of deposition is also displayed on the front panel. On the hardware level, the three K-type thermocouples are connected to the input board on channel number 0, 1 and 2. The thermocouple on channel 0 is connected to the thermocouple feedthrough of the heater assembly and measures the temperature behind the heater. The thermocouple on channel 1 and 2 measures the temperature of Zr evaporator and Y evaporator, respectively. The four solenoid valves are connected in parallel to a 120 V power source and to the output terminal of a solid state relay (SSR) whose input is connected to the output board on channel number 13. The SSR acts like a switch to turn on or off the 120 V power source that drives the solenoid valves. When the input voltage on the SSR is higher than 3 V, the four solenoid valves switch simultaneously.

2.2.5 Emissivity-correcting pyrometer sub-program

Emissivity-correcting pyrometer (ECP) sub-program is the most challenging part of this software. The ECP was shipped with its own data acquisition and control software developed by SVT Associates. We basically rebuilt all the functionalities of the commercial software by using LabVIEW. The ECP sub-program has three tabs in the front panel, as shown in Fig. 17 to 19. The first tab is Engine tab in which the program allows user to acquire thermal radiation intensity at 950 and 850 nm and reflected light intensity at 950 and 470 nm, to enable or disable data acquisition, to turn on or off LED light source, and to switch between manual and auto mode for gain control. In manual mode, the program allows user to change the electric gain by using the scale bar on the right-hand side of the plots. If the gain is set too high, the electric amplifiers may saturate, so the manual gain must be used with care. In auto mode, the program automatically adjust the gain to maximize the signal but not exceeds 2000 mV. The Clear Graph button clears plots on three tabs simultaneously. The second tab is Reflectance tab in which the program calculates reflectance at 950 and 470 nm based on the low calibration and high calibration point. The program allows user to specify the reflectance value at both low and high calibration points and to calibrate the reflectance using Calibrate High and Calibrate Low buttons. Once calibrated, the value of reflectance and intensity at both low and high calibration points are saved in the hard disk for future use. The third tab is temperature tab in which the program calculates single and dual-wavelengths temperature of the substrate surface from 950 nm thermal radiation intensity and the intensity ratio of 950 to 850 nm, respectively. The temperature calculation only occurs when the thermal radiation intensity at both 950 and 850 nm exceed a threshold value of 0.05 mV. The program also allows the user to calibrate the single wavelength pyrometer with dual-wavelength temperature reading by using the Calibrate Ratio Temp button. The geometric constant obtained in the calibration is displayed in



Figure 17: Engine tab of ECP sub-program.

the front panel and also saved in the hard disk for future use. The program is placed in an event structure. When there is no user input, the program either does nothing if communication and LED light source is off, or acquires thermal radiation, reflected light intensity, reflectance and temperature and display them on the front panel if the communication is on. When user enable or disable the communication, turn on or off the LED light source, change the mode of gain control, manually change the gain, change the reflectance calibration value, calibrate reflectance, or calibrate temperature, the program will capture the user input and automatically write a comment to the data file to record when and what change has been made. On the hardware level, as shown in Fig. 13, the ECP communicates with the computer through COM1 port. The syntax of the command is provided by SVT Associates and is attached in the Appendix.

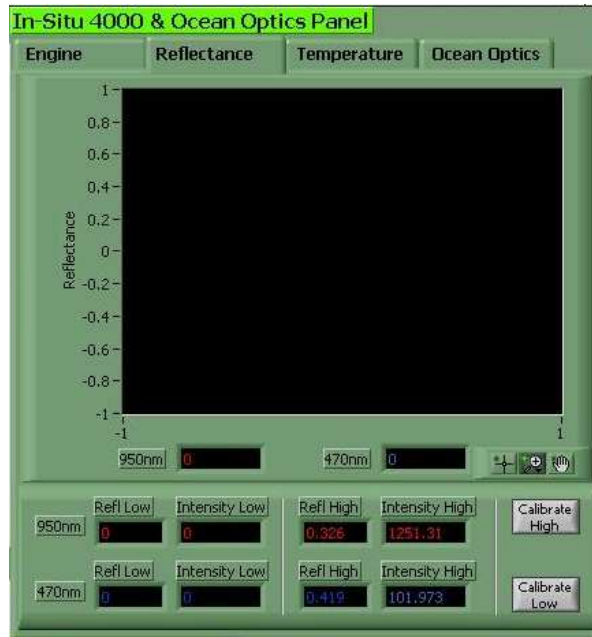


Figure 18: Reflectance tab of ECP sub-program.

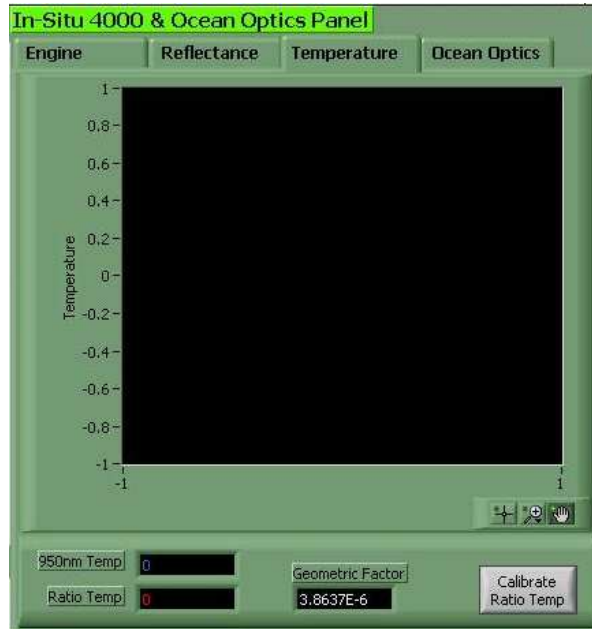


Figure 19: Temperature tab of ECP sub-program.

2.2.6 UV spectrometer sub-program

Figure 20 shows the front panel of UV spectrometer sub-program. The program allows user to acquire spectral transmitted light intensity, to calibrate spectral absorbance by using dark and reference spectrum, and to turn on or off three optical channels. The program also calculates the mole flow rate of Zr and Y precursors based on Eq. (1) and allows PID control of mole flow rate by adjusting carrier argon flow rate. User can specify PID parameters and enable or disable the controller in a popup window once the PID button is clicked. The user specified PID parameters are saved in the hard disk for future use. The program is placed in an event structure. When there is no user input, the program either does nothing if the optical channels are off or acquires spectral transmitted light intensity and display them on the front panel if the optical channels are on. When user stores dark or reference spectrum, or activate the PID controller, the program will capture the user input and automatically write a comment to the data file to record when and what change has been made. On the hardware level, as shown in Fig. 13, the UV spectrometer communicates with the computer through a USB port. The LabVIEW driver for the UV spectrometer can be obtained from Ocean Optics or downloaded from Instrument Driver Network on National Instruments website [http://sine.ni.com/apps/utf8/niid-web-displays.model-page?p_model_id=2843].

2.2.7 Data logging sub-program

Data logging sub-program allows user to specify where to save the data, how frequently to save the data, to write comments that are not built into the software, and to stop the program. The program also displays elapsed time since the program started and elapsed time since deposition started, i.e. when the solenoid valves are switched. The data file has 30 columns and they are time, thermal radiation intensity at 950 and 850 nm, reflected light intensity at 950 and 470 nm, calibrated reflectance

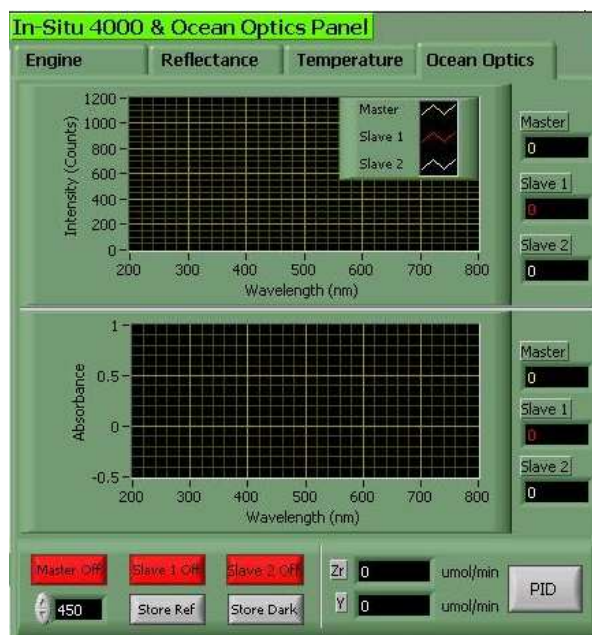


Figure 20: Front panel of UV spectrometer sub-program.

at 950 and 470 nm, temperature from dual and single wavelength pyrometer, temperature behind the heater, Zr and Y evaporators, heating voltage and current, six channels of gas flow rate (oxygen and Ar1 5), pressure, three channels of transmitted light intensity and calibrated absorbance at 286 nm, calculated Zr and Y precursor mole flow rate, and finally comments including both built-in and user entered comments. The data file can be directly opened by Microsoft Excel. An Excel VB script was written to automatically plot the data, summarize comments and output an Excel workbook file that can be loaded into Matlab for further analysis.

2.3 Operation of CVD system

A detailed procedure for operating this chemical vapor deposition testbed is attached in the Appendix. It is written by Derek Jamrog who worked in our group as an undergraduate research assistant in summer semester 2007. He wrote this procedure from the perspective of a brand new user. In the rest of this section, we summarize some practical lessons we have learned in operating this CVD testbed.

- Do not touch any vacuum components with bare hands when packing the evaporators and loading the substrate on the heater assembly.
- Always load the substrate in the same orientation, e.g. face the flat edge of the wafer toward the user. If the substrate does not have a flat edge, use a diamond cutter to make a small mark on the substrate. Knowing the orientation of the substrate can help us to investigate the effect of flow direction and pattern on the film uniformity.
- Pressure inside the deposition chamber can affect the reflectance when pumping down or venting the system. This is because the pressure difference between inside and outside of the deposition chamber put a force on the heater assembly which is held to the chamber by a hinge clamp.
- The reflectance change during heating up and cooling down the substrate is difficult to predict even when a thermal diffuse plate is used. This is because the measured reflectance is an overall response to the optical properties change and thermal deformation of the substrate. However, reflectance will stabilize after the heating voltage and oven temperature are stabilized and that reflectance is what is important to us. Once the reflectance is stabilized, we can adjust the position of the ECP to maximize the reflected light intensity which is attained at normal incidence. We can also calibrate reflectance using high temperature refractive index of silicon.
- After the deposition, do not cool down the reactor immediately. Wait for around 10 minutes to allow any unreacted precursors to be consumed or flushed out of the system. We have observed that quick cooling down of the reactor caused remaining precursors in the chamber to condense on the film. The resulting film appears dirty and it introduces error in *ex situ* surface characterization such as AFM.

- After the deposition, the temperature inside the chamber is not uniform. The pressure transducer is close to the liquid nitrogen trap and thus has a much lower temperature while other parts are still hot. When flowing argon to bring the system back to normal pressure, we have observed that argon stopped flowing even though the pressure transducer read a much smaller pressure than atmospheric pressure. This indicated that the pressure in the upstream is much higher than downstream due to temperature difference. Later when downstream temperature increases due to the evaporation of liquid nitrogen, the pressure in the chamber increases sharply and sometimes exceed the atmospheric pressure. This is quite dangerous for the quartz viewport. Therefore we should wait for the system to cool down before flowing argon to bring the system back to the atmospheric pressure.

CHAPTER III

SENSOR MODELS AND OBSERVABILITY

In order to extract thin film properties such as film thickness, refractive index and surface roughness from the reflectance measurements, we must have an optical sensor model that quantifies the relationship between thin film properties and the reflectance. In this chapter, we start with a simple optical model for light reflection on a film/substrate system with perfectly smooth surface. We then study two additional optical models that consider the surface roughness effect, namely scalar scattering model and effective medium model. We discuss the conditions for validity of the two models and present model validation results using *ex situ* characterization. Based on the sensor models, we study the effect of film growth rate, extinction coefficient and roughness on the reflectance. Finally, we discuss the observability based on the sensor model and a simple process dynamic model.

3.1 Sensor models

3.1.1 Reflection on film/substrate with smooth surface

Figure 21 shows the schematic of light reflection on a film/substrate system with perfectly smooth surface. n_1 , n_2 and n_3 are the complex refractive index of vacuum, the film and the substrate, respectively. In the complex refractive index, $n = n_r - ik$, the real part n_r is the refractive index and the imaginary part k is the extinction coefficient, which indicates the amount of absorption loss when light propagates through the material. The incident light travels in the direction SB_1 with an incident angle of θ and upon reflection at B_1 it is divided into two beams, one reflected in the direction B_1C_1 and the other transmitted into the film in the direction B_1D_1 . The transmitted beam is further divided upon reflection at D_1 , one transmitted in the direction D_1E_1

which is assumed to be totally absorbed by the substrate, and the other reflected back into the film in the direction D_1B_2 . Such division of light continues infinitely as shown in the figure. The reflected beams that leave the film surface have different amplitude and phase and this is what causes interference. For each reflected beam, the amplitude is determined by its corresponding incident beam based on the Fresnel formula and its phase differs from that of the preceding reflected beam by an amount of which corresponds to a double traversal of the film, $\delta = \frac{4\pi}{\lambda}n_2h\cos\theta'$, where θ' is the refractive angle. At normal incidence the phase difference is

$$\delta = \frac{4\pi}{\lambda}n_2h \quad (2)$$

where h is the thickness of the film and λ is the wavelength of the light in vacuum. Therefore, if the amplitude of the incident light is $A^{(i)}$, the amplitude of reflected beams that leave the film surface are $r_{12}A^{(i)}$, $t_{12}t_{21}r_{23}A^{(i)}e^{-i\delta}$, $t_{12}t_{21}r_{23}^2r_{21}A^{(i)}e^{-2i\delta}$, \dots , $t_{12}t_{21}r_{23}^p r_{21}^{p-1}A^{(i)}e^{-pi\delta}$, \dots . The quantities r_{12} , r_{23} , r_{21} are the Fresnel coefficient for reflected light that goes from medium 1 to 2, medium 2 to 3 and medium 2 to 1, respectively. The quantities t_{12} and t_{21} are the Fresnel coefficient for transmitted light that goes from medium 1 to 2 and medium 2 to 1, respectively. In the above analysis, the incident light is assumed to be linearly polarized with the electric vector either parallel (p -polarization) or perpendicular (s -polarization) to the plane of incidence. If the incident light has both p and s component, each component must be dealt with separately because the reflectance depends on the polarization of the incident light. In the case of normal incidence, however, the difference between the reflectance of p - and s -polarization disappears and we can use the Fresnel coefficients of either p or s -polarization. For s -polarization, the Fresnel coefficients are expressed by [18].

$$r_{12} = \frac{n_1 - n_2}{n_1 + n_2}, \quad r_{23} = \frac{n_2 - n_3}{n_2 + n_3}, \quad t_{12} = \frac{2n_1}{n_1 + n_2}, \quad t_{21} = \frac{2n_2}{n_1 + n_2} \quad (3)$$

The amplitude of the reflected light is obtained by superposing all individual reflected beams that leave the film surface, $A^{(r)} = [r_{12} + t_{12}t_{21}r_{23}e^{-i\delta} \sum_{p=0}^{\infty} (r_{23}r_{21}e^{-i\delta})^p]A^{(i)}$.

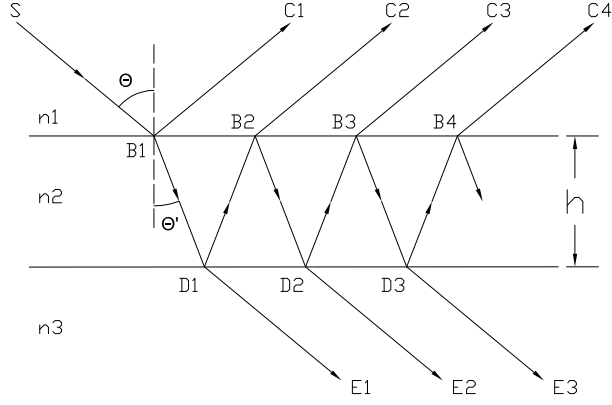


Figure 21: Reflection on a film/substrate system with perfectly smooth surface.

When $p \rightarrow \infty$, using $\sum_{p=0}^{\infty} x^p = \frac{1}{1-x}$ and $r_{12} \times r_{21} + t_{12} \times t_{21} = 1$, we obtained

$$A^{(r)} = \frac{r_{12} + r_{23}e^{-i\delta}}{1 + r_{12}r_{23}e^{-i\delta}} A^{(i)} \quad (4)$$

The reflectance is defined as $\left| \frac{A^{(r)}}{A^{(i)}} \right|^2$ and therefore for light reflection on a film/substrate system with perfectly smooth surface, the normal reflectance is

$$R = \left| \frac{r_{12} + r_{23}e^{-i\delta}}{1 + r_{12}r_{23}e^{-i\delta}} \right|^2 \quad (5)$$

This model is what used in [20] but one should note that there is a mistake in Eq. (6) in that paper when calculating R from r .

3.1.2 Scalar scattering model

When the surface is rough, the incident light is partially scattered and this causes the reflected light intensity to decrease. This macroscopic observation can be explained by microscopic events. On a microscopic level, the specular reflection is the net result of interference among a large number of reflected beams in various directions. Therefore, when the surface is optically rough, the net result of interference may change due to the phase difference induced by the roughness and cause the reflected light to redistribute in other directions which will be seen as scattered light. This idea is illustrated in Fig 22. As shown, two normal incident beams of A and B reflect

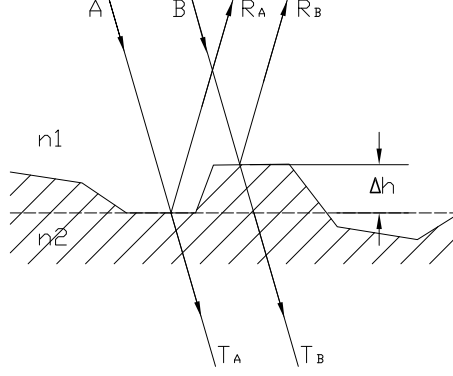


Figure 22: Reflection on a rough surface. The height irregularity induced phase difference.

on a rough surface. The irregularities of height Δh causes a difference in the optical path r between the two reflected beams A_R and B_R , $r = 2\Delta h n_1$ and thus phase difference $\Delta\Phi_R = \frac{4\pi\Delta h n_1}{\lambda}$. When the surface has a Gaussian distribution of height, it was shown that the reflection coefficient is given by $r'_{12} = r_{12}\exp[-(\Delta\Phi_R)^2] = r_{12}\exp\left[-\left(\frac{4\pi\sigma n_1}{\lambda}\right)^2\right]$, where r_{12} is the Fresnel coefficient for the smooth surface and σ is the root mean square (RMS) roughness and is proportional to $(\sum \Delta h^2)^{1/2}$ [11, 43, 24]. Similarly, the phase difference between two transmitted beams T_A and T_B is $\Delta\Phi_T = \frac{2\pi\Delta h(n_1-n_2)}{\lambda}$ and the transmission coefficient is $t'_{12} = t_{12}\exp\left[-\left(\frac{2\pi\sigma(n_1-n_2)}{\lambda}\right)^2\right]$.

With the new reflection and transmission coefficient, the amplitude of the reflected beams in Fig. 21 are $r_{12}S_{12}A^{(i)}$, $t_{12}t_{21}S_t^2r_{23}A^{(i)}e^{-i\delta}$, $t_{12}t_{21}S_t^2r_{23}^2r_{21}S_{21}A^{(i)}ie^{-2i\delta}$, \dots , $t_{12}t_{21}S_t^2r_{23}^p r_{21}^{p-1} S_{21}^{p-1} A^{(i)} ie^{-pi\delta}$, \dots , where the scattering factors $S_{12} = \exp\left[-\left(\frac{4\pi\sigma n_1}{\lambda}\right)^2\right]$, $S_{21} = \exp\left[-\left(\frac{4\pi\sigma n_2}{\lambda}\right)^2\right]$ and $S_t = \exp\left[-\left(\frac{2\pi\sigma(n_1-n_2)}{\lambda}\right)^2\right]$. Following the same procedures in the smooth case, we superpose all individual reflected beams and obtained the normal reflectance on a film/substrate with rough surface

$$R = \left| \frac{S_{12}r_{12} + (S_t^2 t_{12} t_{21} + S_{12} S_{21} r_{12}^2) r_{23} e^{-i\delta}}{1 + r_{12} r_{23} S_{21} e^{-i\delta}} \right|^2 \quad (6)$$

Obviously, when the surface is smooth, $S_{12} = S_{21} = S_t = 1$, and Eq. (6) reduces to Eq. (5).

3.1.3 Effective medium model

The scalar scattering model is valid when the surface is macroscopically rough, i.e. the length scale of the irregularities is of the order of or exceeds the wavelength of light. When the surface is microscopically rough, i.e. the mean height and correlation length of the irregularities are both much less than the wavelength of light, the multiple-scattering is not significant and the roughness is commonly modeled by the effective medium model, in which the roughness is modeled as a thin homogeneous layer with refractive index intermediate to the refractive indices of the two adjacent optical media [5]. Three effective medium approximation (EMA) models, namely Lorentz-Lorentz approximation, Maxwell-Garnett approximation and Bruggeman approximation, are used to calculate the refractive index of the effective layer. These models are jointly expressed by $\frac{\langle \epsilon \rangle - \epsilon_h}{\langle \epsilon \rangle + 2\epsilon_h} = \sum_j f_j \frac{\epsilon_j - \epsilon_h}{\epsilon_j + 2\epsilon_h}$, where $\langle \epsilon \rangle$ is the dielectric function of the effective medium, ϵ_h is the dielectric function of the host material, f_j is the fraction of the j^{th} constituent. Refractive index is related to the dielectric constant by $n = \sqrt{\epsilon}$. The only difference between the three EMA models is the choice of the host material. The Bruggeman approximation consisting of 50% voids and 50% material underneath has been found to model surface roughness better than the other two EMA models and has been successful in interpreting spectral ellipsometric data. In the Bruggeman EMA, $\epsilon_h = \langle \epsilon \rangle$, i.e. the host material is just the EMA dielectric function [146]. Using $n = \sqrt{\epsilon}$, the refractive index of the effective layer can be expressed by

$$\langle n \rangle = \sqrt{\langle \epsilon \rangle} = \frac{\sqrt{\sqrt{\Omega^2 + 8n_1^2 n_3^2} + \Omega}}{2} \quad (7)$$

where $\Omega = (n_1^2 + n_3^2)/2$ and n_1 and n_3 represent the refractive index of the ambient and the film underneath, respectively.

For this rough/film/substrate system (rough is the effective layer), we can certainly use the ray tracing method to calculate normal reflectance, as in the smooth

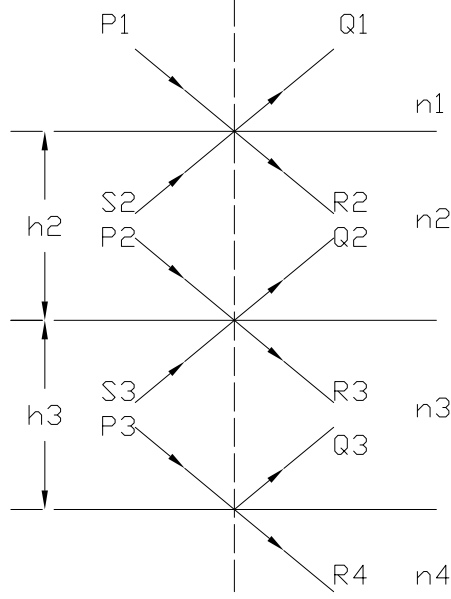


Figure 23: Light propagation in a system of 4 layers.

and scalar scattering model but this becomes more tedious as number of layers increases. A more elegant way is to use propagation matrices to keep track of light propagation in multilayer structures [34, 146]. Figure 23 shows light propagation on a four layer structure, in which layers 1 to 4 represent ambient, roughness layer, film, and substrate, respectively. Each layer is characterized by four distinct beams, traveling upwards (S and Q) and downwards (P and R) in the layer, and they are related by

$$\begin{bmatrix} P_{k-1} \\ Q_{k-1} \end{bmatrix} = \frac{1}{t_{k-1,k}} \begin{bmatrix} 1 & r_{k-1,k} \\ r_{k-1,k} & 1 \end{bmatrix} \begin{bmatrix} R_k \\ S_k \end{bmatrix} \quad (8)$$

and

$$\begin{bmatrix} R_k \\ S_k \end{bmatrix} = \begin{bmatrix} \exp(i\delta_k) & 0 \\ 0 & \exp(-i\delta_k) \end{bmatrix} \begin{bmatrix} P_k \\ Q_k \end{bmatrix} \quad (9)$$

where $\delta_k = 2\pi n_k h_k / \lambda$. Eq. (8) ensures the continuity condition at each interface and Eq. (9) represents the phase change after light passing a distance of h_k through layer k .

For the film/substrate system, applying Eq. (8) and Eq. (9), we have

$$\begin{aligned}
\begin{bmatrix} P_1 \\ Q_1 \end{bmatrix} &= \frac{1}{t_{12}} \begin{bmatrix} 1 & r_{12} \\ r_{12} & 1 \end{bmatrix} \begin{bmatrix} R_2 \\ S_2 \end{bmatrix} \\
\begin{bmatrix} R_2 \\ S_2 \end{bmatrix} &= \begin{bmatrix} \exp(i\delta_2) & 0 \\ 0 & \exp(-i\delta_2) \end{bmatrix} \begin{bmatrix} P_2 \\ Q_2 \end{bmatrix} \\
\begin{bmatrix} P_2 \\ Q_2 \end{bmatrix} &= \frac{1}{t_{23}} \begin{bmatrix} 1 & r_{23} \\ r_{23} & 1 \end{bmatrix} \begin{bmatrix} R_3 \\ S_3 \end{bmatrix}
\end{aligned} \tag{10}$$

Because there is no light coming back from the substrate, $S_3 = 0$, Eq. (10) becomes

$$\begin{bmatrix} P_1 \\ Q_1 \end{bmatrix} = \frac{1}{t_{12}t_{23}} \begin{bmatrix} (r_{12}e^{i\delta} + r_{23}e^{-i\delta})R_3 \\ (e^{i\delta} + r_{12}r_{23}e^{-i\delta})R_3 \end{bmatrix} \tag{11}$$

From Eq. (11), the reflection coefficient is

$$\frac{Q_1}{P_1} = \frac{r_{12} + r_{23}e^{-i2\delta}}{1 + r_{12}r_{23}e^{-i2\delta}} \tag{12}$$

and this is the same result as Eq. (5).

Similarly, the reflection coefficient for rough/film/substrate system with the effective medium model can be obtained by simply multiplying the propagation matrices and is

$$\frac{Q_1}{P_1} = \frac{r_{12} + r_{23}e^{-i2\delta_2} + r_{34}e^{-i2(\delta_2+\delta_3)} + r_{12}r_{23}r_{34}e^{-i2\delta_3}}{1 + r_{12}r_{23}e^{-i2\delta_2} + r_{12}r_{34}e^{-i2(\delta_2+\delta_3)} + r_{23}r_{34}e^{-i2\delta_3}} \tag{13}$$

Therefore, the reflectance is expressed by

$$R = \left| \frac{r_{12} + r_{23}e^{-i2\delta_2} + r_{34}e^{-i2(\delta_2+\delta_3)} + r_{12}r_{23}r_{34}e^{-i2\delta_3}}{1 + r_{12}r_{23}e^{-i2\delta_2} + r_{12}r_{34}e^{-i2(\delta_2+\delta_3)} + r_{23}r_{34}e^{-i2\delta_3}} \right|^2 \tag{14}$$

3.2 Sensor model validation

The surface roughness is modeled by the scalar scattering model (SSM) and effective medium model (EMA), which are fundamentally different approaches. In SSM, the roughness is modeled as the root mean square of height irregularities and it can be

measured directly by a surface profiling technique such as atomic force microscopy (AFM). In EMA, however, the roughness is modeled as the thickness of an effective layer based on the optical response and it can be measured by ellipsometry. Some researchers have attempted to find the relationship between the RMS roughness and the effective layer thickness, and different results have been reported. For example, some claim that the effective layer thickness is twice that of the RMS roughness, based on both theoretic derivation and experimental work [25, 87, 88, 109], some claim that the effective layer thickness is 1.5 times of RMS roughness [77], while still others claim that it is generally impossible to expect a good agreement between the EMA thickness and RMS roughness reported by AFM [45].

We have deposited yttria films on silicon substrates under different processing conditions and measured their RMS roughness and effective layer thickness using AFM [Molecular Imaging. Model: PicoPlus] and ellipsometer [J.A. Woollam Co. Model: M-2000], respectively. Figure 24 to 28 shows the AFM images of the deposited films with a scan size of $5\mu\text{m} \times 5\mu\text{m}$. The height distribution of each film can be well fit by a Gaussian distribution and thus satisfy the condition of the scalar scattering model. Figure 29 shows a typical height distribution curve and the Gaussian fit. The RMS roughness (σ) and the autocorrelation length (τ) for each film have been obtained by using a AFM data analysis software [Gwyddion] and are summarized in Table 2. The autocorrelation function is also fitted well by Gaussian (Figure not shown). It has been shown that for a surface with a Gaussian autocorrelation function, $\tau > 0.6\lambda$ leads to accurate results for scalar scattering model, and $\tau > 0.4\lambda$ leads to less than 20% error [178]. Considering the range of τ in Table 2, λ should be less than 300 nm for SSM to be accurate. Our *in situ* reflectometer uses two wavelength, 950 nm and 470 nm, both of which are larger than 300 nm. This suggests that SSM may not be a good model for extracting RMS roughness.

Table 2 also summarizes the fitting result of the ellipsometry data which are

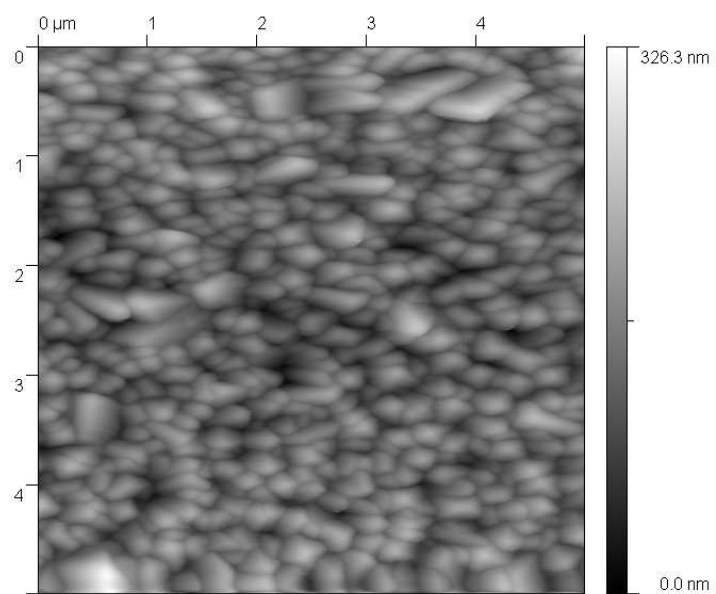


Figure 24: AFM image of yttria film deposited on 8/14/2006.

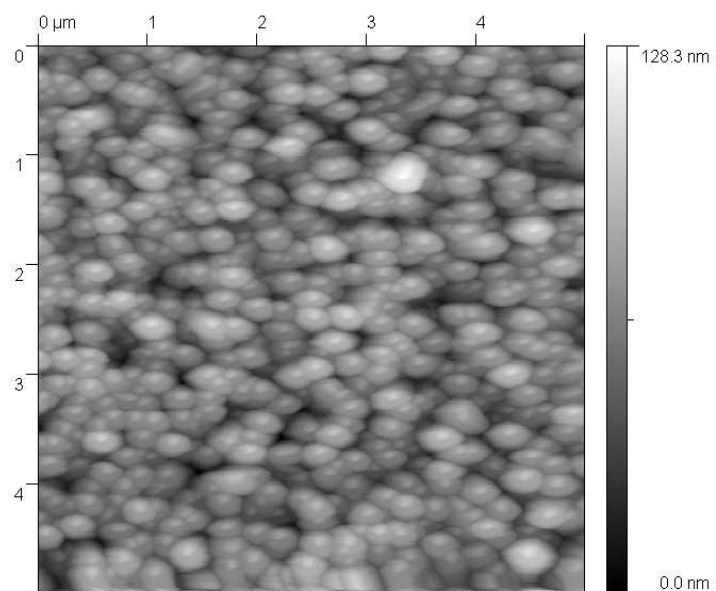


Figure 25: AFM image of yttria film deposited on 8/15/2006.

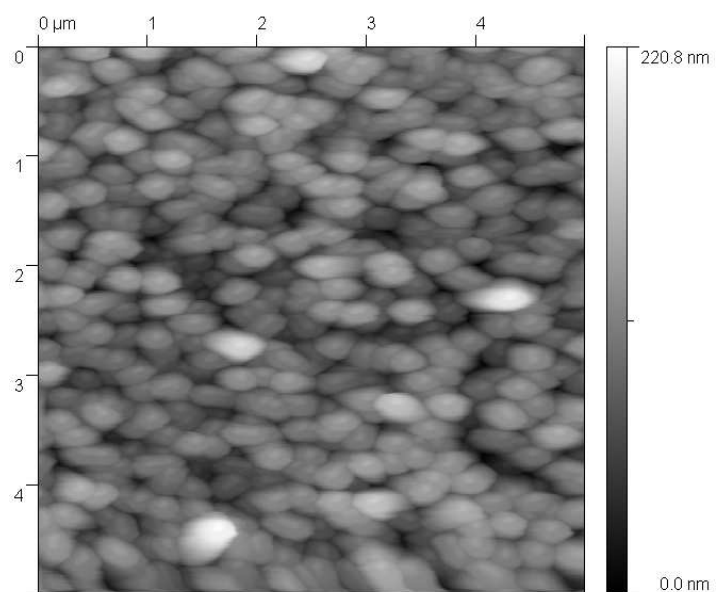


Figure 26: AFM image of yttria film deposited on 8/16/2006.

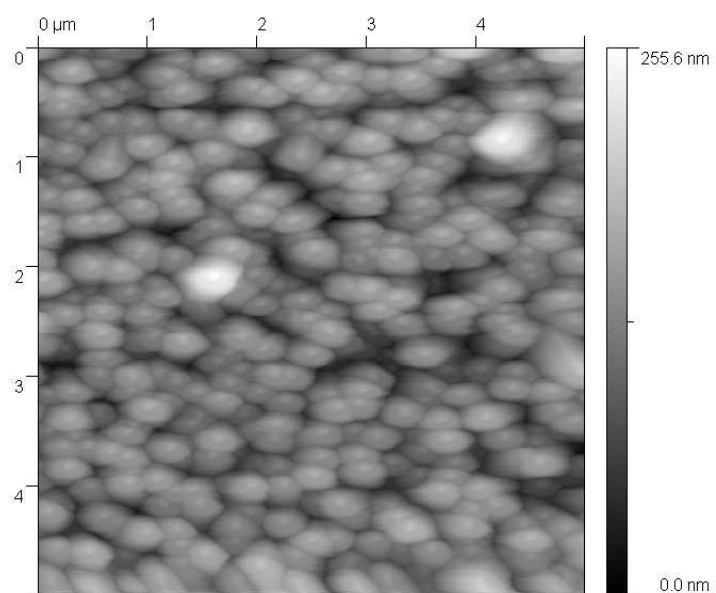


Figure 27: AFM image of yttria film deposited on 8/17/2006.

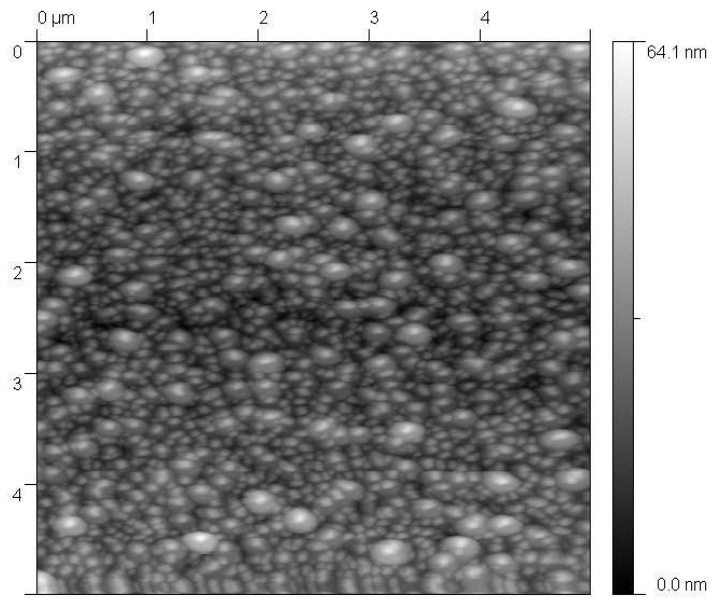


Figure 28: AFM image of yttria film deposited on 8/18/2006.

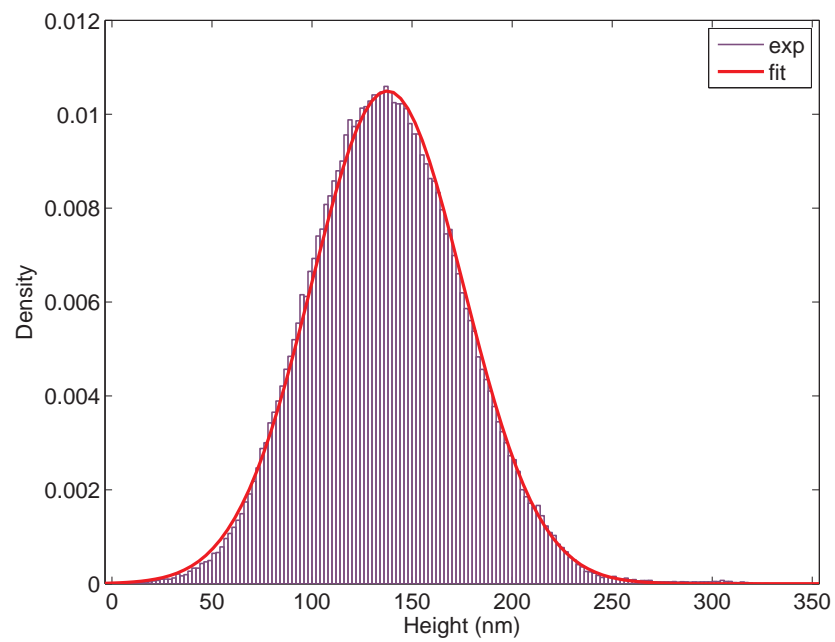


Figure 29: The surface height distribution from the AFM image in Fig. 24. The height distribution is well fit by a Gaussian.

Table 2: *Ex situ* AFM and ellipsometer characterization and optical model validation results.

Date	Ellipsometry					AFM		MSE $\times 10^{-3}$	
	A_n	B_n	A_k	h (nm)	h_e (nm)	σ (nm)	τ (nm)	SSM	EMA
8/14/06	1.866	0.0137	0.0294	623.9	77.7	38.0	141	5.8	3.8
8/15/06	1.845	0.0146	0.0235	378.8	61.1	16.4	135	2.0	1.9
8/16/06	1.895	0.0130	0.0294	503.8	69.7	27.8	179	3.5	2.9
8/17/06	1.868	0.0151	0.0274	650.8	76.1	31.6	176	3.0	2.2
8/18/06	1.867	0.01	0.0314	144.7	32.5	8.1	83	1.4	0.7

based on a three layer model of rough/Cauchy/Silicon. The fitted ellipsometry data are shown in Fig. 30 to 34. The literature value of refractive indices of yttria are 1.9455 and 1.9054 for 470 nm and 950 nm, respectively [106]. The mean refractive indices based on the fitted Cauchy parameters, A_n , B_n and A_k , are 1.9283 and 1.8829 for 470 nm and 950 nm, respectively. This corresponds to an error of only 0.88% and 1.18% for 470 nm and 950 nm. The RMS roughness measured by AFM is plotted against the fitted rough layer thickness and is shown in Fig. 35. As shown, these two quantities have strong correlation and can be best fit by the line $\text{RMS} = 0.5652 \times \text{rough} - 12.4806$. The slope of 0.5652 is close to [77]. However, it is important to note the AFM and ellipsometer are sampling quite a different area. The scan size of AFM is $5 \mu\text{m} \times 5 \mu\text{m}$ but the spot size of the ellipsometer, depending on the incident angle, is around $7 \text{ mm} \times 2 \text{ mm}$. This means that the ellipsometer is probing an area that is around two millions times larger than the area the AFM is scanning.

With the measured RMS roughness and rough layer thickness, we computed spectral normal reflectance using both SSM and EMA models. The film thickness used in SSM model is equal to the thickness of the Cauchy layer plus half of the rough layer thickness. The calculated spectral reflectance are compared with experimentally measured normal reflectance by an *ex situ* reflectometer [Ocean Optics], and are shown in Fig. 36 to 40. The mean squared errors (MSE) for both SSM and EMA are

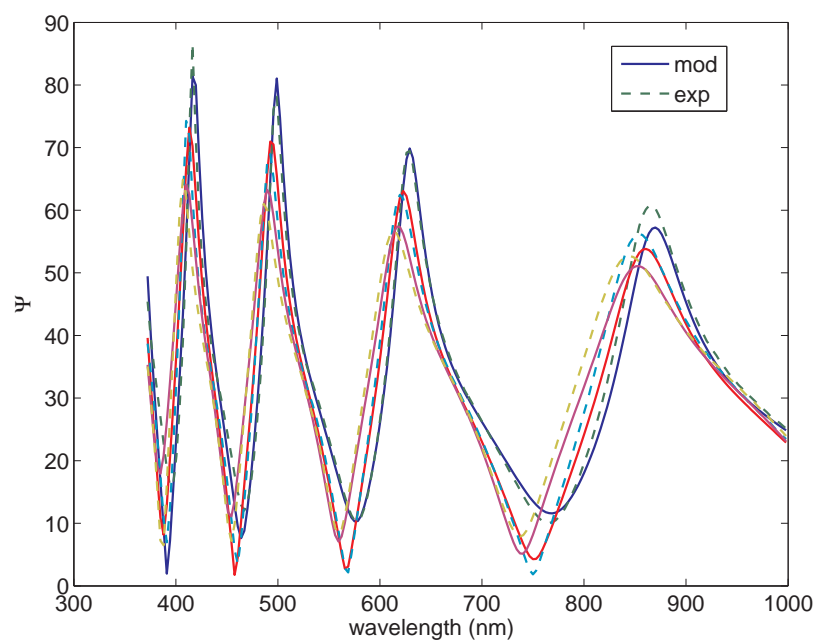


Figure 30: Ellipsometer data and fit of yttria film deposited on 8/14/2006.

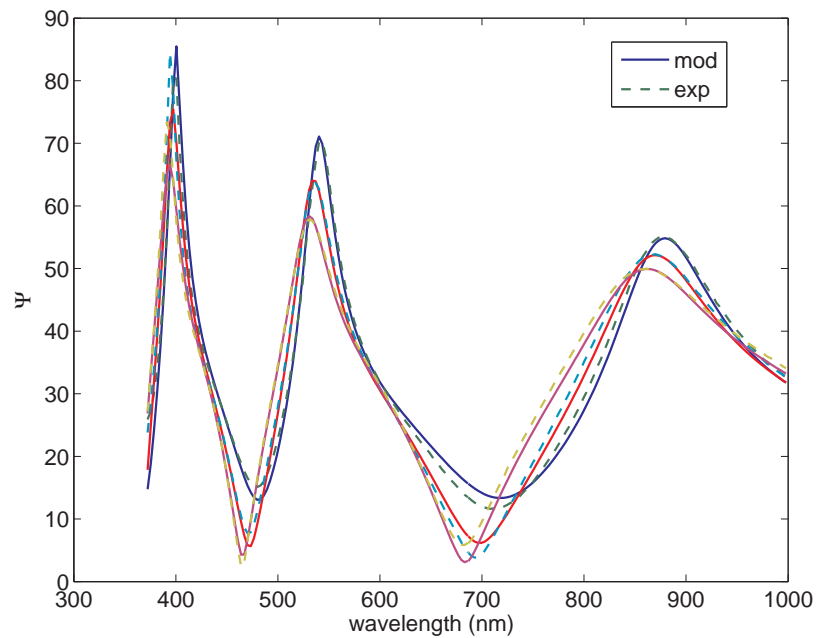


Figure 31: Ellipsometer data and fit of yttria film deposited on 8/15/2006.

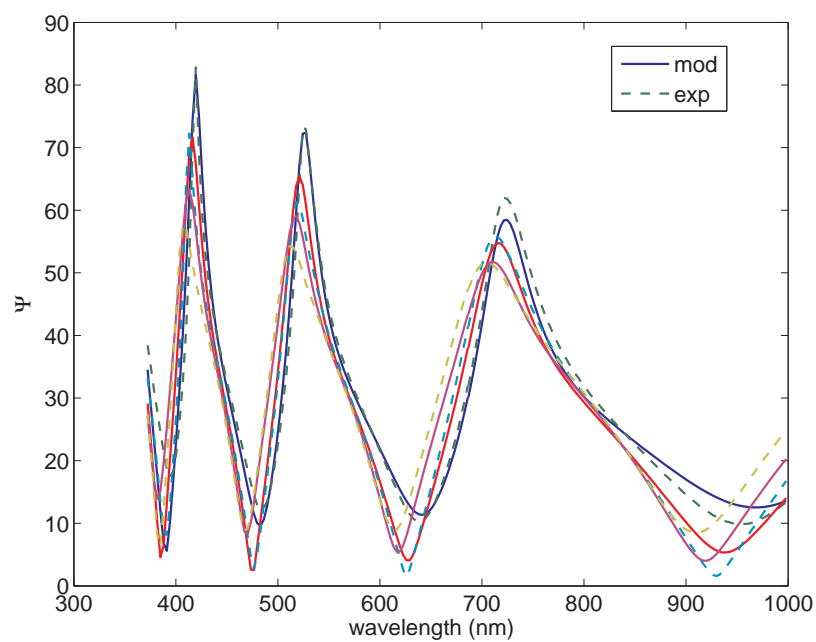


Figure 32: Ellipsometer data and fit of yttria film deposited on 8/16/2006.

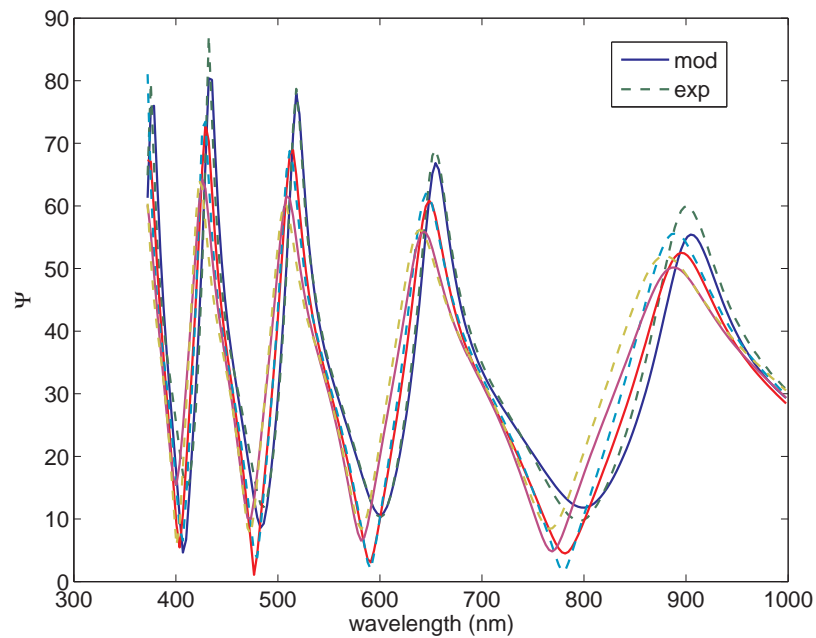


Figure 33: Ellipsometer data and fit of yttria film deposited on 8/17/2006.

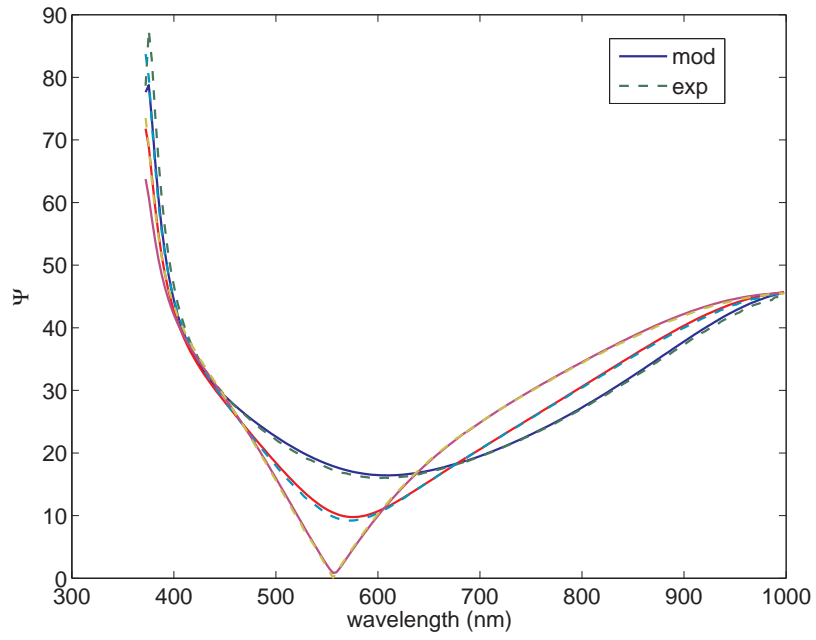


Figure 34: Ellipsometer data and fit of yttria film deposited on 8/18/2006.

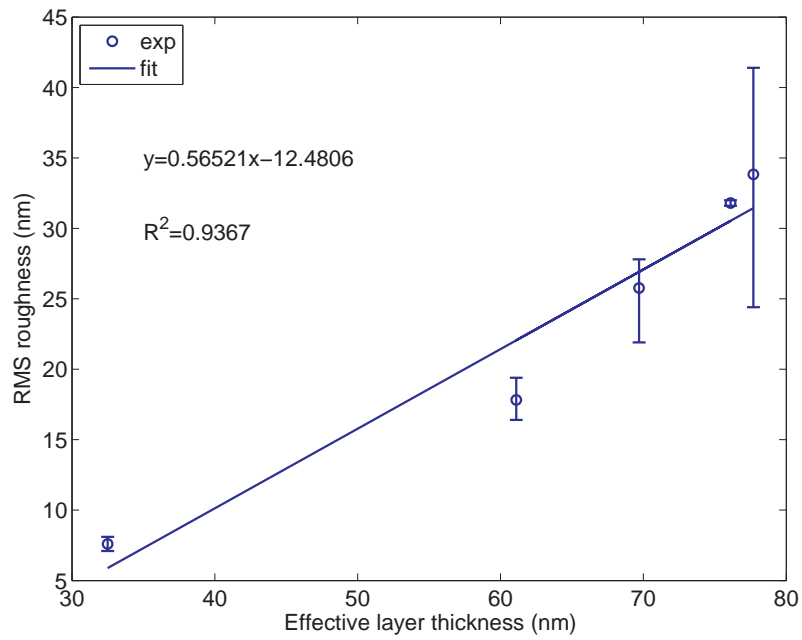


Figure 35: Effective layer thickness shows strong correlation with the RMS roughness.

summarized in Table 2. As shown, the EMA model matches the experimental data better than SSM does in all cases. A common feature in Fig. 36 to 40 is that the trough of the spectral reflectance curve rises as wavelengths decreases. Ideally, if the film is perfectly smooth, we would expect all minimums of the spectral reflectance to be zero due to complete destructive interference. At longer wavelengths, the film appears smoother and so the minimum of the reflectance is close to zero. At shorter wavelengths, however, the film appears rougher and the light may not be completely cancelled out due to the induced phase difference by roughness, and so the minimum of the reflectance is not zero. Comparing the calculated spectral reflectance in Fig. 36 to 40, it is clear that EMA performed better in capturing the rise of the trough of the spectral reflectance curve as wavelength decreases.

Even though EMA matches experimental data better, the offset is still quite large. This may have been due to the different spot size and different sampling location of the ellipsometer and the reflectometer. We found that by slightly changing the fitted parameters in Table 2, better result can be achieved. Figure 41 shows an improved fit of 8/14/06 film when parameters are changed to $A_k = 0.015$, $h = 655$ nm and $h_e = 65$ nm (A_n and B_n are kept unchanged). The MSE decreased from 3.8×10^{-3} to 8.8×10^{-4} . We also calculated spectral reflectance for smooth surface using the same parameters and the result is shown in Fig. 41 as well. As shown, when the surface is smooth, the peak of the reflectance curve at shorter wavelength is higher than that at longer wavelength. This is because the refractive index of the film increases with decreasing wavelength and larger refractive index causes more reflection. In the experimental data, however, the peak of reflectance at shorter wavelength is lower than that at longer wavelength. This indicated that reflectance at shorter wavelength is more sensitive to the surface roughness. The large offset at longer wavelength suggests that EMA model is more accurate at shorter wavelength where the surface roughness effect is more apparent.

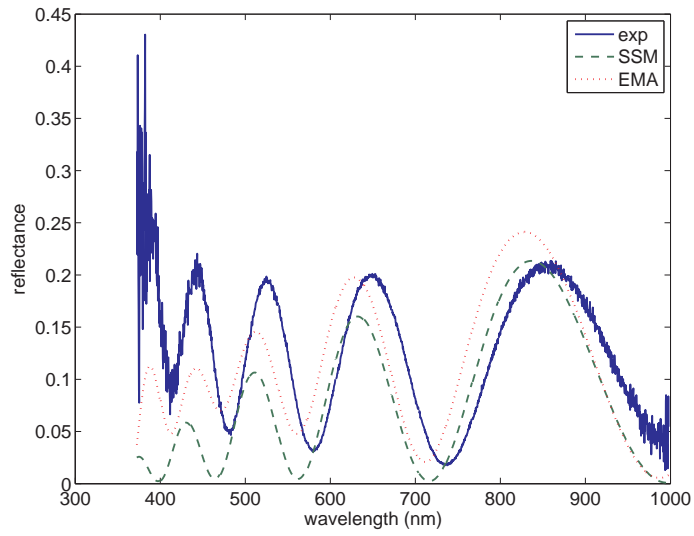


Figure 36: Comparison between *ex situ* spectral reflectance and model prediction by SSM and EMA for yttria film deposited on 8/14/2006.

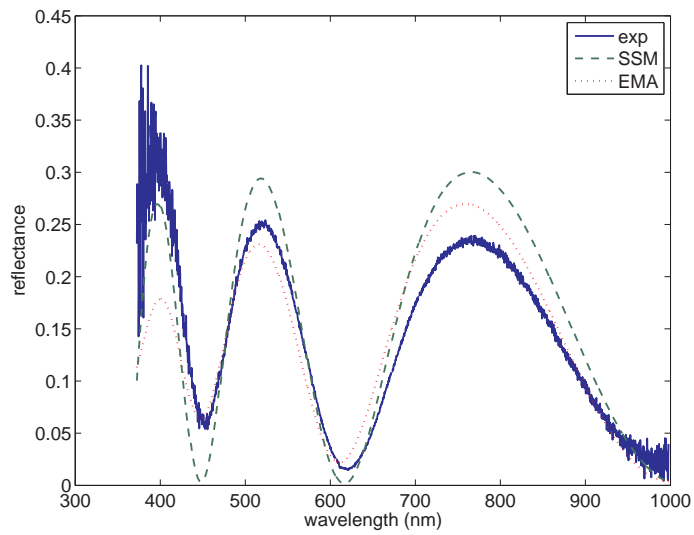


Figure 37: Comparison between *ex situ* spectral reflectance and model prediction by SSM and EMA for yttria film deposited on 8/15/2006.

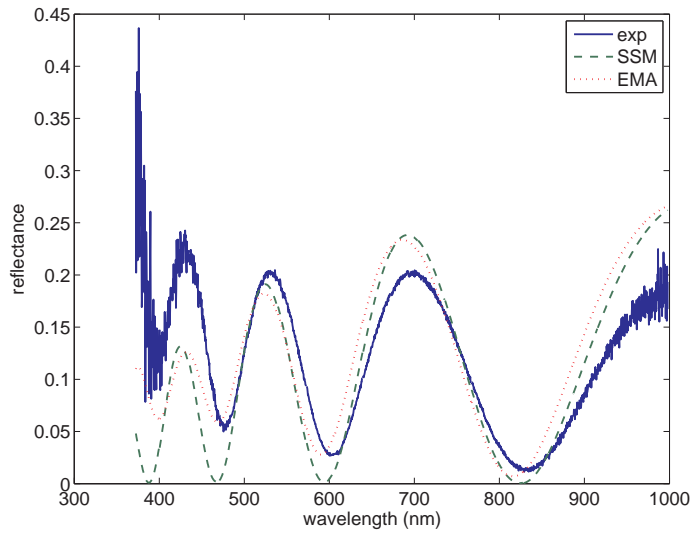


Figure 38: Comparison between *ex situ* spectral reflectance and model prediction by SSM and EMA for yttria film deposited on 8/16/2006.

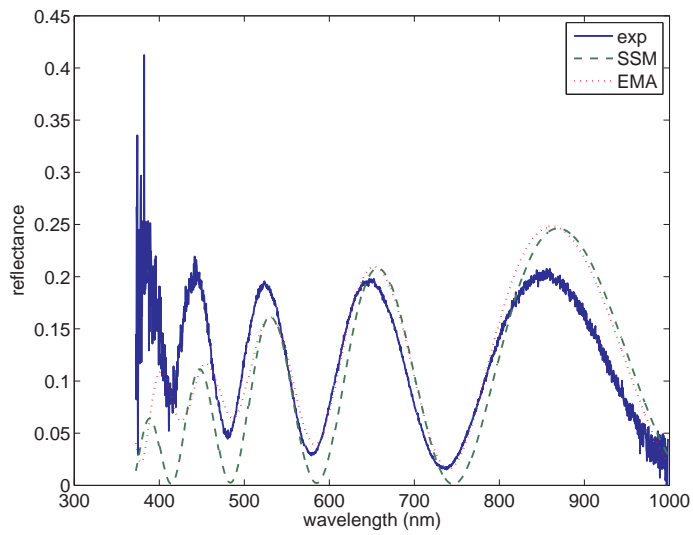


Figure 39: Comparison between *ex situ* spectral reflectance and model prediction by SSM and EMA for yttria film deposited on 8/17/2006.

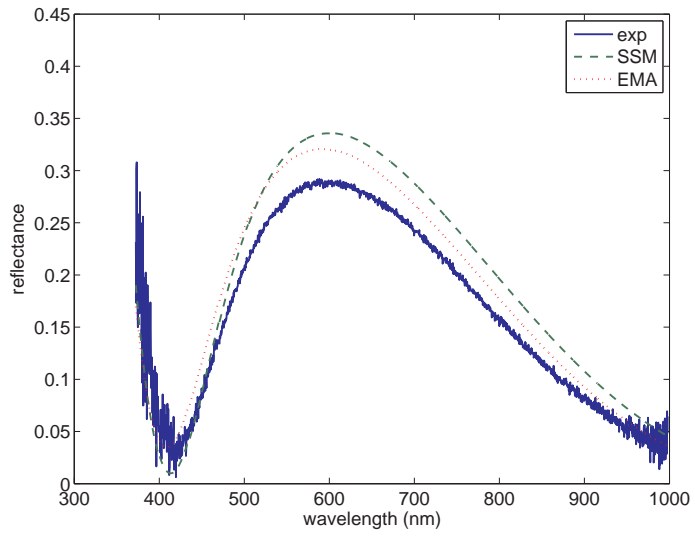


Figure 40: Comparison between *ex situ* spectral reflectance and model prediction by SSM and EMA for yttria film deposited on 8/18/2006.

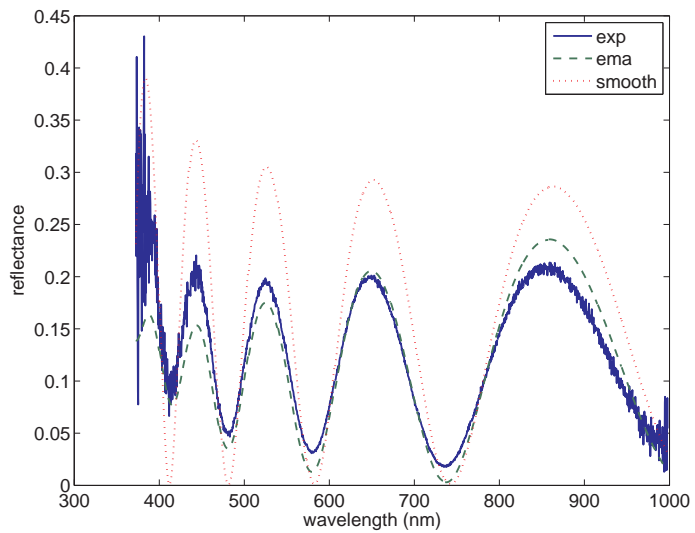


Figure 41: Improved EMA fit and calculated spectral reflectance when the surface is smooth for yttria film deposited on 8/14/2006.

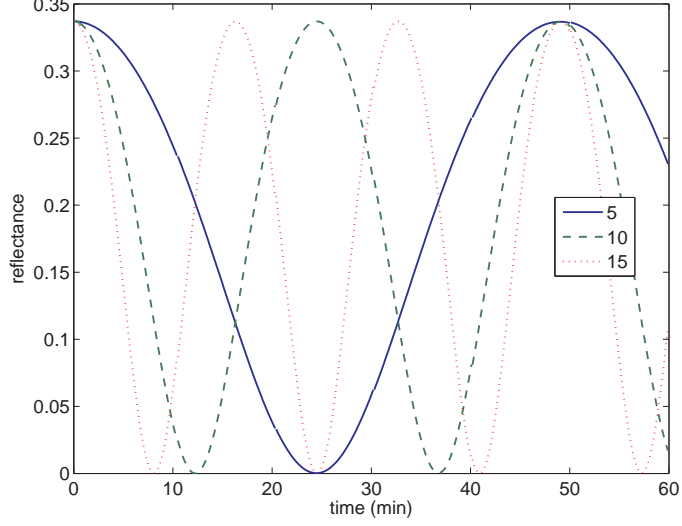


Figure 42: Simulated 950 nm reflectance at three different growth rates (nm/min).

3.3 *Effects of film parameters on reflectance*

With the sensor models, we can now study the effect of various film parameters on the reflectance. Fig. 42 shows the simulated 950 nm reflectance at three different growth rates. The refractive index of the substrate and the film are chosen to be that of silicon and yttria, respectively. Both light absorption and surface roughness are assumed negligible. As shown, a faster growth rate corresponds to a shorter oscillation period. According to Eq. (2), interference minima occurs when $\delta = \pi$. This condition leads to the well-known relationship between the film thickness and the number of reflectance extrema observed

$$h = \frac{m\lambda}{4n_2} \quad (15)$$

where $m = 1$ is the first minimum in reflectance, $m = 2$ the following maximum, and so on. This is the idea behind the peak-counting method and it is obvious that a faster growth rate leads to a thicker film and thus more interference extrema according to Eq. (15).

Fig. 43 shows the simulated 950 nm reflectance at three different extinction coefficients. The film growth rate is assumed to be 15 nm/min and surface is assumed to be

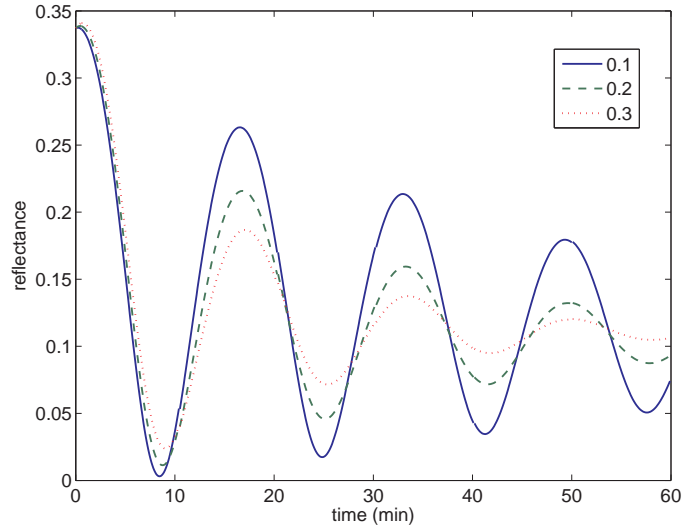


Figure 43: Simulated 950 nm reflectance at three different extinction coefficients.

smooth for all cases. As shown, larger extinction coefficient causes more decay in the oscillation amplitude. This is expected because the extinction coefficient represents the amount of absorption loss when light propagates through the material. On the limiting case when the extinction coefficient is very large or the film is very thick, there will be no light coming back from the film and the reflectance will approach the constant value of a simple reflection from the film surface, which is determined by the refractive index of the film. This idea was exploited by Breiland to extract the refractive index of a GaAs film [20].

For the surface roughness, we have shown that EMA is a better model than SSM. For completeness of the thesis, however, we have used both SSM and EMA model to study the roughness effect on reflectance. Figure 44 shows the simulated 950 nm reflectance at three different RMS roughness using SSM. Figure 45 shows the simulated 950 nm reflectance at three different effective layer thickness using EMA. The film growth rate is assumed to be 15 nm/min and extinction coefficient of the film is assumed to be zero for all cases. As shown, both SSM and EMA model predict reflectance amplitude decrease when the surface is rough. The amount of reduction

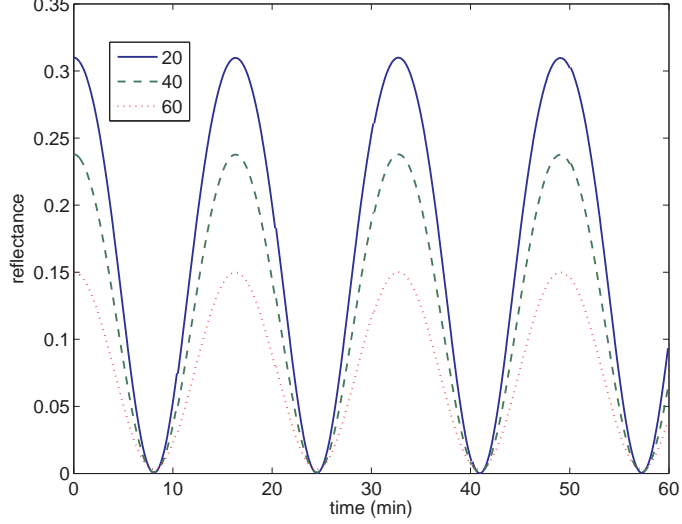


Figure 44: Simulated 950 nm reflectance at three different RMS roughness (nm) using SSM.

in SSM is more than that in EMA because the effective layer thickness used in the calculation is the same as RMS roughness. But as we have shown in the model validation section, the effective layer thickness should be about twice of the RMS roughness to get the same amount of reduction in reflectance. Also notice that in SSM the roughness does not change the position of the reflectance peak. In EMA, however, the effective layer caused the reflectance peak to shift. This is because in SSM the roughness enters the model through the scattering factors, S_{12} , S_{21} and S_t , and these factors do not affect the phase which is determined by the average thickness of the film. In EMA, however, the effective layer causes additional phase change as light propagates through the layer. Also compare to Fig. 43, constant surface roughness does not cause the reflectance to decay with time. This is because the roughness is a surface property and the extinction coefficient is a bulk property. For a constant extinction coefficient, when film becomes thicker, light has to travel longer distance in the film and thus more light will be absorbed. For a constant roughness, however, the reduction of reflectance is not dependent on the thickness of the film.

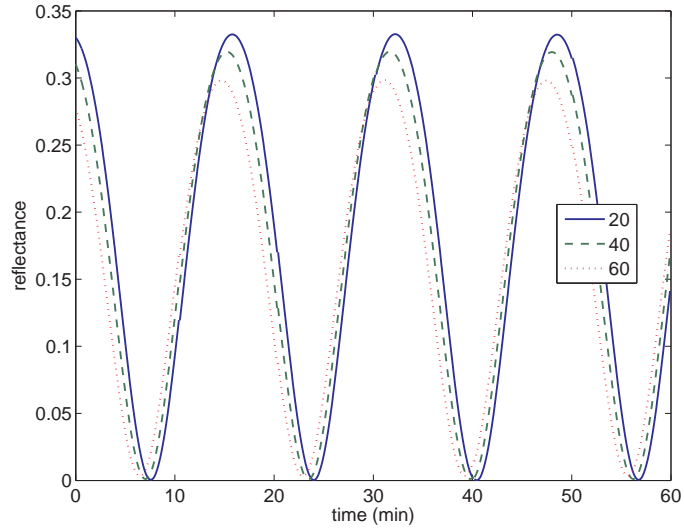


Figure 45: Simulated 950 nm reflectance at three different effective layer thickness (nm) using EMA.

In a real film deposition process, the surface roughness could change with time depending on the processing conditions. If the surface roughness increases during the growth, we then should expect reflectance to decay with time. Figure 46 shows the simulated 950 nm reflectance at three different roughening rate using SSM. Figure 47 shows the simulated 950 nm reflectance at three different effective layer growth rate using EMA. As shown, both SSM and EMA predict reflectance decay over time when surface roughness increases during the growth. However, in SSM only the peak of the reflectance is affected and this is quite different from the effect of the extinction coefficient as shown in Fig. 43. In EMA both peak and trough of the reflectance are affected and the reflectance shows the similar shape to that in Fig. 43. This suggests that it might be difficult to separately estimate the extinction coefficient and the surface roughness.

We have also studied the effect of film nonuniformity on the reflectance. The film nonuniformity can be regarded as surface roughness with an autocorrelation length that is much larger than the wavelength of the light. As we have discussed in Chapter 2, the diameter of the area the reflectometer views is around 0.8" and the film growth

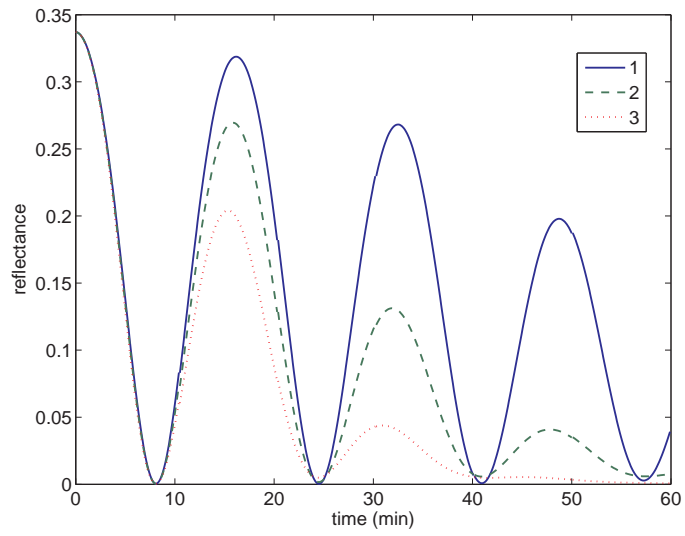


Figure 46: Simulated 950 nm reflectance at three different roughening rate (nm/min) using SSM.

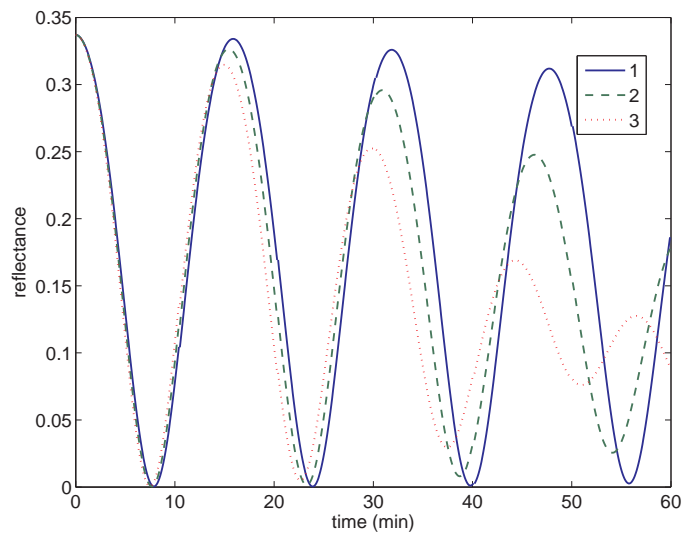


Figure 47: Simulated 950 nm reflectance at three different effective layer growth rate (nm/min) using EMA.

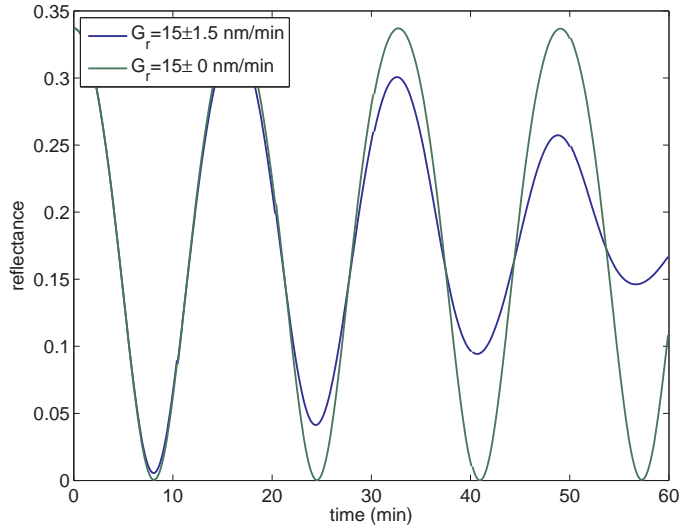


Figure 48: Simulated 950 nm reflectance when the growth rates are varying within 10% of average rate of 15 nm/min.

rate may be different within this area depending on the surface temperature profile across the wafer. Figure 48 shows the simulated 950 nm reflectance when the growth rate in the sampling area of the reflectometer are varying within 10% of average rate of 15 nm/min. The film surface is assumed smooth and the extinction coefficient is assumed to be zero for all cases. The simulated 950 nm reflectance at growth rate of 15 nm/min is also plotted for comparison. As shown, the reflectance again shows the similar shape to that in Fig. 43. This suggests that in order to separately estimate extinction coefficient, it is important to ensure film uniformity and this is why we have made significant efforts to achieve temperature uniformity on the surface of the substrate.

3.4 Observability

The optical models are highly nonlinear and the parameters are highly correlated. For example, the growth rate (G) and refractive index (n) appear in pairs in the optical model, and their product determines the oscillation period as suggested by Eq. (2). A simple simulation was used to visualize the correlation between G and n . In the

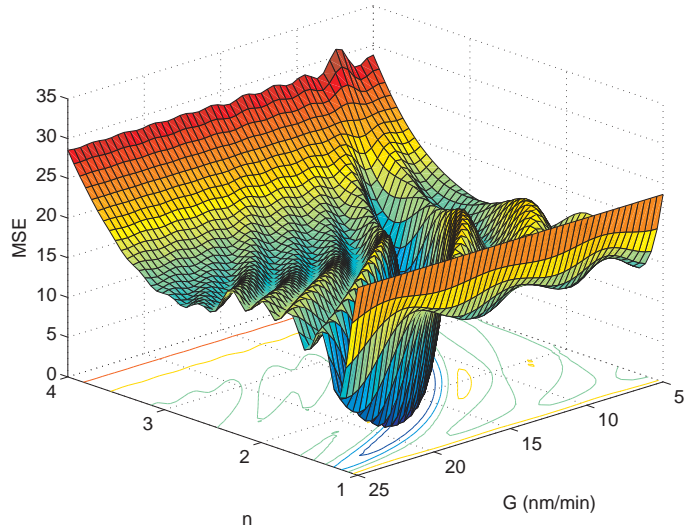


Figure 49: Mean squared error surface shows many local minima indicating strong correlation between G and n .

simulation, we first generated a true 950 nm reflectance using $G = 15$ nm/min and $n = 1.9320$ with the assumption of zero roughness and zero extinction coefficient. Then we used different combinations of $G \in [5, 25]$ and $n \in [1, 4]$ to calculate the reflectance and the mean squared error from the true reflectance. The result is shown in Fig. 49. As shown, the mean squared error surface contains many local minima. At first glance, it is not possible to separately estimate G and n . However, n also affects the amplitude of the reflectance. Figure 50 shows the simulated two 950 nm reflectance curves when $G = 15$ nm/min and $n = 1.8$, and when $G = 18$ nm/min and $n = 1.5$. In these two cases, G and n are different but their product is the same. As shown, the two curves have the same oscillation period but different amplitude of oscillation. It has been shown that if accurate absolute reflectance value can be obtained, then G and n can be separately estimated [20].

More generally, the question of what parameters can be estimated given a sensor model and a process dynamic model can be answered by observability analysis. The

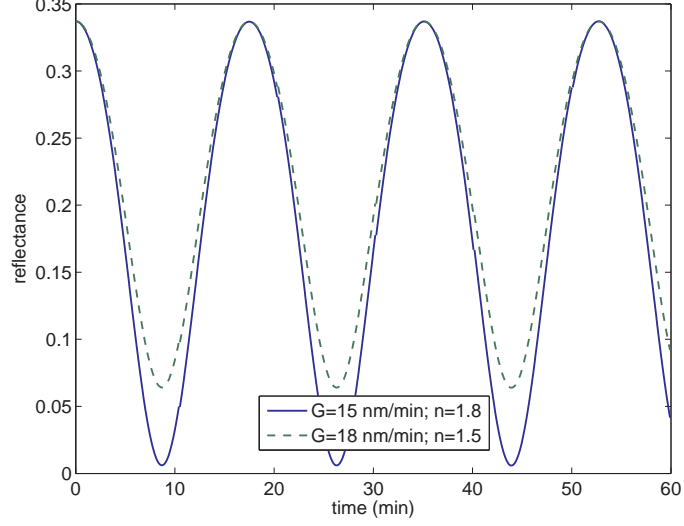


Figure 50: Simulated 950 nm reflectance for two cases with different n and G but the same $n \times G$.

observability of linear system is straightforward. Given a linear system

$$x_{k+1} = Ax_k \quad (16)$$

$$y_k = Cx_k$$

it is completely observable if the observability matrix $O = \begin{bmatrix} C \\ CA \\ \vdots \\ CA^{n-1} \end{bmatrix}$ has a full

rank n , where n is the dimension of state space. If the rank of the observability matrix is equal to k , where $k < n$, then the system is partially observable. In this case, the state space can be decomposed into observable and unobservable subspaces.

The unobservable subspace is the null space of the observability matrix. The basis of the observable and unobservable subspaces can be obtained by performing a singular value decomposition (SVD) on the observability matrix [10].

For a nonlinear system $\begin{cases} x_{k+1} = f(x_k) \\ y_k = g(x_k) \end{cases}$, it is observable if there exists a k on

the time axis such that

$$\begin{bmatrix} y_1 \\ y_2 \\ \vdots \\ y_k \end{bmatrix} = \begin{bmatrix} g(x_1) \\ g(f(x_1)) \\ \vdots \\ g(f^{k-1}(x_1)) \end{bmatrix} \quad (17)$$

has a unique solution x_1 . Once x_1 is obtained, the state in the whole period can be reconstructed from the process dynamic model. Generally this is a very strong condition. In practice, local observability is often considered. The local observability matrix is the same as that in linear system except that a Jacobian matrix of f and g is used instead of A and C . It is expected that the local observability matrix will change over time because the Jacobian matrix is a function of the state.

We have studied the observability based on the sensor model Eq. (5) and a simple process dynamic model. The state space model is expressed by

$$\begin{bmatrix} h \\ G \\ n \\ k \end{bmatrix}_{j+1} = \begin{bmatrix} 1 & \Delta t & 0 & 0 \\ 0 & 1 & 0 & 0 \\ 0 & 0 & 1 & 0 \\ 0 & 0 & 0 & 1 \end{bmatrix} \begin{bmatrix} h \\ G \\ n \\ k \end{bmatrix}_j \quad (18)$$

$$y_j = g(h_j, n_j, k_j) \quad (19)$$

where h is film thickness, G is film growth rate, n and k are the refractive index and the extinction coefficient of the film, respectively. Eq. (18) is the process dynamic model. As shown, h is simply the integration of G with time. The function $g(h, n, k)$ is the optical sensor model and is expressed in Eq. (5). By linearizing the sensor model and calculating the observability matrix, we found that the process and sensor models are not locally observable about any value of the state, due to the lack of coupling between the states in the process model. However, due to the nonlinearity in the sensor model, it is possible to extract all four states if one assumes that they are approximately constant during the deposition. Breiland has used a least squares

fitting method to extract five parameters (growth rate, complex refractive index of GaAs film, and complex refractive index of virtual substrate) from a single wavelength normal reflectance. The results indicated that when the reflectance data contains at least a quarter-wave oscillation, the five parameters can be separately estimated [20].

On the other hand, for a nonlinear system, even if the local observability matrix is full rank, the system may still not be complete observable. Consider a simple nonlinear system

$$\begin{aligned} \begin{bmatrix} x_1 \\ x_2 \end{bmatrix}_{k+1} &= \begin{bmatrix} 0.8 & -0.4 \\ 0 & 1.1 \end{bmatrix} \begin{bmatrix} x_1 \\ x_2 \end{bmatrix}_k \\ y_k &= x_1 \times x_2 \end{aligned}$$

For the first two steps, we have

$$\begin{aligned} y_1 &= x_1 \times x_2 \\ y_2 &= g \left(\begin{bmatrix} 0.8x_1 - 0.4x_2 \\ 1.1x_2 \end{bmatrix} \right) = (0.8x_1 - 0.4x_2) \times 1.1x_2 = 0.88x_1x_2 - 0.44x_2^2 \end{aligned}$$

The rank of the local observability matrix is always equal to 2, which means the system is locally observable during the entire period. It is obvious that $x_1 \times x_2$ and x_2^2 can be uniquely determined from y_1 and y_2 and therefore they are observable. However x_1 and x_2 themselves can not be uniquely determined. For example, when x_1 was estimated with a wrong sign, x_2 must also change the sign to make $x_1 \times x_2$ correct. Therefore, the lesson we learned here is that for a nonlinear system, the local observability does not always guarantee the global observability. For a nonlinear system, one must consider the specific system and mathematical form, because no general approach and practical tools exist, as they do for linear systems.

CHAPTER IV

STATE ESTIMATORS

Once we have a sensor model that quantifies the relationship between the film properties and the reflectance, we can then extract the film properties from the reflectance measurement using various mathematical approaches. In this chapter, we summarize those approaches that have been studied in this project.

4.1 Batch least squares fitting

The simplest method to extract the film properties from the reflectance measurement is batch least squares fitting (BLS). In BLS, some system-specific parameters such as film growth rate, refractive index of the film, and refractive index of the substrate are assumed to be constant and based on these parameters, the temporal reflectance can be calculated from the sensor model. These parameters are estimated by minimizing the summed square of the error between the sensor model predictions and the real measurements. Once the growth rate is estimated, the film thickness can be calculated from the growth rate. In practice, BLS is operated iteratively. When new measurements are acquired, a new fitting cycle is launched to fit all available measurement data. Typically, the initial values used in the new fit are the values determined from the last fit. BLS is the algorithm that is used by RoboMBE, the commercial software that was provided with the emissivity-correcting pyrometer [SVT Associates]. In RoboMBE, there are a total of five parameters to be estimated and they are the refractive index and extinction coefficient of the substrate, the refractive index and extinction coefficient of the film, and film growth rate. The sensor model is similar to Eq. (5), which describes the normal reflectance on a film/substrate system with a smooth surface. The only difference is that the thickness in Eq. (5) is replaced

by the product of growth rate and time. Therefore the sensor model in RoboMBE is a function of time.

Mathematically, let x be the vector containing the system parameters to be estimated, e.g. $x = [G, n, k, n_s, k_s]^T$, where G is the film growth rate, n and k are the refractive index and extinction coefficient of the film, n_s and k_s are the refractive index and extinction coefficient of the substrate. Let $g(x, t)$ be the sensor model, then given a sequence of reflectance measurements y_1 to y_k , the optimum solution of x , x_{opt} , can be obtained by solving the following optimization problem

$$x_{\text{opt}} = \min_x \sum_{l=1}^k v_l^T v_l \quad (20)$$

where $v_l = y_l - g(x, t_l)$ is the error between sensor model prediction and reflectance measurements at time l .

One problem with BLS is that the assumption of constant system parameters during the growth process may not be valid in practice. For example, the film growth rate may change with substrate temperature or decrease due to depletion of the precursor. The refractive index of the film may also change with the temperature, composition, and microstructure. One solution to this problem is to divide the film into sublayers and the growth rate and refractive index is assumed constant within each sublayer [121]. Another solution is to use the recursive least squares fitting that is discussed next.

4.2 Recursive least squares fitting

The idea of recursive least squares fitting (RLS) is to fit the measurement data in a fixed size window of time instead of all available measurement data. When new measurements are acquired, the window is shifted to include new measurements and at the same time to discard part of the old measurements and a new fitting cycle is launched to fit only the data in the new window. The initial values used in the new fit are the values determined from the previous fit. Although RLS still makes

the assumption of constant growth rate and refractive index in each window, the assumption is more acceptable when the windows is sufficiently small and the process does not exhibit rapid variation. On the other hand, however, the window cannot be too small because the fitting algorithm needs a certain amount of data to obtain an optimal solution. It has been shown that at least a quarter-wave oscillation of reflectance is needed to separately estimate five parameters (growth rate, complex refractive index of film, and complex refractive index of substrate) from a single wavelength reflectance measurement [20]. In Chapter 5, we will study the effect of window size on the RLS estimation result.

Mathematically, let x be the vector containing the system parameters and $g(x, t)$ be the sensor model, then given a sequence of reflectance measurements in a window from $k - m + 1$ to k , the optimum solution of x_k, x_k^{opt} , can be obtained by solving the following optimization problem

$$x_k^{\text{opt}} = \min_{x_{k-m+1}} \sum_{l=k-m+1}^k v_l^T v_l \quad (21)$$

where $v_l = y_l - g(x, t_l)$ is the error between sensor model prediction and reflectance measurements at time l . Notice that x_{opt} is the optimum solution in the window from $k - m + 1$ to k and it may change in different windows. In this way, the temporal evolution of parameters like growth rate and refractive index can be captured.

One common problem with BLS and RLS is that they implicitly assumed deterministic process dynamic model by assuming constant film growth rate and refractive index. Therefore the estimation totally relies on the sensor model. If there is sensor model mismatch, the estimation will be wrong and there is no way to correct it. Another problem is that they do not consider *a priori* knowledge of the process. The optimum solution in neighboring window does not have direct connection except that the optimum solution in the previous window is passed into current window as an initial guess. As we have shown in Chapter 3, the sensor model is highly nonlinear

and the error surface contains multiple local minima. Without *a priori* knowledge, the solution may get caught in these local minima. To solve these two problems, we studied the moving horizon estimator that is discussed next.

4.3 Moving horizon estimation

Moving horizon estimation (MHE) is a general least-squares-based state estimation method [124, 125, 117, 118, 58]. To the best of our knowledge, MHE has not been applied to interpret *in situ* sensor data for a thin film growth process. Compared to BLS and RLS, MHE does not assume deterministic process dynamic model. A simple statistical process dynamic model for a thin film growth process can be expressed by

$$\begin{bmatrix} h \\ G \\ n \\ k \end{bmatrix}_{j+1} = \begin{bmatrix} h + G \times \Delta t \\ G \\ n \\ k \end{bmatrix}_j + w_j \quad (22)$$

where h , G , n and k are film thickness, growth rate, refractive index and extinction coefficient at a specific wavelength λ , respectively. Δt is the sampling time. As shown, h at time $j + 1$ is simply $G \times \Delta t$ plus h at time j . G , n and k are assumed to be constant. w represents uncertainty of the process dynamic model and is assumed to be zero-mean and with a Gaussian distribution. If w is neglected, the process dynamic model is deterministic and that is the assumption of BLS and RLS. The process dynamic model can be made more complicated to include other quantities of interest like surface roughness or temperature, or to include more complicated relationships between the states at time j and $j + 1$. Because the process dynamic model is not deterministic, film properties at different time such as thickness and refractive index cannot be determined from one set of system-specific parameters like in BLS and RLS. Instead, they are treated as state variables and are estimated directly by MHE. The sensor models discussed in Chapter 3 can be directly used in MHE because they are a

function of the film properties. Eq. (22) together with a sensor models is collectively referred to as a state space model.

Given a state-space model and a sequence of reflectance measurements in a horizon from $k - m + 1$ to k , the states in this horizon, x_{k-m+1}, \dots, x_k , can be estimated by solving the following minimization problem

$$\min_{x_{k-m+1}, \dots, x_k} \left[(x_{k-m+1}^e)^T P_{k-m+1|k-m}^{-1} x_{k-m+1}^e + \sum_{l=k-m+1}^k v_l^T R^{-1} v_l + \sum_{l=k-m+1}^{k-1} w_l^T Q^{-1} w_l \right] \quad (23)$$

s.t.

$$\begin{aligned} x_{k-m+1}^e &= x_{k-m+1} - x_{k-m+1|k-m} \\ v_l &= y_l - g(x_l) \\ w_l &= x_{l+1} - f(x_l) \end{aligned}$$

As shown, the objective function of MHE consists of three error terms. The second error term, $v_l = y_l - g(x_l)$, also appears in BLS and RLS and represents the error between the sensor model prediction and reflectance measurements at time l . R is the covariance matrix of the sensor model uncertainty. The inverse of R is used as a weighting matrix for v in the objective function. The third error term, $w_l = x_{l+1} - f(x_l)$, represents the error between the estimated state x_{l+1} and the process dynamic model prediction $f(x_l)$, where f is the process dynamic model. Q is the covariance matrix of the process dynamic model uncertainty, e.g. w in Eq. (22). The inverse of Q is used as the weighting matrix for w in the objective function. The first error term, $x_{k-m+1}^e = x_{k-m+1} - x_{k-m+1|k-m}$, represents the error between the initial state x_{k-m+1} and the *a priori* estimate $x_{k-m+1|k-m}$. The term $x_{k-m+1|k-m}$ denotes the estimate at time $k - m + 1$ based on the measurements up to time $k - m$. $P_{k-m+1|k-m}$ is the covariance matrix of the *a priori* estimate. The inverse of $P_{k-m+1|k-m}$ is used as a weighting matrix for x_{k-m+1}^e in the objective function. By including x_{k-m+1}^e in the objective function, MHE penalizes the state variation from the

a *priori* estimate and this may help prevent the solution from being caught in the local minima and from overfitting the sensor measurements when there is noise or modeling error. An additional advantage of MHE is that it explicitly considers uncertainty and the correlations between parameters to be estimated through covariance matrices, which are computed at each time step as will be shown below. In the sensor model the parameters often appear as ratios. To robustly extract maximum information from the *in situ* measurement, a statistical analysis is advantageous.

The above minimization problem estimates states in the horizon from $k - m + 1$ to k . When new measurement data are acquired, MHE shifts the horizon to include the new measurements and discard some old measurements. This is necessary to prevent the minimization problem from growing in size without bound. When the horizon shifts, a *priori* knowledge about the initial state $x_{k-m+2|k-m+1}$ and its covariance matrix $P_{k-m+2|k-m+1}$ must be updated so that the information obtained in the previous horizon can be passed into the current horizon. The update scheme for MHE currently remains an open question in the state estimation community [58]. A common scheme is to use the extended Kalman filter (EKF) algorithm [125]. The measurement-correction terms of EKF are

$$\begin{aligned}
L_{k-m+1} &= P_{k-m+1|k-m} C_{k-m+1|k}^T (C_{k-m+1|k} P_{k-m+1|k-m} C_{k-m+1|k}^T + R)^{-1} \\
x_{k-m+1|k-m+1} &= x_{k-m+1|k-m} + L_{k-m+1} [y_{k-m+1} - g(x_{k-m+1|k}) \\
&\quad - C_{k-m+1|k} (x_{k-m+1|k-m} - x_{k-m+1|k})] \\
P_{k-m+1|k-m+1} &= (I - L_{k-m+1} C_{k-m+1|k}) P_{k-m+1|k-m}
\end{aligned} \tag{24}$$

The measurement-prediction terms of EKF are

$$\begin{aligned}
x_{k-m+2|k-m+1} &= f(x_{k-m+1|k}) + A_{k-m+1|k} (x_{k-m+1|k-m+1} - x_{k-m+1|k}) \\
P_{k-m+2|k-m+1} &= A_{k-m+1|k} P_{k-m+1|k-m+1} A_{k-m+1|k}^T + Q
\end{aligned} \tag{25}$$

where $C_{k-m+1|k} = \left. \frac{\partial g(x)}{\partial x} \right|_{x=x_{k-m+1|k}}$ and $A_{k-m+1|k} = \left. \frac{\partial f(x)}{\partial x} \right|_{x=x_{k-m+1|k}}$. Note Eq. (24)

and (25) are slightly different from the standard EKF because the EKF is linearized around the smoothed estimate, $x_{k-m+1|k}$.

MHE provides a general framework for the least-squares-based estimation. Consider the following two limiting cases. First, when the process model is uncertain, then Q is the infinity matrix, so MHE totally relies on the sensor model. As a result, the state is estimated independently at each time step, with no relationship between the fits of x_{j+1} and x_j . Second, when the sensor model is uncertain, then R is the infinity matrix, so MHE totally relies on the process dynamic model and the *a priori* estimate. In between these two limiting cases, MHE uses both the process dynamic model and the sensor model to obtain a balanced estimate. RLS can be seen as a special case of MHE if the process model f is deterministic (Q is the zero matrix) and the *a priori* estimate is neglected ($P_{k-m+1|k-m}$ is the infinity matrix). Once x_{k-m+1} is estimated, other states in the horizon can be reconstructed through process model f . Because RLS only estimates x at one time step, x_{k-m+1} , its computation is much faster than MHE. However it loses the advantage of the *a priori* estimate in MHE and it does not allow for a stochastic process dynamic model. In addition RLS does not have much control over the optimization. On the other hand, MHE allows users to tune the weighting matrices Q and R to obtain an improved estimate. The main problem with MHE is that it is computationally expensive. For example, if the state vector has four elements like in Eq. (22) and the horizon size is 10, then we have to solve 40 variables in each optimization iteration. This is a very slow process for nonlinear systems and limits the application of MHE in *in situ* sensor data interpretation. To solve this problem, we proposed the modified moving horizon estimator that is discussed next.

4.4 Modified moving horizon estimator

The idea of the modified moving horizon estimator (mMHE) is to assume a deterministic process model in order to reduce the computation in MHE. Because the process dynamic model is deterministic, only the initial state, instead of all states in the horizon, must be estimated. Once the initial state is estimated, other states in the horizon can be reconstructed from the process model. However, different from RLS, mMHE considers the error from the *a priori* estimate, i.e. it does not force $P_{k-m+1|k-m}$ to be the infinity matrix in each new horizon. Instead it uses EKF to update the *a priori* estimate and its covariance matrix, as in MHE. In this way mMHE combines the advantage of the computational efficiency in RLS and the *a priori* estimate in MHE. The assumption of the deterministic process model is acceptable because thin film growth process usually does not exhibit rapid variation, but slow drift over time.

Mathematically, given a sequence of measurements in a horizon starting from $k - m + 1$ to k , the initial state in this horizon, x_{k-m+1} , can be estimated by solving the following minimization problem

$$\min_{x_{k-m+1}} \left[(x_{k-m+1}^e)^T P_{k-m+1|k-m}^{-1} x_{k-m+1}^e + \sum_{l=k-m+1}^k v_l^T R^{-1} v_l \right] \quad (26)$$

s.t.

$$\begin{aligned} x_{k-m+1}^e &= x_{k-m+1} - x_{k-m+1|k-m} \\ v_l &= y_l - g(f^{l-(k-m+1)}(x_{k-m+1})) \end{aligned}$$

where $f^{l-(k-m+1)}(x_{k-m+1})$ means the process model f is applied to x_{k-m+1} for $l - (k - m + 1)$ times to calculate the state at time l . Compared to Eq. (26), the w term is neglected because of the assumption of the deterministic process dynamic model. The EKF update scheme for $x_{k-m+2|k-m+1}$ and $P_{k-m+2|k-m+1}$ is the same as for MHE and is expressed by Eq. (24) and (25). One thing to notice is that in Eq. (25), $P_{k-m+2|k-m+1} = A_{k-m+1|k} P_{k-m+1|k-m+1} A_{k-m+1|k}^T + Q$, Q is supposed to be

a zero matrix because of the assumption of deterministic process dynamic model. In practice, however, Q is not forced to be a zero matrix. Instead it is used as a tuning matrix in mMHE to represent the added uncertainty when the horizon shifts. Although we assumed deterministic process dynamic model in one horizon, it is intended to reduce the computation in mMHE and the process model in reality is not completely deterministic. Therefore we should add some uncertainty to the *a priori* estimate when the horizon shifts.

4.5 Extended Kalman filter

It has also been shown that the Kalman filter is a special case of MHE when the system is linear and the horizon size is equal to 1 [125]. For a nonlinear system, the extended Kalman filter (EKF) is by far the most popular state estimator in the literature [91, 30] and has been implemented in thin film deposition and etching processes [165, 158, 157]. In fact, EKF is the first state estimator we studied in this project. For a nonlinear system $x_{k+1} = f(x_k) + w_k$ and $y_k = g(x_k) + v_k$, the extended Kalman filter equations are

$$\begin{aligned}
P_{k|k-1} &= \left(\frac{\partial f}{\partial x} \Big|_{\hat{x}_{k-1}} \right) P_{k-1|k-1} \left(\frac{\partial f}{\partial x} \Big|_{\hat{x}_{k-1}} \right)^T + Q \\
\hat{x}_{k|k-1} &= f(\hat{x}_{k-1}) \\
G_k &= P_{k|k-1} \left(\frac{\partial g}{\partial x} \Big|_{\hat{x}_{k|k-1}} \right)^T \cdot \left[\left(\frac{\partial g}{\partial x} \Big|_{\hat{x}_{k|k-1}} \right) P_{k|k-1} \left(\frac{\partial g}{\partial x} \Big|_{\hat{x}_{k|k-1}} \right)^T + R \right]^{-1} \\
P_{k|k} &= \left[I - G_k \left(\frac{\partial g}{\partial x} \Big|_{\hat{x}_{k|k-1}} \right) \right] P_{k|k-1} \\
\hat{x}_{k|k} &= \hat{x}_{k|k-1} + G_k [y_k - g(\hat{x}_{k|k-1})]
\end{aligned} \tag{27}$$

where Q and R are the covariance matrix of w and v , respectively. G_k is the Kalman gain at time k . $P_{k|k-1}$ and $P_{k|k}$ are the *a priori* and *a posteriori* error covariance matrices, respectively. EKF utilizes one measurement at a time so it is more computationally efficient than MHE. However, as we have discussed before, we need certain

amount of measurement data that exhibit enough curvature in the reflectance oscillation in order to separately estimate film properties. In this sense, MHE is a more reliable state estimator than EKF. Another advantage of MHE is that it can handle state constraints, e.g. the growth rate and the refractive index of the film must be positive.

In the next two chapters, we will compare the performance of the state estimators discussed in this chapter in both simulation and experimental study.

CHAPTER V

SIMULATION

In this chapter, we compare the performance of the state estimators discussed in Chapter 4 using simulated film growth processes. We first consider the case of process model mismatch, in which the process model used in simulating the process is different from that used in the state estimators. Under the case of process model mismatch, we study several subcases in the order of complexity including single-wavelength reflection on a smooth surface, dual-wavelength reflection on a smooth surface and dual-wavelength reflection on a rough surface. Following that, we consider the case of sensor model mismatch, in which the sensor model used in simulating the process is different from that used in the state estimators.

5.1 Process model mismatch

5.1.1 Single-wavelength reflection on smooth surface

In the case of process model mismatch, we simulate a process in which the film growth rate slowly decreases with time. The growth rate decay is frequently observed in real CVD processes due to depletion of precursors or decrease of substrate temperature. The process model used to simulate the process is expressed by `simuprocmodelSS`

$$\begin{bmatrix} h \\ G \\ n \\ k \end{bmatrix}_{j+1} = \begin{bmatrix} h + G \times \Delta t \\ G \times 0.99 \\ n \\ k \end{bmatrix}_j + w_j \quad (28)$$

where h , G , n and k are film thickness, growth rate, refractive index and extinction coefficient, respectively. Δt is the sampling time. As shown, h at time $j + 1$ is simply

$G \times \Delta t$ plus h at time j . Growth rate at time $j + 1$, G_{j+1} , is 99% of the previous rate, G_j . n and k are assumed to be constant. w represents uncertainty of the process dynamic model and is assumed to be zero-mean and with a Gaussian distribution. The sensor model is expressed by Eq. (5) for single-wavelength reflection on a smooth surface. In addition to Eq. (5), we add a sensor noise term, v , to represent sensor noise and uncertainty of the sensor model. v is assumed to be zero-mean and with a Gaussian distribution. The wavelength is chosen to be the same as the reflectometer in our CVD testbed, $\lambda = 950$ nm. The substrate is chosen to be silicon and at 500°C its complex refractive index at 950 nm is $3.7687 - 0.0281j$ [66, 67]. The film is chosen to be yttria and its refractive index at 950 nm is 1.9054 [106]. The extinction coefficient of yttria is not available and is assumed to be 0.05 for this simulation. The initial growth rate is assumed to be 15 nm/min. Therefore the initial state used to simulate the process is $x_i = [0, 15, 1.9054, 0.05]^T$. The covariance matrices of w and v are $\text{diag}(x_i) \times 10^{-6}$ and 10^{-6} , respectively. $\text{diag}(x_i)$ denotes a diagonal matrix with x_i being the diagonal elements and is used as a scaling factor for the covariance of each state. 10^{-6} represents an error in the third decimal place. The time interval is $\Delta t = 1$ min, and the total growth time is 120 minutes. The simulated measurement and states are shown in Fig. 51. The circles are the sampled points. Notice that the oscillation period gradually increases due to the decrease of growth rate.

We first use BLS to estimate the states from the simulated reflectance measurement. The process dynamic model used in BLS is expressed by Eq. (22), in which the growth rate is assumed to be constant. The sensor model is the same as that used in simulating the process. The initial guess is expressed by $x_1 = x_i \times \text{normrnd}(\text{ones}(4, 1), 0.1)$, where $\text{normrnd}(\text{ones}(4, 1), 0.1)$ denotes a 4×1 Gaussian random vector with mean 1 and standard deviation 0.1. This means that the initial guess is around 10% offset from the true initial state. To quantify the quality of the estimation, we defined estimation error as $e = \sqrt{\sum((x - x_{\text{est}})/\bar{x})^2}$, where \bar{x} is

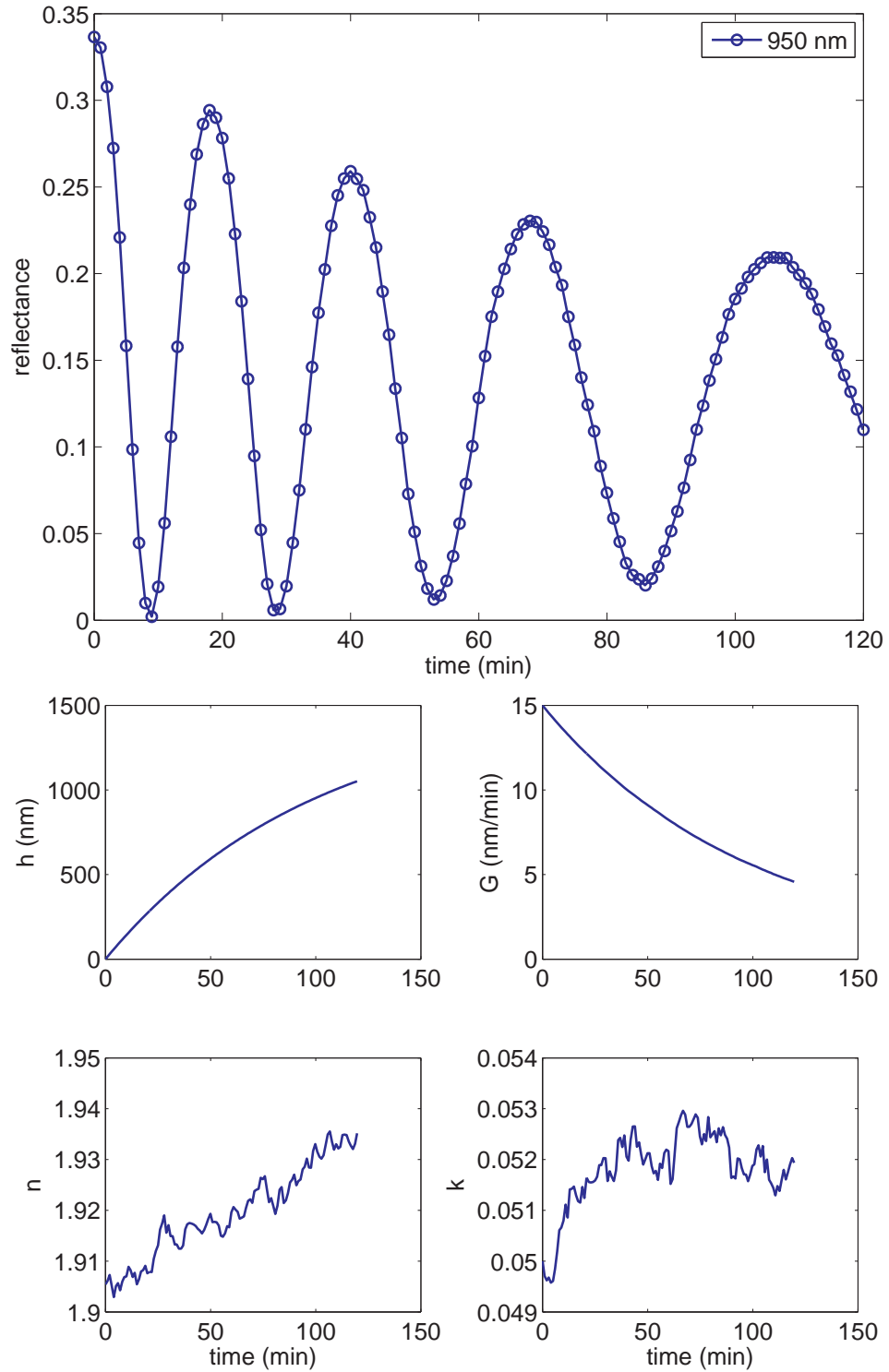


Figure 51: Simulated film growth process with decreasing growth rate. The sensor model is based on single-wavelength reflection on a smooth surface. (top) reflectance at 950 nm (bottom) states.

the mean of the true state and is used to normalize the estimation error. By using the random vector, we tested five random initial guesses and they all converge to the same solution. The estimation error is $e = 21.9130$. Figure 52 shows the estimated states and fitted measurement. As shown, BLS did not yield satisfactory estimates due to the inappropriate assumption of constant growth rate in the entire growth process. The estimated growth rate is actually the average growth rate of the growth process. Because growth rate and refractive index and extinction coefficient are closely coupled, the estimate of the refractive index and extinction coefficient also have large offset. BLS is what the commercial software RoboMBE is based on and we have observed similar fitting result when using RoboMBE in our CVD experiments. In addition to the parameters in Eq. (28), RoboMBE also fits the refractive index and extinction coefficient of the substrate. However, we have found it quite difficult to separately estimate the refractive index and extinction coefficient of the film and the substrate because they are highly correlated. In this simulation, the refractive index and the extinction coefficient of the substrate are assumed known in the sensor model. This is a reasonable assumption because the refractive index and the extinction coefficient of silicon is well known in the literature and in the experiment they are used as reflectance reference to calibrate the raw reflected light intensity data.

Next we use RLS to estimate the states from the same reflectance. The process dynamic model and the sensor model are the same as BLS. The initial guess is also expressed by $x_1 = x_i \times \text{normrnd}(\text{ones}(4, 1), 0.1)$. The only difference is that RLS needs an additional parameter, i.e. horizon size. We tested four different horizon sizes, 10, 20, 30 and 40 and for each horizon size, we tested five random initial guesses and calculated the mean estimation error. The resulting estimation errors are summarized in Table 3 (row of Single Smooth). Figure 53 shows a typical estimation result at $N = 10, 20$ and 30 . The result clearly shows that best estimate was obtained when window size equals 20. This confirmed what we have discussed in Chapter 4,

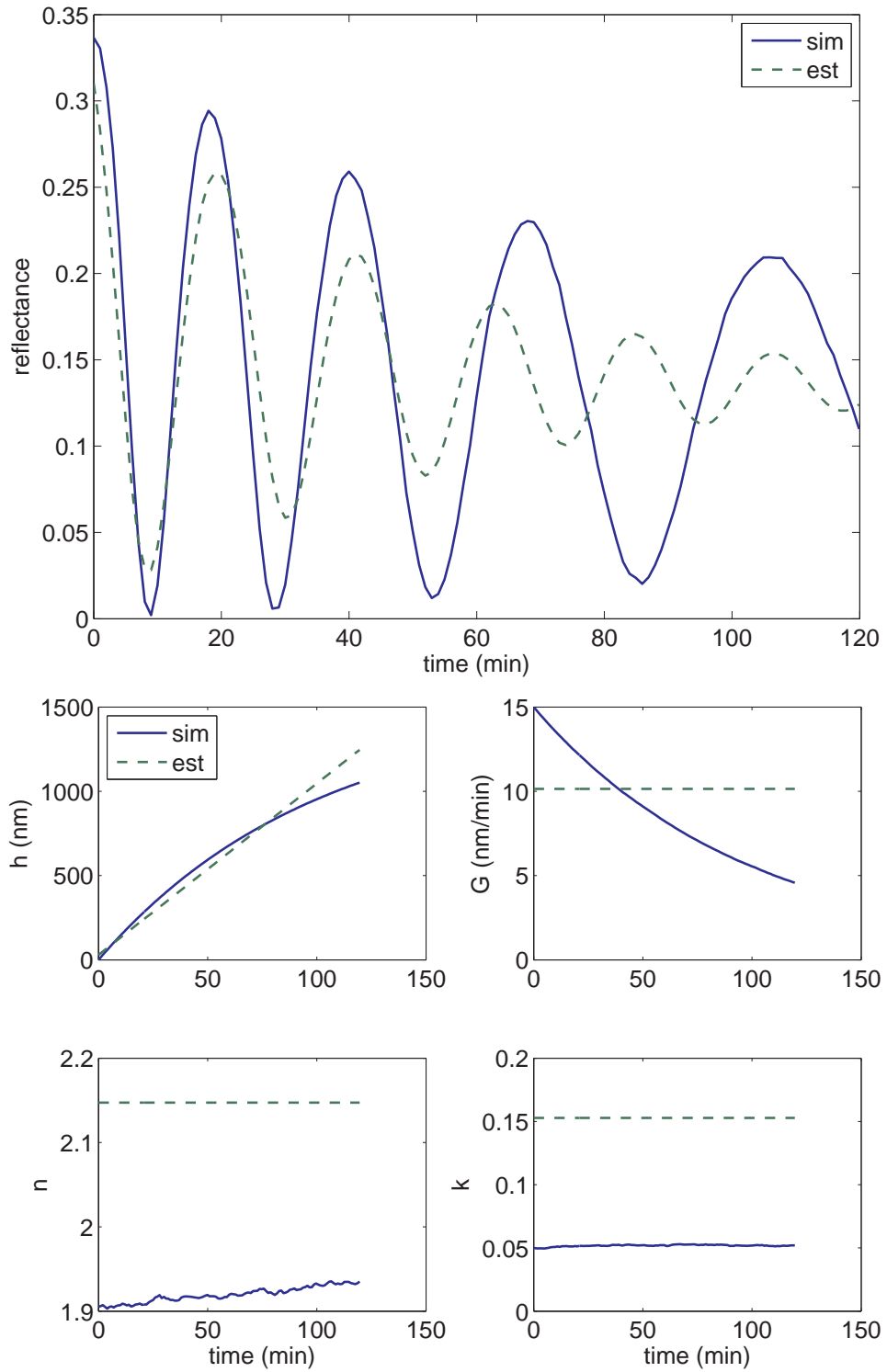


Figure 52: Estimation result by BLS from the reflectance measurement in Fig. 51. The initial guess is 10% offset from the true initial state. (top) fitted reflectance at 950 nm (bottom) true and estimated states.

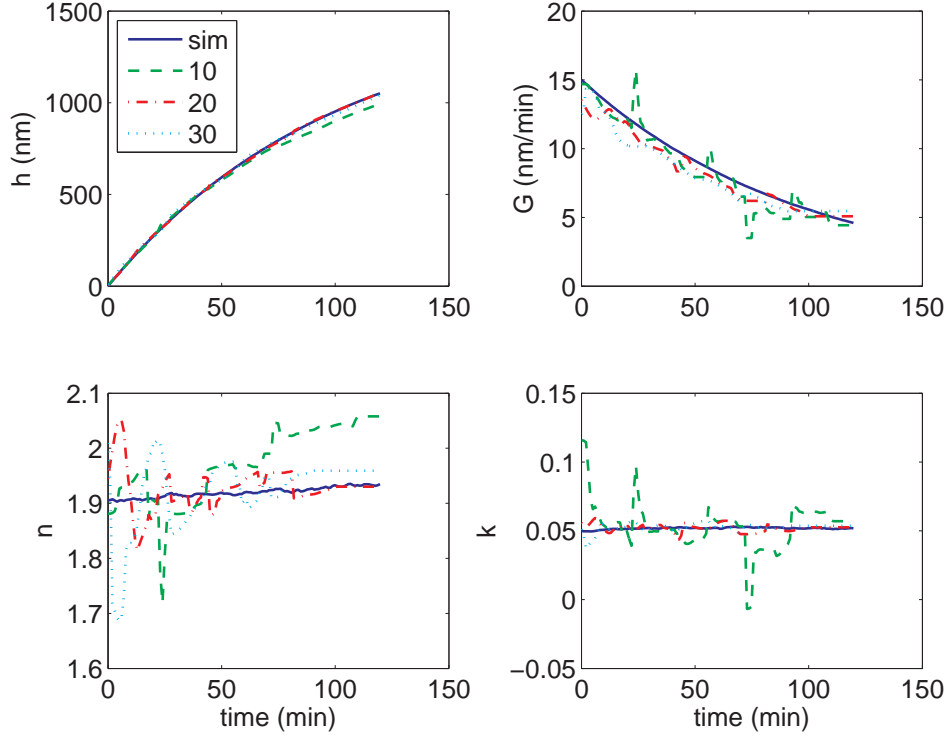


Figure 53: Estimated states by RLS from the reflectance measurement in Fig. 51 with horizon size equal to 10, 20 and 30.

the horizon size cannot be either too short or too long. The window size has two competing effects on the performance of RLS. First, window size should be short so that the assumption of constant film parameters is more acceptable. On the other hand, the window size cannot be too short. The sensor model is highly nonlinear and film parameters are correlated with each other. If the window size is too short, the fitting algorithm may not be able to separately estimate these parameters. As shown in Fig. 51, $N = 20$ corresponds to a quarter-wave oscillation of reflectance and this is consistent with the conclusion of [20]. We should also notice that as growth rate decreases, the window size of 20 may not include enough curvature of reflectance in the later part of the process. Ideally the window size should be optimized during the growth and this can be one of the future work suggestions for RLS.

Next we use mMHE to estimate the states from the same simulated reflectance data. The process dynamic model and the sensor model are the same as in RLS.

Table 3: Average estimation error by RLS and mMHE with different horizon size. Process dynamic model mismatch

	N	10	20	30	40
Single Smooth	RLS	3.8744	1.2473	1.4812	5.3383
	mMHE	1.4765	1.1343	1.4435	1.4320
Dual Smooth	RLS	1.1918	1.1091	1.5957	1.9809
	mMHE	1.0544	1.1064	1.5819	2.0100
Dual Rough	RLS	26.2015	35.6655	34.7872	32.8599
	mMHE	2.3437	3.4856	4.8320	N/A

The initial guess is also expressed by $x_1 = x_i \times \text{normrnd}(\text{ones}(4, 1), 0.1)$. The only difference is that mMHE uses the information from both the process dynamic model and the sensor model, which is represented by three additional tuning matrices, i.e. the initial covariance matrix $P_{1|0}$, the covariance matrix for the sensor model uncertainty R , and the covariance matrix for the process model uncertainty Q . In this example, R is chosen to be the same as that used in simulating the process $R = 10^{-6}$ because we know in this example the sensor model is correct. Q represents the added uncertainty when the horizon shifts. Because the process dynamic model of mMHE assumes constant G , n and k , the model mismatch mainly lies in G . Therefore we choose $Q = \text{diag}([10^{-1}, 10^{-1}, 10^{-6}, 10^{-6}])$ with the second element being large to indicate the large model uncertainty in G . 10^{-1} represents an error in the first decimal place. The covariance of the first element h is also large because h is computed from G and so the error in G propagates into h . $P_{1|0}$ is chosen to be $\text{diag}(x_i) \times 10^{-2}$ which represents that the initial guess is around 10% from the true initial state. With the chosen $P_{1|0}$, R and Q , we tested four different horizon sizes, 10, 20, 30 and 40 and for each horizon size, we tested five random initial guesses and calculated the mean estimation error. The resulting estimation errors are summarized in Table 3 (row of Single Smooth). Figure 54 shows a typical estimation result at $N = 10, 20$ and 30 .

As shown, the effect of horizon size on the estimation in mMHE has a similar

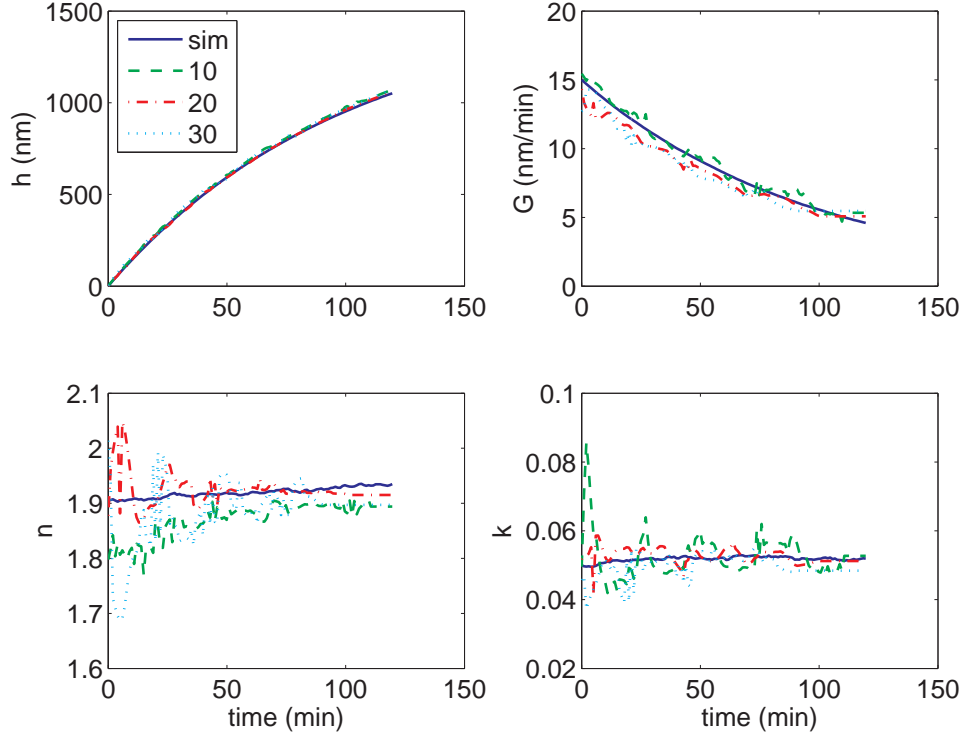


Figure 54: Estimated states by mMHE from the reflectance measurement in Fig. 51 with horizon size equal to 10, 20 and 30.

pattern as in RLS, i.e. there exists an optimum horizon size. Furthermore, the estimation error of mMHE decreased in all horizon sizes compared to RLS. The estimated states in Fig. 54 are also less oscillatory than in Fig. 53 (notice different y axis scale). The improved estimation in mMHE is due to the additional information of the process dynamic model and the inclusion of the *a priori* estimate. Initially, the inverse of $P_{1|0}$ limits the search space for the optimum solution. After the first iteration, P is updated by EKF. If a good fit is obtained in the first window, P should become small to indicate more confidence on the *a priori* estimate for the next window. Then in the next window, the optimization algorithm weights more on the *a priori* estimate and limits the change of the parameters. In RLS, however, the *a priori* estimate is not used in the objective function and so the solution of RLS in Fig. 53 oscillates more between windows, especially for longer horizon size since the process is changing over this window. Figure 55 shows the evolution of variance of

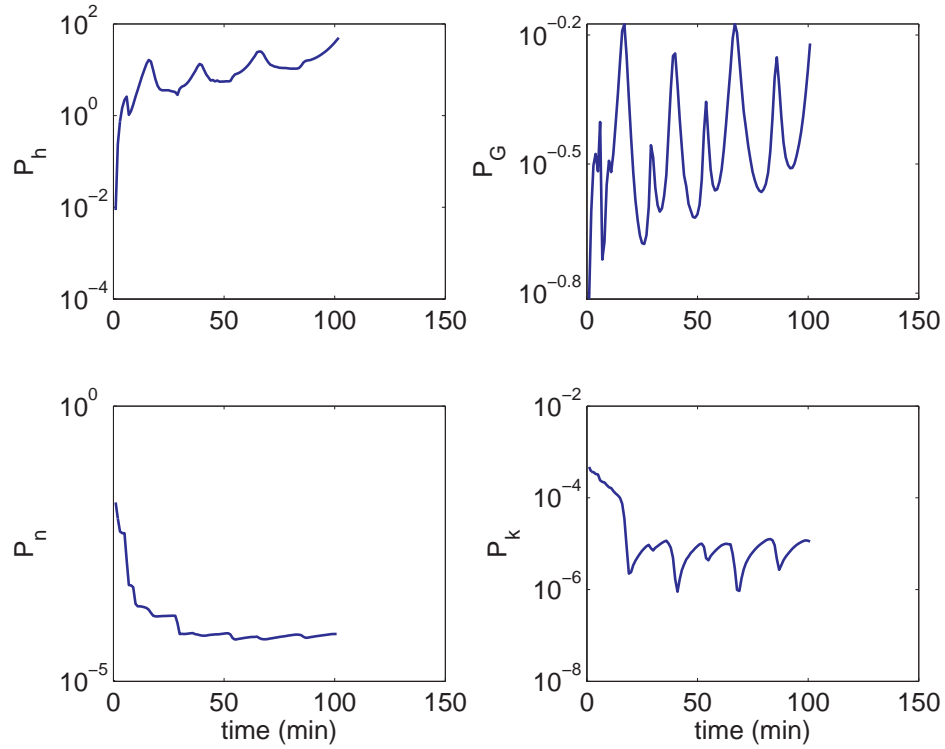


Figure 55: Variance of estimated states in Fig. 54 when $N = 20$.

each state after the measurement update in mMHE, when $N = 20$. As shown, the variance of n and k are in the order of 10^{-5} and 10^{-6} indicating an error in around second and the third decimal place, respectively, which is confirmed by comparing the true and estimated n and k . The variance of G and h are much larger due to the process dynamic model mismatch. It is an additional advantage of mMHE to explicitly consider the covariance matrix P because it measures the confidence on the estimate and also the correlations between states.

We also used full MHE to estimate the states from the same reflectance. The process dynamic model, the sensor model and tuning matrices are the same as mMHE. The initial guess is also expressed by $x_1 = x_i \times \text{normrnd}(\text{ones}(4, 1), 0.1)$. Figure 56 shows a typical estimation result at $N = 10$. The estimation error is 2.7297. As shown, there is no significant improvement using full MHE. In fact the estimation error is even slightly larger than mMHE. However, the major problem of MHE is that

it is computationally expensive. When $N = 10$ and $x \in \mathbf{R}^4$, there are 40 variables to solve in each iteration. For this particular example, MHE takes 8 minutes and 33 seconds while mMHE takes only 22 second on a Pentium(R) D CPU 3.20GHz computer. In addition, the computation requirement increases exponentially with the horizon size and this makes MHE impractical for many applications of *in situ* sensor data interpretation.

Finally we used EKF to estimate the states from the same reflectance. The process dynamic model, the sensor model and tuning matrices are the same as mMHE. By using the random vector, we tested five random initial guesses and the average estimation error is $e = 2.9599$, higher than both mMHE and RLS. Figure 57 shows a typical estimated states and variance. As shown, EKF yielded reasonable estimate as well, although it is significantly more oscillatory compared to mMHE. Among the state estimators studied, EKF is the fastest because it uses only one measurement at a time. However, based on our experience, we find that mMHE is more robust than EKF when the initial guess is wrong because mMHE can converge to the solution faster by using more measurement data that exhibit curvature in the reflectance oscillation.

5.1.2 Dual-wavelength reflection on smooth surface

We now consider a slightly more complicated case, i.e. dual-wavelength reflection on smooth surface. The *in situ* emissivity-correcting pyrometer in our CVD testbed uses two wavelengths, $\lambda_1 = 950$ nm and $\lambda_2 = 470$ nm. Ideally with more independent measurement we should obtain a better estimate. The process model used to simulate

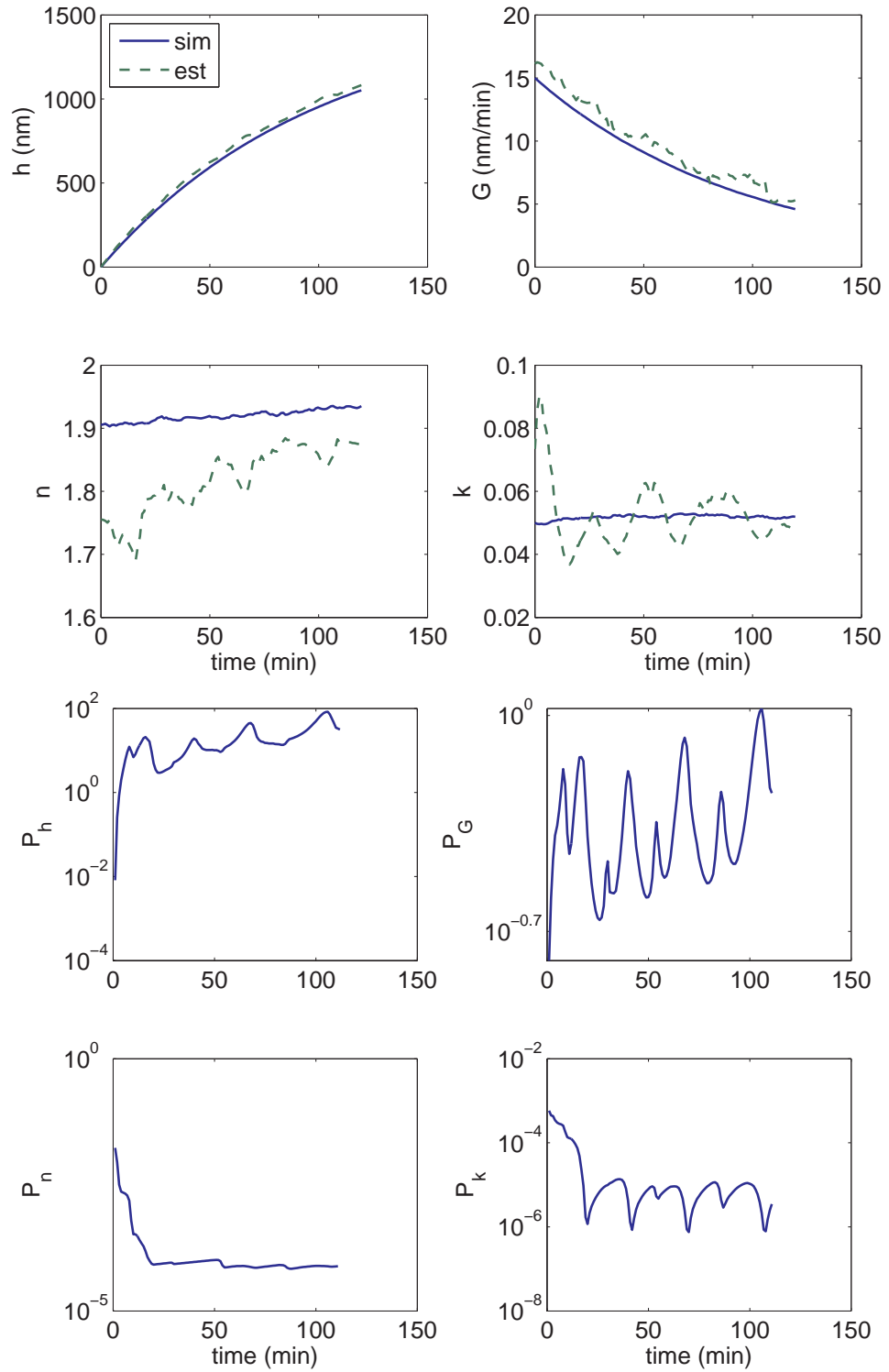


Figure 56: Estimation result by MHE from the reflectance measurement in Fig. 51. The initial guess is 10% offset from the true initial state. (top) true and estimated states (bottom) variance of estimated states.

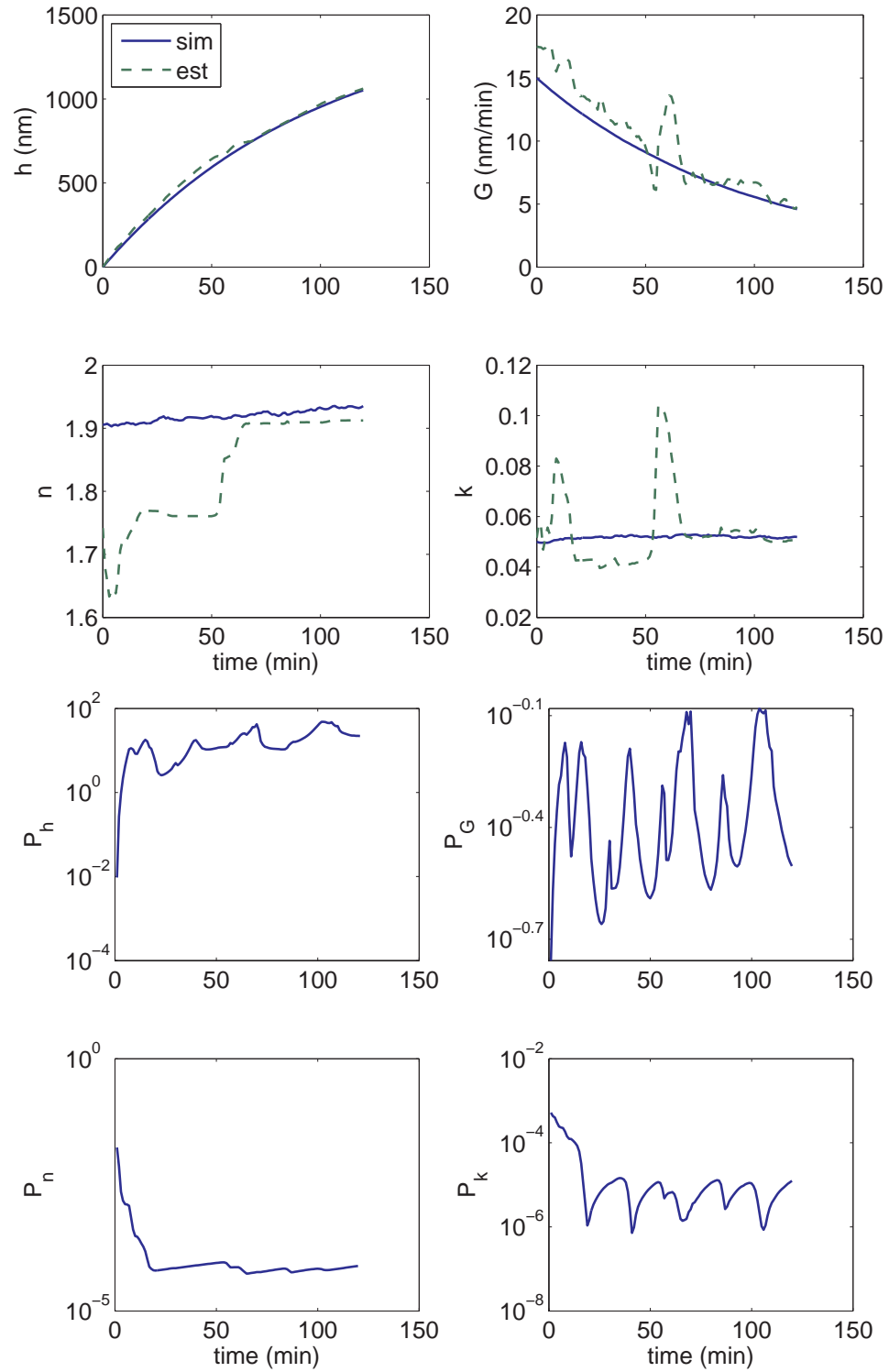


Figure 57: Estimation result by EKF from the reflectance measurement in Fig. 51. The initial guess is 10% offset from the true initial state. (top) true and estimated states (bottom) variance of estimated states.

the process is expressed by

$$\begin{bmatrix} h \\ G \\ n_1 \\ k_1 \\ n_2 \\ k_2 \end{bmatrix}_{j+1} = \begin{bmatrix} h + G \times \Delta t \\ G \times 0.99 \\ n_1 \\ k_1 \\ n_2 \\ k_2 \end{bmatrix}_j + w_j \quad (29)$$

where subscript 1 and 2 correspond to 950 nm and 470 nm, respectively. The parameters used to simulate the process are the same as the single-wavelength case. The additional parameter is the complex refractive index of silicon at 470 nm, $4.8438 - 0.1528j$ [66, 67]. The refractive index of yttria at 470 nm is 1.9455 [106]. The extinction coefficient of yttria is not available and is assumed to be 0.1 for this simulation. So the initial state used to simulate the process is $x_i = [0, 15, 1.9054, 0.05, 1.9455, 0.1]^T$. The covariance matrix $R = \text{eye}(2) \times 10^{-6}$, where $\text{eye}(2)$ denotes an 2×2 identity matrix. Keep in mind, however, that in practice the sensor may have different sensitivity at different wavelength and so R may not be an identity matrix. The simulated measurement and states are shown in Fig. 58. Notice that the 470 nm reflectance curve oscillates faster than 950 nm, as predicted by Eq. (15).

Following the same logic as in the single-wavelength case, we first use BLS to estimate the states from the simulated reflectance measurement. The process dynamic model used in BLS assumes constant growth rate and is expressed by

$$\begin{bmatrix} h \\ G \\ n_1 \\ k_1 \\ n_2 \\ k_2 \end{bmatrix}_{j+1} = \begin{bmatrix} h + G \times \Delta t \\ G \\ n_1 \\ k_1 \\ n_2 \\ k_2 \end{bmatrix}_j \quad (30)$$

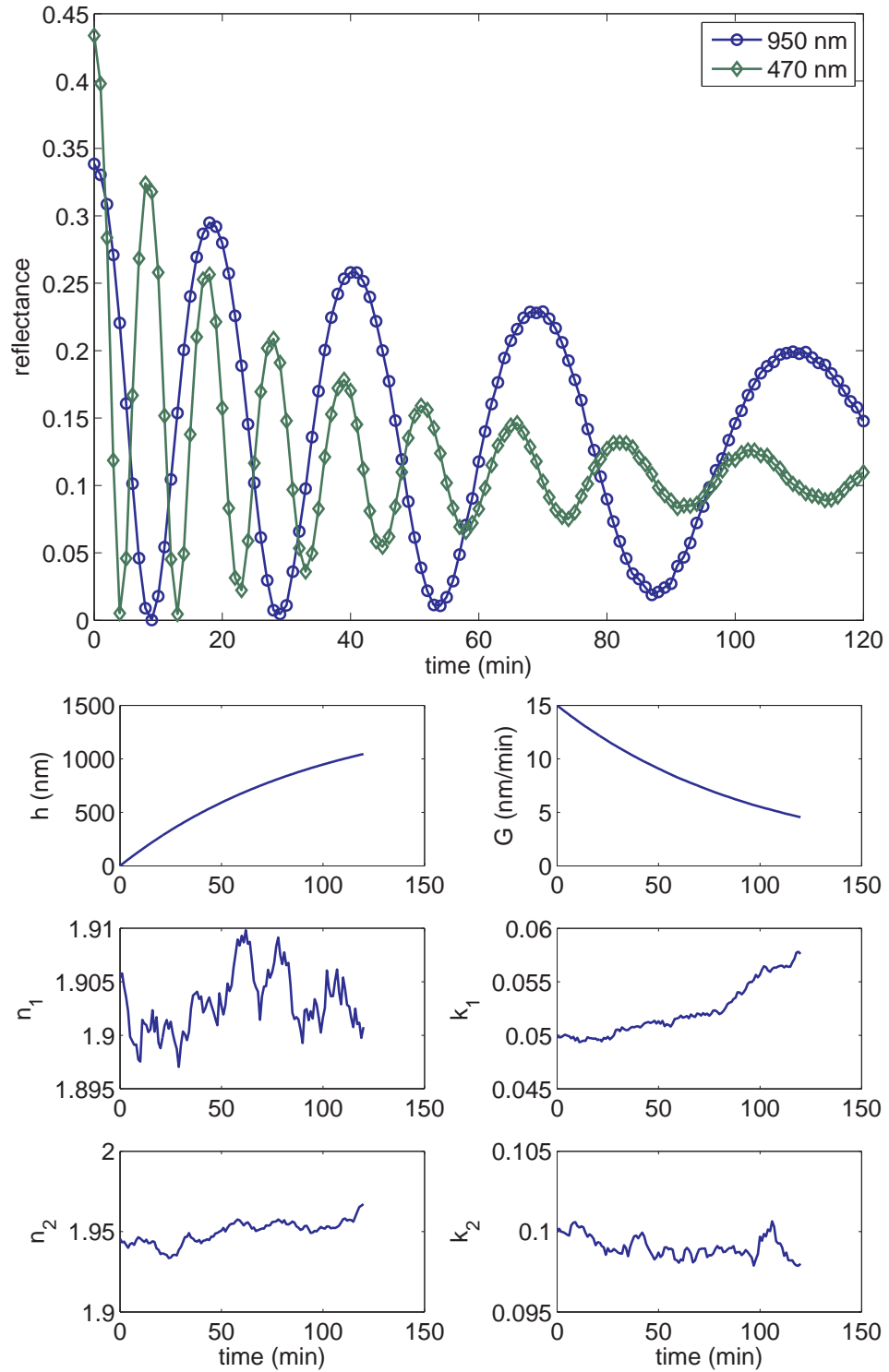


Figure 58: Simulated film growth process with decreasing growth rate. The sensor model is based on dual-wavelength reflection on a smooth surface. (top) reflectance at 950 nm and 470 nm (bottom) states.

The initial guess is expressed by $x_1 = x_i \times \text{normrnd}(\text{ones}(4, 1), 0.1)$. We tested five random initial guesses and they all converge to the same solution. The estimation error is $e = 25.6640$. Figure 59 shows the estimated states and fitted measurement. Again, BLS did not yield satisfactory estimates due to the inappropriate assumption of constant growth rate in the entire growth process.

Next we use RLS to estimate the states from the same reflectance. The process dynamic model and the sensor model are the same as BLS. The initial guess is also expressed by $x_1 = x_i \times \text{normrnd}(\text{ones}(6, 1), 0.1)$. We tested four different horizon sizes, 10, 20, 30 and 40 and for each horizon size, we tested five random initial guesses and calculated the mean estimation error. The resulting estimation errors are summarized in Table 3 (row of Dual Smooth). Figure 60 shows a typical estimation result at $N = 10, 20$ and 30 . Compared to single-wavelength case, we found that by including an additional independent measurement, the horizon size can be shortened. For example, the estimation error at $N = 10$ for the dual-wavelength case is similar to $N = 20$ for the single-wavelength case. In our view, it would be even better if the *in situ* sensor measures spectral reflectance. The spectral wavelength range should be chosen such that the sensor model is valid at all wavelengths. If the dielectric function of the film can be modeled by Lorentz oscillator, the spectral refractive index of the film can be described by the Cauchy layer with several fitting parameters like in the ellipsometry [146]. In this way, we have more measurement data and less fitting parameters and thus should obtain better estimation. This can be one of the future work for the *in situ* sensor.

Next we use mMHE to estimate the states from the same reflectance. The process dynamic model and the sensor model are the same as RLS. The initial guess is also expressed by $x_1 = x_i \times \text{normrnd}(\text{ones}(6, 1), 0.1)$. Following the same tuning guideline in the single-wavelength case, we let $R = \text{eye}(2) \times 10^{-6}$, $Q = \text{diag}([10^{-1}, 10^{-1}, 10^{-6}, 10^{-6}, 10^{-6}, 10^{-6}])$ and $P_{1|0} = \text{diag}(x_i) \times 10^{-2}$. With the chosen

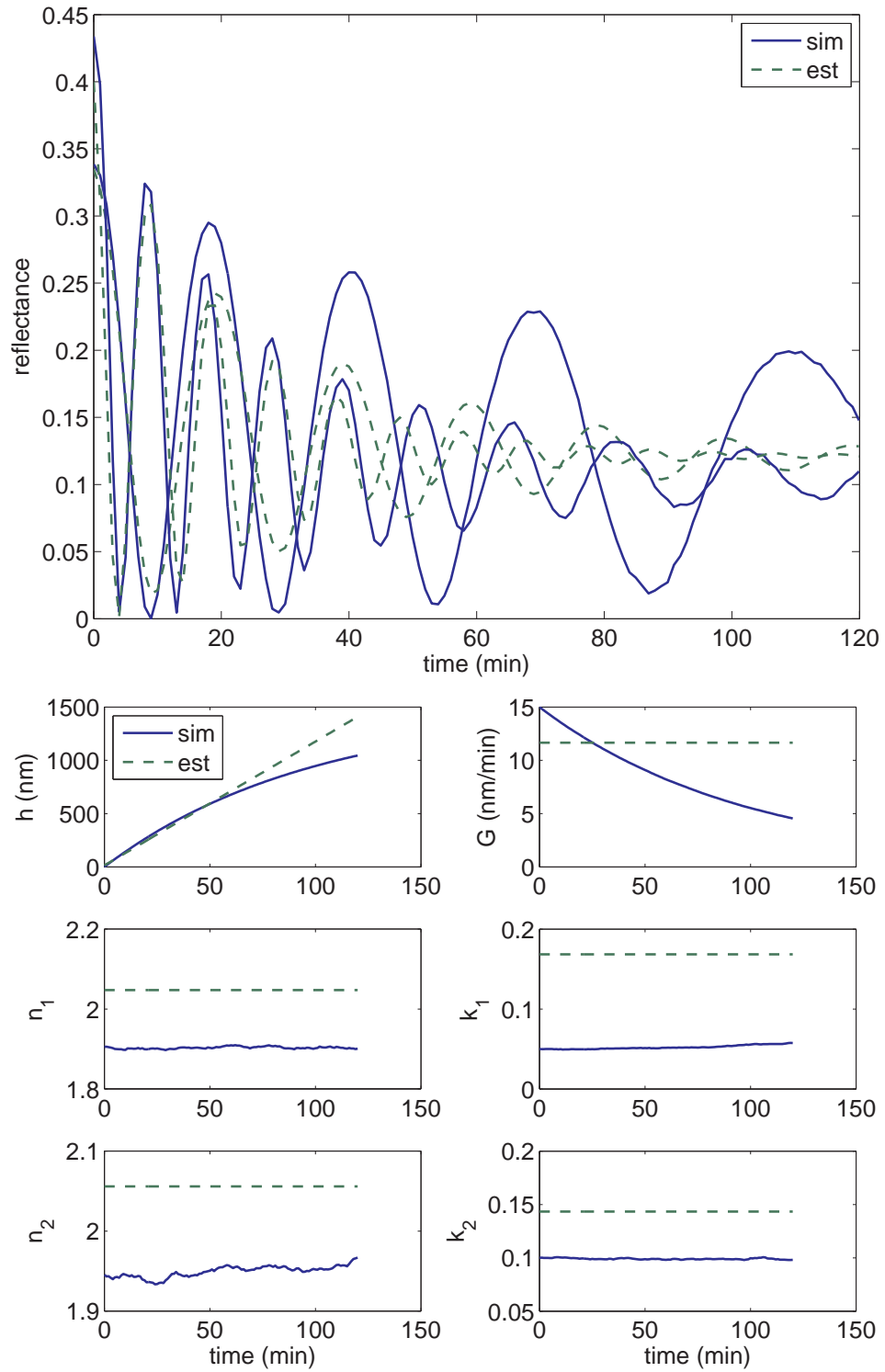


Figure 59: Estimation result by BLS from the reflectance measurement in Fig. 58. The initial guess is 10% offset from the true initial state. (top) fitted reflectance at 950 nm and 470 nm (bottom) true and estimated states.

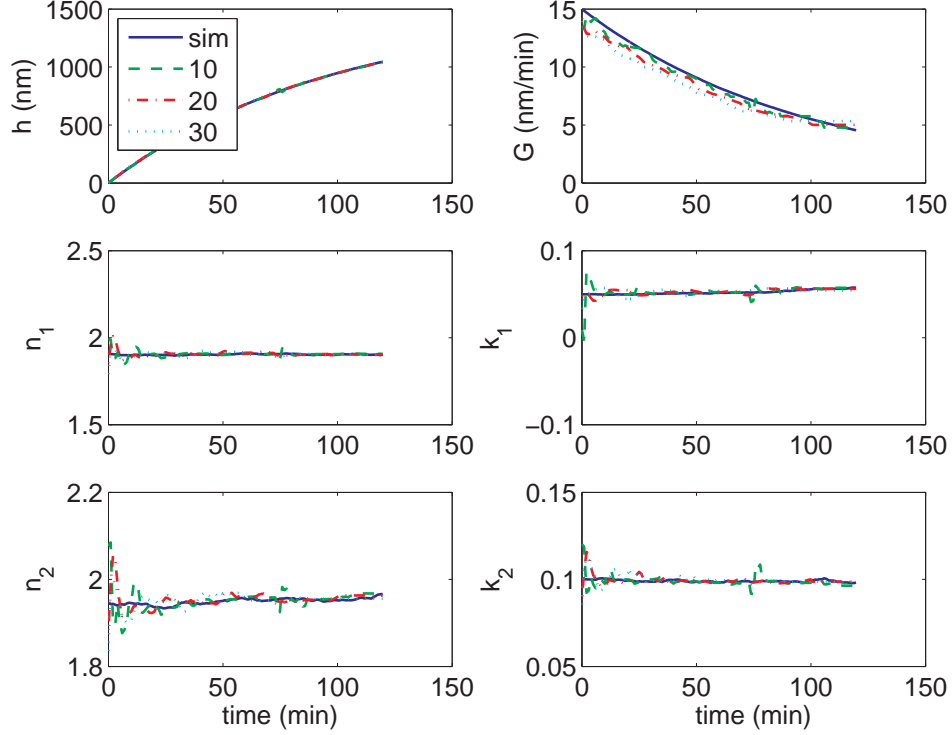


Figure 60: Estimated states by RLS from the reflectance measurement in Fig. 58 with horizon size equal to 10, 20 and 30.

$P_{1|0}$, R and Q , we tested four different horizon sizes, 10, 20, 30 and 40 and for each horizon size, we tested five random initial guesses and calculated the mean estimation error. The resulting estimation errors are summarized in Table 3 (row of Dual Smooth). Figure 61 shows a typical estimation result at $N = 10, 20$ and 30 . Figure 62 shows the evolution of variance of each state after the measurement update in mMHE when $N = 20$. As shown, mMHE again consistently yields better estimate than RLS. Notice that at $N = 40$, mMHE sometimes has difficulty to converge.

We also used full MHE to estimate the states from the same reflectance. The process dynamic model, the sensor model and tuning matrices are the same as mMHE. The initial guess is also expressed by $x_1 = x_i \times \text{normrnd}(\text{ones}(6, 1), 0.1)$. Figure 63 shows a typical estimation result at $N = 10$. The estimation error is 1.8952. For this particular example, MHE takes 17 minutes and 44 seconds on a Pentium(R) D CPU 3.20GHz computer. Compared to single-wavelength, the computation time doubled

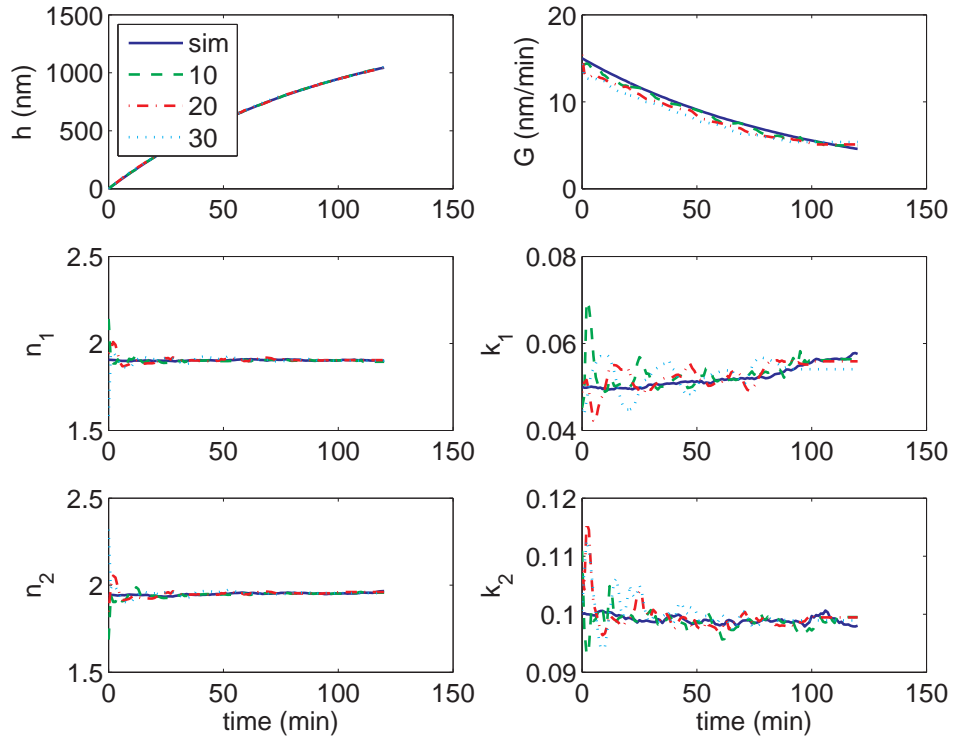


Figure 61: Estimated states by mMHE from the reflectance measurement in Fig. 58 with horizon size equal to 10, 20 and 30.

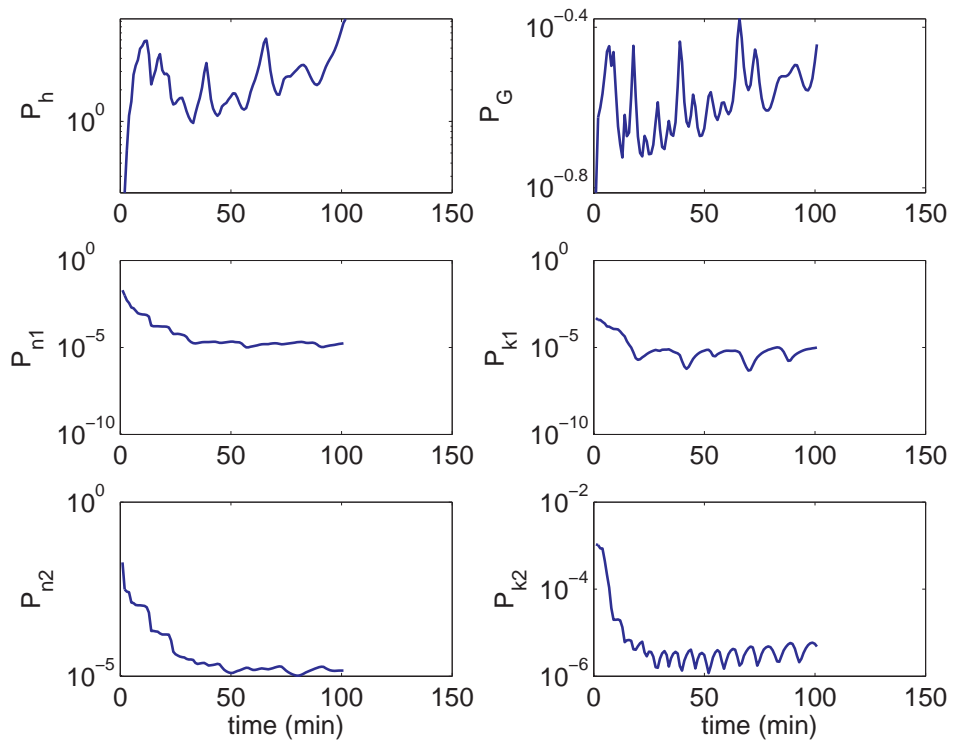


Figure 62: Variance of estimated states in Fig. 61 when $N = 20$.

when two additional states are optimized.

Finally we used EKF to estimate the states from the same reflectance. The process dynamic model, the sensor model and tuning matrices are the same as mMHE. We tested five random initial guesses and the average estimation error is $e = 1.3071$. Figure 64 shows a typical estimated states and variance. As in the single-wavelength case, EKF is more oscillatory than mMHE and RLS, but also performs reasonably well.

5.1.3 Dual-wavelength reflection on rough surface

Now we consider an even more complicated case, i.e. dual-wavelength reflection on a rough surface. As we have shown in Chapter 3, surface roughness and film extinction coefficient both cause reflectance to decrease and so in the experiment, the measured reflectance is a combined result of both light scattering by roughness and light absorption by extinction coefficient. Therefore, the purpose of this simulation is to study whether the state estimators can separately estimate extinction coefficient and surface roughness. The process model used to simulate the process is expressed by

$$\begin{bmatrix} h \\ G \\ h_e \\ G_e \\ n_1 \\ k_1 \\ n_2 \\ k_2 \end{bmatrix}_{j+1} = \begin{bmatrix} h + G \times \Delta t \\ G \times 0.99 \\ h_e + G_e \times \Delta t \\ G_e \times 0.99 \\ n_1 \\ k_1 \\ n_2 \\ k_2 \end{bmatrix}_j + w_j \quad (31)$$

where h_e and G_e represent the effective layer thickness and effective layer growth rate. As shown, the effective layer growth rate G_e at time $j + 1$ is 99% of the previous rate. It has been observed in our experiment that the roughness initially

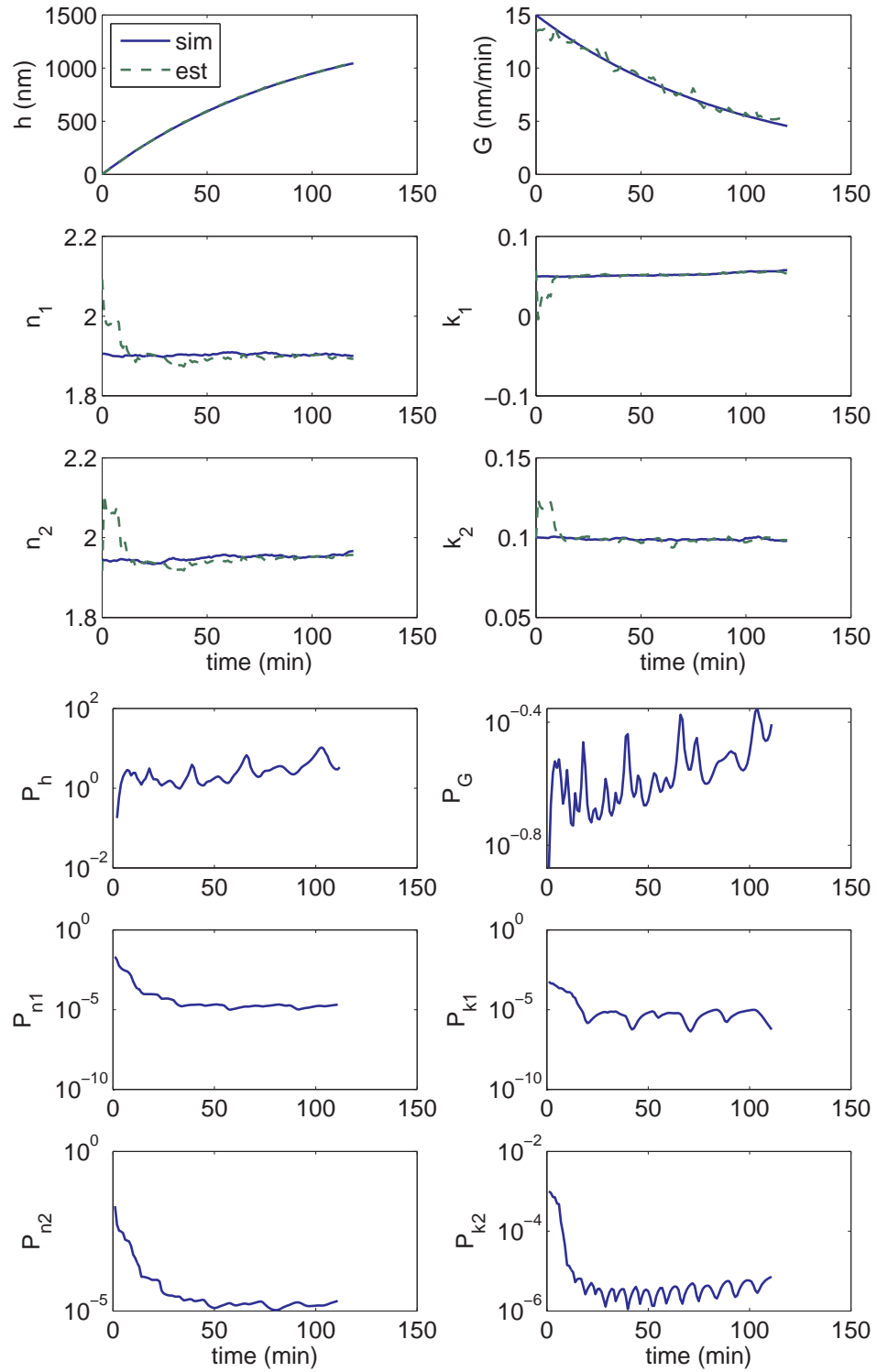


Figure 63: Estimation result by MHE from the reflectance measurement in Fig. 58. The initial guess is 10% offset from the true initial state. (top) true and estimated states (bottom) variance of estimated states.

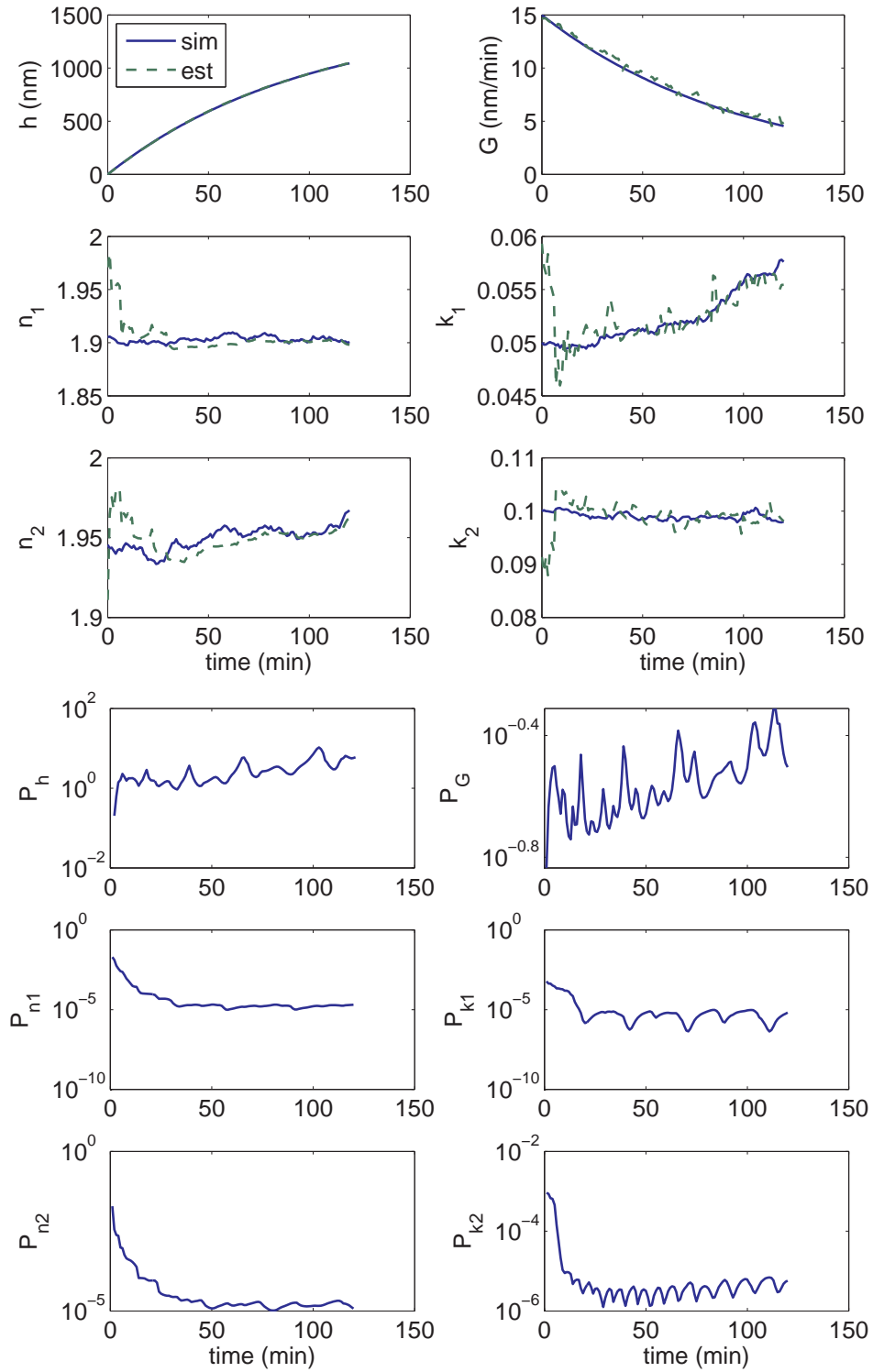


Figure 64: Estimation result by EKF from the reflectance measurement in Fig. 58. The initial guess is 10% offset from the true initial state. (top) true and estimated states (bottom) variance of estimated states.

increases and then saturates after a certain thickness is achieved. The sensor model is expressed by Eq. (14) for reflection on a rough surface. We use EMA model because it is better than SSM as discussed in Chapter 3. The complex refractive index of the substrate and wavelengths are the same as in the case of dual-wavelength reflection on smooth surface. The initial state used to simulate the process is $x_i = [0, 15, 0, 1, 1.9054, 0.05, 1.9455, 0.1]^T$. The covariance matrices are $R = \text{eye}(2) \times 10^{-6}$ and $Q = \text{diag}(x_i) \times 10^{-6}$. The simulated measurement and states are shown in Fig. 65. Compared to Fig. 58, the reflectance at both wavelengths decreases with time due to increasing surface roughness. Also notice that the reflectance at 470 nm is affected more by the roughness, which is consistent with the discussion in Chapter 3.

Following the same logic in the dual-wavelength smooth case, we first use BLS to estimate the states from the simulated reflectance measurement. The process dynamic model used in BLS assumes constant growth rate of the film and the effective layer and is expressed by

$$\begin{bmatrix} h \\ G \\ h_e \\ G_e \\ n_1 \\ k_1 \\ n_2 \\ k_2 \end{bmatrix}_{j+1} = \begin{bmatrix} h + G \times \Delta t \\ G \\ h_e + G_e \times \Delta t \\ G_e \\ n_1 \\ k_1 \\ n_2 \\ k_2 \end{bmatrix}_j + w_j \quad (32)$$

The initial guess is expressed by $x_1 = x_i \times \text{normrnd}(\text{ones}(8, 1), 0.1)$. We tested five random initial guesses and they all converge to the same solution. The estimation error is $e = 26.0206$. Figure 66 shows the estimated states and fitted measurement. Again, BLS did not yield satisfactory estimates due to the inappropriate assumption

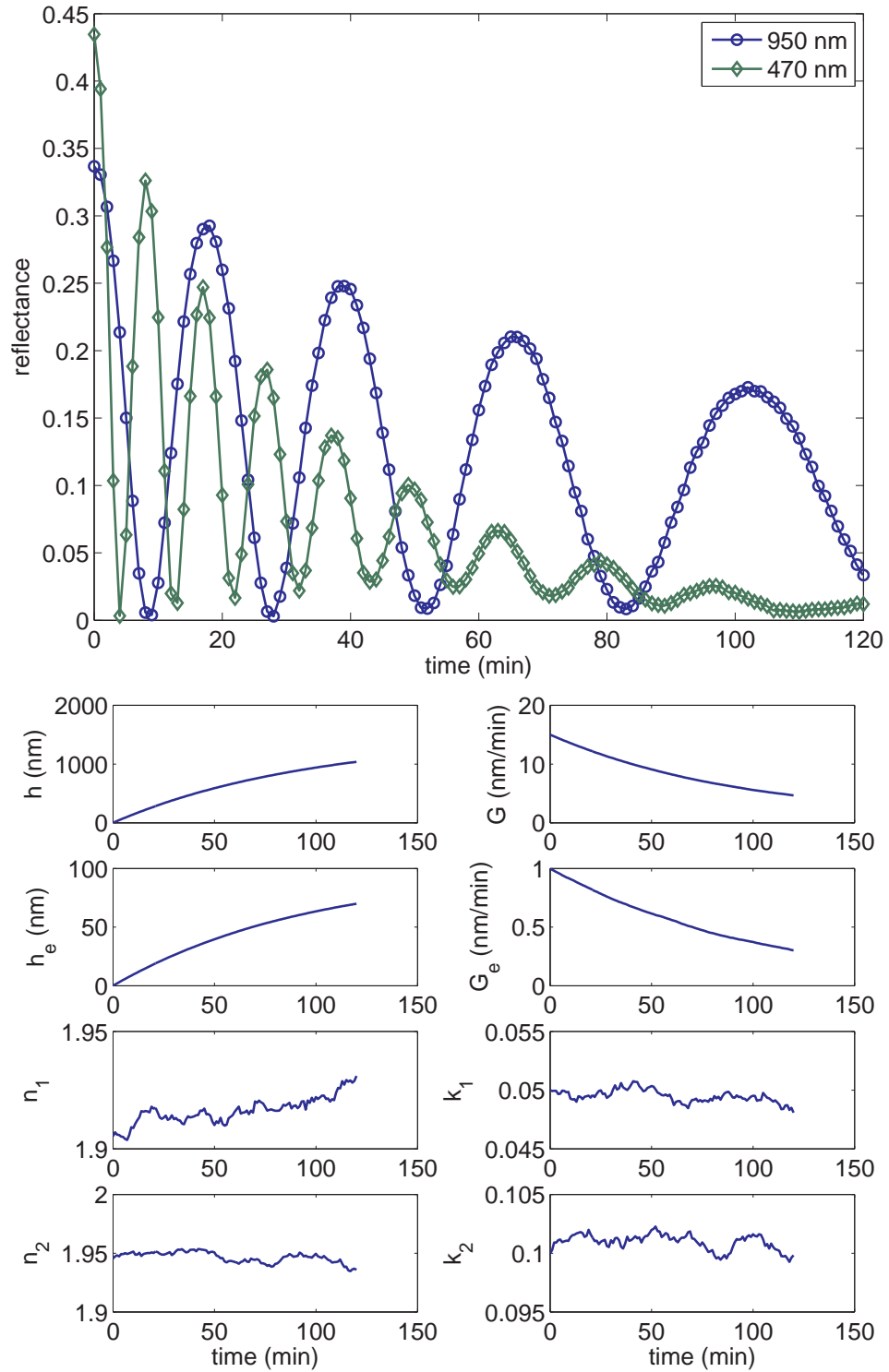


Figure 65: Simulated film growth process with decreasing film growth rate and effective layer growth rate. The sensor model is based on dual-wavelength reflection on a rough surface. (top) reflectance at 950 nm and 470 nm (bottom) states.

of constant growth rate in the entire growth process.

Next we use RLS to estimate the states from the same reflectance. The process dynamic model and the sensor model are the same as BLS. The initial guess is also expressed by $x_1 = x_i \times \text{normrnd}(\text{ones}(8, 1), 0.1)$. We tested four different horizon sizes, 10, 20, 30 and 40 and for each horizon size, we tested five random initial guesses and calculated the mean estimation error. The resulting estimation errors are summarized in Table 3 (row of Dual Rough). Figure 67 shows a typical estimation result at $N = 10, 20$ and 30. Compared to the dual-wavelength smooth case, we found that by including two additional states, RLS did not yield a good result. Figure 67 shows that sometimes h_e is estimated to be negative. This is because the initial guess of both h_e and G_e is close to zero, and without positive constraint the fitting algorithm may find a local minima at negative region. In this case, it would be helpful to have a spectral reflectance measurement to estimate roughness.

Next we use mMHE to estimate the states from the same simulated reflectance data. The process dynamic model and the sensor model are the same as RLS. The initial guess is also expressed by $x_1 = x_i \times \text{normrnd}(\text{ones}(8, 1), 0.1)$. Following the same tuning guideline in the single-wavelength case, we let $R = \text{eye}(2) \times 10^{-6}$, $Q = \text{diag}([10^{-1}, 10^{-1}, 10^{-3}, 10^{-3}, 10^{-6}, 10^{-6}, 10^{-6}, 10^{-6}])$ and $P_{1|0} = \text{diag}(x_i) \times 10^{-2}$. The third and fourth element of Q are chosen to be 10^{-3} to indicate relative small uncertainty of h_e and G_e because h_e and G_e are smaller than h and G by one order of magnitude. With the chosen $P_{1|0}$, R and Q , we tested four different horizon sizes, 10, 20, 30 and 40 and for each horizon size, we tested five random initial guesses and calculated the mean estimation error. The resulting estimation errors are summarized in Table 3 (row of Dual Rough). Figure 68 shows a typical estimation result at $N = 10, 20$ and 30. Figure 69 shows the evolution of variance of each state after the measurement update in mMHE when $N = 20$.

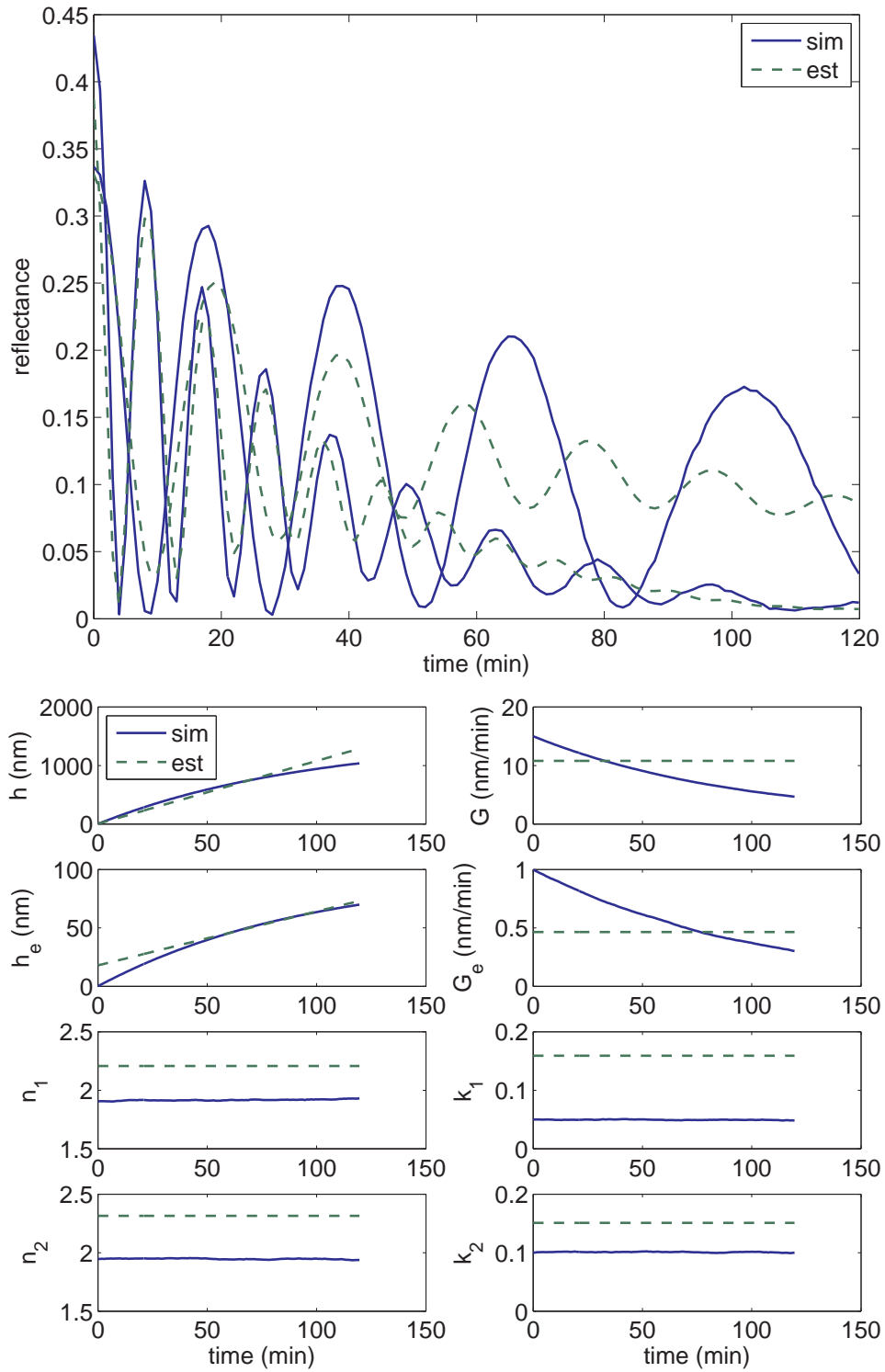


Figure 66: Estimation result by BLS from the reflectance measurement in Fig. 65. The initial guess is 10% offset from the true initial state. (top) fitted reflectance at 950 nm and 470 nm (bottom) true and estimated states.

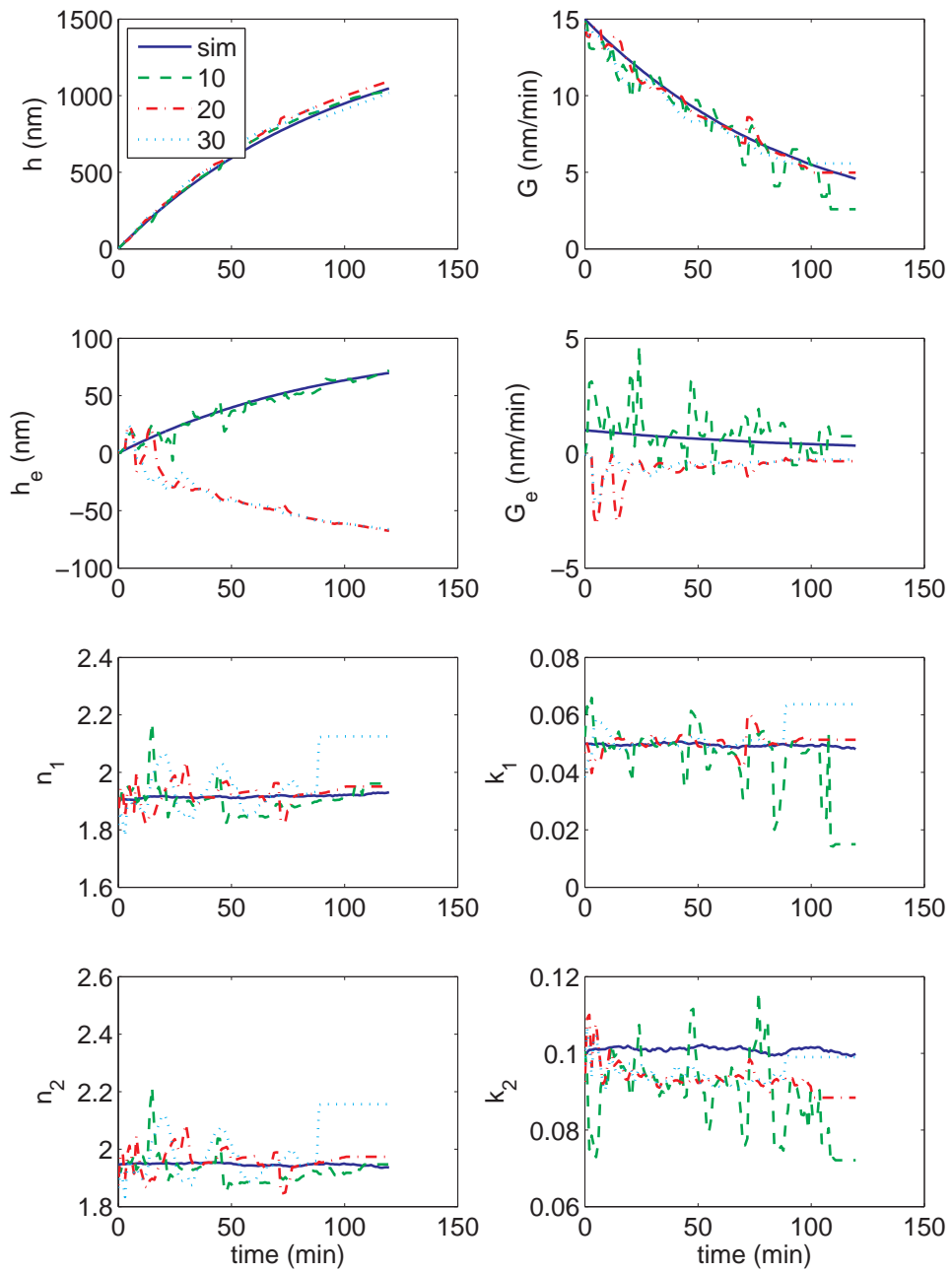


Figure 67: Estimated states by RLS from the reflectance measurement in Fig. 65 with horizon size equal to 10, 20 and 30.

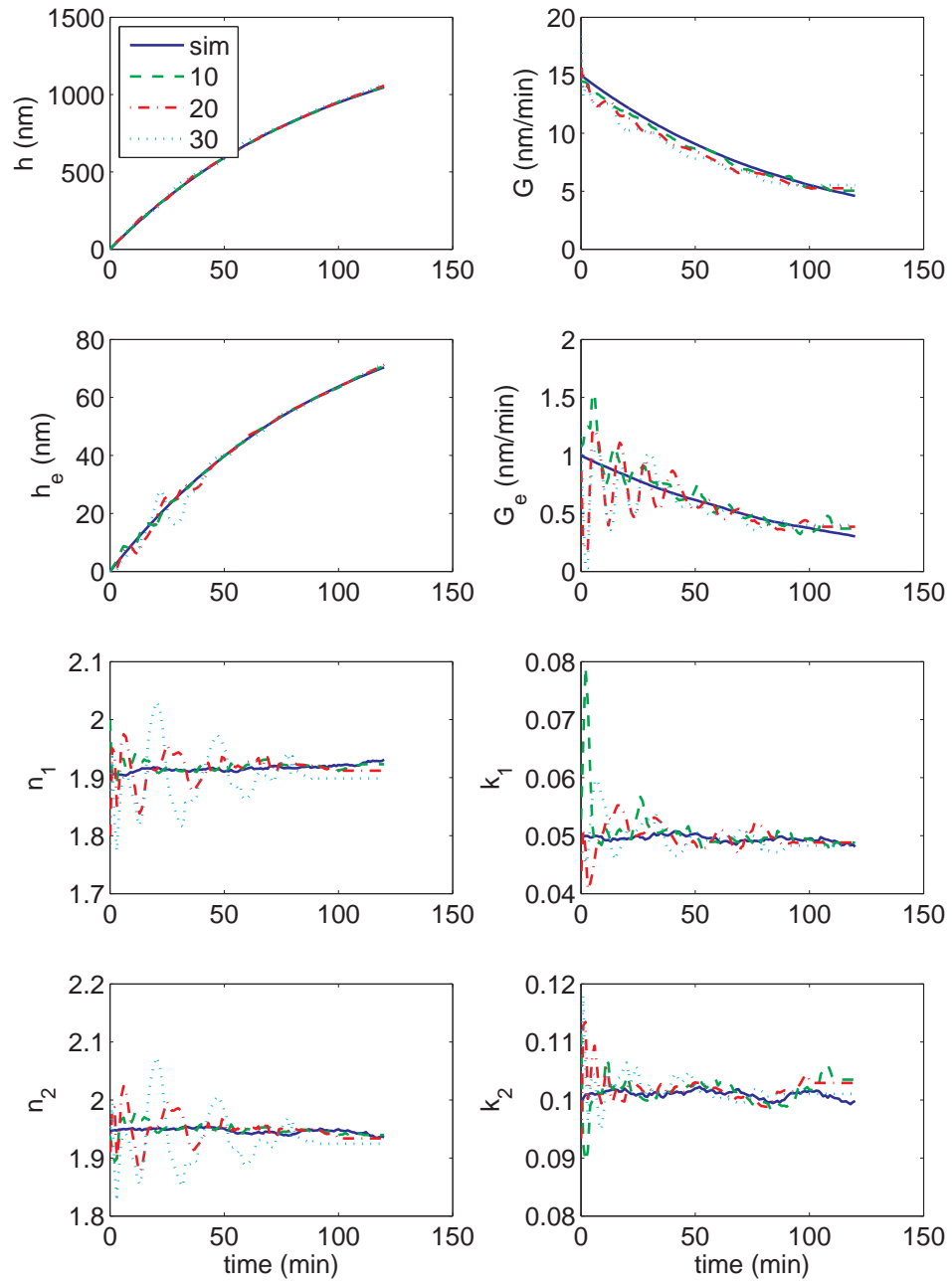


Figure 68: Estimated states by mMHE from the reflectance measurement in Fig. 65 with horizon size equal to 10, 20 and 30.

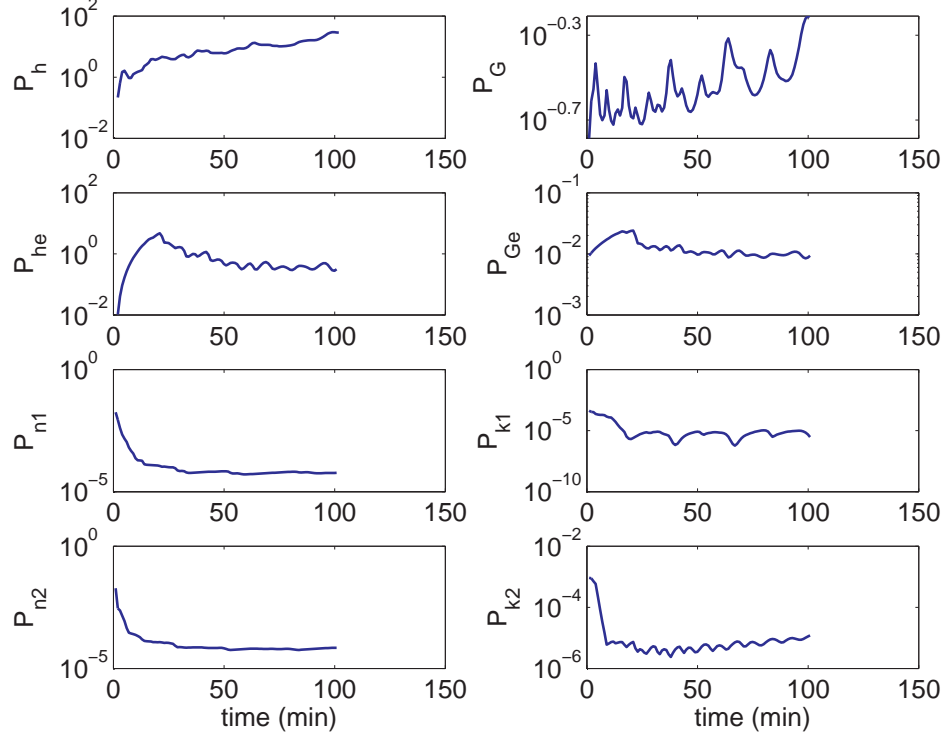


Figure 69: Variance of estimated states in Fig. 68 when $N = 20$.

As shown, mMHE again consistently yielded better estimate than RLS and separately estimated roughness and extinction coefficient. Neither h_e or G_e is estimated to be negative because the *a priori* estimate limits the search space for the optimum solution. It is clear from this simulation that by utilizing both process dynamic model and the sensor model instead of using only the sensor model, a better estimate can be obtained. Also notice that at $N = 40$, mMHE has difficulty to converge. This maybe because at the longer horizon, the estimated growth, i.e. averaged growth rate in the horizon, has more offset from the true growth rate. Therefore when the horizon shifts, there will be more added uncertainty. Thus, selecting a window size that is appropriate can also be important for mMHE.

We tested the sensitivity of mMHE to tuning matrices $P_{1|0}$, Q , and R by scaling the matrices by $1/10$ and 10 . The estimation error at $N = 10$ for different tuning matrices are summarized in Table 4. As shown, mMHE gave better results than RLS

Table 4: Estimation error by mMHE at $N = 10$ with different $P_{1|0}$, Q , and R

	$R/10$			R			$R \times 10$		
	$Q/10$	Q	$Q \times 10$	$Q/10$	Q	$Q \times 10$	$Q/10$	Q	$Q \times 10$
$P_{1 0}/10$	2.238	3.848	8.338	1.399	1.542	3.661	1.627	1.540	1.484
$P_{1 0}$	5.385	5.920	8.282	2.273	2.328	3.814	1.898	2.253	2.160
$P_{1 0} \times 10$	5.621	6.882	8.643	5.655	5.033	4.129	3.325	2.075	2.456

(estimation error is 26.2015) in all cases, indicating a good robustness to the tuning matrices. Also notice there is a trend that the estimation error increases when Q and $P_{1|0}$ increase and R decreases. This is expected because increasing Q and $P_{1|0}$ indicates less confidence on the *a priori* estimate and decreasing R indicates more weight on the measurement. This is essentially approaching to RLS and therefore the estimation error increases.

Finally we used EKF to estimate the states from the same reflectance. The process dynamic model, the sensor model and tuning matrices are the same as mMHE. We tested five random initial guesses and the average estimation error is $e = 2.9233$. Figure 70 shows a typical estimated states and variance. Again, EKF yielded acceptable result by using both the process dynamic model and the sensor model.

5.2 *Sensor model mismatch*

5.2.1 Single-wavelength reflection on smooth surface

In the previous section, we found that even if there is process dynamic model mismatch, most of the time RLS can still yield a reasonable estimate. This is because RLS is solely dependent on the sensor model and the sensor model in the previous section is assumed to be correct. In this section, we study a worse but common scenario, when there is sensor model mismatch. As we have shown in Chapter 3, the EMA model may be less accurate at longer wavelength and there is a systematic error of around 150% at 950 nm. Inspired by that, we consider a sensor model that

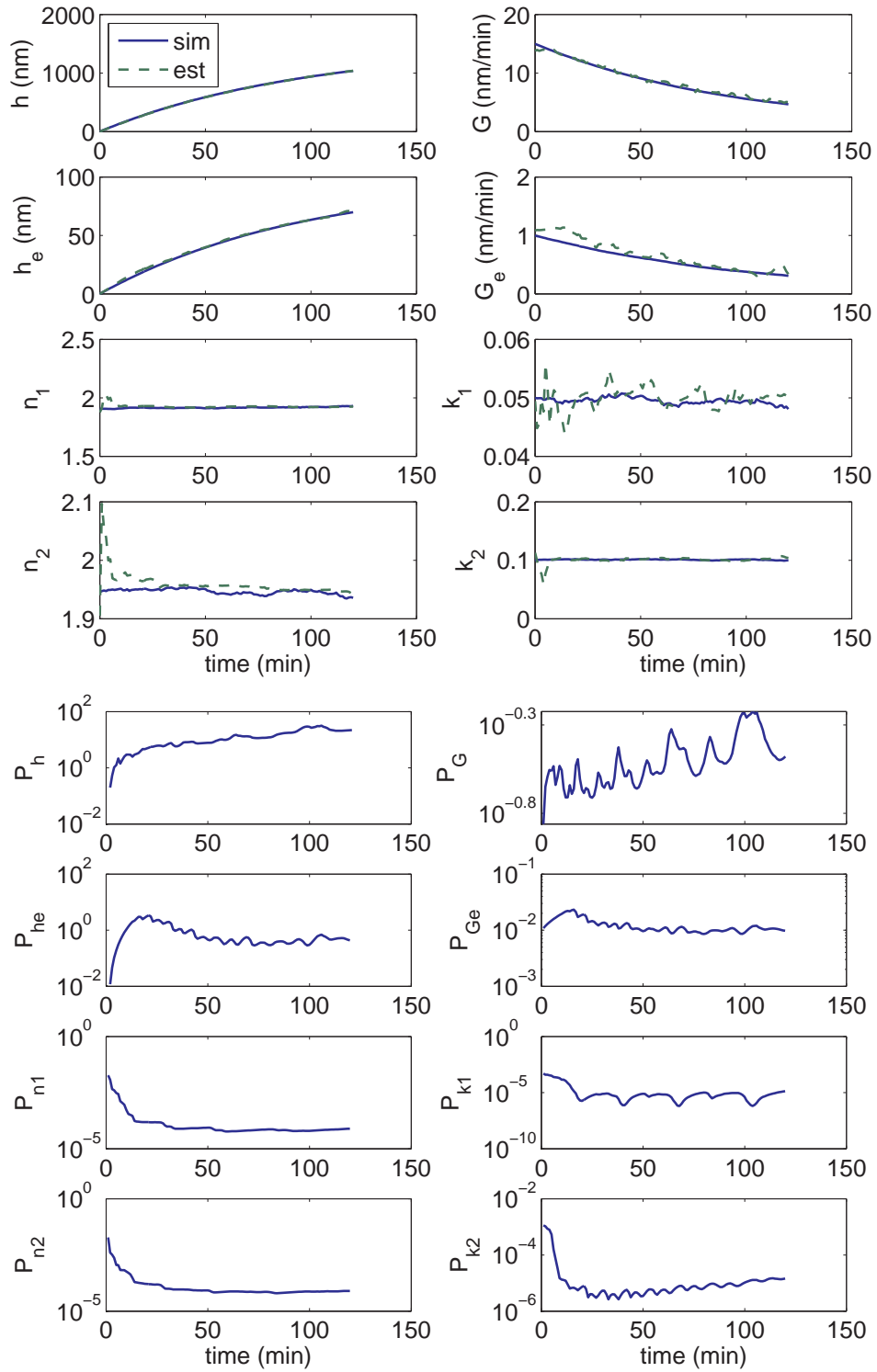


Figure 70: Estimation result by EKF from the reflectance measurement in Fig. 65. The initial guess is 10% offset from the true initial state. (top) true and estimated states (bottom) variance of estimated states.

simply multiplies the reflectance calculated from Eq. (5) by 1.5. The process dynamic model is the same as in the previous section and is expressed by Eq. (28). The initial state used to simulate the process is $x_i = [0, 15, 1.9054, 0.05]^T$. The parameters used to simulate the process are the same as in the previous section of single-wavelength reflection on smooth surface. The simulated measurement and states are shown in Fig. 71. Notice that the reflectance is about 1.5 times larger than that in Fig. 51.

We first use RLS to estimate the states from the simulated reflectance measurement. The process dynamic model and the sensor model are the same as in the previous section of single-wavelength reflection on smooth surface. Strictly speaking, there are actually both process dynamic model mismatch and the sensor model mismatch. The initial guess is expressed by $x_1 = x_i \times \text{normrnd}(\text{ones}(4, 1), 0.1)$. We tested four different horizon sizes, 10, 20, 30 and 40 and for each horizon size, we tested five random initial guesses and calculated the mean estimation error. The resulting estimation errors are summarized in Table 5 (row of Single Smooth). Figure 72 shows a typical estimation result at $N = 10, 20$ and 30 . As shown, the horizon size effect on RLS is different from the case of process model mismatch. In this case, RLS yielded more reasonable estimates at longer horizon size. As shown in Fig. 72, at $N = 10$, the reflectance is perfectly fitted even though the sensor model has mismatch. At longer horizon size, however, the reflectance in the latter part of the curve is fitted better than that in the beginning part of the curve. This suggested that at a longer horizon size, the fitting algorithm sacrificed the early part of the reflectance to obtain an overall good fit. Because the reflectance at latter part decreases due to light absorption, the absolute value of the error is small and thus easy to fit. In all cases, comparing the estimation error to the case without sensor model mismatch (Table 3), the estimation errors in Table 5 dramatically increase due to the sensor model mismatch.

Next we use mMHE to estimate the states from the same reflectance. The process dynamic model and the sensor model are the same as RLS. The initial guess is also

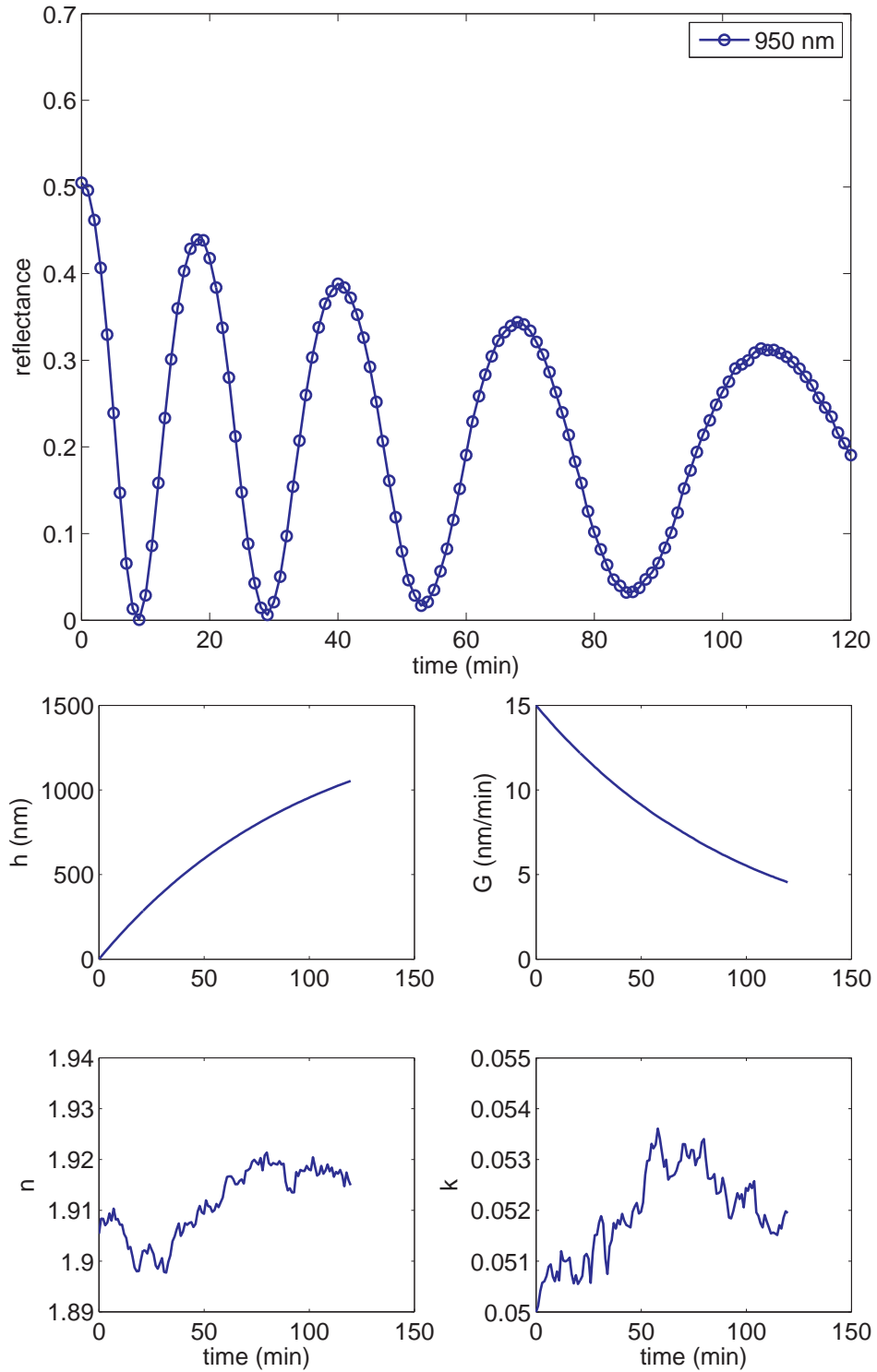


Figure 71: Simulated film growth process with decreasing growth rate. The sensor model simply times the reflectance calculated from Eq. (5) by 1.5 (top) reflectance at 950 nm (bottom) states.

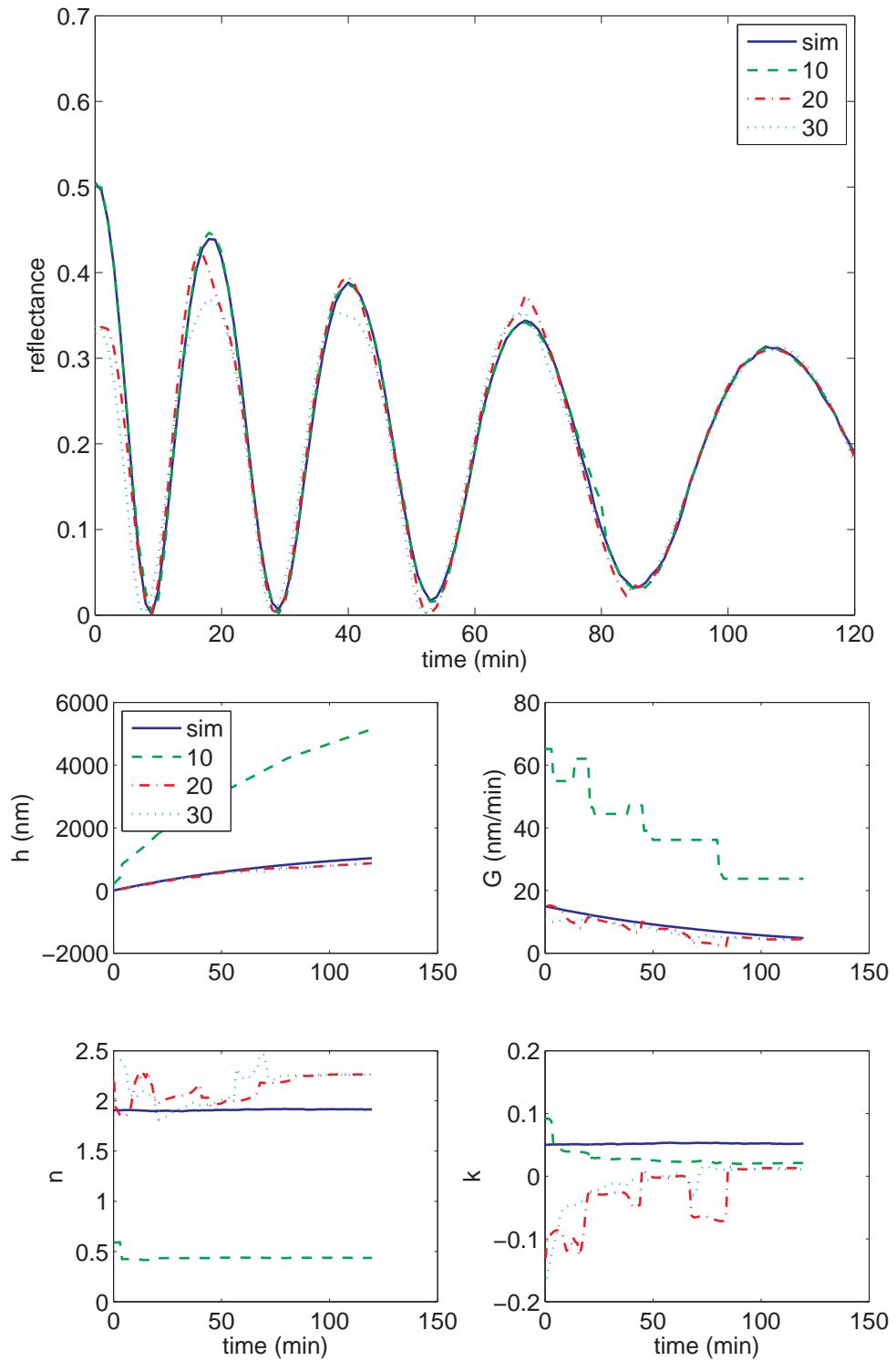


Figure 72: Estimation result by RLS from the reflectance measurement in Fig. 71. The initial guess is 10% offset from the true initial state. (top) fitted output (bottom) true and estimated states.

Table 5: Average estimation error by RLS and mMHE with different horizon size. Sensor model mismatch

	N	10	20	30	40
Single Smooth	RLS	63.7467	18.6942	15.7699	12.6263
	mMHE	14.3809	13.5225	12.5319	12.2089
Dual Smooth	RLS	23.6251	15.8848	13.3726	12.3946
	mMHE	14.9746	14.7775	13.4799	N/A

expressed by $x_1 = x_i \times \text{normrnd}(\text{ones}(4, 1), 0.1)$. In this simulation, we choose $R = 10^{-3}$ to represent the large uncertainty of the sensor model and 10^{-3} corresponds to an error in the second decimal place. Q and R are kept the same as in the previous study, i.e. $Q = \text{diag}([10^{-1}, 10^{-1}, 10^{-6}, 10^{-6}])$ and $P_{1|0} = \text{diag}(x_i) \times 10^{-2}$. With the chosen $P_{1|0}$, R and Q , we tested four different horizon sizes, 10, 20, 30 and 40 and for each horizon size, we tested five random initial guesses and calculated the mean estimation error. The resulting estimation errors are summarized in Table 5 (row of Single Smooth). Figure 73 shows a typical estimation result at $N = 10, 20$ and 30 . As shown, mMHE did not yield significant improvement over RLS except at $N = 10$ because the *a priori* estimate prevents the optimal solution to be far from the initial guess. This is confirmed by the poor fit of the reflectance at the early part of the curve. Figure 74 shows the evolution of variance of each state after the measurement update in mMHE when $N = 20$. Compared to Fig. 55, the variance of all states become larger by two orders of magnitude indicating much less confidence on the estimated states.

5.2.2 Dual-wavelength reflection on smooth surface

From the above simulation, we can see that if there is a sensor model mismatch, either RLS and mMHE will give good estimate, although mMHE performs significantly better than RLS for short horizon. We have shown in Chapter 3 that the EMA model is accurate at shorter wavelength like 470 nm. Therefore in the last simulation

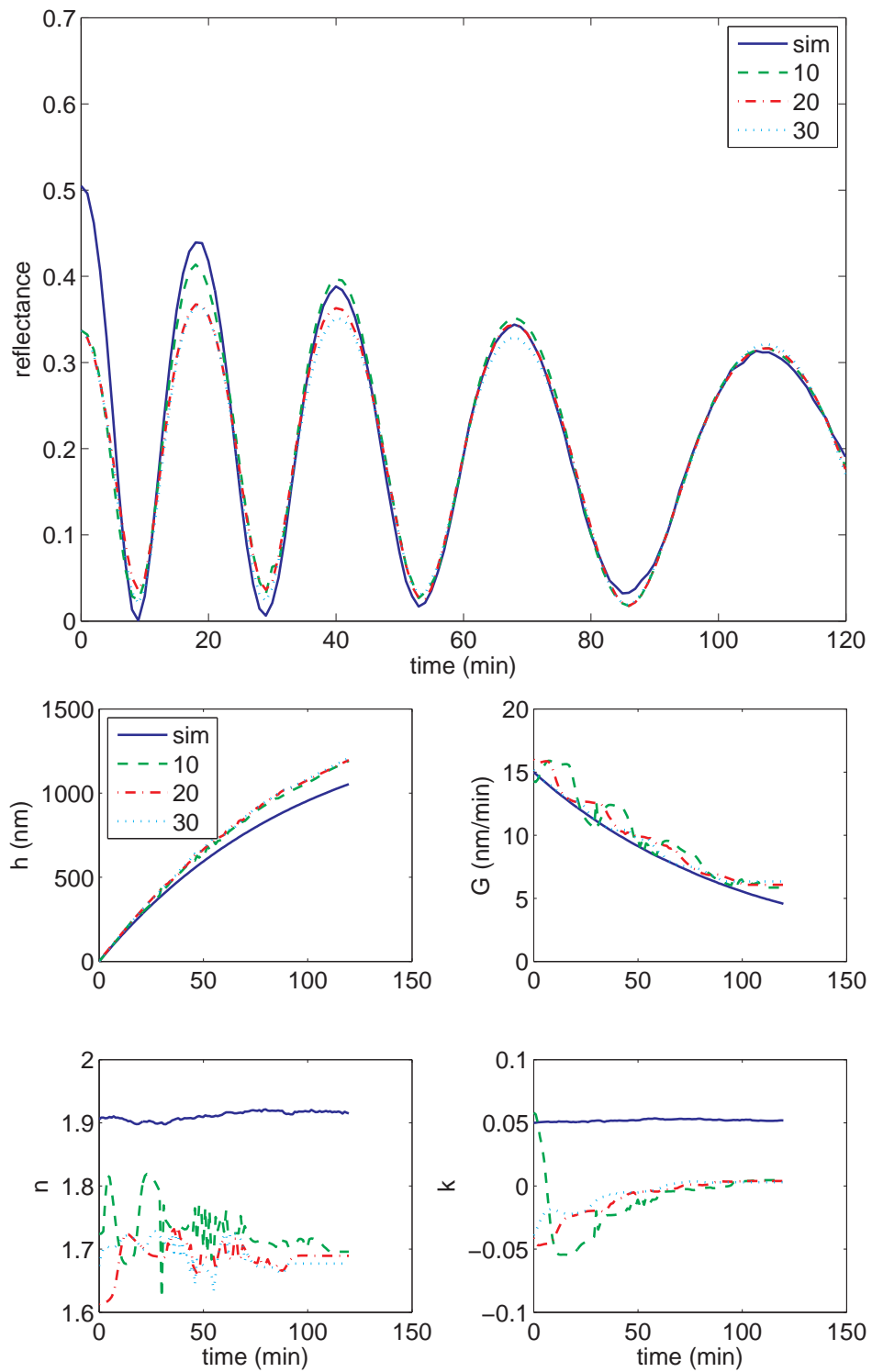


Figure 73: Estimation result by mMHE from the reflectance measurement in Fig. 71. The initial guess is 10% offset from the true initial state. (top) fitted output (bottom) true and estimated states.

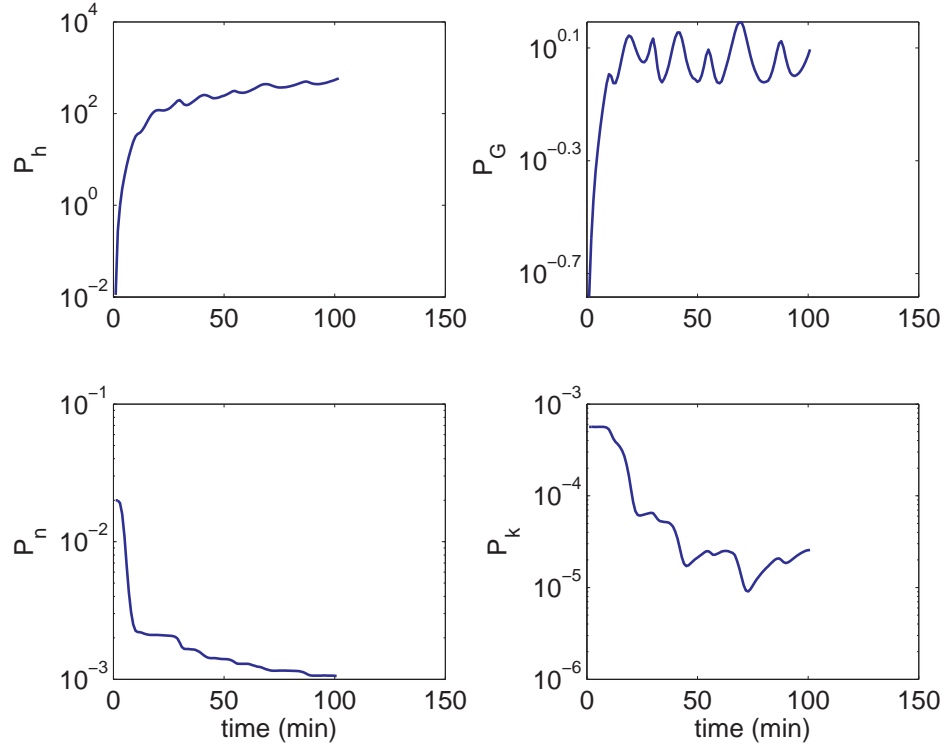


Figure 74: Variance of estimated states in Fig. 73 when $N = 20$.

study, we considered dual-wavelength reflection on a smooth surface, in which the reflectance at 950 nm is 1.5 times larger than that calculated by Eq. (5) while the reflectance at 470 nm is accurately calculated by Eq. (5). The simulated measurement and states are shown in Fig. 75. Notice that 950 nm reflectance is even larger than 470 nm in the beginning due to the amplification of 1.5.

We first use RLS to estimate the states from the simulated reflectance measurement. The process dynamic model and the sensor model are the same as in previous section of dual-wavelength reflection on smooth surface. The initial guess is expressed by $x_1 = x_i \times \text{normrnd}(\text{ones}(6, 1), 0.1)$. We tested four different horizon sizes, 10, 20, 30 and 40 and for each horizon size, we tested five random initial guesses and calculated the mean estimation error. The resulting estimation errors are summarized in Table 5 (row of Dual Smooth). Figure 76 shows a typical estimation result at $N = 10$, 20 and 30. As shown, by including the reflectance at 470 nm, improved estimates are

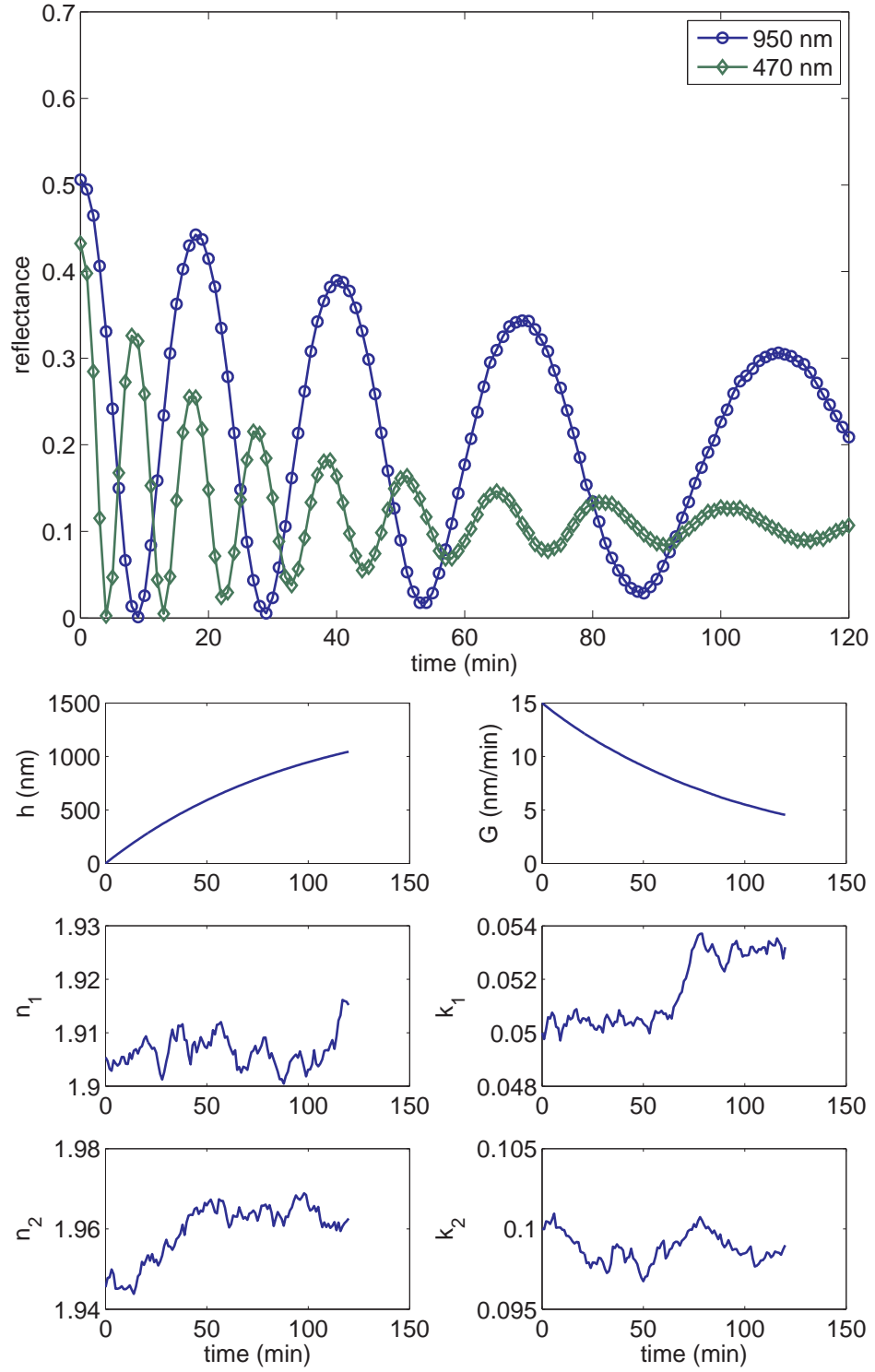


Figure 75: Simulated film growth process with decreasing growth rate. 950 nm reflectance is 1.5 times of that calculated from Eq. (5) and 470 nm reflectance is calculated from Eq. (5) (top) reflectance at 950 nm and 470 nm (bottom) states.

obtained even at $N = 10$.

Next we use mMHE to estimate the states from the same reflectance. The process dynamic model and the sensor model are the same as RLS. The initial guess is also expressed by $x_1 = x_i \times \text{normrnd}(\text{ones}(6, 1), 0.1)$. In this simulation, we choose $R = \text{diag}([10^{-3}, 10^{-6}])$ with the first element of 10^{-3} representing the large uncertainty at 950 nm and the second element of 10^{-6} representing more confidence on 470 nm. Q and R are kept the same as in the previous study, i.e. $Q = \text{diag}([10^{-1}, 10^{-1}, 10^{-6}, 10^{-6}, 10^{-6}, 10^{-6}])$ and $P_{1|0} = \text{diag}(x_i) \times 10^{-2}$. With the chosen $P_{1|0}$, R and Q , we tested four different horizon sizes, 10, 20, 30, 40 and for each horizon size, we tested five random initial guesses and calculated the mean estimation error. The resulting estimation errors are summarized in Table 5 (row of Dual Smooth). Figure 77 shows a typical estimation result at $N = 10, 20$ and 30. As shown, mMHE had slightly improvement on the estimate at $N = 10$. At other horizon sizes, there is no significant improvement. Figure 78 shows the evolution of variance of each state after the measurement update in mMHE when $N = 20$. Again, compared to Fig. 74, the variance of all states become smaller due to the additional measurement at 470 nm, which indicates improved confidence on the estimated states.

From the above simulations, we learned that when there is a sensor model mismatch, either state estimator will give good result. However, relatively speaking, mMHE is still a better state estimator in that it utilizes the information from both process dynamic model and sensor model. In the limiting case, if we know the process dynamic model perfectly, we can ignore the measurement and predict states solely based on the process model. This can be done by simply making R infinitely large. The nice thing about mMHE is that it provided a general framework for least-squares-based estimation. Plus it explicitly considers the uncertainty and correlation between the estimated states. In all cases, mMHE works at least as well as RLS and in many

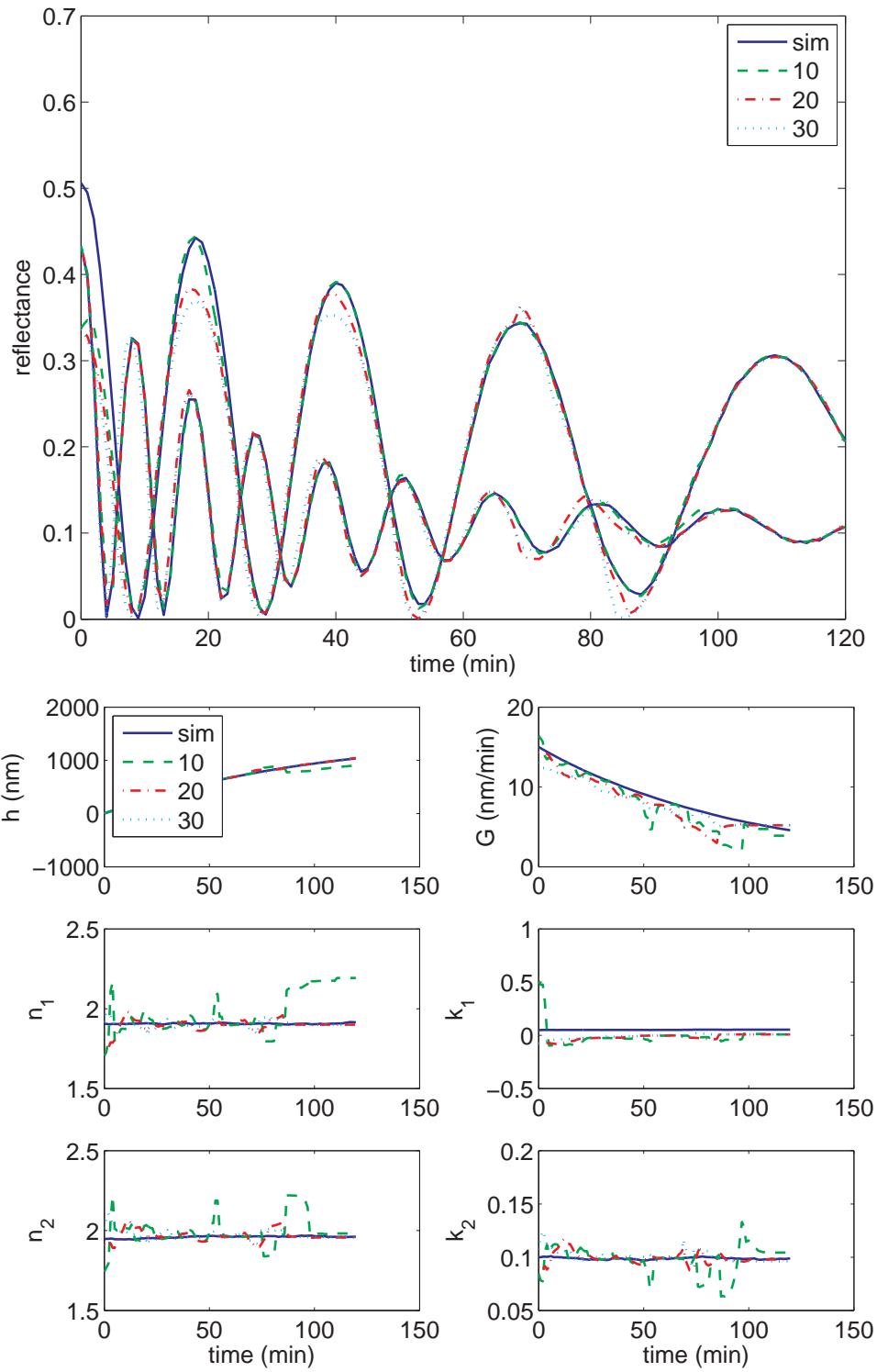


Figure 76: Estimation result by RLS from the reflectance measurement in Fig. 75. The initial guess is 10% offset from the true initial state. (top) fitted output (bottom) true and estimated states.

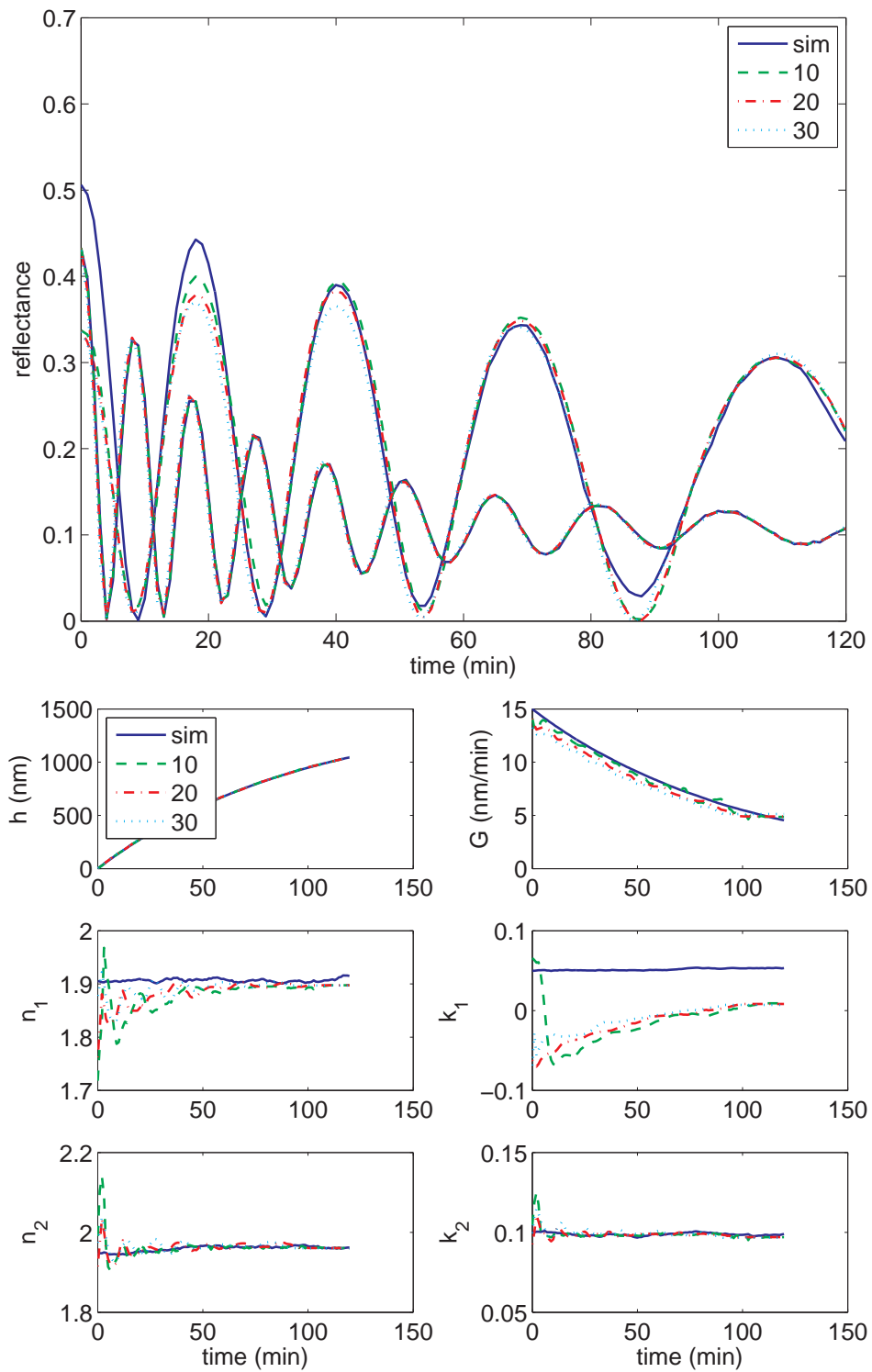


Figure 77: Estimation result by mMHE from the reflectance measurement in Fig. 75. The initial guess is 10% offset from the true initial state. (top) fitted output (bottom) true and estimated states.

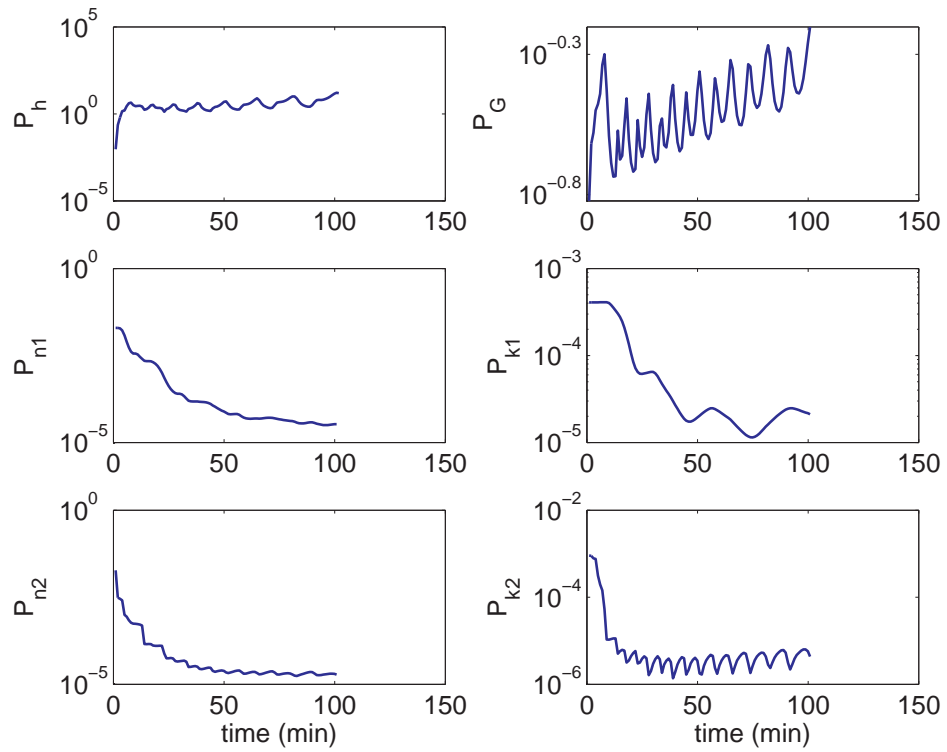


Figure 78: Variance of estimated states in Fig. 77 when $N = 20$.

cases, especially for shorter horizon, it provides significant improvements. It requires no more computation than RLS and it is more robust to change in horizon size. It does require designing reasonable weighting matrices, which requires some understanding of the uncertainties in the process and sensor model.

CHAPTER VI

EXPERIMENTAL

In this chapter, we compare the performance of the state estimators discussed in Chapter 4 using experimental reflectance data. The experimental data is different from the simulation data in that it is less ideal and has uncontrolled uncertainties. Therefore in the first section, we briefly discuss the acquisition of experimental reflectance data and some of the nonidealities. Then we choose one experimental data set as a benchmark to compare the state estimators. For this data set, we consider two sensor models. One is dual-wavelength reflection on a smooth surface and the other one is dual-wavelength reflection on a rough surface. The estimated film properties are compared with *ex situ* film characterization results. Finally we show some additional data sets obtained under different deposition conditions to study the robustness of the state estimators.

6.1 Practical issues in the experimental data

The *in situ* sensor in our CVD testbed is an emissivity-correcting pyrometer (ECP) [SVT Associates. Model: In-Situ 4000]. The ECP measures thermal radiation intensity at 950 and 850 nm and normal reflected light intensity at 950 and 470 nm. The bandwidths of both thermal radiation and reflection channels are around 15 nm. In this project, we only consider the reflectance measurement. The reflectometer measures reflected light intensity in millivolts using a photodiode and this raw data must be calibrated to obtain reflectance. The calibration is done by using a zero reflectance (low point) and the known reflectance of the silicon substrate (high point). The zero reflectance can be obtained when the heater assembly is removed from the chamber so that there is no object in the chamber to reflect light back. This case represents

a baseline measurement in which stray light is accounted for. The reflectance of the silicon substrate is used as the calibration high point and can be calculated from the complex refractive index of silicon by

$$R = \left(\frac{n_s - 1}{n_s + 1} \right)^2 \quad (33)$$

where n_s is the complex refractive index of silicon [18]. The calculated room temperature reflectance of silicon at 950 nm and 470 nm are 0.326 and 0.419, respectively. The calibration established a linear relationship between the raw intensity data and the reflectance. The slope of the calibration line contains the information about the relative geometric position between the substrate and the reflectometer. However, we have found that during heating up the silicon substrate, the substrate experienced thermal deformation due to temperature nonuniformity across the heater surface and this caused the geometric position to change. Therefore in practice, we do not use room temperature reflectance of silicon to calibration high point. Instead, we wait until the reflected light intensity stabilizes after reaching the desired deposition temperature and then calibrate the reflectance using the reflectance of silicon at that temperature. The deposition temperature is measured by the pyrometer channel of the ECP and the reflectance of silicon at high temperature can be calculated from Eq. (33) using the high temperature refractive index of silicon [66, 67, 140]. The calibration step could introduce error to the reflectance measurement because the surface temperature measured by ECP may not be accurate and thus the calculated high temperature reflectance of silicon may not be accurate. However, a simple calculation indicated that this error should not be significant. At a wavelength of 470 nm, the refractive index of silicon at 600 °C and 800 °C are 4.9206-0.1868j and 5.0742-0.2791j, respectively. Using Eq. (33), the reflectance of silicon at 600 °C and 800 °C are 0.4391 and 0.4511, respectively. This means that the temperature error of 200°C only caused an error of 2.7% in the reflectance. The error for 950 nm reflectance is even less because the refractive index of silicon at 950 nm is less sensitive to temperature and the

calculated error is about 2.1%.

The major nonideality in our experimental data is caused by film nonuniformity. Figure 79 shows the schematic of a typical nonuniform film deposited on our CVD testbed. As shown, the film appears to have three distinct zones. Zone 1 and 3 appear darker and zone 2 appears brighter with naked eyes, indicating different thickness. The average thickness measured by an ellipsometer in zone 1, 2 and 3 are 388.6 nm, 478.3 nm and 511.3 nm, respectively. As shown, the thickness in different zones are quite different. The film in zone 2 is averagely 89.7 nm thicker than that in zone 1, corresponding to a difference of 17.8%. On the other hand, the thickness in each zone appear to be quite uniform with variance less than 4%. There are two reasons for film nonuniformity. One is the temperature nonuniformity of the substrate and the other one is the nonuniformity of the mass transfer. Figure 79 shows that thickness isoline is close to a ring shape with the same center of the substrate. Considering the same shape of the thermal isolines in Fig. 9 by COMSOL simulation, it is reasonable to believe that the temperature nonuniformity caused different growth rate and thus different thickness on the substrate. The shifting of zone 1 toward right-hand side may have been due to the flow toward vacuum pump on the left-hand side. As shown in Fig. 5, the material inside the chamber has a tendency of moving toward the pump side and this may have caused more material to be deposited on the left-hand side. Therefore we believe that the substrate temperature nonuniformity is the major cause of film nonuniformity and gas flow contributes to the shifting of the nonuniformity pattern.

As we have discussed in Chapter 3, the film nonuniformity can affect the reflectance and make *in situ* sensor data interpretation difficult. Figure 80 shows an experimental reflectance curve of a nonuniform film (circles). The average thickness is measured *ex situ* by an ellipsometer and is around 270 nm. The growth time is 87.3 min and thus the average growth rate is around 3.1 nm/min. Using the average

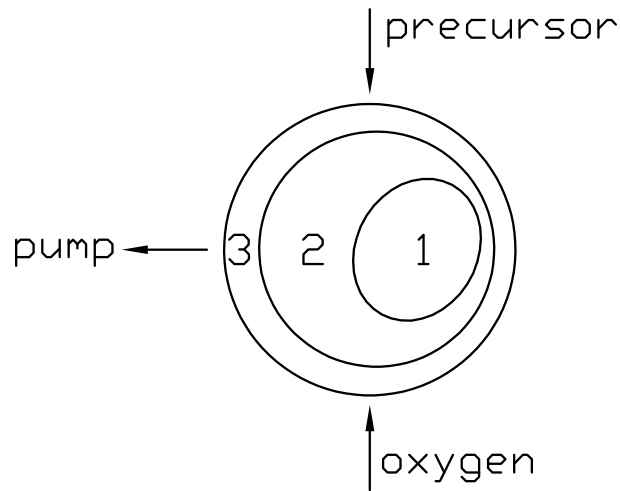


Figure 79: Schematic of different growth zones on a nonuniform film (Date acquired: 5/30/2006).

growth rate, we calculated temporal reflectance based on Eq. (5) and is shown as solid line in Fig. 80. As shown, the oscillation period of the calculated reflectance matches well with experimental data. However, the amplitude especially at the second trough has a large offset. If we use a mean growth rate of 3.1 nm/min with a variance of 13%, then the calculated temporal reflectance can match the experimental data quite well, as indicated by the dash line in Fig. 80. This simple example indicated the importance of film nonuniformity in the experimental data. That is why we have made significant efforts to improve film uniformity. These efforts include making a thermal diffuse plate and a sensor shutter, which have been discussed in details in Chapter 2.

The nonideality of experimental data also occurs at the early stage of the growth, in which there are only discrete islands formed on the substrate and these islands have not yet coalesced to form an optically smooth film. However, the sensor model in Chapter 3 all assume that optically smooth film is formed from the very beginning of the growth. Therefore there may be some problems when interpreting the sensor data at early stages of growth. Other causes of the nonideality of the experimental

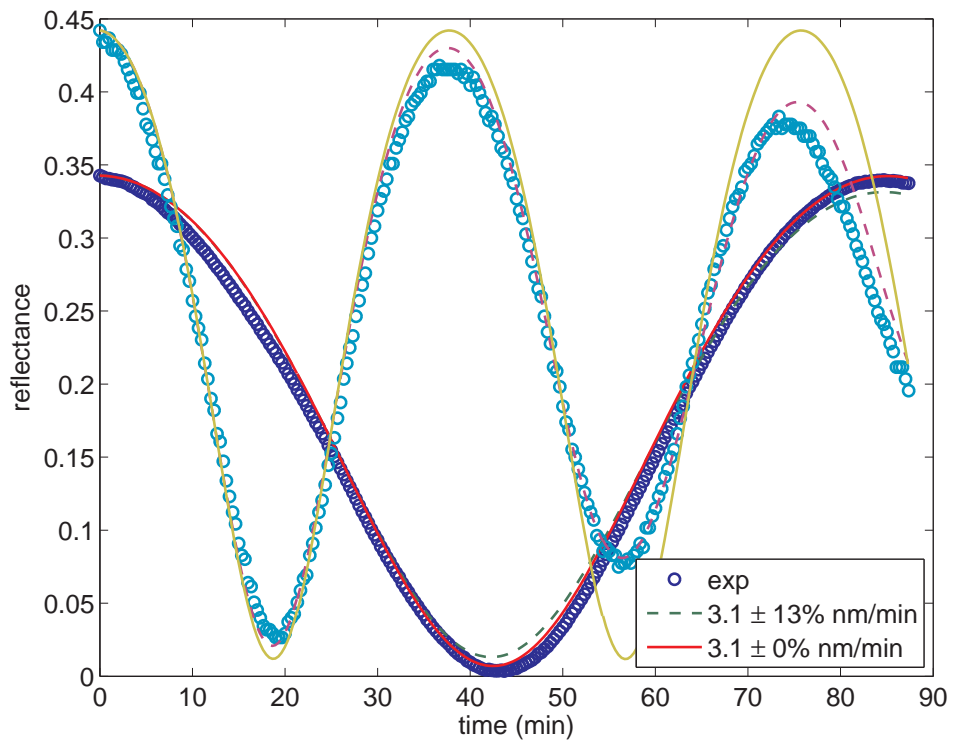


Figure 80: Experimental reflectance curve of a nonuniform film and fitting result with and without assumption of film nonuniformity (Date acquired: 4/26/2007).

Table 6: Experimental conditions. Ar2 is main carrier argon, Ar3 is precursor carrier argon, Ar5 is dummy argon. See Fig. 1 for details.

Date	10/1/2007	10/3/2007
Pressure (torr)	2	2
O ₂ flow rate (sccm)	50	50
Ar2 flow rate (sccm)	20	20
Ar3 flow rate (sccm)	120	120
Ar5 flow rate (sccm)	140	140
Voltage (V)	18	20
Current (A)	8.1	8.7
Evaporator temp (°C)	175	177

data include the bandwidth of the sensor, non-normal incidence and possible wobbling of the substrate during the growth. With these nonidealities in mind, we now consider a specific experimental data set and use state estimators to interpret the sensor data.

6.2 *Dual-wavelength reflection on smooth surface*

Figure 81 shows an experimental reflectance curve at 950 nm and 470 nm. The sampling interval is 20 seconds and total deposition time is 73 minutes. The deposition conditions are summarized in Table 6 (column of 10/1/2007). An Inconel thermal diffuse plate was used to improve temperature uniformity. The reflectance was calibrated using the reflectance of silicon at 650 °C. This temperature was measured by the pyrometer channel of the ECP. The refractive indices of silicon at 650 °C are 3.8231-0.0379j for 950 nm and 4.9590-0.2065j for 470 nm, respectively [66, 67, 140]. Using Eq. (33), the reflectance of silicon at 650 °C is calculated to be 0.3427 at 950 nm and 0.4421 at 470 nm, respectively. Notice that the first trough of the 470 nm reflectance curve did not go to zero, which indicates either absorption or partially destructive interference. This may have been partly due to the calibration error and should be further investigated.

Following the same logic as in the simulation study in Chapter 5, we first use

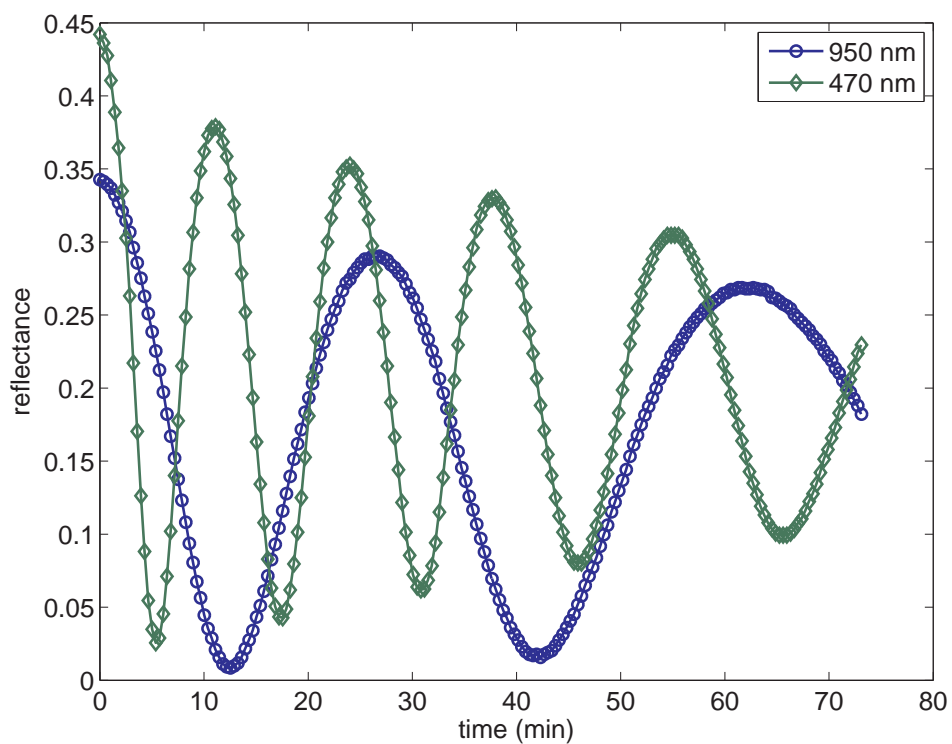


Figure 81: Experimental reflectance at 950 nm and 470 nm (Date acquired: 10/1/2007).

BLS to estimate the states from the experimental reflectance measurement. The process dynamic model used in BLS assumes constant growth rate and is expressed by Eq. (30). The sensor model is based on dual-wavelength reflection on a smooth surface, as discussed in Chapter 5. The initial guess is $x_1 = [0, 8, 1.9054, 0.05, 1.9455, 0.1]^T$. The initial guess of growth rate 8 nm/min is obtained from a calibration run. The initial guess of the refractive index and extinction coefficient of the film are the same as in the simulation study in Chapter 5. Figure 82 shows the estimated states and fitted measurement. As shown, the fitted reflectance curve does not match all the peaks in the experimental curve. This is because the fitting algorithm tries to fit a constant growth rate while the true growth rate is slowly decreasing, as indicated by the gradually increasing oscillation period. Notice that the amplitude of the fitted reflectance at 470 nm decreases much faster than that of the experimental data. This seems have caused large error between the fitted estimates and the experimental data. We decreased the initial guess of extinction coefficient at 470 nm from 0.1 to 0.05 but the fitting algorithm converged to the same solution.

Next we use RLS to estimate the states from the same experimental reflectance. The process dynamic model, the sensor model and the initial guess are the same as in BLS. We have found that for the experimental data, some states like the extinction coefficient have frequently been estimated to be negative, which is not physically possible. Therefore in the experimental study, we apply positive constraints on all states when solving the optimization problem. We have tested three different horizon sizes, 10, 20 and 30 and the estimation results are shown in Fig. 83. The estimated states at the end of the growth are summarized in Table 7. Compared to BLS, the fitted reflectance curve matches all the peaks in the experimental curve. The growth rate is estimated to decrease at all horizons. However, the estimated states at the shortest horizon are more oscillatory than at the longer horizons. This is consistent with what we have observed in the simulation study (in the case of sensor model

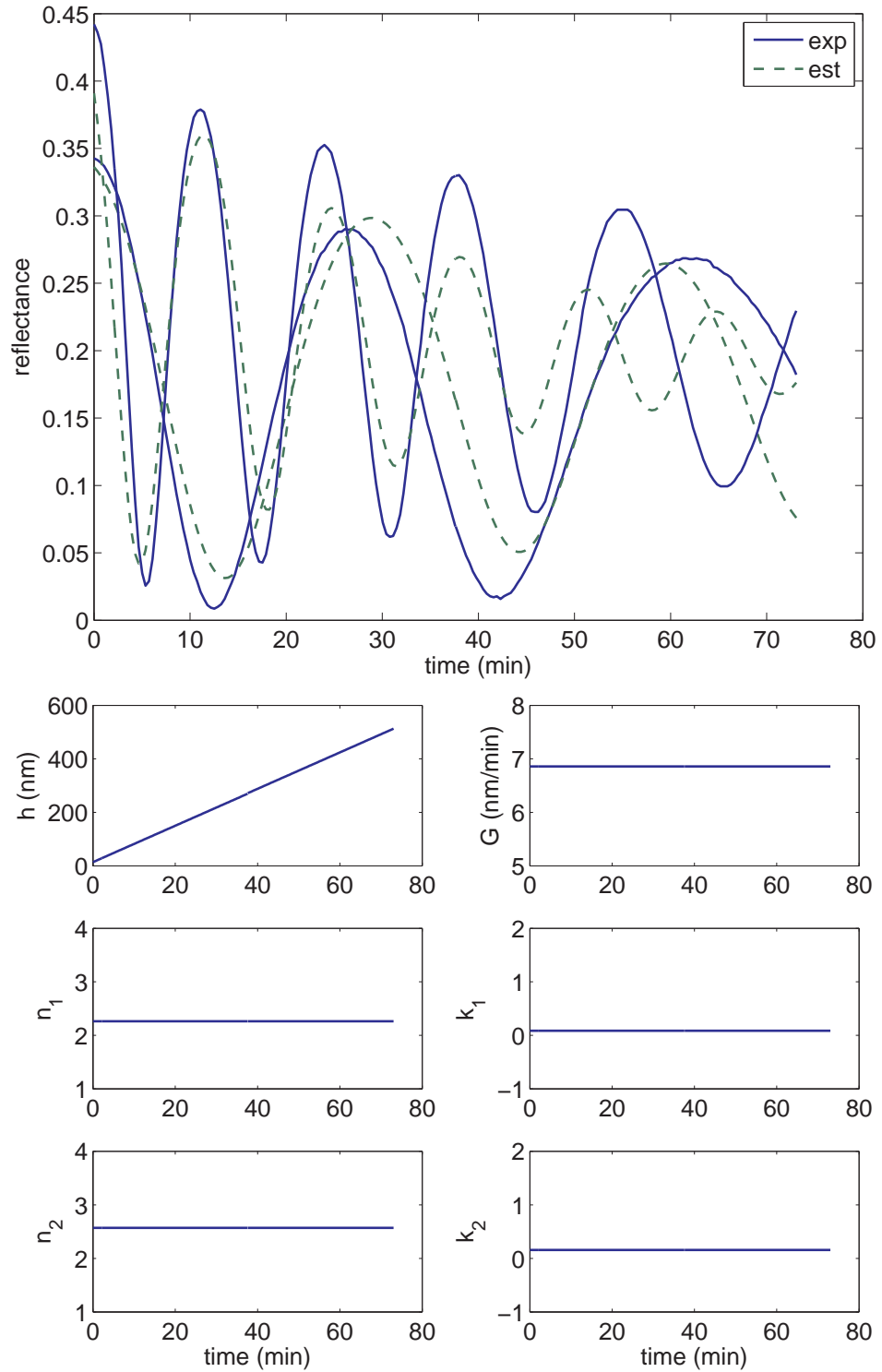


Figure 82: Estimation result by BLS from reflectance measurement in Fig. 81. The sensor model is based on dual-wavelength reflection on a smooth surface. (top) fitted reflectance at 950 nm and 470 nm (bottom) estimated states.

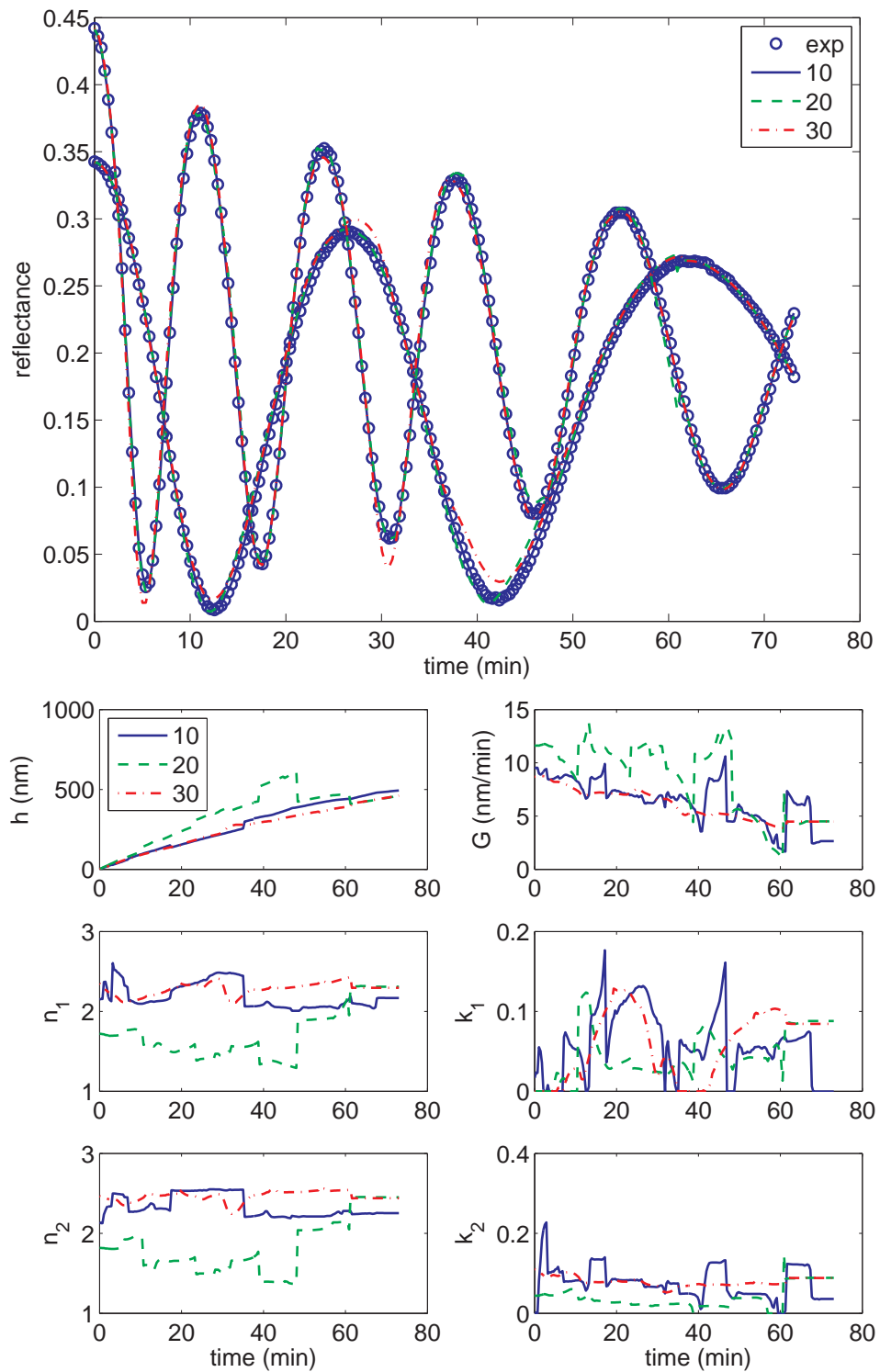


Figure 83: Estimation result by RLS from the reflectance measurement in Fig. 81. The sensor model is based on dual-wavelength reflection on a smooth surface. (top) fitted output (bottom) true and estimated states.

Table 7: Estimated states at the end of the growth and *ex situ* ellipsometry characterization. The sensor model is based on dual-wavelength reflection on a smooth surface. This film was deposited on 10/1/2007.

	RLS			mMHE			EKF	<i>ex situ</i> ellipsometry
	10	20	30	10	20	30		
h (nm)	498.6	464.2	466.2	567.2	562.9	564.4	559.2	540.1
n_1	2.1659	2.3103	2.2997	1.8716	1.8846	1.8814	1.8940	1.8315
k_1	0	0.0879	0.0846	0.0429	0.0449	0.0444	0.0462	0.0012
n_2	2.2541	2.4521	2.4424	2.0125	2.0354	2.0241	2.0355	1.8828
k_2	0.0355	0.0888	0.0885	0.0342	0.0449	0.0406	0.0704	0.0092

mismatch). Because of the positive constraints, k_1 and k_2 constantly bounce between zero and some positive value.

Next we use mMHE to estimate the states from the same experimental reflectance. The process dynamic model, the sensor model and the initial guess are the same as in RLS. The only difference is that mMHE requires three additional tuning matrices. For this particular data set, we choose $R = \text{diag}([10^{-4}, 10^{-3}])$ with the first element being smaller to represent more confidence on 950 nm reflectance because the reflectometer has stronger signal level on 950 nm channel. Furthermore, the film appears smoother at longer wavelength so the sensor model based on reflection on a smooth surface is more accurate. We use 10^{-4} to indicate a larger uncertainty in the sensor model because we know the sensor model is not perfect, as in the case of sensor model mismatch in Chapter 5. 10^{-4} corresponds to an error in the second decimal place. We choose $Q = \text{diag}([10^{-6}, 10^{-6}, 10^{-6}, 10^{-6}, 10^{-6}, 10^{-6}])$. The last four elements are the same as in the simulation study because we know that the refractive index and the extinction coefficient of the film will not change a lot. The first and second element are much smaller than 10^{-1} which is used in the simulation study. In the simulation study, the sampling interval and horizon size are in units of minutes and the growth rate has a unit of nm/min. But in the experimental system, the sampling interval and horizon size are in the unit of second and the growth rate is converted

to nm/sec in mMHE. Because the growth rate in experimental is smaller than that in simulation by two orders of magnitude, we need to decrease the variance as well. We choose $P_{1|0} = \text{diag}(x_1) \times 10^{-6}$ to indicate more confidence on the initial guess. It has been shown that with a calibration run, one could obtain a quite accurate initial guess [20]. With the chosen $P_{1|0}$, R and Q , We tested three different horizon sizes, 10, 20 and 30 and the estimation results are shown in Fig. 84. The estimated states at the end of the growth are summarized in Table 7. As shown, the estimation results are not as sensitive to horizon size as RLS does and this is consistent with what we have observed in the simulation study. The estimated states are much less oscillatory than RLS due to the *a priori* estimate. The positive constraint is not necessary in mMHE because the *a priori* estimate limits the search space for the optimal solution. Compared to the estimation result by BLS, we notice that k_2 is estimated to decrease so that the peak of 470 nm reflectance can be now matched. As expected, the 950 nm reflectance is better fitted than 470 nm reflectance. Notice that there is a large offset for the trough of 470 nm reflectance indicating that the sensor model cannot explain the rise of the trough. This could be due in part to the surface roughness and will be discussed in the next section. The variance of estimated states are shown in Fig. 85 and are in a reasonable range.

Finally we used EKF to estimate the states from the same reflectance. The process dynamic model, the sensor model and tuning matrices are the same as mMHE. Figure 87 shows the estimated states and variance. The estimated states at the end of the growth are summarized in Table 7. As shown, EKF also yielded acceptable results by using both the process dynamic model and the sensor model, although it is more oscillatory compared to mMHE.

The deposited film was characterized *ex situ* using an ellipsometer. The ellipsometer data can be fitted well with a three layer model of rough/Cauchy/Silicon. The fitted ellipsometry data are shown in Fig. 86 and the fitted result is summarized

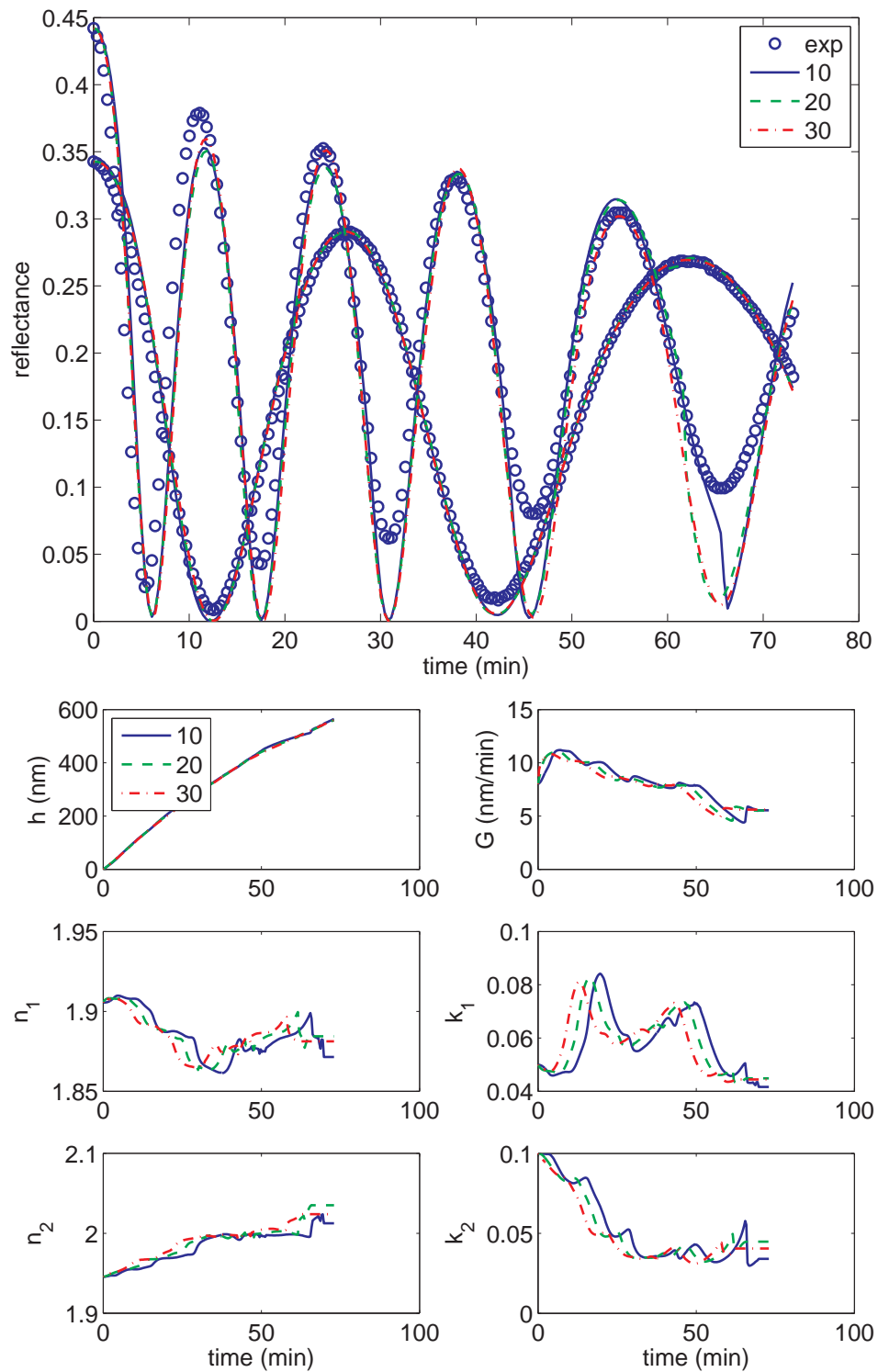


Figure 84: Estimation result by mMHE from the reflectance measurement in Fig. 81. The sensor model is based on dual-wavelength reflection on a smooth surface. (top) fitted output (bottom) true and estimated states.

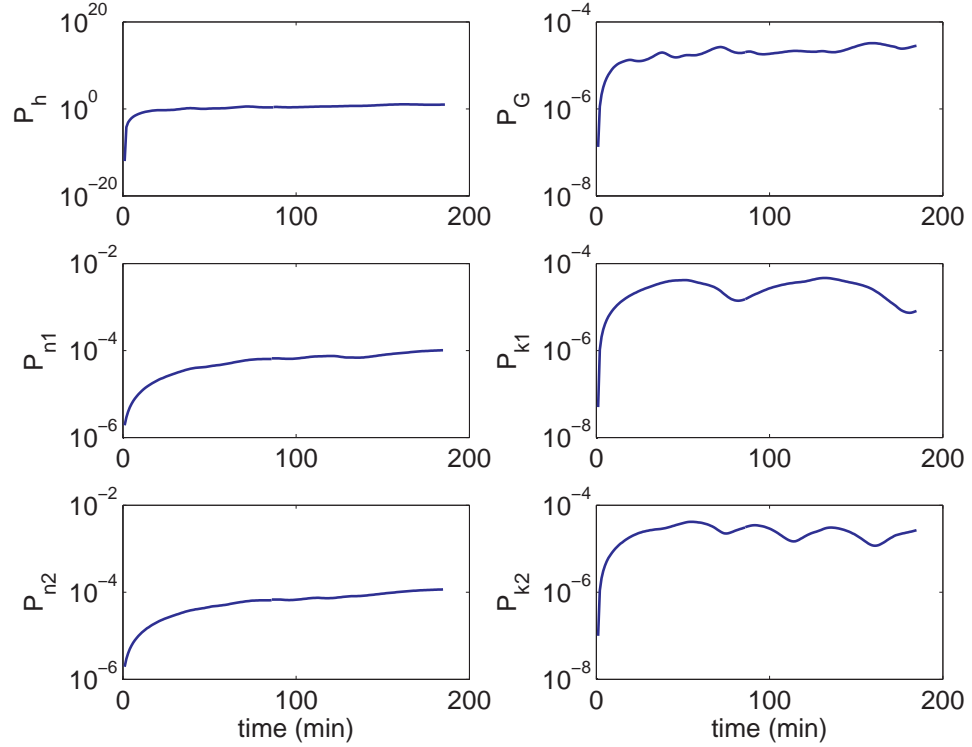


Figure 85: Variance of estimated states in Fig. 84 when $N = 20$.

in Table 7. The thickness reported by ellipsometer is equal to the thickness of the Cauchy layer plus half of the rough layer thickness. As shown, the estimated thickness by RLS are all smaller than *ex situ* characterization and accordingly the refractive indices are estimated larger. The estimated thickness and refractive indices by mMHE and EKF are more reasonable. This suggested that by using both process dynamic model and the sensor model, mMHE and EKF successfully decoupled thickness and refractive index which are highly correlated in the sensor model. The estimated refractive indices in mMHE and EKF are larger than *ex situ* measurements. This is expected because the *ex situ* characterization is done at room temperature but the estimation is done using high temperature reflectance measurements. It has been observed that the refractive index of yttria increases with temperature and at 632.8 nm, the temperature coefficient is $dn/dT = 8.1 \times 10^{-6}$ [106, 107, 145]. Therefore at the deposition temperature of 650 °C, $dn = 8.1 \times 10^{-6} \times (650 - 25) = 0.005$. Considering

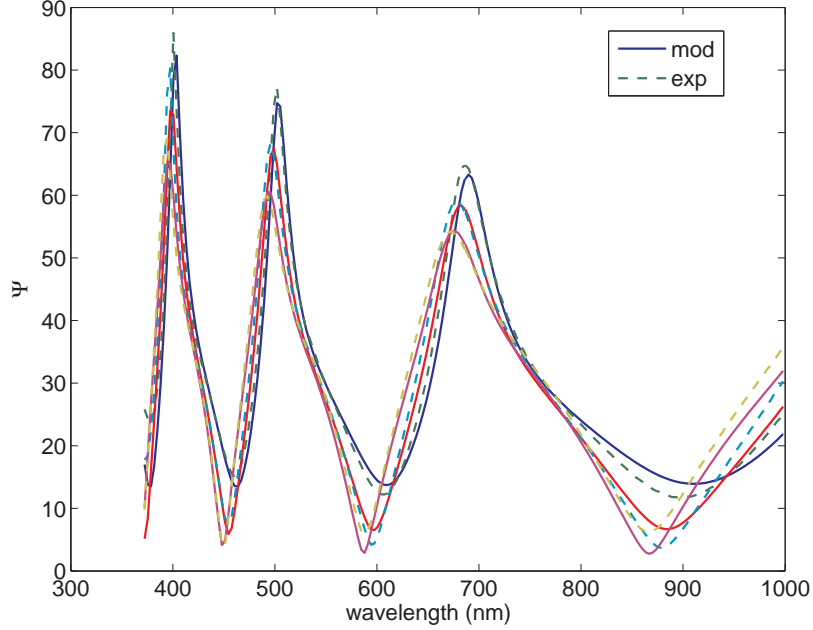


Figure 86: Ellipsometer data and fit of yttria film deposited on 10/1/2007.

that the refractive index of yttria at 632.8 nm is 1.9291, this is about 0.26% increase. In Table 7, however, the estimated refractive index by mMHE at $N = 10$ are 2.2% larger for 950 nm and 0.69% larger for 470 nm. Considering the large discrepancy, it may be arguable that this is solely caused by temperature difference. However, considering the uncertainties involved in both estimation and *ex situ* characterization, we think the slightly higher refractive index estimated by mMHE and EKF are acceptable. Comparing the data in Table 7, it is clear that mMHE consistently yielded better estimation results. Figure 84 shows there is still quite large oscillation in n and k indicating partial correlation. We think with more measurements like spectral reflectance, further improvement can be achieved.

6.3 Dual-wavelength reflection on rough surface

Figure 84 shows that there is a large mismatch at the troughs of 470 nm reflectance. This suggested that the sensor model of reflection on smooth surface cannot describe the measurement data. This may be due to the effect of surface roughness,

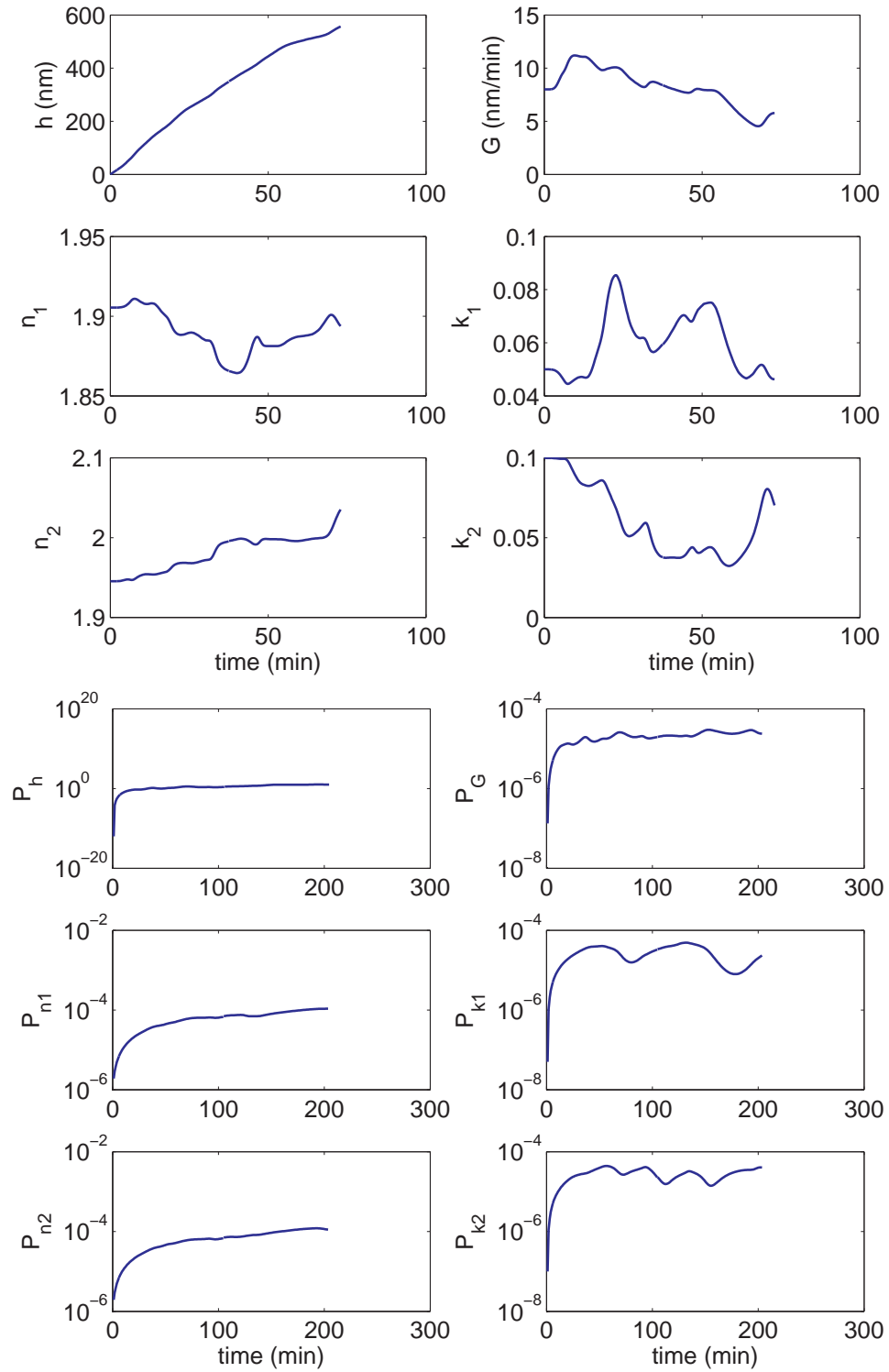


Figure 87: Estimation result by EKF from the reflectance measurement in Fig. 81. The sensor model is based on dual-wavelength reflection on a smooth surface. (top) true and estimated states (bottom) variance of estimated states.

as suggested by Fig. 47 in Chapter 3. In fact, the *ex situ* ellipsometer and AFM characterization also suggested that the surface is rough. We now consider the sensor model of dual-wavelength reflection on a rough surface using the EMA model and attempt to estimate roughness in addition to the other states.

We first use RLS to estimate the states from the experimental reflectance in Fig. 81. The process model is shown in Eq. (32), which assumes constant film growth rate and constant roughness layer growth rate. The sensor model is based on dual-wavelength reflection on a rough surface, as discussed in Chapter 5. The initial guess is $x_1 = [0, 8, 0, 1, 1.9054, 0.05, 1.9455, 0.1]^T$. The additional two states (the second and the third element) are the thickness and growth rate of the roughness layer. Again, all states are constrained to be positive. We have tested three different horizon sizes, 10, 20 and 30 and the estimation results are shown in Fig. 88. The estimated states at the end of the growth are summarized in Table 8. As shown, by including two additional states, the estimation results by RLS become significantly worse. This is the same as what we observed in the simulation study, because adding states created additional coupling and correlation between states. Without additional constraints, the fitting algorithm tends to overfit especially at shorter horizon, as shown by the excellent agreement between the estimated and measured reflectance in Fig. 88. When horizon size increases to 30, there are enough data for the fitting algorithm to converge to a more reasonable solution.

Next we use mMHE to estimate the states from the same experimental reflectance. The process dynamic model, the sensor model and the initial guess are the same as in RLS. For the tuning matrices, we keep R and $P_{1|0}$ the same as in the smooth case, i.e. $R = \text{diag}([10^{-4}, 10^{-3}])$ and $P_{1|0} = \text{diag}(x_1) \times 10^{-6}$. We choose $Q = \text{diag}([10^{-6}, 10^{-6}, 10^{-8}, 10^{-8}, 10^{-6}, 10^{-6}, 10^{-6}, 10^{-6}])$. Notice that the variance of the original six states are kept the same as in the smooth case. The only difference is the additional two elements, the second and the third, which represents the variance of

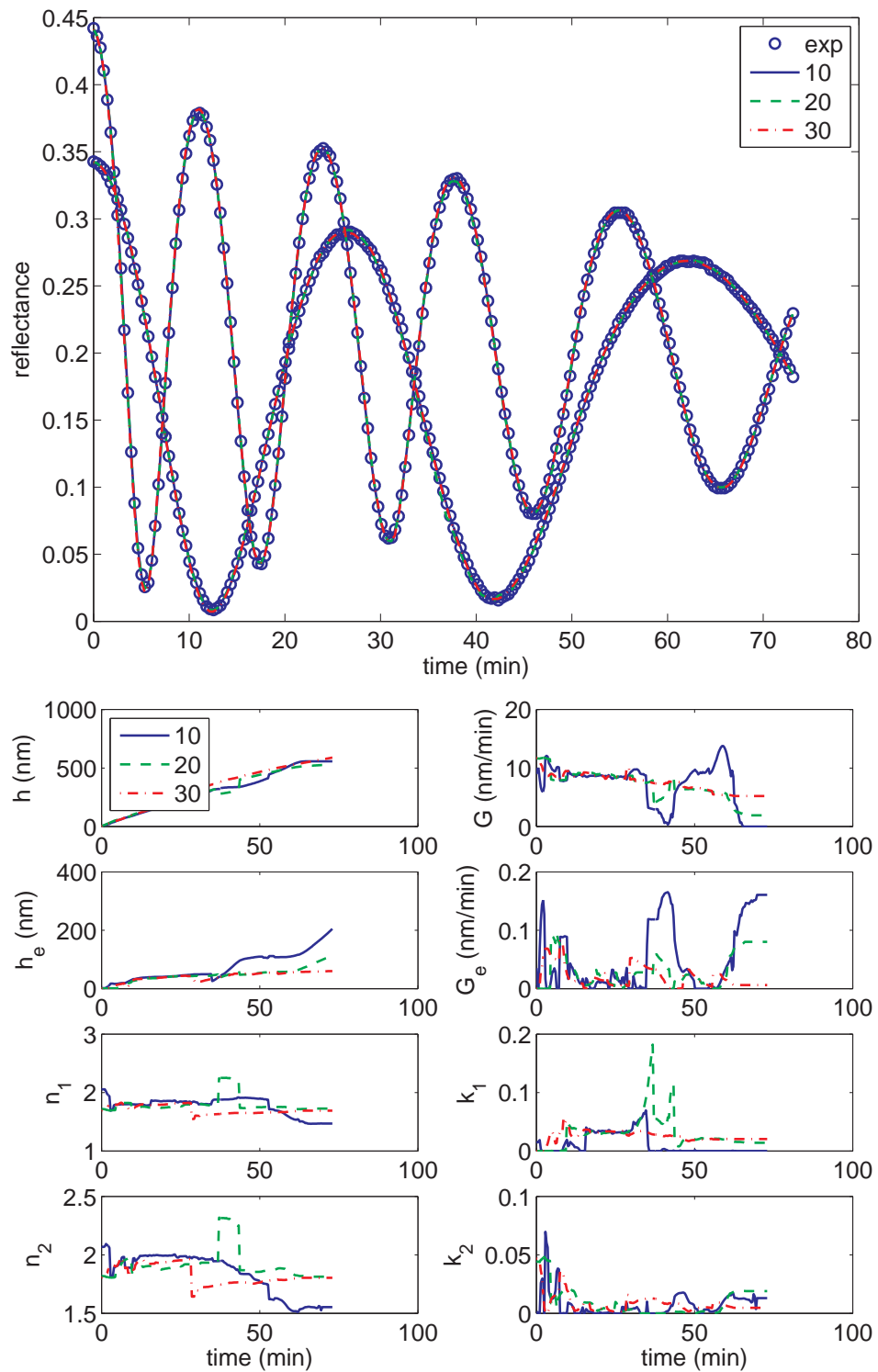


Figure 88: Estimation result by RLS from the reflectance measurement in Fig. 81. The sensor model is based on dual-wavelength reflection on a rough surface. (top) fitted output (bottom) true and estimated states.

Table 8: Estimated states at the end of the growth and *ex situ* ellipsometry characterization. The sensor model is based on dual-wavelength reflection on a rough surface. This film was deposited on 10/1/2007.

	RLS			mMHE			EKF	<i>ex situ</i> ellipsometry
	10	20	30	10	20	30		
h (nm)	562.2	537.9	596.4	540.3	536.8	536.2	534.1	510.0
h_e (nm)	206.2	116.2	61.8	73.4	71.7	71.6	73.5	60.4
n_1	1.4661	1.7261	1.6930	1.8479	1.8551	1.8562	1.8612	1.8315
k_1	0	0.0138	0.0204	0.0143	0.0187	0.0194	0.0158	0.0012
n_2	1.5513	1.8127	1.8062	1.9753	1.9847	1.9862	1.9847	1.8828
k_2	0.0130	0.0190	0.0046	0.0025	0.0018	0.0017	-0.0002	0.0092

h_e and G_e , respectively. The reason for choosing 10^{-8} is the same as in the simulation study, i.e. because h_e and G_e are smaller than h and G by one order of magnitude. With the chosen $P_{1|0}$, R and Q , we tested three different horizon sizes, 10, 20 and 30 and the estimation results are shown in Fig. 89. The estimated states at the end of the growth are summarized in Table 8. As shown, the troughs of 470 nm reflectance curve can now be fitted much better than with the smooth assumption in the sensor model. This suggests that by adding roughness, the sensor model can describe the measurement data well. The inclusion of roughness also helped to estimate other states more accurately. For example, the film thickness is estimated to decrease and accordingly the roughness layer thickness increases. The extinction coefficients are also estimated to be smaller and become closer to *ex situ* measured value, because the fitting algorithm can now use the roughness layer to account for the amplitude change instead of using a large extinction coefficient. This suggested that for this particular film, the roughness is the main factor that affects the reflectance amplitude, especially at 470 nm. The estimated refractive indices also decrease from those in Table 7. The offset from the *ex situ* room temperature refractive indices now become 0.89% for 950 nm and 0.49% for 470 nm, respectively. Considering the discrepancy of 0.26% caused by the temperature difference, we can now be more confident to claim that

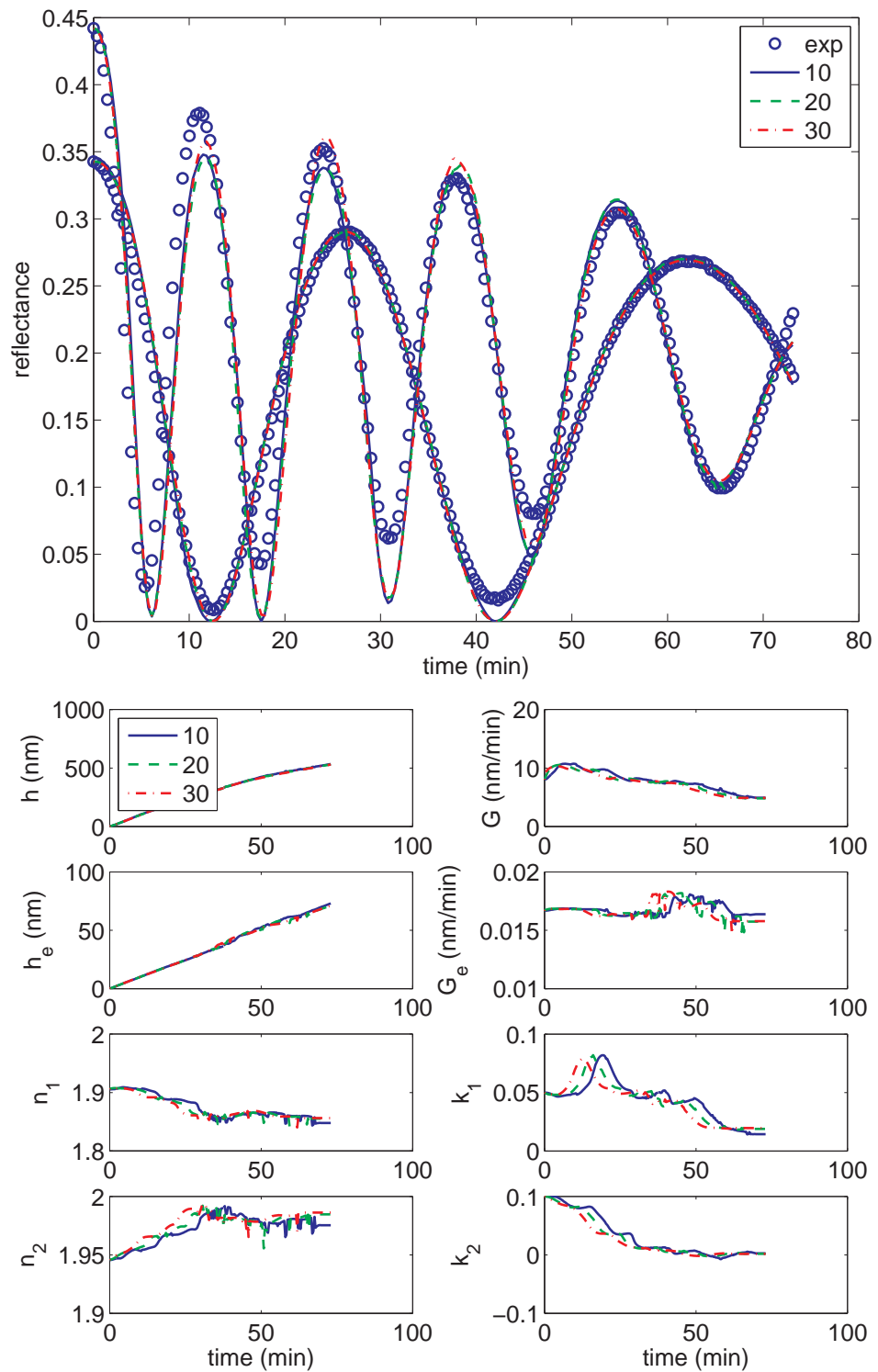


Figure 89: Estimation result by mMHE from the reflectance measurement in Fig. 81. The sensor model is based on dual-wavelength reflection on a rough surface. (top) fitted output (bottom) true and estimated states.

Table 9: Estimated states at end point by mMHE at $N = 10$ with different $P_{1|0}$, Q , and R

	h	h_e	n_1	k_1	n_2	k_2
mean	571.2	69.6	1.7791	0.0215	1.8952	0.0167
std	38.9	30.2	0.1654	0.0195	0.1894	0.0217
<i>ex situ</i>	510.4	60.4	1.8315	0.0012	1.8828	0.0092
RLS	562.2	206.2	1.4661	0	1.5513	0.0130

the slightly higher estimated refractive indices are in fact caused by a temperature difference. We tested the sensitivity of mMHE to tuning matrices $P_{1|0}$, Q , and R by scaling the matrices by 1/10 and 10. The estimated states for different tuning matrices are shown in Fig. 90. The mean of estimated states at end point and the standard deviation are shown in Table 9. Compared to the simulation study, mMHE appears more sensitive to tuning matrices. However, in all cases, the mean estimated states are reasonably close to *ex situ* characterization and are better than RLS at $N = 10$. In most cases, the estimated states have a correct trend. The standard deviation shows that extinction coefficient and effective layer thickness are the most sensitive to the tuning matrices.

We have also measured RMS roughness using AFM. Figure 91 shows the AFM images of the deposited film with a scan size of $5\mu\text{m} \times 5\mu\text{m}$. The RMS roughness is 26.1 nm. According to the linear relationship in Fig. 35, the EMA thickness of 60.4 nm corresponds to RMS roughness of 21.6 nm, which is quite close to 26.1 nm measured by AFM, considering the fluctuation in the data used to establish the linear fit. The variance of the estimated states are shown in Fig. 92 and are in a reasonable range. Compared to Fig. 85, there is no significant decrease in the estimated variances.

Finally we used EKF to estimate the states from the same reflectance. The process dynamic model, the sensor model and tuning matrices are the same as mMHE. Figure 93 shows estimated states and variance. The estimated states at the end of the growth are summarized in Table 8. As shown, EKF also yielded reasonable result by

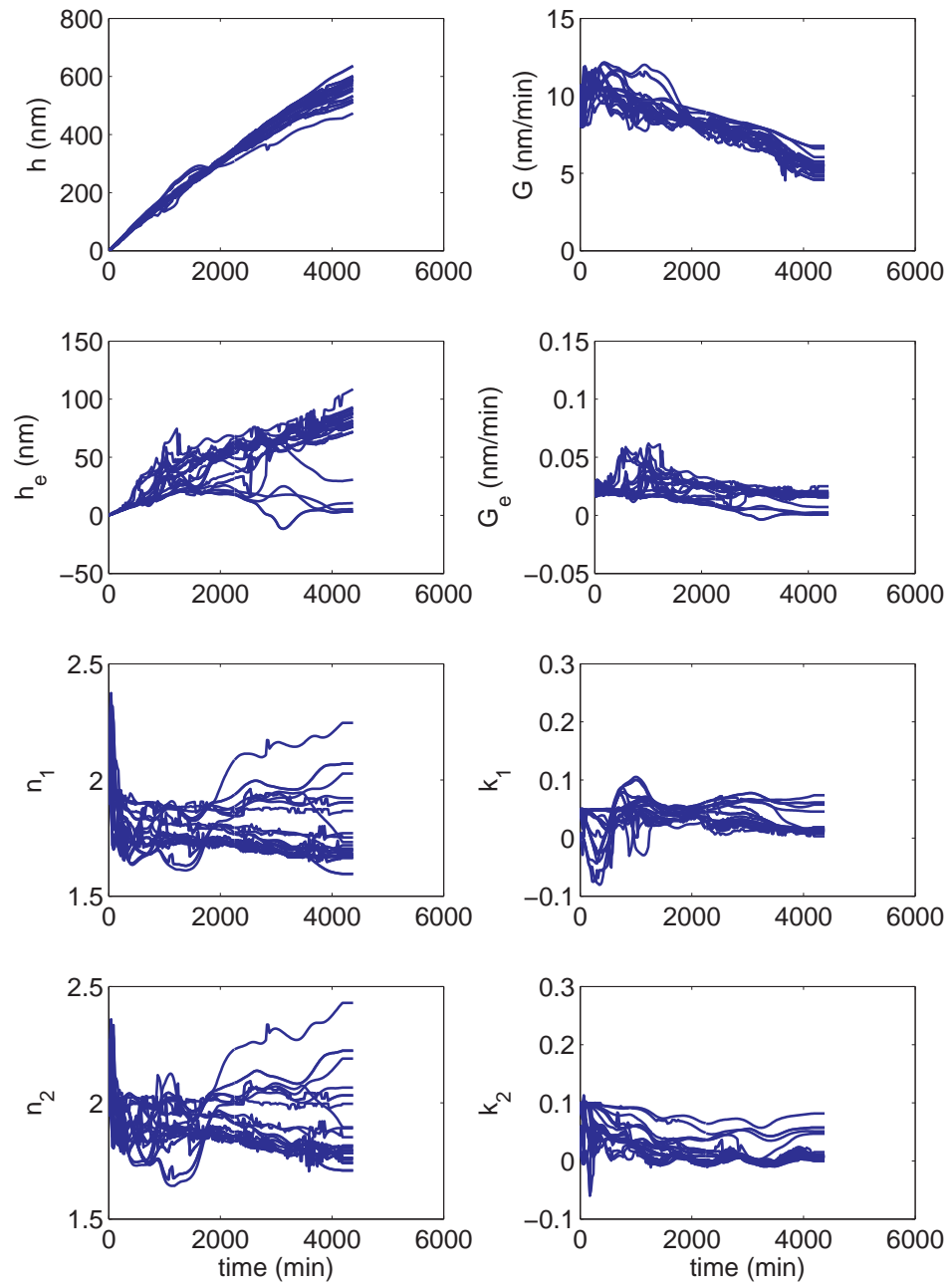


Figure 90: Estimated states by mMHE from the reflectance measurement in Fig. 81 with different tuning matrices. $N = 10$.

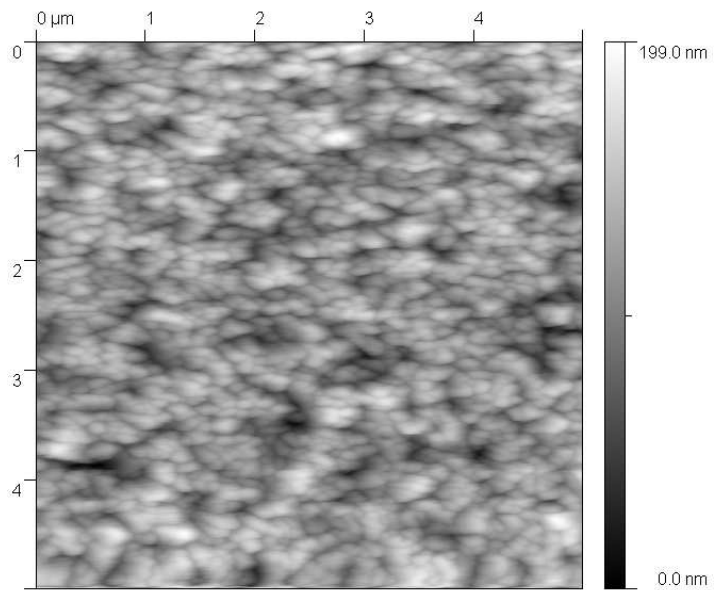


Figure 91: AFM image of yttria film deposited on 10/1/2007.

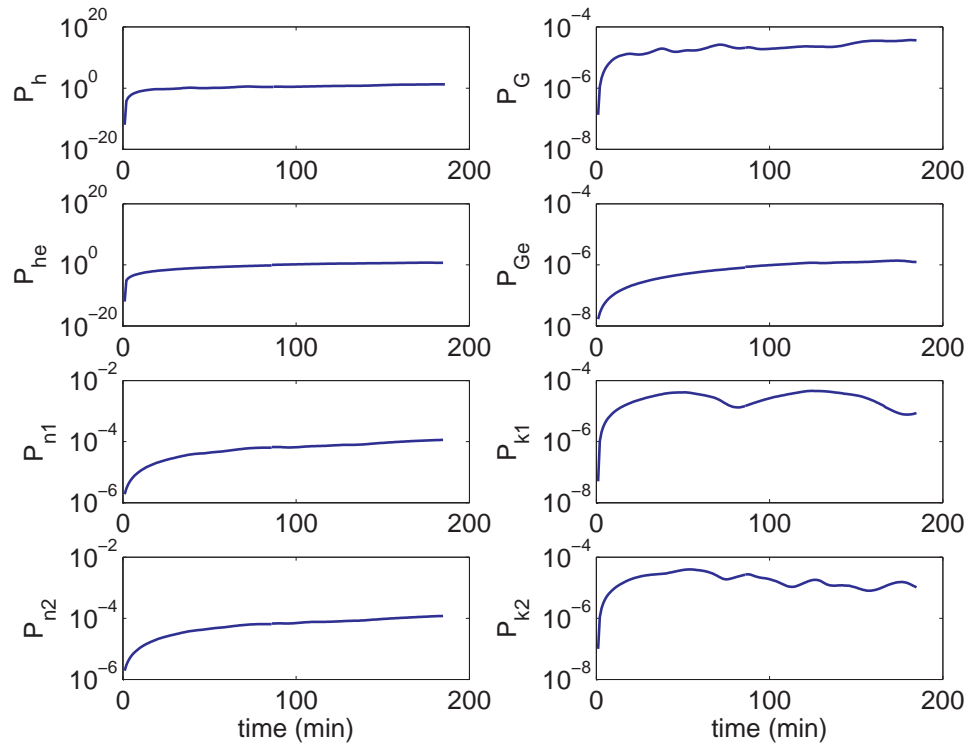


Figure 92: Variance of estimated states in Fig. 89 when $N = 20$.

using both the process dynamic model and the sensor model, although it is more oscillatory compared to mMHE. Also notice that the extinction coefficient at 470 nm was estimated to be negative which is not physically possible. However in this study, we have not encountered many cases that the EKF estimates negative states. However, this is not uncommon in the literature especially for some highly nonlinear systems [58]. One of the advantages of mMHE over EKF is that it can handle state constraints. In this sense, mMHE is a more robust estimator than EKF.

6.4 Additional example

To show the robustness and general applicability of the state estimators, we now consider another set of experimental reflectance data, which is shown in Fig. 94. The sampling interval is 10 seconds and total deposition time is 21.6 minutes. The deposition conditions are also summarized in Table 6 (column of 10/3/2007). As shown, the conditions are the same as 10/1/2007 except that the heating voltage is increased to 20 volts. The higher heating voltage causes higher substrate temperature and thus higher growth rate. The average growth rate in a calibration run is around 12 nm/min which is 1.5 times of that on 10/1/2007. Another interesting point about this experiment is that we know we are running out of precursor and so we anticipate that the growth rate should decrease quickly. This is confirmed by the rapidly increasing oscillation period in Fig. 94.

We first use RLS to estimate the states from the experimental reflectance in Fig. 94. The process model and the sensor model are the same as in 10/1/2007 case. The initial guess is $x_1 = [0, 12, 1.9054, 0.05, 1.9455, 0.1]^T$. The positive constraint is applied to all states. We have tested three different horizon sizes, 10, 20 and 30. When $N = 30$, the fitting algorithm did not converge. This is because for this particular data set, the growth rate changes quickly and thus $N = 30$ is too long for the assumption of constant growth rate. The estimation results at horizon size

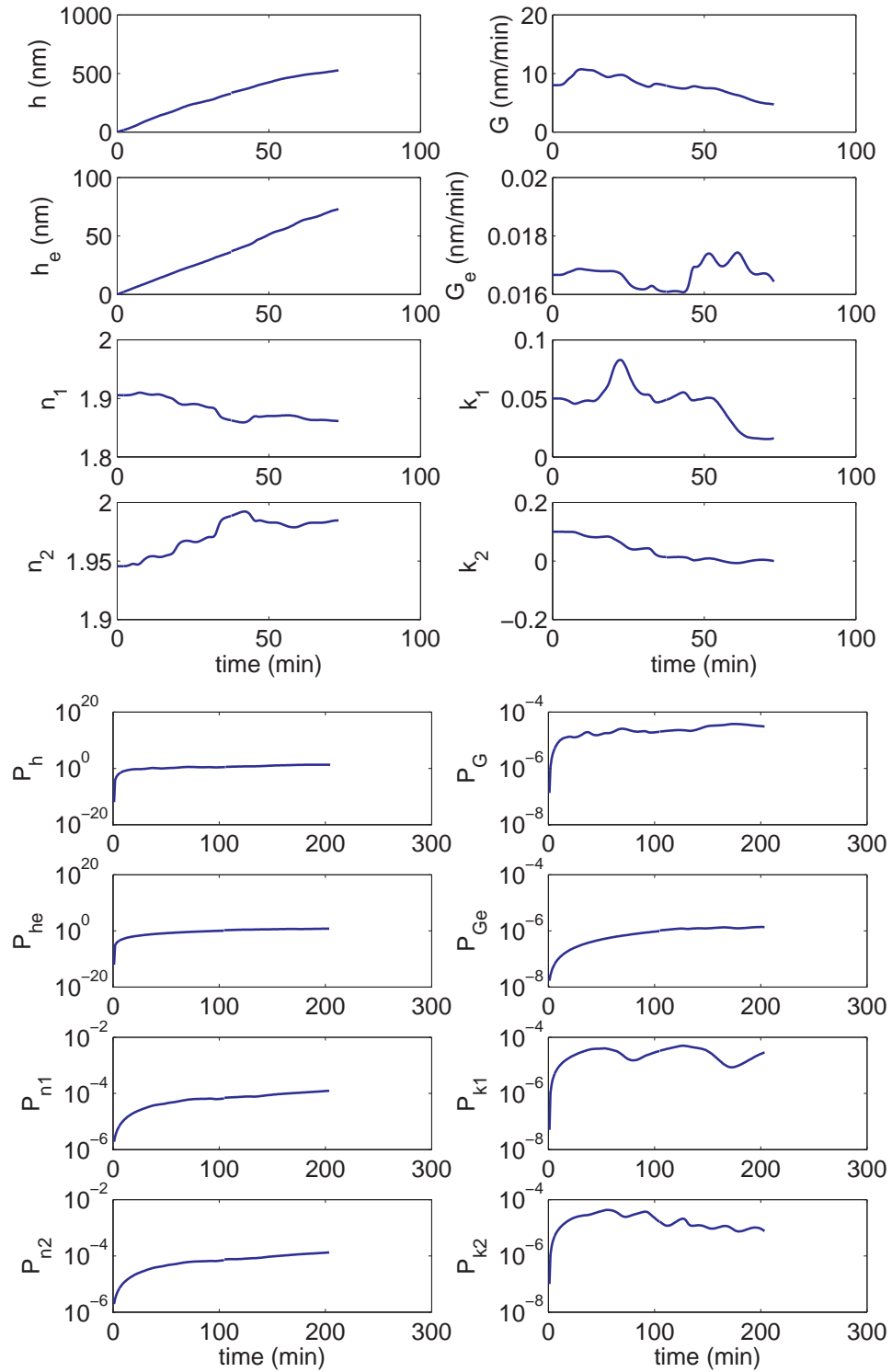


Figure 93: Estimation result by EKF from the reflectance measurement in Fig. 81. The sensor model is based on dual-wavelength reflection on a rough surface. (top) true and estimated states (bottom) variance of estimated states.

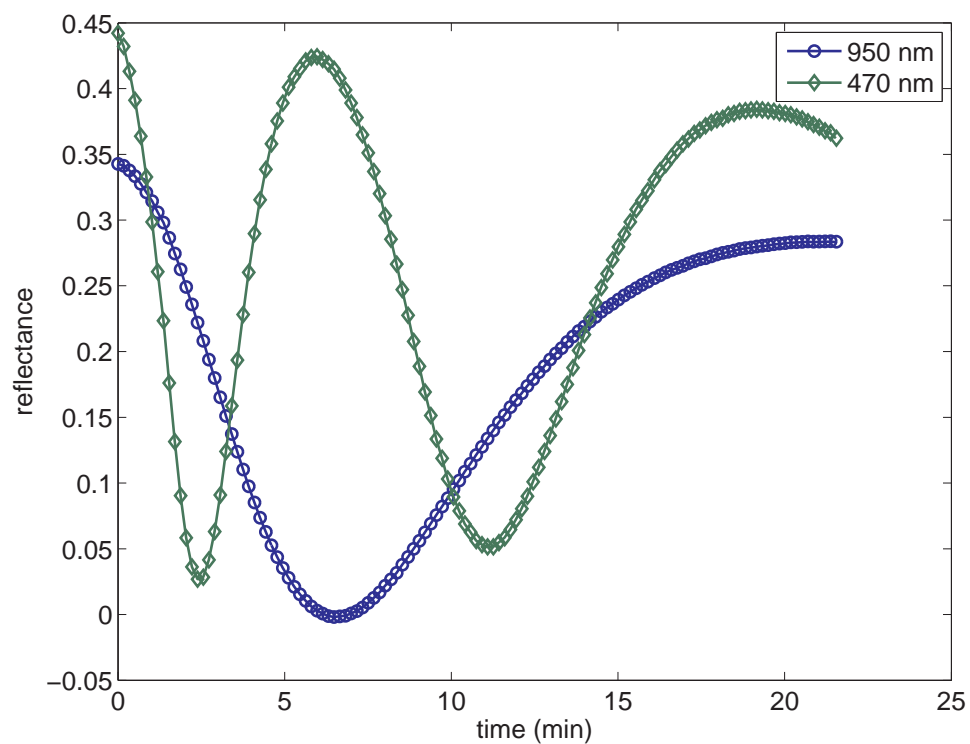


Figure 94: Experimental reflectance at 950 nm and 470 nm (Date acquired: 10/3/2007).

Table 10: Estimated states at the end of the growth and *ex situ* ellipsometry characterization. The sensor model is based on dual-wavelength reflection on a smooth surface. This film was deposited on 10/3/2007.

	RLS			mMHE			EKF	<i>ex situ</i> ellipsometry
	10	20	30	10	20	30		
h (nm)	254.4	310.5	N/A	251.6	251.8	252.8	249.8	257.4
n_1	1.8934	1.5433	N/A	1.8964	1.8956	1.8962	1.8988	1.7904
k_1	0.07	0.0406	N/A	0.0693	0.0689	0.0685	0.0697	0.0008
n_2	1.9340	1.5880	N/A	1.9564	1.9565	1.9562	1.9561	1.8314
k_2	0.0240	0.0154	N/A	0.0261	0.0264	0.0261	0.0282	0.0060

of 10 and 20 are shown in Fig. 95. The estimated states at the end of the growth are summarized in Table 10. As shown, the estimated states at $N = 10$ are more reasonable than $N = 20$. Again this is most likely due to the rapid change of growth rate in this data set.

Next we use mMHE to estimate the states from the same experimental reflectance. The process dynamic model, the sensor model and the initial guess are the same as in RLS. For the tuning matrices, we keep R and $P_{1|0}$ the same as in 10/1/2007, i.e. $R = \text{diag}([10^{-4}, 10^{-3}])$ and $P_{1|0} = \text{diag}(x_1) \times 10^{-6}$. We choose

$$Q = \text{diag}([10^{-4}, 10^{-4}, 10^{-6}, 10^{-6}, 10^{-6}, 10^{-6}]).$$

Compared to Q in 10/1/2007, the variance of h and G are set larger to indicate our anticipation of fast growth rate decay. With the chosen $P_{1|0}$, R and Q , we tested three different horizon sizes, 10, 20 and 30. mMHE had no problems with convergence even at $N = 30$. The estimation results are shown in Fig. 96. The variance of estimated states are shown in Fig. 97. The estimated states at the end of the growth are summarized in Table 10. As shown, mMHE yielded almost identical results for all horizon sizes indicating strong robustness of the estimator.

Finally we used EKF to estimate the states from the same reflectance. The process

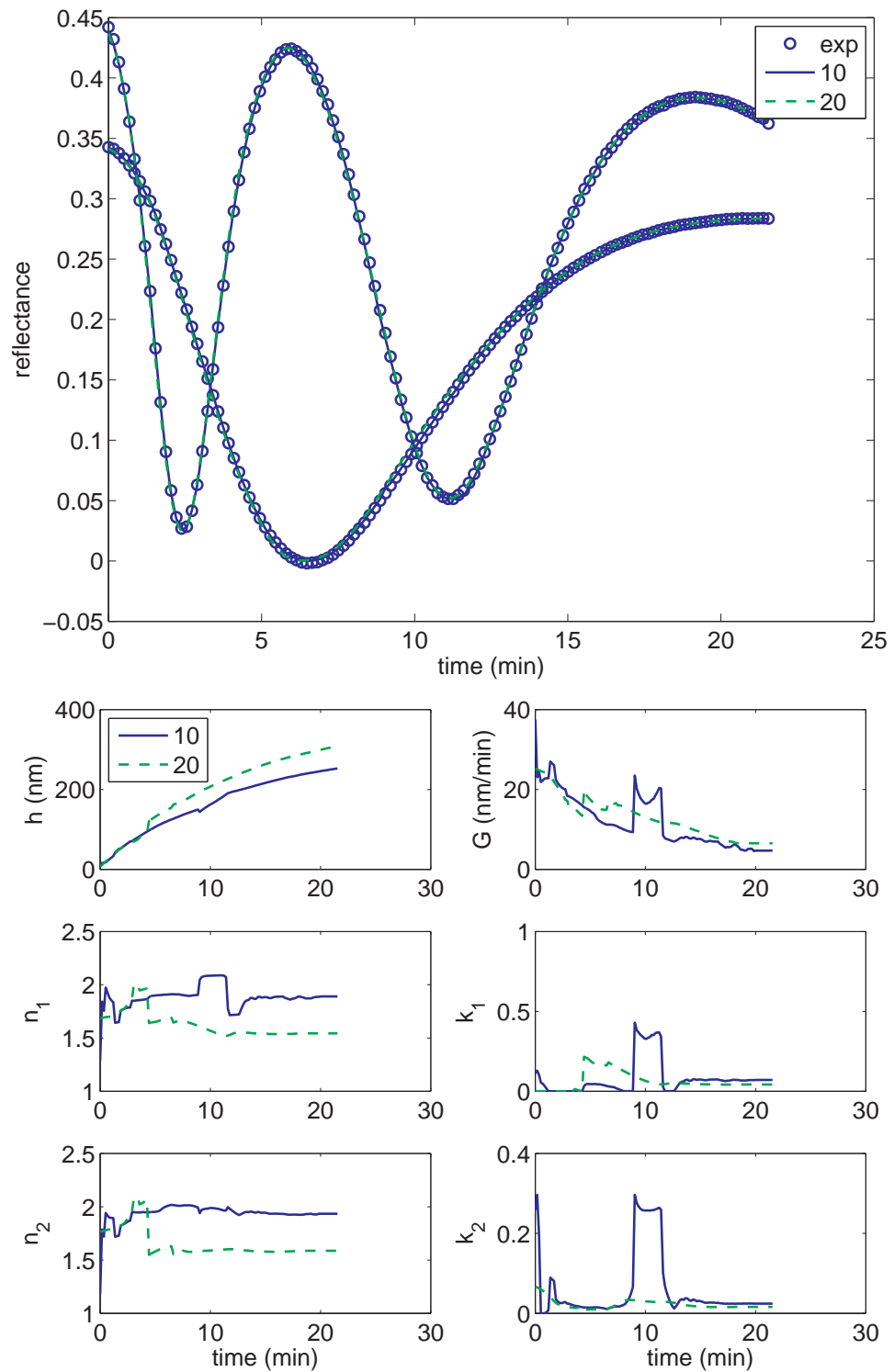


Figure 95: Estimation result by RLS from the reflectance measurement in Fig. 94. The sensor model is based on dual-wavelength reflection on a smooth surface. (top) fitted output (bottom) true and estimated states.

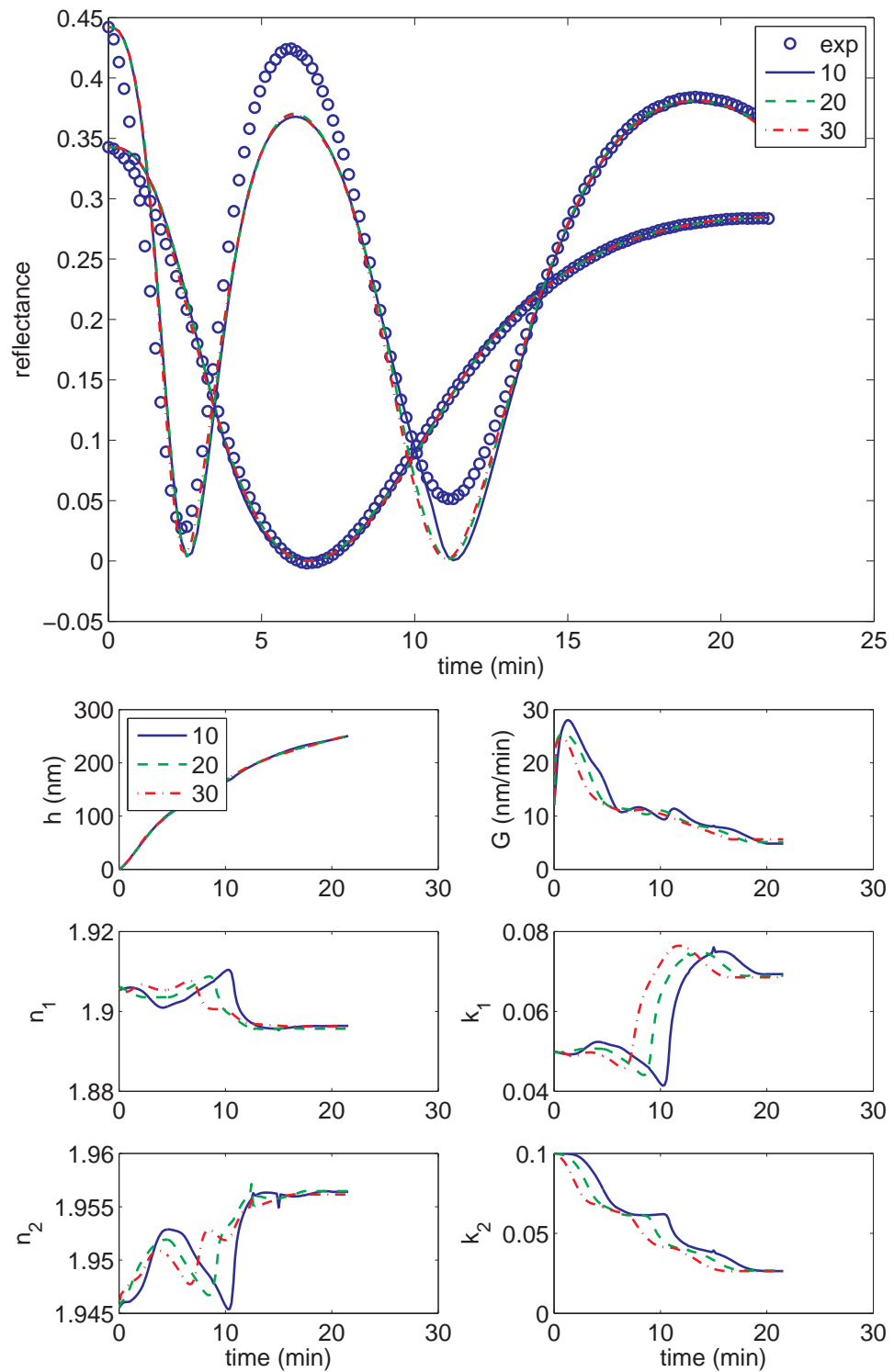


Figure 96: Estimation result by mMHE from the reflectance measurement in Fig. 94. The sensor model is based on dual-wavelength reflection on a smooth surface. (top) fitted output (bottom) true and estimated states.

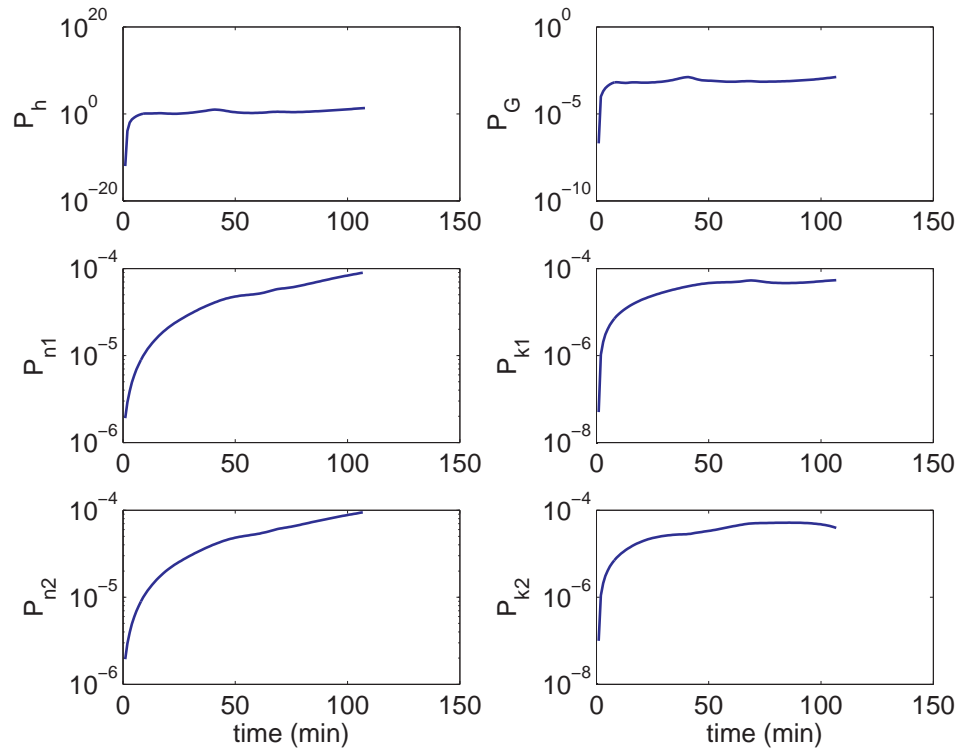


Figure 97: Variance of estimated states in Fig. 96 when $N = 20$.

dynamic model, the sensor model and tuning matrices are the same as mMHE. Figure 98 shows estimated states and variance. The estimated states at the end of the growth are summarized in Table 10.

The deposited film was characterized *ex situ* using an ellipsometer. The ellipsometer data can be fitted well with a three layer model of rough/Cauchy/Silicon. The fitted ellipsometry data are shown in Fig. 86 and the fitted result is summarized in Table 10. The thickness reported by ellipsometer is equal to the thickness of the Cauchy layer plus half of the rough layer thickness. Table 10 clearly indicates that mMHE consistently yield more reasonable results indicating strong robustness.

Similar to 10/1/2007, we have also estimated roughness from the reflectance measurement in Fig. 94. For RLS, the initial guess is $x_1 = [0, 12, 0, 1, 1.9054, 0.05, 1.9455, 0.1]^T$. All states are constrained to be positive. We have tested three different horizon sizes, 10, 20 and 30 and the estimation results are shown in Fig. 99. When $N = 30$, the

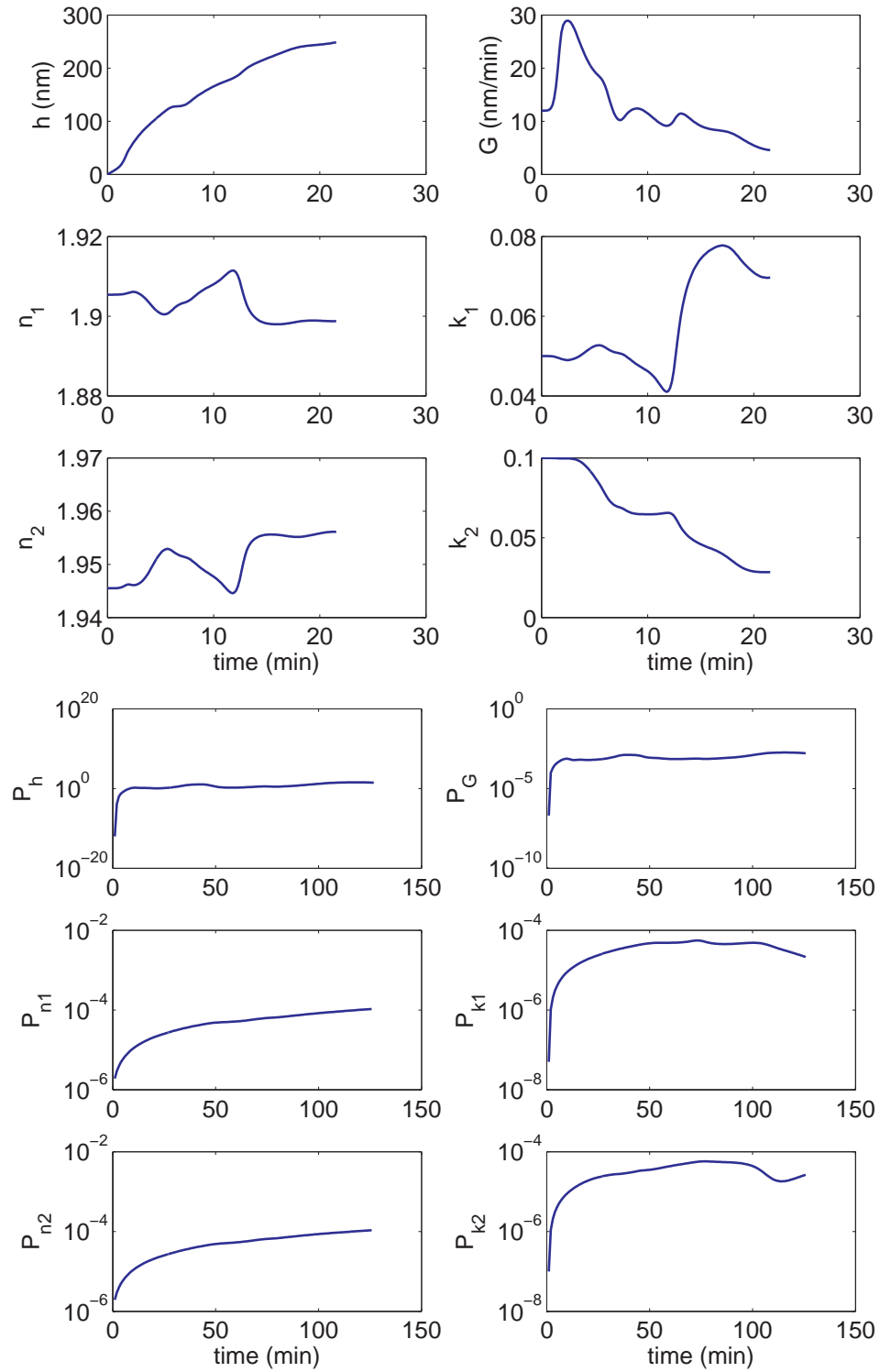


Figure 98: Estimation result by EKF from the reflectance measurement in Fig. 94. The sensor model is based on dual-wavelength reflection on a smooth surface. (top) true and estimated states (bottom) variance of estimated states.

Table 11: Estimated states at the end of the growth and *ex situ* ellipsometry characterization. The sensor model is based on dual-wavelength reflection on a rough surface. This film was deposited on 10/3/2007.

	RLS			mMHE			EKF	<i>ex situ</i> ellipsometry
	10	20	30	10	20	30		
h (nm)	240.4	242.8	N/A	242.2	242.5	243.6	239.6	241.9
h_e (nm)	39.2	38.2	N/A	21.4	21.4	21.4	21.4	31.0
n_1	1.8590	1.8543	N/A	1.8967	1.8959	1.8962	1.8990	1.7904
k_1	0.0473	0.0478	N/A	0.0636	0.0634	0.0631	0.0636	0.0008
n_2	1.9069	1.9020	N/A	1.9556	1.9557	1.9554	1.9552	1.8314
k_2	0.0001	0	N/A	0.0186	0.0189	0.0187	0.0211	0.0060

fitting algorithm still had difficulty in converging. The estimated states at the end of the growth are summarized in Table 11. Compared to smooth case, estimation result at $N = 20$ improved significantly. This is different from the case of 10/1/2007, in which adding roughness made the estimation result worse.

For mMHE, we keep R and $P_{1|0}$ the same as in the smooth case. We choose $Q = \text{diag}([10^{-4}, 10^{-4}, 10^{-8}, 10^{-8}, 10^{-6}, 10^{-6}, 10^{-6}, 10^{-6}])$. Again, the variance of the original six states are kept the same as in the smooth case. The only difference is the additional two elements, the second and the third, which represents the variance of h_e and G_e , respectively. With the chosen $P_{1|0}$, R and Q , we tested three different horizon sizes, 10, 20 and 30 and the estimation results are shown in Fig. 100. The estimated states at the end of the growth are summarized in Table 11. The variance of estimated states are shown in Fig. 101 and are in reasonable range. Compared to Fig. 97, there is no significant decrease in the estimated variances.

Finally for EKF, the estimated states at the end of the growth are summarized in Table 11. As shown, EKF also yielded acceptable result by using both the process dynamic model and the sensor model, although it is more oscillatory compared to mMHE.

By comparing all the estimation results in Table 7 to 11, it is clear that mMHE

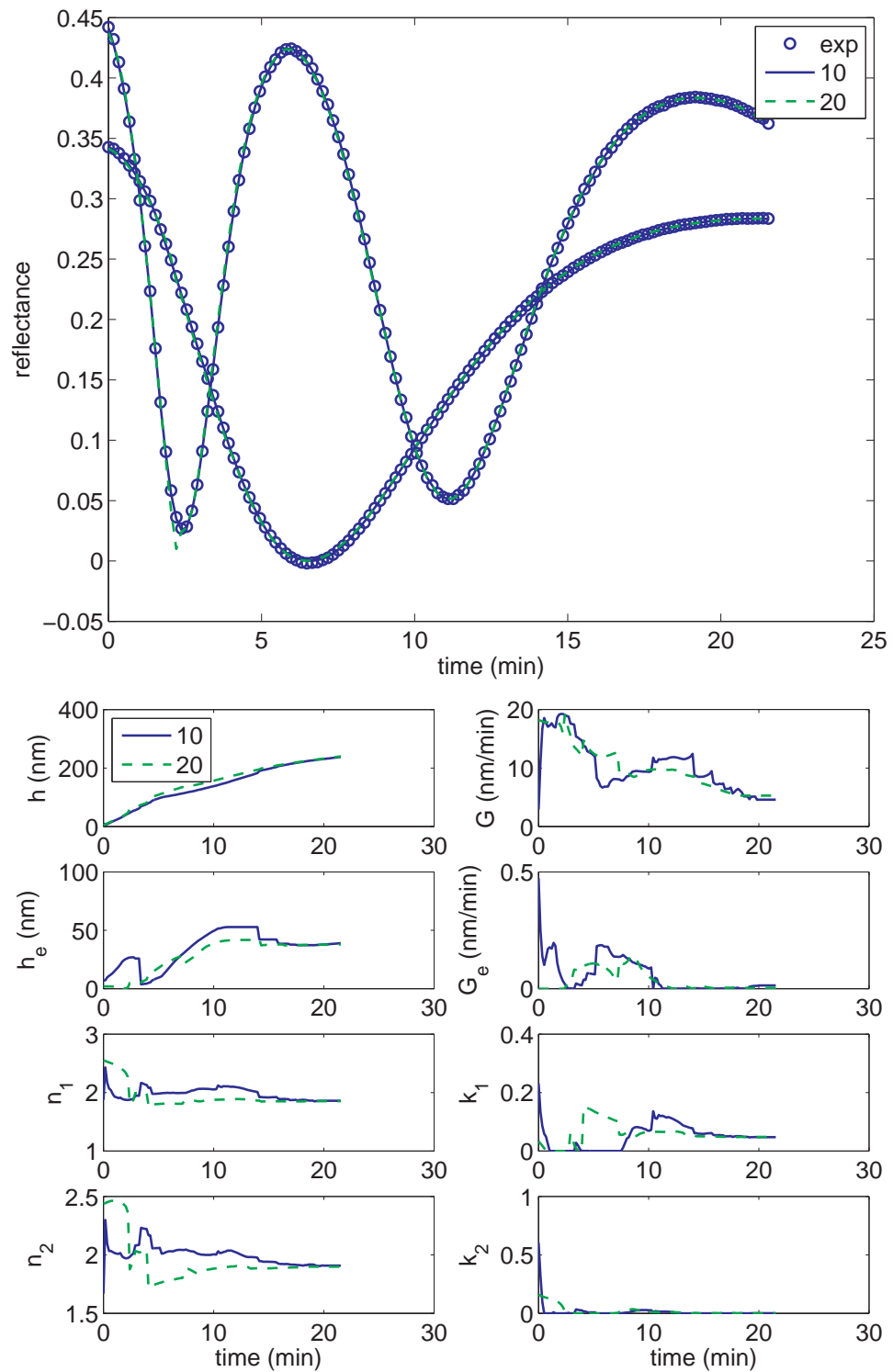


Figure 99: Estimation result by RLS from the reflectance measurement in Fig. 94. The sensor model is based on dual-wavelength reflection on a rough surface. (top) fitted output (bottom) true and estimated states.

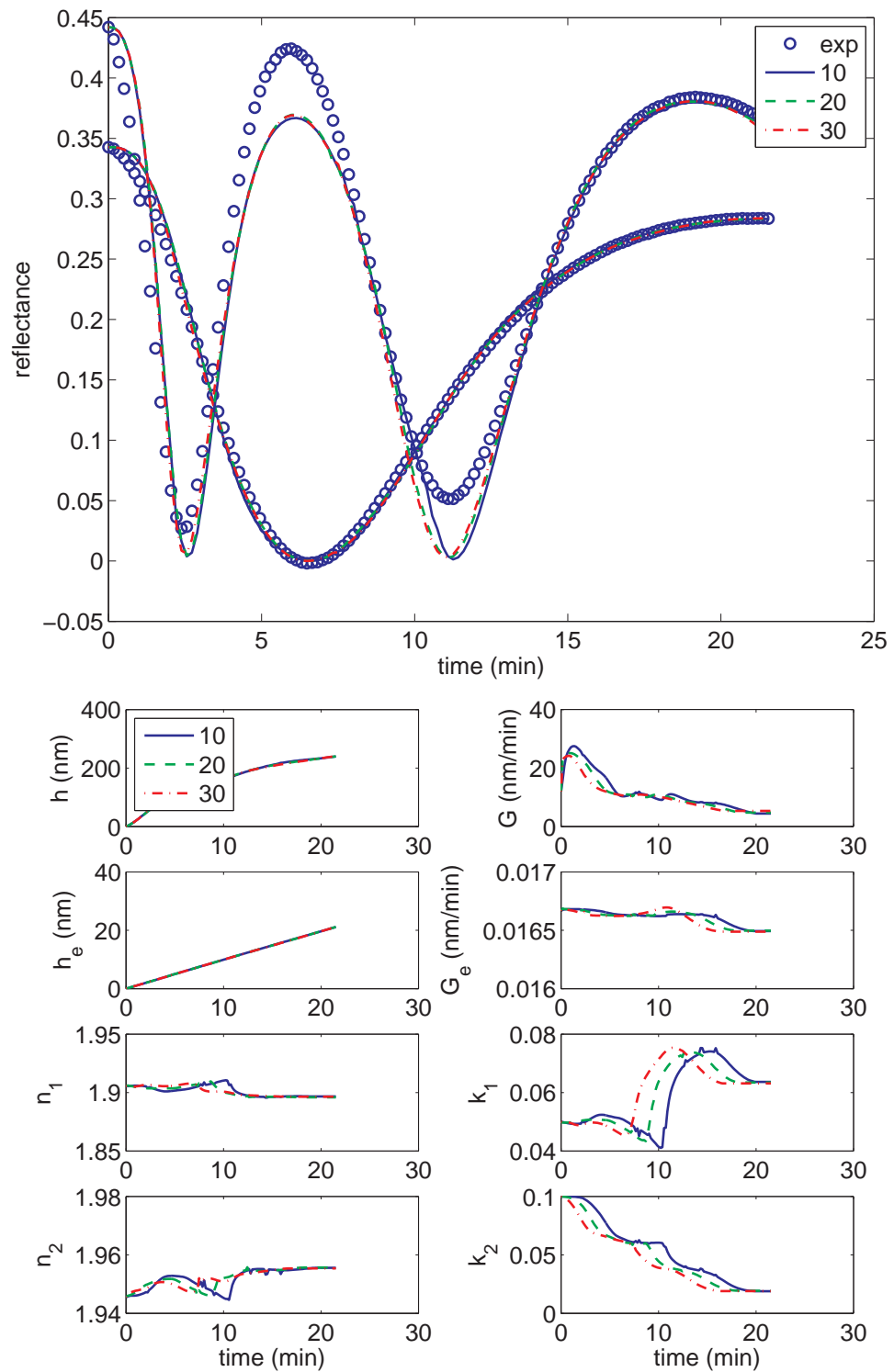


Figure 100: Estimation result by mMHE from the reflectance measurement in Fig. 94. The sensor model is based on dual-wavelength reflection on a rough surface. (top) fitted output (bottom) true and estimated states.

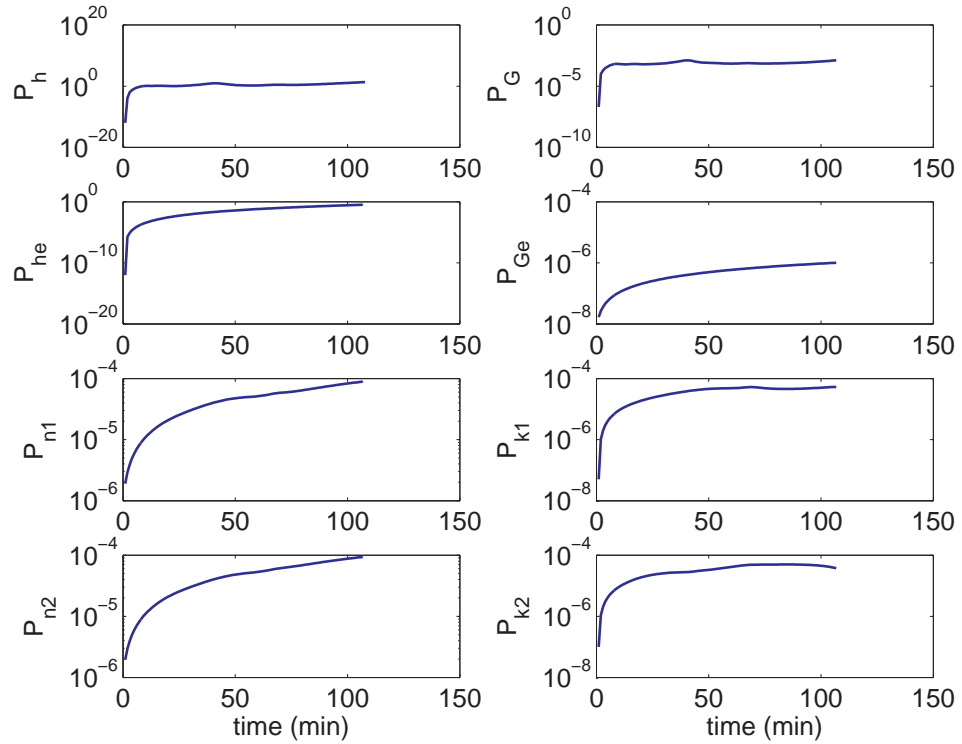


Figure 101: Variance of estimated states in Fig. 100 when $N = 20$.

consistently yielded better estimates for processes under quite different deposition conditions. This indicated that mMHE is a useful and robust state estimator for *in situ* sensor data interpretation. By using the information from both the process and the sensor model, one can obtain a better estimate. The nice thing of mMHE is that it provides such a versatile framework to organize all these useful information and gives a user the opportunity to interact with fitting and make wise decision in the *in situ* sensor data interpretation.

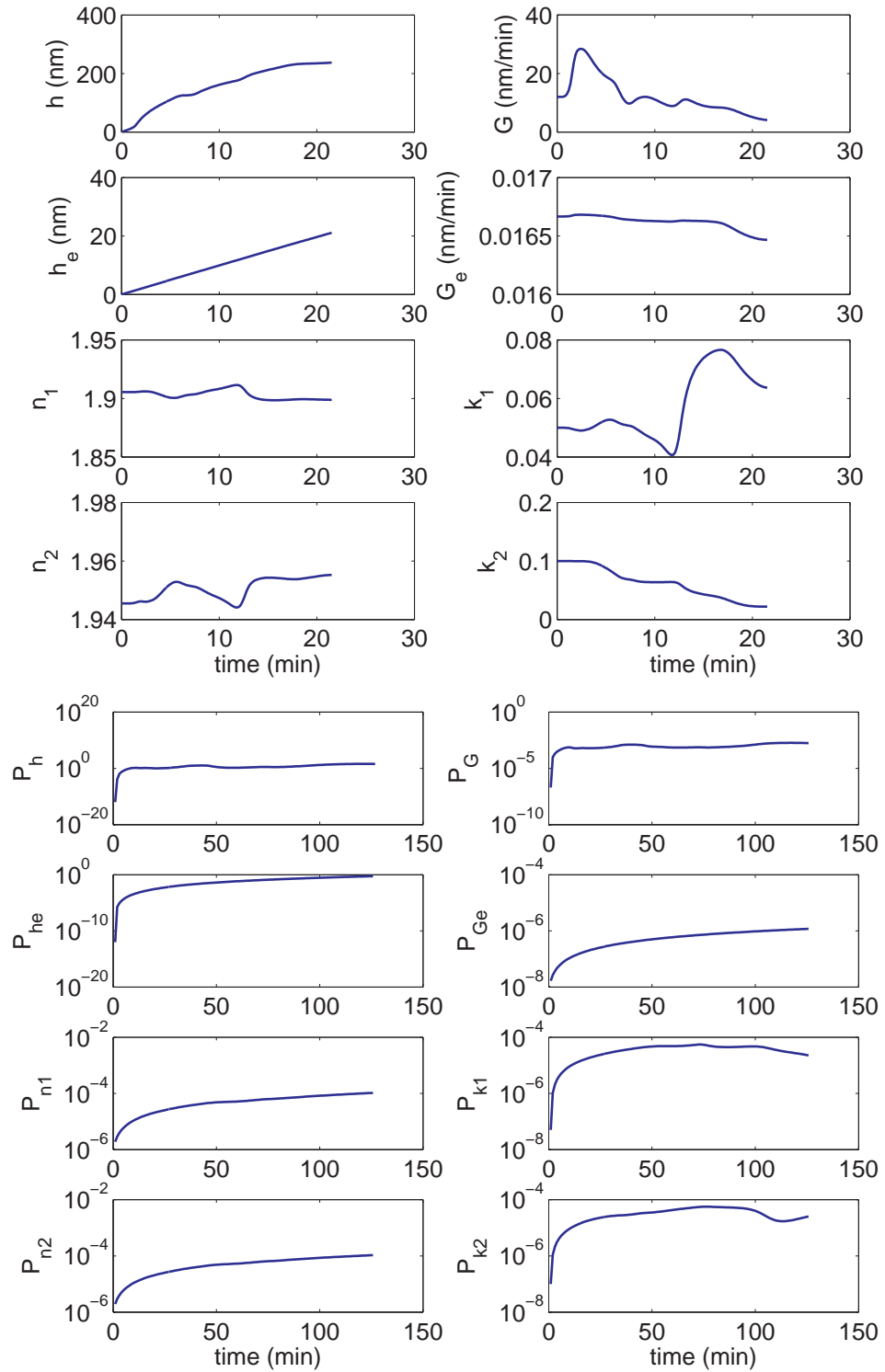


Figure 102: Estimation result by EKF from the reflectance measurement in Fig. 94. The sensor model is based on dual-wavelength reflection on a rough surface. (top) true and estimated states (bottom) variance of estimated states.

CHAPTER VII

CONCLUSIONS AND FUTURE WORK

7.1 *Conclusions*

In this project, we systematically studied the application of state estimators in *in situ* sensor data interpretation for a chemical vapor deposition process. We have studied optical models for light reflection on both smooth and rough surfaces. The model validation results indicate that the effective medium model is better than the scalar scattering model when the surface is microscopically rough, i.e. the mean height and correlation length of the irregularities are both much less than the wavelength of light. Based on the sensor model, we studied the effect of film parameters on the reflectance. The results indicate that extinction coefficient, roughness and film nonuniformity can have similar effect on the reflectance, which suggests difficulty in separately estimating these parameters. We studied the observability based on the sensor model and a simple process dynamic model. We found that for a nonlinear system, the local observability does not always guarantee the global observability. For a nonlinear system, one must consider the specific system and mathematical form, because no general approach and practical tools exist, as they do for linear systems.

We have studied several state estimation techniques including batch least squares fitting (BLS), recursive least squares fitting (RLS), extended Kalman filter (EKF), and moving horizon estimation (MHE). It has been shown that MHE is the general least-squares-based state estimation and BLS, RLS, and EKF are special cases of MHE. The advantage of MHE is that it can handle state constraints and it explicitly considers uncertainty and the correlations between the states. To reduce the computational requirement of MHE, we developed a modified moving horizon estimator

(mMHE) that combines the advantage of the computational efficiency in RLS and the *a priori* estimate in MHE.

We compared the performance of the state estimators using simulated film growth processes. When there is a process model mismatch but the sensor model error is negligible, both RLS and mMHE work well in the case of single and dual-wavelength reflection on a smooth surface. There exists an optimum horizon size for both RLS and mMHE, although mMHE is less sensitive to the horizon size and performs better than RLS at all horizon sizes. In the case of dual-wavelength reflection on a rough surface, RLS failed to give a reasonable estimate due to the strong correlation between roughness and the extinction coefficient. However, mMHE successfully estimated the extinction coefficient and surface roughness by using the *a priori* estimate. We also found that there is no significant improvement using full MHE. When there is a sensor model mismatch, either state estimator will give a good result. However, relatively speaking, mMHE is still a better state estimator. In the case of both single and dual-wavelength reflection on a smooth surface, mMHE works at least as well as RLS and in many cases, especially for shorter horizon, it provides significant improvements. mMHE requires no more computation than RLS and it is more robust to change in horizon size. It does require designing reasonable weighting matrices, which requires some understanding of the uncertainties in the process and sensor model.

To test the state estimators in a real world environment, we built a cold-wall low-pressure chemical vapor deposition testbed with an *in situ* emissivity-correcting pyrometer. We developed a fully automatic data-acquisition and instrument-control software for the CVD testbed using LabVIEW. We successfully used the CVD testbed to deposit yttria thin film on silicon substrate, as verified by the *ex situ* characterization. We compared the performance of the state estimators using two experimental reflectance data sets acquired from the CVD testbed under different deposition conditions. The estimated film properties are compared with *ex situ* film characterization

results. We considered the cases of dual-wavelength reflection on both smooth and rough surface. In all cases, mMHE consistently yielded better estimates for processes under quite different deposition conditions. This indicated that mMHE is a useful and robust state estimator for *in situ* sensor data interpretation. By using the information from both the process and the sensor model, one can obtain a better estimate. A good feature of mMHE is that it provides such a versatile framework to organize all these useful information and gives a user the opportunity to interact with fitting and make wise decisions in the *in situ* sensor data interpretation.

7.2 Future work

For the future work, first, we can make further improvements on the CVD testbed to obtain more reliable experimental data. For example, we can use a more thermally conductive material to make a thermal diffuse plate so that the temperature uniformity on the substrate can be improved. We can also make a shower head to distribute process gases more uniformly. Currently, the pump port is on the side of the chamber. As we have shown, this arrangement caused nonuniform flow inside the chamber. If possible, we should move the pump port to the bottom of the chamber. The heater assembly should not be inserted from the bottom of the chamber. Instead it should be fixed inside the chamber and the substrate can be loaded into the chamber from a side window. In this way, we can have better repeatability in terms of geometric position between the substrate and the reflectometer. The evaporator in current design is difficult to be disconnected for repacking. It also takes a long time to heat up the evaporator using the convective oven. In fact, it is the most time-consuming step in one CVD experiment. If possible, the evaporator should have its own temperature control system and should be designed such that it can be easily disconnected for repacking.

The current *in situ* ECP sensor has a large field of view and film uniformity could

be a problem because it affects reflectance measurement and makes it more difficult for sensor data interpretation. If possible, we should consider a laser reflectometer which samples small area and we can use multiple channels to sample different areas to obtain the thickness profile. On the other hand, with the current sensor, we can try to estimate film nonuniformity directly from the *in situ* reflectance measurement, if the effect of nonuniformity is important. In this project, we only consider the reflectance measurement. For future work, we should utilize the pyrometer measurement to complement the estimation of film properties. We should also consider to measure spectral reflectance because with more independent measurements, we can obtain better estimates as we have demonstrated in this study. The spectral wavelength can be chosen in such a combination that longer wavelength is used to measure thickness and growth rate, and shorter wavelength is used to measure roughness and other microscopic properties. We can even consider use multiple sensors such as combination of ellipsometer and reflectometer. In fact, in our view, the real-time sensing in the future is most likely to be a combination of different types of sensors. The nice thing about the state estimator is that it provide a framework to incorporate different types of measurement and makes a balanced estimation. In this project, we only consider slowly drifting CVD processes. To broaden the application of the state estimators, we should also test them in rapid changing processes, for example, a process during which a sudden change in the deposition condition occurs. This can be easily done in simulation first.

The sensor models used in this project only consider thickness, complex refractive index and roughness. In order to estimate more film properties from optical measurements, further work need to be done to develop a more detailed sensor models. In this project, we only consider a very simple process dynamic model. Ideally, the more we know about a process, the better we can estimate the film properties. Therefore, in the future, we should work to develop more detailed process dynamic model. In

general, a detailed process dynamic model for thin film growth is inherently multi-scale and multi-dimensional in nature. Our group has separate projects in model reduction to obtain a reduced order process model with aim of rational design and control of the process. It could be a possible direction to combine the reduced order process model with *in situ* sensing based on state estimation. Recently some other novel state estimators, such as unscented Kalman filters and particle filters, are receiving more attention. They seem to perform much better than conventional state estimators like EKF. Therefore, in the future, we should also explore the possibility of applying these novel state estimators to *in situ* data interpretation. Finally with the progress in state estimator based *in situ* sensing, we now have improved visibility of the process. Then a natural direction for future work should be process monitoring, fault detection and eventually feedback control of the thin film deposition process. One immediate direction is to combine the *in situ* sensing with run-to-run controller which is commonly employed in the semiconductor industry.

APPENDIX A

IN-SITU 4000 COM PORT PROTOCOL

SVT Associates In-situ 4000 Serial Interface using RS-232

Baud rate: 9600 bytes/second

Framing: 8 bit, no parity, 1 stop bit

A.1 DATA SENT TO THE Instrument

Sending 1 byte equal to 128 (hex 80) starts sending data.

Sending 1 byte equal to 0 stops sending data.

Sending 1 byte equal to 16 (hex 10) turns on the LED.

Sending 1 byte equal to 0 turns off the LED.

Sending 144 (hex 90) starts sending data and turns on the LED.

A.2 DATA SENT FROM THE Instrument

Each data group has four 16-bit integers. These 4 values correspond to the following 4 channels

- Temp-950-Channel
- Temp-850-Channel
- Refl-950-Channel
- Refl-470-Channel

Once the instrument starts sending data, it keeps doing so. If you poll data once every second, you will get about 88 bytes of data on each read. It will help a lot to read each time a number of bytes equally divisible by 8. Otherwise, partial data

groups must be dealt with. Just by looking at the raw data, you cannot tell which byte does what. Hence, the only way to synchronize is to stop the data (send 0 or 16) and then restart the data (send 128 or 144). Then you know that the 1st 8 bytes are a data group, followed by more data groups.

The 16-bit integer values are converted to volts by $\text{volts} = \text{int_value}/3.2768$. Intensity is then equal to volts for all channels. The many other conversions performed in the RoboMBE software are beyond the scope of this writeup.

APPENDIX B

CVD PROCEDURE

This CVD procedure is written by Derek Jamrog who worked in our group as an undergraduate research assistant in summer semester 2007. He wrote this procedure from the perspective of a brand new user.

B.1 Start procedure

1. OPEN Labview
2. TURN ON precursor oven (Default 150 F - precursor heats SO slowly)
3. TURN ON pump
4. OPEN Ar, O2 and N2 containers
5. RAISE the pressure in the reactor by flowing Dummy Ar into the reactor (Use 3000-4000 sccm)
6. PUT ON gloves
7. REMOVE heater from the reactor
8. PLACE previously grown film into a case, and date it
9. CLEAN new wafer
 - FILL one beaker with DI water
 - PUT ON heavy duty black gloves over regular gloves
 - FILL second beaker with roughly 10ml H₂O₂ and 30ml H₂SO₄

- PLACE wafer into the acid solution
 - WAIT 8-10 minutes
 - TAKE wafer out of the acid solution and drop it in the water beaker
 - RINSE wafer with DI water
 - DRY wafer with N₂
 - Remember to CLEAN and DISPOSE of waste properly
10. SAVE file
 11. CLICK the Comm On and LEDs On under the Engine Tab in Labview
 12. CLICK Calibrate Low under the Reflectance Tab
 13. LOAD new wafer on the heater and PLACE it in the reactor
 14. REMOVE gloves (optional)
 15. TURN ON voltage device
 16. REATTACH thermocouple and voltage wires
 17. TURN ON the TV
 18. PUMP down the reactor to ≈ 1 torr
 19. ADJUST the camera so the spots appear in the center of the TV screen.
 20. FLOW Dummy Ar at specified amount (Default: 100 sccm)
 21. CALIBRATE high reflectance by clicking that button in the Reflectance Tab
 22. CALIBRATE UV Cell
 - TURN ON UV Lamp. Flip switch on UV cell panel

- TURN ON Master, Slave 1, and Slave 2 under the Ocean Optics Tab
 - TAKE out UV cord from the source
 - COVER the cord end with your finger and click Store Dark
 - SCREW cord back in and click Store Reference
23. TURN ON main oven (Default: 400 F)
 24. TURN ON fan and blow it on the valve (side with N2 Trap)
 25. SET voltage and ramp rate (Default: 15 V at 0.5 V/min)
 26. SET actuator temperature, the green numbers next to the low pressure meter (Default: 150-200 C)
 27. WAIT for system to heat up (Time: 60 min)
 28. FLOW O2 (Default: 50 sccm)
 29. FILL N2 trap
 - WEAR big blue gloves
 - PLACE tank tube into the liquid N2 container
 - SLOWLY open liquid N2 tank, then once gas has passed and it cools down open it more
 - SLOWLY pour liquid N2 into the catcher on the left side of the oven
 30. FLOW Carrier Ar (Default 120 sccm)
 31. PUT ON white heat resistant gloves
 32. OPEN precursor chamber exit valve
 33. OPEN valve leading into the precursor chamber

34. FLOW Precursor Ar (Default: 20 sccm)
35. CHECK absorbance in the Ocean Optics Tab to ensure precursor is flowing
36. *If necessary, ADJUST Ar flow rates and valve openings to achieve desired absorbance
37. SWITCH solenoid valve to Yes to start deposition
38. WAIT as film grows
 - WATCH absorbance to make sure precursor doesn't run out
 - WATCH Ar and O2 flow rates to make sure they are present
 - MONITOR Labview for any problems

B.2 Shut down procedure

1. SWITCH solenoid valve to No to stop precursor flow to the reactor
2. TURN OFF Precursor Ar flow
3. PUT ON white heat resistant gloves
4. CLOSE valve entering the precursor chamber
5. CLOSE valve exiting the precursor chamber
6. TURN OFF precursor oven
7. WAIT for Absorbance to go down then TURN OFF Carrier Ar
8. WAIT for reflectance to stabilize indicating the end of deposition
9. DISABLE the master and slaves under the Ocean Optics Tab
10. TURN OFF the UV Lamp

11. TURN OFF the main oven
12. STEP the voltage to zero
13. SET the actuator temperature to 25 C
14. DISABLE Comm and LEDs under the Engine Tab
15. TURN OFF the TV
16. TURN OFF the voltage source
17. TURN OFF O2
18. OPEN the ovens and MOVE the fan to blow into oven (Fastest fan spd. is 3)
19. WAIT until heater temp ≥ 200 C (Time: 20-30 min)
20. TURN OFF Dummy Ar
21. CLOSE Ar, O2 and N2 tanks
22. CLOSE Pump Valve on Labview
23. TURN OFF the Pump
24. QUIT Labview
25. TURN OFF the Fan
26. GO HOME. You deserve it!!

B.3 Evaporator repack procedure

1. Take out the evaporator
2. Open the evaporator
3. Weight precursor

4. Grind precursor and coat on ball bearings
5. Load ball bearings into the evaporator
6. Close the evaporator
7. Install evaporator back to the system
8. Open inlet and outlet valves of the evaporator, pump down the system
9. Close both inlet and outlet valves to keep the evaporator under vacuum

Reflectance calibration is performed with the following steps: 1) Remove the wafer so that the LED reflection is no longer visible on the video image. Wait at least 3 seconds for the reading to stabilize. 2) Calibrate reflectance as zero 3) Load the wafer so that the LED reflection is visible on the video image. Wait at least 3 seconds for the reading to stabilize. 4) Calibrate reflectance as reflectance of silicon at room temperature.

REFERENCES

- [1] AHN, K. H., PARK, Y. B., and PARK, D. W., “Kinetic and mechanistic study on the chemical vapor deposition of titanium dioxide thin films by in situ FT-IR using TTIP,” *Surface & Coatings Technology*, vol. 171, pp. 198–204, July 2003.
- [2] AKAZAWA, H., “In situ characterization of thin Si_{1-x}Gex films on Si(100) by spectroscopic ellipsometry,” *Thin Solid Films*, vol. 369, pp. 157–160, July 2000.
- [3] AKKERMAN, Z. L., SONG, Y., YIN, Z., SMITH, F. W., and GAT, R., “In situ determination of the surface roughness of diamond films using optical pyrometry,” *Applied Physics Letters*, vol. 72, no. 8, pp. 903–905, 1998.
- [4] AMASSIAN, A., DESJARDINS, P., and MARTINU, L., “Study of TiO₂ film growth mechanisms in low-pressure plasma by in situ real-time spectroscopic ellipsometry,” *Thin Solid Films*, vol. 447, pp. 40–45, Jan. 2004.
- [5] ASPNES, D. E. and THEETEN, J. B., “Investigation of effective-medium models of microscopic surface-roughness by spectroscopic ellipsometry,” *Physical Review B*, vol. 20, no. 8, pp. 3292–3302, 1979.
- [6] ATKINSON, P. and NIXON, M., “Monitoring a deposition process using an extended adaptive Kalman filter,” *Iee Proceedings-D Control Theory And Applications*, vol. 131, no. 1, pp. 1–7, 1984.
- [7] BALMER, R. S., PICKERING, C., PIDDUCK, A. J., and MARTIN, T., “Modelling of high temperature optical constants and surface roughness evolution during MOVPE growth of GaN using *in situ* spectral reflectometry,” *Journal Of Crystal Growth*, vol. 245, pp. 198–206, Nov. 2002.
- [8] BARRAT, S., PIGEAT, P., DIEGUEZ, I., BAUERGROSSE, E., and WEBER, B., “Observation of spectral and normal emissivity as a method of surface control during the growth of diamond films deposited by a microwave plasma-assisted CVD technique,” *Thin Solid Films*, vol. 263, pp. 127–133, July 1995.
- [9] BARRAT, S., PIGEAT, P., DIEGUEZ, I., BAUERGROSSE, E., and WEBER, B., “Initial growth phase of diamond thin films observed by thermal emission spectrometry,” *Thin Solid Films*, vol. 304, pp. 98–105, July 1997.
- [10] BAY, J. S., *Fundamentals of linear state space systems*. Boston: WCB/McGraw-Hill, 1998.
- [11] BECKMANN, P. and SPIZZICHINO, A., *The scattering of electromagnetic waves from rough surfaces*. Oxford, New York,: Pergamon Press; distributed in the Western Hemisphere by Macmillan New York, 1963.

- [12] BENEDIC, F., BELMAHI, H., EASWARAKHANTHAN, T., and ALNOT, P., “In situ optical characterization during MPACVD diamond film growth on silicon substrates using a bichromatic infrared pyrometer under oblique incidence,” *Journal Of Physics D-Applied Physics*, vol. 34, no. 7, pp. 1048–1058, 2001.
- [13] BENEDIC, F., BRUNO, P., and PIGEAT, P., “Real-time optical monitoring of thin film growth by in situ pyrometry through multiple layers and effective media approximation modeling,” *Applied Physics Letters*, vol. 90, p. 134104, Mar. 2007.
- [14] BIERMANN, K., HASE, A., and KUNZEL, H., “Optical pyrometry for in situ control of MBE growth of (Al,Ga)As_{1-x}Sb_x compounds on InP,” *Journal Of Crystal Growth*, vol. 202, pp. 36–39, May 1999.
- [15] BOEBEL, F. G., MOLLER, H., HERTEL, B., GROTHE, H., SCHRAUD, G., SCHRODER, S., and CHOW, P., “In-situ film thickness and temperature control of molecular-beam epitaxy growth by pyrometric interferometry,” *Journal Of Crystal Growth*, vol. 150, pp. 54–61, May 1995.
- [16] BOHER, P. and STEHLE, J. L., “In situ spectroscopic ellipsometry: Present status and future needs for thin film characterisation and process control,” *Materials Science And Engineering B-Solid State Materials For Advanced Technology*, vol. 37, pp. 116–120, Feb. 1996.
- [17] BONANNI, A., STIFTER, D., MONTAIGNE-RAMIL, A., SCHMIDEGG, K., HINGERL, K., and SITTER, H., “In situ spectroscopic ellipsometry of MOCVD-grown GaN compounds for on-line composition determination and growth control,” *Journal Of Crystal Growth*, vol. 248, pp. 211–215, Feb. 2003.
- [18] BORN, M. and WOLF, E. R., *Principles of optics: electromagnetic theory of propagation, interference and diffraction of light*. Oxford; New York: Pergamon, 6th ed., 1980.
- [19] BREILAND, W. G., “Reflectance-correcting pyrometry in thin film deposition applications,” tech. rep., Sandia National Laboratories, 2003.
- [20] BREILAND, W. G. and KILLEEN, K. P., “A virtual interface method for extracting growth rates and high temperature optical constants from thin semiconductor films using *in situ* normal incidence reflectance,” *Journal Of Applied Physics*, vol. 78, no. 11, pp. 6726–6736, 1995.
- [21] BRUNO, P., BENEDIC, F., MOHASSEB, F., SILVA, F., and HASSOUNI, K., “Effects of substrate temperature on nanocrystalline diamond growth: an in-situ optical study using pyrometric interferometry,” *Thin Solid Films*, vol. 482, pp. 50–55, June 2005.
- [22] BUZEA, C. and ROBBIE, K., “State of the art in thin film thickness and deposition rate monitoring sensors,” *Reports On Progress In Physics*, vol. 68, no. 2, pp. 385–409, 2005.

- [23] CAO, B., XU, K., ISHITANI, Y., and YOSHIKAWA, A., “In-situ spectroscopic ellipsometry investigation and control of GaN growth mode in metal-organic vapor phase epitaxy at low pressures of 20 Torr,” *Thin Solid Films*, vol. 455-56, pp. 661–664, May 2004.
- [24] CARNIGLIA, C. K., “Scalar scattering theory for multilayer optical coatings,” *Optical Engineering*, vol. 18, no. 2, pp. 104–115, 1979.
- [25] CARNIGLIA, C. K. and JENSEN, D. G., “Single-layer model for surface roughness,” *Applied Optics*, vol. 41, no. 16, pp. 3167–71, 2002.
- [26] CATLEDGE, S. A., COMER, W., and VOHRA, Y. K., “In situ diagnostics of film thickness and surface roughness of diamond films on a Ti-6Al-4V alloy by optical pyrometry,” *Applied Physics Letters*, vol. 73, pp. 181–183, July 1998.
- [27] CHAN, H. Y. H., TAKOUDIS, C. G., and WEAVER, M. J., “In-situ monitoring of chemical vapor deposition at ambient pressure by surface-enhanced Raman spectroscopy: Initial growth of tantalum(V) oxide on platinum,” *Journal Of The American Chemical Society*, vol. 121, pp. 9219–9220, Oct. 1999.
- [28] CHEN, S., MASON, M. G., GYSLING, H. J., PAZPUJALT, G. R., BLANTON, T. N., CASTRO, T., CHEN, K. M., FICTORIE, C. P., GLADFELTER, W. L., FRANCIOSI, A., COHEN, P. I., and EVANS, J. F., “Ultrahigh-vacuum metalorganic chemical-vapor-deposition growth and in-situ characterization of epitaxial TiO₂ films,” *Journal Of Vacuum Science & Technology A-Vacuum Surfaces And Films*, vol. 11, no. 5, pp. 2419–2429, 1993.
- [29] CHOWDHURY, A. I., READ, W. W., RUBLOFF, G. W., TEDDER, L. L., and PARSONS, G. N., “Real-time process sensing and metrology in amorphous and selective area silicon plasma enhanced chemical vapor deposition using in situ mass spectrometry,” *Journal Of Vacuum Science & Technology B*, vol. 15, no. 1, pp. 127–132, 1997.
- [30] CHUI, C. K. and CHEN, G., *Kalman filtering: with real-time applications*. Berlin; New York: Springer, 3rd ed., 1999.
- [31] COLLINS, R. W., CONG, Y., NGUYEN, H. V., AN, I., VEDAM, K., BADZIAN, T., and MESSIER, R., “Real-time spectroscopic ellipsometry characterization of the nucleation of diamond by filament-assisted chemical vapor-deposition,” *Journal Of Applied Physics*, vol. 71, pp. 5287–5289, May 1992.
- [32] COMINA, G., RODRIGUEZ, J., SOLIS, J. L., and ESTRADA, W., “In situ laser reflectometry measurements of pyrolytic ZnO film growth,” *Measurement Science & Technology*, vol. 16, pp. 685–690, Mar. 2005.
- [33] CONG, Y., AN, I., NGUYEN, H. V., VEDAM, K., MESSIER, R., and COLLINS, R. W., “Real-time monitoring of filament-assisted chemically vapor-deposited diamond by spectroscopic ellipsometry,” *Surface & Coatings Technology*, vol. 49, pp. 381–386, Dec. 1991.

- [34] CROOK, A. W., “The reflection and transmission of light by any system of parallel isotropic films,” *Journal Of The Optical Society Of America*, vol. 38, no. 11, pp. 954–964, 1948.
- [35] CUI, R., BHAT, I., O’QUINN, B., and VENKATASUBRAMANIAN, R., “In-situ monitoring of the growth of Bi₂Te₃ and Sb₂Te₃ films and Bi₂Te₃-Sb₂Te₃ superlattice using spectroscopic ellipsometry,” *Journal Of Electronic Materials*, vol. 30, pp. 1376–1381, Nov. 2001.
- [36] DEATCHER, C. J., LIU, C., PEREIRA, S., LADA, M., CULLIS, A. G., SUN, Y. J., BRANDT, O., and WATSON, I. M., “In situ optical reflectometry applied to growth of indium gallium nitride epilayers and multi-quantum well structures,” *Semiconductor Science And Technology*, vol. 18, pp. 212–218, Apr. 2003.
- [37] DESISTO, W. J. and RAPPOLI, B. J., “Ultraviolet absorption sensors for precursor delivery rate control for metalorganic chemical vapor deposition of multiple component oxide thin films,” *Journal Of Crystal Growth*, vol. 191, pp. 290–293, July 1998.
- [38] DRAGO, M., SCHMIDTLING, T., WERNER, C., PRISTOVSEK, M., POHL, U. W., and RICHTER, W., “Inn growth and annealing investigations using in-situ spectroscopic ellipsometry,” *Journal Of Crystal Growth*, vol. 272, pp. 87–93, Dec. 2004.
- [39] DUNCAN, W. M., HENCK, S. A., KUEHNE, J. W., LOEWENSTEIN, L. M., and MAUNG, S., “High-speed spectral ellipsometry for in-situ diagnostics and process-control,” *Journal Of Vacuum Science & Technology B*, vol. 12, no. 4, pp. 2779–2784, 1994.
- [40] EBERT, M., BELL, K. A., YOO, S. D., FLOCK, K., and ASPNES, D. E., “In situ monitoring of MOVPE growth by combined spectroscopic ellipsometry and reflectance-difference spectroscopy,” *Thin Solid Films*, vol. 364, pp. 22–27, Mar. 2000.
- [41] EDGAR, T. F., BUTLER, S. W., CAMPBELL, W. J., PFEIFFER, C., BODE, C., HWANG, S. B., BALAKRISHNAN, K. S., and HAHN, J., “Automatic control in microelectronics manufacturing: Practices, challenges, and possibilities,” *Automatica*, vol. 36, no. 11, pp. 1567–1603, 2000.
- [42] FIGGE, S., BOTTCHE, T., EINFELDT, S., and HOMMEL, D., “In situ and ex situ evaluation of the film coalescence for GaN growth on GaN nucleation layers,” *Journal Of Crystal Growth*, vol. 221, pp. 262–266, Dec. 2000.
- [43] FILINSKI, I., “Effects of sample imperfections on optical spectra,” *Physica Status Solidi B-Basic Research*, vol. 49, no. 2, p. 577, 1972.

- [44] FITOURI, H., BENZARTI, Z., HALIDOU, I., BOUFADEN, T., and EL JANI, B., "Laser-reflectometry monitoring of the gan growth by movpe using sin treatment: study and simulation," *Physica Status Solidi A-Applications And Materials Science*, vol. 202, pp. 2467–2473, Oct. 2005.
- [45] FRANTA, D. and OHLIDAL, I., "Comparison of effective medium approximation and rayleigh-rice theory concerning ellipsometric characterization of rough surfaces," *Optics Communications*, vol. 248, pp. 459–467, Apr. 2005.
- [46] FUJIWARA, H., KOH, J., ROVIRA, P. I., and COLLINS, R. W., "Assessment of effective-medium theories in the analysis of nucleation and microscopic surface roughness evolution for semiconductor thin films," *Physical Review B*, vol. 61, pp. 10832–10844, Apr. 2000.
- [47] FUKAREK, W. and KERSTEN, H., "Application of dynamic in-situ ellipsometry to the deposition of tin-doped indium oxide-films by reactive direct-current magnetron sputtering," *JOURNAL OF VACUUM SCIENCE & TECHNOLOGY A-VACUUM SURFACES AND FILMS*, vol. 12, no. 2, pp. 523–528, 1994.
- [48] FULEM, M., RUZICKA, K., RUZICKA, V., SIMECEK, T., HULICIUS, E., and PANGRAC, J., "Vapour pressure and heat capacities of metal organic precursors, Y(thd)(3) and Zr(thd)(4)," *Journal of Crystal Growth*, vol. 264, no. 1-3, pp. 192–200, 2004.
- [49] GABOR, T. and BLOCHER, J. M., "In situ transmission electronmicroscopic study of crystal growth by chemical vapor deposition," *Journal Of Vacuum Science & Technology*, vol. 6, no. 5, pp. 815–&, 1969.
- [50] GALARZA, C. G., KHARGONEKAR, P. P., LAYADI, N., VINCENT, T. L., RIETMAN, E. A., and LEE, J. T. C., "A new algorithm for real-time thin film thickness estimation given in situ multiwavelength ellipsometry using an extended Kalman filter," *Thin Solid Films*, vol. 313, pp. 156–160, Feb. 1998.
- [51] GAO, Y., "In-situ IR and spectroscopic ellipsometric analysis of growth process and structural properties of Ti1-xNbxO2 thin films by metal-organic chemical vapor deposition," *Thin Solid Films*, vol. 346, pp. 73–81, June 1999.
- [52] GASQUERES, C., MAURY, F., and OSSOLA, F., "In-situ optical pyrometry in the CVD of metallic thin films for real time control of the growth," *Chemical Vapor Deposition*, vol. 9, pp. 34–39, Jan. 2003.
- [53] GOUGOUSI, T., XU, Y. H., KIDDER, J. N., RUBLOFF, G. W., and TILFORD, C. R., "Process diagnostics and thickness metrology using in situ mass spectrometry for the chemical vapor deposition of W from H-2/WF6," *Journal Of Vacuum Science & Technology B*, vol. 18, no. 3, pp. 1352–1363, 2000.

- [54] HANAOKA, K., OHNISHI, H., and TACHIBANA, K., “In-situ measurement of gas-phase reactions in metal-organic chemical-vapor-deposition of copper-films by Fourier-transform infrared-spectroscopy,” *Japanese Journal Of Applied Physics Part 1-Regular Papers Short Notes & Review Papers*, vol. 32, pp. 4774–4778, Oct. 1993.
- [55] HANAOKA, K., OHNISHI, H., and TACHIBANA, K., “In-situ monitoring of selective copper deposition processes in a metal-organic chemical-vapor-deposition using Fourier-transform infrared reflection-absorption spectroscopy,” *Japanese Journal Of Applied Physics Part 1-Regular Papers Short Notes & Review Papers*, vol. 34, pp. 2430–2439, May 1995.
- [56] HANAOKA, K., TACHIBANA, K., and OHNISHI, H., “In-situ measurement of gas-phase reactions during the metal-organic chemical-vapor-deposition of copper using Fourier-transform infrared-spectroscopy,” *Thin Solid Films*, vol. 262, pp. 209–217, June 1995.
- [57] HARDTDEGEN, H., KALUZA, N., SCHMIDT, R., STEINS, R., YAKOVLEV, E. V., TALALAEV, R. A., MAKAROV, Y. N., and ZETTLER, J. T., “Mocpe growth and in situ characterization of GaN layers on sapphire substrates,” *Physica Status Solidi A-Applied Research*, vol. 201, pp. 312–319, Jan. 2004.
- [58] HASELTINE, E. L. and RAWLINGS, J. B., “Critical evaluation of extended kalman filtering and moving-horizon estimation,” *Industrial & Engineering Chemistry Research*, vol. 44, pp. 2451–2460, Apr. 2005.
- [59] HAUSMANN, A., WEIDNER, G., WEIDNER, M., and RITTER, G., “Investigation of thin Al layer growth with in situ infrared spectroscopic ellipsometry,” *Thin Solid Films*, vol. 318, pp. 124–127, Apr. 1998.
- [60] HAYASHI, Y., DRAWL, W., COLLINS, R. W., and MESSIER, R., “In-process ellipsometric monitoring of diamond film growth by microwave plasma enhanced chemical vapor-deposition,” *Applied Physics Letters*, vol. 60, pp. 2868–2870, June 1992.
- [61] HEIL, S. B. S., LANGEREIS, E., KEMMEREN, A., ROOZEBOOM, F., DE SANDEN, M. C. M. V., and KESSELS, W. M. M., “Plasma-assisted atomic layer deposition of TiN monitored by in situ spectroscopic ellipsometry,” *Journal Of Vacuum Science & Technology A*, vol. 23, no. 4, pp. L5–L8, 2005.
- [62] HEITZ, T. and DREVILLON, B., “In situ infrared ellipsometry study of the growth of hydrogenated amorphous carbon thin films,” *Thin Solid Films*, vol. 313, pp. 704–707, Feb. 1998.
- [63] IRENE, E. A. and WOOLAM, J. A., “In-situ ellipsometry in microelectronics,” *MRS Bulletin*, vol. 20, pp. 24–28, May 1995.

- [64] IRVINE, S. J. C., HARTLEY, A., and STAFFORD, A., "In situ monitoring of the MOCVD growth of CdS/CdTe," *Journal Of Crystal Growth*, vol. 221, pp. 117–123, Dec. 2000.
- [65] JACOB, W., "Surface reactions during growth and erosion of hydrocarbon films," *Thin Solid Films*, vol. 326, pp. 1–42, Aug. 1998.
- [66] JELLISON, G. E. and BURKE, H. H., "The temperature dependence of the refractive index of silicon at elevated temperatures at several laser wavelengths," *Journal Of Applied Physics*, vol. 60, no. 2, pp. 841–843, 1986.
- [67] JELLISON, G. E. and MODINE, F. A., "Optical functions of silicon at elevated temperatures," *Journal Of Applied Physics*, vol. 76, no. 6, pp. 3758–3761, 1994.
- [68] JOHS, B., HERZINGER, C., DINAN, J. H., CORNFELD, A., BENSON, J. D., DOCTOR, D., OLSON, G., FERGUSON, I., PELCZYNSKI, M., CHOW, P., KUO, C. H., and JOHNSON, S., "Real-time monitoring and control of epitaxial semiconductor growth in a production environment by in situ spectroscopic ellipsometry," *Thin Solid Films*, vol. 313, pp. 490–495, Feb. 1998.
- [69] JONAS, S., PTAK, W. S., SADOWSKI, W., WALASEK, E., and PALUSZKIEWICZ, C., "FTIR in-situ studies of the gas-phase reactions in chemical-vapor-deposition of SiC," *Journal Of The Electrochemical Society*, vol. 142, pp. 2357–2362, July 1995.
- [70] KALOYEROS, A. E., ZHENG, B., LOU, I. S., LAU, J., and HELLGETH, J. W., "In-situ mass-spectral and IR studies of the role of auxiliary reagents in the enhancement of copper growth in the chemical-vapor-deposition of Cu(II) beta-diketonate precursors," *Thin Solid Films*, vol. 262, pp. 20–30, June 1995.
- [71] KANEKO, T., AKAO, N., HARA, N., and SUGIMOTO, K., "In situ ellipsometry analysis on formation process of Al_2O_3 - Ta_2O_5 films in ion beam sputter deposition," *JOURNAL OF THE ELECTROCHEMICAL SOCIETY*, vol. 152, no. 4, pp. B133–B139, 2005.
- [72] KAYS, W. M. and CRAWFORD, M. E., *Convective heat and mass transfer*. New York : McGraw-Hill, 3rd ed. ed., 1993.
- [73] KELLERMAN, B. K., CHASON, E., ADAMS, D. P., MAYER, T. M., and WHITE, J. M., "In-situ X-ray reflectivity investigation of growth and surface morphology evolution during Fe chemical vapor deposition on Si(001)," *Surface Science*, vol. 375, pp. 331–339, Apr. 1997.
- [74] KHARCHENKO, A., LISCHKA, K., SCHMIDEGG, K., SITTER, H., BETHKE, J., and WOITOK, J., "In situ and real-time characterization of metal-organic chemical vapor deposition growth by high resolution X-ray diffraction," *Review Of Scientific Instruments*, vol. 76, p. 033101, Mar. 2005.

- [75] KIM, M., THIEME, H. J., LIPPERT, G., and OSTEN, H. J., “Optical in situ measurements of temperature and layer thickness in Si molecular beam epitaxy,” *Journal Of Crystal Growth*, vol. 169, pp. 681–688, Dec. 1996.
- [76] KLIE, R. F., BROWNING, N. D., CHOWDHURI, A. R., and TAKOUDIS, C. G., “Analysis of ultrathin SiO₂ interface layers in chemical vapor deposition of Al₂O₃ on Si by in situ scanning transmission electron microscopy,” *Applied Physics Letters*, vol. 83, pp. 1187–1189, Aug. 2003.
- [77] KOH, J., LU, Y. W., WRONSKI, C. R., KUANG, Y. L., COLLINS, R. W., TSONG, T. T., and STRAUSSER, Y. E., “Correlation of real time spectroellipsometry and atomic force microscopy measurements of surface roughness on amorphous semiconductor thin films,” *Applied Physics Letters*, vol. 69, pp. 1297–1299, Aug. 1996.
- [78] KUSZELEWICZ, R., RAFFLE, Y., AZOULAY, R., DUGRAND, L., and LEROUX, G., “In-situ metalorganic growth-control of GaAlAs thick layers using 1.32- μ m laser reflectometry,” *Journal Of Crystal Growth*, vol. 147, pp. 251–255, Feb. 1995.
- [79] LANGEREIS, E., HEIL, S. B. S., VAN DE SANDEN, M. C. M., and KESSELS, W. M. M., “In situ spectroscopic ellipsometry study on the growth of ultrathin tin films by plasma-assisted atomic layer deposition,” *JOURNAL OF APPLIED PHYSICS*, vol. 100, p. 023534, July 2006.
- [80] LARCIPRETE, R., COZZI, S., MASETTI, E., and MONTECCHI, M., “Uhv-cvd Ge/Si(100) heteroepitaxy monitored by in situ ellipsometry,” *Applied Surface Science*, vol. 102, pp. 52–56, Aug. 1996.
- [81] LEE, J. S., SUGOU, S., and MASUMOTO, Y., “In situ observation of ellipsometry monolayer oscillations of metalorganic vapor-phase epitaxy-grown III-V compound materials,” *Journal Of Crystal Growth*, vol. 209, pp. 614–620, Feb. 2000.
- [82] LEVI, D. H., NELSON, B. P., IWANIZCKO, E., and TEPLIN, C. W., “In-situ studies of the growth of amorphous and nanocrystalline silicon using real time spectroscopic ellipsometry,” *Thin Solid Films*, vol. 455-56, pp. 679–683, May 2004.
- [83] LEVI, D. H., NELSON, B. P., PERKINS, J. D., and MOUTINHO, H. R., “In situ studies of the amorphous to microcrystalline transition of hot-wire chemical vapor deposition si : H films using real-time spectroscopic ellipsometry,” *JOURNAL OF VACUUM SCIENCE & TECHNOLOGY A*, vol. 21, no. 4, pp. 1545–1549, 2003.
- [84] LI, X., HAYASHI, Y., and NISHINO, S., “In-situ ellipsometry study of initial stage of bias-enhanced nucleation and heteroepitaxy of diamond on silicon(100)

by hot filament chemical vapor deposition,” *Diamond And Related Materials*, vol. 6, pp. 1117–1123, July 1997.

- [85] LIU, C., STEPANOV, S., SHIELDS, P. A., GOTT, A., WANG, W. N., STEIMETZ, E., and ZETTLER, J. T., “In situ monitoring of GaN epitaxial lateral overgrowth by spectroscopic reflectometry,” *Applied Physics Letters*, vol. 88, p. 101103, Mar. 2006.
- [86] LIU, C. W. and WATSON, I. M., “Quantitative simulation of in situ reflectance data from metal organic vapour phase epitaxy of GaN on sapphire,” *Semiconductor Science And Technology*, vol. 22, pp. 629–635, June 2007.
- [87] LIU, Q., SPANOS, L., ZHAO, C., and IRENE, E. A., “Morphology study of the thermal-oxidation of rough silicon surfaces,” *Journal Of Vacuum Science & Technology A-Vacuum Surfaces And Films*, vol. 13, no. 4, pp. 1977–1983, 1995.
- [88] LIU, Q., WALL, J. F., and IRENE, E. A., “Si/sio2 interface studies by spectroscopic immersion ellipsometry and atomic-force microscopy,” *Journal Of Vacuum Science & Technology A-Vacuum Surfaces And Films*, vol. 12, no. 5, pp. 2625–2629, 1994.
- [89] LUO, J. L., YING, X. T., WANG, P. N., and CHEN, L. Y., “Study on the growth of CVD diamond thin films by *in situ* reflectivity measurement,” *Diamond And Related Materials*, vol. 11, pp. 1871–1875, 2002.
- [90] MANTESE, L., SELINIDIS, K., WILSON, P. T., LIM, D., JIANG, Y. Y., EKERDT, J. G., and DOWNER, M. C., “In situ control and monitoring of doped and compositionally graded SiGe films using spectroscopic ellipsometry and second harmonic generation,” *Applied Surface Science*, vol. 154, pp. 229–237, Feb. 2000.
- [91] MAYBECK, P. S., *Stochastic models, estimation and control*. Mathematics in science and engineering; v. 141, New York: Academic Press, 1979.
- [92] MCFALL, W. D., MCKENZIE, D. R., and NETTERFIELD, R. P., “Use of in situ ellipsometry to observe phase transitions during boron nitride thin film deposition,” *Surface & Coatings Technology*, vol. 81, pp. 72–78, May 1996.
- [93] MEYNE, C., GENSCHE, M., PETERS, S., POHL, U. W., ZETTLER, J. T., and RICHTER, W., “In situ monitoring of ZnS/GaP and ZnSe/GaAs metalorganic vapor phase epitaxy using reflectance anisotropy spectroscopy and spectroscopic ellipsometry,” *Thin Solid Films*, vol. 364, pp. 12–15, Mar. 2000.
- [94] MIDDLEBROOKS, S. A., *Modelling and control of silicon and germanium thin film chemical vapor deposition*. PhD thesis, University of Wisconsin-Madison, 2001.

- [95] MIDDLEBROOKS, S. A. and RAWLINGS, J. B., "Model predictive control of Si_{1-x}G_x thin film chemical-vapor deposition," *IEEE Transactions On Semiconductor Manufacturing*, vol. 20, pp. 114–125, May 2007.
- [96] MOMOSE, S., NAKAMURA, T., and TACHIBANA, K., "Effects of gas-phase thermal decompositions of chemical vapor deposition source molecules on the deposition of (Ba, Sr)TiO₃ films: A study by in situ Fourier transform infrared spectroscopy," *Japanese Journal Of Applied Physics Part 1-Regular Papers Short Notes & Review Papers*, vol. 39, pp. 5384–5388, Sept. 2000.
- [97] MOMOSE, S., SAHARA, R., NAKAMURA, T., and TACHIBANA, K., "Diagnosis of oxidation reactions in metalorganic chemical vapor deposition of (Ba, Sr)TiO₃ films by in situ Fourier transform infrared spectroscopy," *Japanese Journal Of Applied Physics Part 1-Regular Papers Short Notes & Review Papers*, vol. 40, pp. 5501–5506, Sept. 2001.
- [98] MORITANI, A., KITAHARA, K., KITAMURA, T., KATAYAMA, H., KANAYAMA, N., and SUZUKI, M., "In situ spectroscopic ellipsometry of carbon nucleation and growth on si in a deposition process by dc glow discharge of methane," *THIN SOLID FILMS*, vol. 386, pp. 137–141, May 2001.
- [99] MOYNE, J., DEL CASTILLO, E., and HURWITZ, A. M., *Run-to-run control in semiconductor manufacturing*. Boca Raton, FL: CRC Press, 2001.
- [100] MURTHY, S. D. and BHAT, I. B., "In situ monitoring of CdTe nucleation on GaAs(100) using spectroscopic ellipsometry," *Journal Of Crystal Growth*, vol. 170, pp. 193–197, Jan. 1997.
- [101] MURTY, M. V. R., STREIFFER, S. K., STEPHENSON, G. B., EASTMAN, J. A., BAI, G. R., MUNKHOLM, A., AUCIELLO, O., and THOMPSON, C., "In situ x-ray scattering study of PbTiO₃ chemical-vapor deposition," *Applied Physics Letters*, vol. 80, pp. 1809–1811, Mar. 2002.
- [102] MUTOH, K., TAKEYAMA, S., YAMADA, Y., and MIYATA, T., "In-situ auger-electron spectroscopy of silicon thin-films fabricated using arf excimer laser-induced chemical-vapor-deposition and the oxidation process," *Applied Surface Science*, vol. 80, pp. 459–464, May 1994.
- [103] NAKAMURA, S., "Analysis of real-time monitoring using interference effects," *Japanese Journal Of Applied Physics Part 1-Regular Papers Short Notes & Review Papers*, vol. 30, pp. 1348–1353, July 1991.
- [104] NAKAMURA, S., "In situ monitoring of GaN growth using interference effects," *Japanese Journal Of Applied Physics Part 1-Regular Papers Short Notes & Review Papers*, vol. 30, pp. 1620–1627, Aug. 1991.
- [105] NAKAMURA, T., MOMOSE, S., SAHARA, R., and TACHIBANA, K., "Reaction mechanism of alkoxy derivatives of titanium diketonates as source molecules in

- liquid source metalorganic chemical vapor deposition of (Ba,Sr)TiO₃ films: A study by in situ infrared absorption spectroscopy,” *Japanese Journal Of Applied Physics Part 1-Regular Papers Short Notes & Review Papers*, vol. 41, pp. 6624–6627, Nov. 2002.
- [106] PALIK, E. D., *Handbook of optical constants of solids*. Orlando: Academic Press, 1985.
- [107] PALIK, E. D. and GHOSH, G. R., *Handbook of optical constants of solids*. San Diego: Academic Press, 1998.
- [108] PETERS, S., SCHMIDTLING, T., TREPKE, T., POHL, U. W., ZETTLER, J. T., and RICHTER, W., “In situ monitoring of GaN metal-organic vapor phase epitaxy by spectroscopic ellipsometry,” *Journal Of Applied Physics*, vol. 88, pp. 4085–4090, Oct. 2000.
- [109] PETRIK, P., BIRO, L. P., FRIED, M., LOHNER, T., BERGER, R., SCHNEIDER, C., GYULAI, J., and RYSSEL, H., “Comparative study of surface roughness measured on polysilicon using spectroscopic ellipsometry and atomic force microscopy,” *Thin Solid Films*, vol. 315, pp. 186–191, Mar. 1998.
- [110] PIERSON, H. O., *Handbook of chemical vapor deposition (CVD): principles, technology, and applications*. Norwich, N.Y.: Noyes Publications/William Andrew Pub., 2nd ed., 1999.
- [111] PIRNGRUBER, G. D., ROY, P. K., and WEIHER, N., “An in situ x-ray absorption spectroscopy study of N₂O decomposition over Fe-ZSM-5 prepared by chemical vapor deposition of FeCl₃,” *Journal Of Physical Chemistry B*, vol. 108, pp. 13746–13754, Sept. 2004.
- [112] PITTAL, S., JOHS, B., HE, P., WOOLLAM, J. A., MURTHY, S. D., and BHAT, I. B., “In-situ monitoring and control of MOCVD growth using multi-wavelength ellipsometry,” *Compound Semiconductors 1994*, no. 141, pp. 41–44, 1995.
- [113] PULVER, M., NEMETZ, W., and WAHL, G., “CVD of ZrO₂, Al₂O₃ and Y₂O₃ from metalorganic compounds in different reactors,” *Surface & Coatings Technology*, vol. 125, no. 1-3, pp. 400–406, 2000.
- [114] PULVER, M., WAHL, G., SCHEYTT, H., and SOMMER, M., “Deposition of ZrO₂ and Y₂O₃-stabilized ZrO₂ from beta-diketonates,” *Journal De Physique Iv*, vol. 3, no. C3, pp. 305–312, 1993.
- [115] RAM, G. B. B., GUPTA, S. K., and SARAF, D. N., “Free-radical polymerizations associated with the trommsdorff effect under semibatch reactor conditions .4. on-line inferential-state estimation,” *Journal Of Applied Polymer Science*, vol. 64, pp. 1861–1877, June 1997.

- [116] RAMIL, A. M., SCHMIDEGG, K., BONANNI, A., SITTER, H., STIFTER, D., LI, S. F., AS, D. J., and LISCHKA, K., "In-situ growth monitoring by spectroscopy ellipsometry of MOCVD cubic-GaN(001)," *Thin Solid Films*, vol. 455-56, pp. 684-687, May 2004.
- [117] RAO, C. V., RAWLINGS, J. B., and LEE, J. H., "Constrained linear state estimation using a moving horizon approach," *Automatica*, vol. 37, pp. 1619-1628, Oct. 2001.
- [118] RAO, C. V., RAWLINGS, J. B., and MAYNE, D. Q., "Constrained state estimation for nonlinear discrete-time systems: Stability and moving horizon approximations," *IEEE Transaction On Automatic Control*, vol. 48, pp. 246-258, Feb. 2003.
- [119] RAPPOLI, B. J. and DESISTO, W. J., "Gas phase ultraviolet spectroscopy of high-temperature superconductor precursors for chemical vapor deposition processing," *Applied Physics Letters*, vol. 68, pp. 2726-2728, May 1996.
- [120] REBEY, A., HABCHI, M. M., BCHETNIA, A., and EL JANI, B., "In situ reflectance monitoring of the growth and etching of AlAs/GaAs structures in MOVPE," *Journal Of Crystal Growth*, vol. 261, pp. 450-457, Feb. 2004.
- [121] REBEY, A., HABCHI, M. M., BENZARTI, Z., and EL JANI, B., "Study of GaAs layers grown on Ge substrates by MOVPE and in situ monitored by laser reflectometry," *Microelectronics Journal*, vol. 35, pp. 179-184, Feb. 2004.
- [122] REENTILA, O., MATTILA, M., SOPANEN, M., and LIPSANEN, H., "In situ determination of InGaAs and GaAsN composition in multiquantum-well structures," *Journal Of Applied Physics*, vol. 101, p. 033533, Feb. 2007.
- [123] REIJNEN, L., MEESTER, B., GOOSSENS, A., and SCHOONMAN, J., "In situ mass spectrometric study of pyrite (FeS₂) thin film deposition with metal-organic chemical vapor deposition," *Journal Of The Electrochemical Society*, vol. 147, pp. 1803-1806, May 2000.
- [124] ROBERTSON, D. G. and LEE, J. H., "A least-squares formulation for state estimation," *Journal Of Process Control*, vol. 5, pp. 291-299, Aug. 1995.
- [125] ROBERTSON, D. G., LEE, J. H., and RAWLINGS, J. B., "A moving horizon-based approach for least-squares estimation," *AIChE Journal*, vol. 42, pp. 2209-2224, Aug. 1996.
- [126] ROSMAN, N., ABELLO, L., CHABERT, J. P., VERVEN, G., and LUCAZEAU, G., "In-situ Raman characterization of a diamond film during its growth-process in a plasma-jet chemical-vapor-deposition reactor," *Journal Of Applied Physics*, vol. 78, pp. 519-527, July 1995.

- [127] SCHINELLER, B. and HEUKEN, M., “Recent advances in MOCVD process technology for the growth of compound semiconductor devices,” *Applied Physics A-Materials Science & Processing*, vol. 87, pp. 479–483, June 2007.
- [128] SCHMIDEGG, K., KHARCHENKO, A., BONANNI, A., SITTER, H., BETHKE, J., and LISCHKA, K., “Characterization of metalorganic chemical vapor deposition growth of cubic GaN by in situ x-ray diffraction,” *Journal Of Vacuum Science & Technology B*, vol. 22, no. 4, pp. 2165–2168, 2004.
- [129] SCHMIDEGG, K., NEUWIRT, G., STIFTER, D., SITTER, H., and BONANNI, A., “In situ optical analysis of low temperature MOCVD GaN nucleation layer formation via multiple wavelength ellipsometry,” *Journal Of Crystal Growth*, vol. 272, pp. 106–110, Dec. 2004.
- [130] SCHMIDTLING, T., POHL, U. W., RICHTER, W., and PETERS, S., “In situ spectroscopic ellipsometry study of GaN nucleation layer growth and annealing on sapphire in metal-organic vapor-phase epitaxy,” *Journal Of Applied Physics*, vol. 98, p. 033522, Aug. 2005.
- [131] SESHAN, K., *Handbook of thin-film deposition processes and techniques : principles, methods, equipment and applications*. Norwich, N.Y.: Noyes Publications/William Andrew Pub., 2nd ed., 2002.
- [132] SHIRAI, H., DREVILLON, B., and SHIMIZU, I., “Role of hydrogen plasma during growth of hydrogenated microcrystalline silicon-in-situ uv-visible and infrared ellipsometry study,” *Japanese Journal Of Applied Physics Part 1-Regular Papers Short Notes & Review Papers*, vol. 33, pp. 5590–5598, Oct. 1994.
- [133] SIMBRUNNER, C., SCHMIDEGG, K., BONANNI, A., KHARCHENKO, A., BETHKE, J., WOITOK, J., LISCHKA, K., and SITTER, H., “In-situ and real-time monitoring of MOCVD growth of III-nitrides by simultaneous multi-wavelength-ellipsometry and X-ray-diffraction,” *Physica Status Solidi A-Applications And Materials Science*, vol. 203, pp. 1704–1707, May 2006.
- [134] SNAIL, K. A. and MARKS, C. M., “In situ diamond growth rate measurement using emission interferometry,” *Applied Physics Letters*, vol. 60, no. 25, pp. 3135–3137, 1992.
- [135] STAFFORD, A., IRVINE, S. J. C., BOUGRIOUA, Z., JACOBS, K., MOERMAN, I., THRUSH, E. J., and CONSIDINE, L., “Quantifying the smoothing of GaN epilayer growth by in situ laser interferometry,” *Journal Of Crystal Growth*, vol. 221, pp. 142–148, Dec. 2000. ok.
- [136] STAFFORD, A., IRVINE, S. J. C., HESS, K. L., and BAJAJ, J., “The use of in situ laser interferometry for MOCVD process control,” *Semiconductor Science And Technology*, vol. 13, pp. 1407–1411, Dec. 1998.

- [137] STEIMETZ, E., ZETTLER, J. T., SCHIENLE, F., TREPKE, T., WETHKAMP, T., RICHTER, W., and SIEBER, I., "In situ monitoring of InAs-on-GaAs quantum dot formation in MOVPE by reflectance-anisotropy-spectroscopy and ellipsometry," *Applied Surface Science*, vol. 107, pp. 203–211, Nov. 1996.
- [138] SUDO, S., NAKANO, Y., SUGIYAMA, M., SHIMOGAKI, Y., KOMIYAMA, H., and TADA, K., "In-situ As-P exchange monitoring in metal-organic vapor phase epitaxy of InGaAs/InP heterostructure by spectroscopic and kinetic ellipsometry," *Thin Solid Films*, vol. 313, pp. 604–608, Feb. 1998.
- [139] SUGAI, K., OKABAYASHI, H., KOBAYASHI, A., YAKO, T., and KISHIDA, S., "In-situ monitoring of Al growth in chemical-vapor-deposition by detecting reflected laser-light intensity," *Japanese Journal Of Applied Physics Part 2-Letters*, vol. 34, pp. L429–L432, Apr. 1995.
- [140] SUN, Y. K., ZHANG, X. A., and GRIGOROPOULOS, C. P., "Spectral optical functions of silicon in the range of 1.13-4.96 eV at elevated temperatures," *International Journal Of Heat And Mass Transfer*, vol. 40, pp. 1591–1600, May 1997.
- [141] TACHIBANA, K., SHIRAFUJI, T., HAYASHI, Y., MAEKAWA, S., and MORITA, T., "In-situ ellipsometric monitoring of the growth of polycrystalline silicon thin-films by RF plasma chemical-vapor-deposition," *Japanese Journal Of Applied Physics Part 1-Regular Papers Short Notes & Review Papers*, vol. 33, pp. 4191–4194, July 1994.
- [142] TANIYASU, Y. and YOSHIKAWA, A., "In-situ monitoring of surface stoichiometry and growth kinetics study of GaN (0001) in MOVPE by spectroscopic ellipsometry," *Journal Of Electronic Materials*, vol. 30, pp. 1402–1407, Nov. 2001.
- [143] TEDDER, L. L., RUBLOFF, G. W., COHAGHAN, B. F., and PARSONS, G. N., "Dynamic rate and thickness metrology during poly-Si rapid thermal chemical vapor deposition from SiH₄ using real time in situ mass spectrometry," *Journal Of Vacuum Science & Technology A-Vacuum Surfaces And Films*, vol. 14, no. 2, pp. 267–270, 1996.
- [144] TEDDER, L. L., RUBLOFF, G. W., SHAREEF, I., ANDERLE, M., KIM, D. H., and PARSONS, G. N., "Real-time process and product diagnostics in rapid thermal chemical-vapor-deposition using in-situ mass-spectrometric sampling," *Journal Of Vacuum Science & Technology B*, vol. 13, no. 4, pp. 1924–1927, 1995.
- [145] THOMAS, M. E., JOSEPH, R. I., and TROPF, W. J., "Infrared transmission properties of sapphire, spinel, yttria, and ALON as a function of temperature and frequency," *Applied Optics*, vol. 27, pp. 239–245, 1988.

- [146] TOMPKINS, H. G. and IRENE, E. A., *Handbook of ellipsometry*. Norwich, NY : William Andrew Pub. ; Heidelberg, Germany : Springer, 2005.
- [147] TOMPKINS, H. G. and MCGAHAN, W. A., *Spectroscopic ellipsometry and reflectometry: a user's guide*. New York: Wiley, 1999.
- [148] TREPKE, T., ZORN, M., ZETTLER, J. T., KLEIN, M., and RICHTER, W., "Spectroscopic ellipsometry applied for in-situ control of lattice matched III-V growth in MOVPE," *Thin Solid Films*, vol. 313, pp. 496–500, Feb. 1998.
- [149] TRIPATHI, A. B., *In-situ diagnostics for metalorganic chemical vapor deposition of YBCO*. PhD thesis, California Institute of Technology, 2001.
- [150] TYLER, M. L., ASANO, K., and MORARI, M., "Application of moving horizon estimation based fault detection to cold tandem steel mill," *International Journal Of Control*, vol. 73, pp. 427–438, Mar. 2000.
- [151] URBAN, F. K. and COMFORT, J. C., "Numerical ellipsometry enhancement of new algorithms for real-time, in-situ film growth monitoring," *THIN SOLID FILMS*, vol. 253, pp. 262–268, Dec. 1994.
- [152] URBAN, F. K. and TABET, M. F., "Virtual interface method for in-situ ellipsometry of films grown on unknown substrates," *JOURNAL OF VACUUM SCIENCE & TECHNOLOGY A-VACUUM SURFACES AND FILMS*, vol. 11, no. 4, pp. 976–980, 1993.
- [153] URBAN, F. K. and TABET, M. F., "Development of artificial neural networks for in-situ ellipsometry of films growing on unknown substrates," *JOURNAL OF VACUUM SCIENCE & TECHNOLOGY A-VACUUM SURFACES AND FILMS*, vol. 12, no. 4, pp. 1952–1956, 1994.
- [154] VALDES-GONZALEZ, H., FLAUS, J. M., and ACUNA, G., "Moving horizon state estimation with global convergence using interval techniques: application to biotechnological processes," *Journal Of Process Control*, vol. 13, pp. 325–336, June 2003.
- [155] VALLEE, C., GOULLET, A., NICOLAZO, F., GRANIER, A., and TURBAN, G., "In situ ellipsometry and infrared analysis of pecvd sio2 films deposited in an o-2/teos helicon reactor," *JOURNAL OF NON-CRYSTALLINE SOLIDS*, vol. 216, pp. 48–54, Aug. 1997.
- [156] VERGOHL, M., HUNSCHE, B., MALKOMES, N., MATTHEE, T., and SZYSZKA, B., "Stabilization of high-deposition-rate reactive magnetron sputtering of oxides by in situ spectroscopic ellipsometry and plasma diagnostics," *JOURNAL OF VACUUM SCIENCE & TECHNOLOGY A-VACUUM SURFACES AND FILMS*, vol. 18, no. 4, pp. 1709–1712, 2000.

- [157] VINCENT, T. L., KHARGONEKAR, P. P., and TERRY, F. L., J., “An extended Kalman filter based method for fast *in situ* etch rate measurements,” *Materials Research Society Symposium Proceedings*, vol. 406, no. Diagnostic Techniques for Semiconductor Materials Processing II, pp. 87–93, 1996.
- [158] VINCENT, T. L., KHARGONEKAR, P. P., and TERRY, FRED L., J., “End point and etch rate control using dual-wavelength laser reflectometry with a nonlinear estimator,” *Journal Of The Electrochemical Society*, vol. 144, no. 7, pp. 2467–2472, 1997.
- [159] VON KEUDELL, A., SCHWARZ-SELINGER, T., and JACOB, W., “Surface relaxation during plasma chemical vapor deposition of diamond-like carbon films, investigated by in-situ ellipsometry,” *Thin Solid Films*, vol. 308, pp. 195–198, Oct. 1997.
- [160] VONKEUDELL, A. and JACOB, W., “Growth and erosion of hydrocarbon films investigated by in situ ellipsometry,” *Journal Of Applied Physics*, vol. 79, pp. 1092–1098, Jan. 1996.
- [161] VONKEUDELL, A. and JACOB, W., “Surface relaxation during plasma-enhanced chemical vapor deposition of hydrocarbon films, investigated by in situ ellipsometry,” *Journal Of Applied Physics*, vol. 81, pp. 1531–1535, Feb. 1997.
- [162] VONKEUDELL, A., JACOB, W., and FUKAREK, W., “Role of hydrogen-ions in plasma-enhanced chemical-vapor-deposition of hydrocarbon films, investigated by in-situ ellipsometry,” *APPLIED PHYSICS LETTERS*, vol. 66, pp. 1322–1324, Mar. 1995.
- [163] WALL, J. F., CLAUBERG, E., MURRAY, R. W., and IRENE, E. A., “Real-time monitoring of the deposition and growth of thin organic films by in-situ ellipsometry,” *Journal Of Vacuum Science & Technology A-Vacuum Surfaces And Films*, vol. 13, no. 5, pp. 2348–2354, 1995.
- [164] WEIDNER, M., WEIDNER, G., HAUSMANN, P., and RITTER, G., “In situ infrared spectroscopic ellipsometry for blanket aluminum chemical vapor deposition on tin and on SiO_2/Si ,” *THIN SOLID FILMS*, vol. 313, pp. 737–741, Feb. 1998.
- [165] WOO, W. W., SVORONOS, S. A., SANKUR, H. O., BAJAJ, J., and IRVINE, S. J. C., “*In situ* estimation of MOCVD growth rate via a modified Kalman filter,” *AICHE Journal*, vol. 42, pp. 1319–1325, May 1996.
- [166] XIONG, R. T. and GALLIVAN, M. A., “Moving horizon estimation for *in situ* monitoring of chemical vapor deposition process,” in *Proceedings Of the American Control Conference*, (New York), July 2007.

- [167] XIONG, R. T., WISSMANN, P. J., and GALLIVAN, M. A., “An extended Kalman filter for *in situ* sensing of yttria-stabilized zirconia in chemical vapor deposition,” *Computers & Chemical Engineering*, vol. 30, pp. 1657–1669, 2006.
- [168] XU, Y., GOUGOUSI, T., HENN-LECORDIER, L., LIU, Y., CHO, S., and RUBLOFF, G. W., “Thickness metrology and end point control in w chemical vapor deposition process from SiH₄/WF₆ using *in situ* mass spectrometry,” *Journal Of Vacuum Science & Technology B*, vol. 20, no. 6, pp. 2351–2360, 2002.
- [169] YAMAMOTO, S., SUGAI, S., MATSUKAWA, Y., SENGOKU, A., TOBISAKA, H., HATTORI, T., and ODA, S., “*In situ* growth monitoring during metalorganic chemical vapor deposition of YBa₂Cu₃O_x thin films by spectroscopic ellipsometry,” *Japanese Journal Of Applied Physics Part 2-Letters*, vol. 38, pp. L632–L635, June 1999.
- [170] YAMAUCHI, Y., UWAI, K., and KOBAYASHI, N., “*In-situ* spectrum observation of Ga deposition process during GaAsGaAs metal-organic chemical-vapor-deposition using surface photoabsorption,” *Japanese Journal Of Applied Physics Part 2-Letters*, vol. 32, pp. L1380–L1382, Oct. 1993.
- [171] YANG, Y., JAYARAMAN, S., SPERLING, B., KIM, D. Y., GIROLAMI, G. S., and ABELSON, J. R., “*In situ* spectroscopic ellipsometry analyses of hafnium diboride thin films deposited by single-source chemical vapor deposition,” *JOURNAL OF VACUUM SCIENCE & TECHNOLOGY A*, vol. 25, no. 1, pp. 200–206, 2007.
- [172] YIN, Z., TAN, H. S., and SMITH, F. W., “Determination of the optical constants of diamond films with a rough growth surface,” *Diamond And Related Materials*, vol. 5, no. 12, pp. 1490–1496, 1996.
- [173] YOSHIKAWA, A., XU, K., TANIYASU, Y., and TAKAHASHI, K., “Spectroscopic ellipsometry *in-situ* monitoring/control of GaN epitaxial growth in MBE and MOVPE,” *Physica Status Solidi A-Applied Research*, vol. 190, pp. 33–41, Mar. 2002.
- [174] ZHENG, B., BRAECKELMANN, G., KUJAWSKI, K., LOU, I., LANE, S., and KALOYEROS, A. E., “*In-situ* mass-spectral and infrared studies of the gas-phase evolution and decomposition pathways of Cu-II(HFAC)(2) application in the development of plasma-assisted chemical-vapor-deposition of copper,” *Journal Of The Electrochemical Society*, vol. 142, pp. 3896–3903, Nov. 1995.
- [175] ZHENG, B., GOLDBERG, C., EISENBRAUN, E. T., LIU, J., KALOYEROS, A. E., TOSCANO, P. J., MURARKA, S. P., LOAN, J. F., and SULLIVAN, J., “*In-situ* quadrupole mass-spectroscopy studies of water and solvent coordination to copper(II) beta-diketonate precursorsimplications for the chemical-vapor-deposition of copper,” *Materials Chemistry And Physics*, vol. 41, pp. 173–181, Aug. 1995.

- [176] ZHENG, Y. D., MIZUTA, H., TSUCHIYA, Y., ENDO, M., SATO, D., and ODA, S., “In situ real-time spectroscopic ellipsometry study of hfo₂ thin films grown by using the pulsed-source metal-organic chemical-vapor deposition,” *JOURNAL OF APPLIED PHYSICS*, vol. 97, p. 023527, Jan. 2005.
- [177] ZUIKER, C. D., GRUEN, D. M., and KRAUSS, A. R., “Laser-reflectance interferometry measurements of diamond-film growth,” *MRS Bulletin*, vol. 20, pp. 29–31, 1995.
- [178] ZUIKER, C. D., GRUEN, D. M., and KRAUSS, A. R., “In situ laser reflectance interferometry measurement of diamond film growth,” *Journal Of Applied Physics*, vol. 79, pp. 3541–3547, 1996.

VITA

Rentian Xiong was born in Jingdezhen, Jiangxi, China. He attended Zhejiang University in 1994 and received his Bachelor of Science degree in Chemical Engineering in 1998. He then worked as a research assistant in the National Laboratory of Secondary Resources Chemical Engineering in China, with a particular focus on supercritical fluid chromatography and its application to separate high purity Omega-3 fatty acids from fish oil. He attended the University of Cincinnati in 2001 and received the Master of Science degree in Chemical Engineering in 2003. His M.S. research under the supervision of Dr. Jerry Lin focused on the development of novel inorganic adsorbent for high temperature carbon dioxide separation. In 2003, he joined Dr. Martha Gallivan's group at Georgia Institute of Technology to pursue his doctoral degree. His PhD research is focused on *in situ* sensing for chemical vapor deposition based on estimation theory.

This dissertation was typeset by the author using L^AT_EX 2_ε